

**Plasma surface interactions in nanoscale processing:  
Preservation of low-*k* integrity and high-*k* gate-stack etching with Si selectivity**

by

**Juline Shoeb**

A dissertation submitted to the graduate faculty  
in partial fulfillment of the requirements for the degree of

DOCTOR OF PHILOSOPHY

Major: Electrical Engineering

Program of Study Committee:  
Mark J. Kushner, Major Professor  
Vikram L. Dalal  
Arun K. Somani  
Scott Chumbley  
Santosh Pandey

Iowa State University

Ames, Iowa

2012

Copyright © Juline Shoeb, 2012. All rights reserved.

## TABLE OF CONTENTS

	Page
ACKNOWLEDGEMENTS.....	iv
ABSTRACT.....	vi
CHAPTER 1. INTRODUCTION.....	1
1.1 Plasmas and Applications.....	1
1.2 Plasma Processing of Semiconductors.....	2
1.3 Low- <i>k</i> Dielectric Integrity.....	7
1.4 High- <i>k</i> Etching With Si Selectivity.....	10
1.5 Summary.....	11
1.6 Figures.....	13
1.7 References.....	20
CHAPTER 2. HYBRID PLASMA EQUIPMENT MODEL.....	24
2.1 Introduction.....	24
2.2 The Electromagnetics Module.....	25
2.3 The Fluid Kinetics Module.....	26
2.4 The Electron Energy Transport Module.....	29
2.4.1 The Electron Energy Equation Method.....	30
2.4.2 The Electron Monte Carlo Simulation.....	31
2.5 The Plasma Chemistry Monte Carlo Module.....	32
2.6 Monte Carlo Radiation Transport Model.....	35
2.7 Surface Chemistry Model.....	38
2.8 Typical Result from the HPEM.....	39
2.9 Figures.....	41
2.9 References.....	44
CHAPTER 3. MONTE CARLO FEATURE PROFILE MODEL.....	46
3.1 Introduction.....	46
3.2 Description of the Model.....	47
3.2.1 Computational Mesh and Particle Motion.....	47
3.2.2 Energetic Particle Interaction.....	50
3.2.3 Porous Material.....	51
3.3 Surface Reaction Mechanisms.....	53
3.4 Integrated Modeling Using MCFPM.....	54
3.5 Figures.....	56
3.6 References.....	59
CHAPTER 4. MECHANISMS FOR SEALING OF POROUS LOW- <i>k</i> SiOCH BY COMBINED He AND NH <sub>3</sub> PLASMA TREATMENT.....	61
4.1 Introduction.....	61
4.2 Reaction Mechanisms.....	63
4.3 Sealing Efficiency.....	68
4.4 Concluding Remarks.....	74
4.5 Figures.....	76
4.6 References.....	82

CHAPTER 5. DAMAGE BY RADICALS AND PHOTONS DURING CLEANING OF POROUS LOW- $k$ SiOCH USING Ar/O <sub>2</sub> AND He/H <sub>2</sub> PLASMAS.....	84
5.1 Introduction.....	84
5.2 Surface Reaction Mechanism.....	87
5.3 Plasma Properties.....	95
5.4 Demethylation.....	97
5.5 Consequences of VUV Photon Fluxes.....	103
5.6 Comparison of trends With Prior Works.....	105
5.7 Concluding Remarks.....	106
5.8 Tables.....	108
5.9 Figures.....	115
5.10 References.....	128
CHAPTER 6. NUMERICAL INVESTIGATION OF LOW- $k$ DEGRADATION BY HUMID AIR.....	131
6.1 Introduction.....	131
6.2 Surface Plasma Reaction Mechanisms.....	134
6.3 Low- $k$ Degradation: Ar/O <sub>2</sub> and He/H <sub>2</sub> Cleaning.....	141
6.4 Low- $k$ Integrity by Pore Sealing.....	143
6.5 Comparison with Experimental Trends.....	145
6.6 Concluding Remark.....	146
6.7 Figures.....	148
6.8 References.....	155
CHAPTER 7. MECHANISMS FOR PLASMA ETCHING OF HfO <sub>2</sub> GATE-STACKS WITH Si SELECTIVITY AND PHOTORESIST TRIMMING.....	158
7.1 Introduction.....	158
7.2 Description of the Model.....	160
7.3 Surface Plasma Reaction Mechanisms for Gate-stack Etching.....	163
7.3.1 Etching of HfO <sub>2</sub> .....	163
7.3.2 TiN Etching.....	167
7.3.3 Photo-resist Trimming, BARC Etching and PR Erosion.....	168
7.4 Plasma and HfO <sub>2</sub> Etch Properties.....	171
7.5 HfO <sub>2</sub> Etch Rate vs. Bias Voltage.....	172
7.5.1 Selectivity: Si-B Bond Formation.....	175
7.5.2 Selectivity: Polymer Deposition.....	176
7.5.3 Selectivity: Polymer Sputtering.....	176
7.6 Concluding Remarks.....	177
7.7 Tables.....	179
7.8 Figures.....	189
7.9 References.....	201
CHAPTER 8. CONCLUSIONS AND FUTURE WORK.....	203
8.1 Conclusions.....	203
8.2 Future Work.....	204
AUTHOR'S BIOGRAPHY.....	207

## ACKNOWLEDGMENTS

I'd like to express my deepest gratitude to Prof. Mark J. Kushner for his patience, guidance and support and for offering me the opportunity to work in his research group. I am thankful to him for sharing his immense knowledge of plasmas, directing my research, involving me in interesting projects and extending his help during my research. Without such support the PhD work would not have succeeded. Sincere thanks to him for the opportunities to participate in well-known conferences which enriched my domain of knowledge. I appreciate the privileges I enjoyed which enabled me to collaborate with important research groups, and which was essential to develop a clear idea in my area of research.

I'd like to sincerely thank Prof. Vikram L. Dalal, Prof. Arun K. Somani, Prof. Alan M. Russell and Prof. Santosh Pandey for their valuable time and contributions as members of my advisory committee. Special thanks to Prof. Vikram Dalal and Prof. Santosh Pandey for their help in the course work and Prof. Arun K. Somani for joining my preliminary exam, from India, via phone. Prof. Scott Chumbley has been very supportive of my research which always encouraged me.

Thanks to my MSEE supervisor Prof. Subbaraya Yuvarajan who initiated my graduate school research. In the modeling of little known surface-plasma reaction mechanisms, the knowledge I gained from my high-school chemistry teachers, Saroj Kumar Hazari and Ashish Kumar, played a significant role and I am grateful to them. Sincere thanks to Adam M. Urbanowicz of IMEC Belgium for helpful discussions and for the collaboration. I am grateful to Prof. Leo McAfee of EECS Dept. at the University of Michigan for all of his remarkable advice.

I am also grateful to the Semiconductor Research Corporation for their financial sup-

port toward my graduate studies. I am thankful to Vicky Thorland Oster and Pam Mayers at Iowa State Electrical Engineering Department for their help and guidance during my stay in Ames and Ann Arbor. Also, thanks to Dilok, Virginia and Becky of the international office at Iowa State for processing all of my requests with great care and expedience. Special thanks to Julia, of our group and Michelle of Rad Lab at the University of Michigan, for being very cooperative and patient.

Sincere thanks to research scientists Dr. Natalia Babaeva and Dr. Andy Xiong, of the group, for sharing their research experiences. They were always available to address all sorts of questions. My special thanks to the past Computational Optical and Discharge Physics group members, Dr. Peter Ventzek, Dr. Shahid Rauf, Dr. Ananth Bhoj, Dr. Ramesh Arakoni, Dr. Ankur Agrawal, Dr. Yang Yang, and Dr. Mingmei Wang for sharing their experiences and guidance throughout my graduate studies. Both Dr. Yang Yang and Dr. Wang deserve special thanks as they helped familiarize me with the group's codes and the systems. I also appreciate all the help and friendship I received from present group members, Jerry, Sang-Heon Song, Michael, Wei and Yiting.

Above all, I am most indebted to my parents, brothers and sister for their encouragement, patience and inspiration in my pursuit of my PhD. I wish to express my thanks to all of my friends in the U.S. and back home. I am thankful to all of my present and past roommates; especially Shishir, Farid, Akhter and Bony who have been very generous in sharing their knowledge.

**ABSTRACT**

Plasma-surface interactions are very important in the fabrication of the nm-sized features of integrated circuits. Plasma processes are employed to produce high-resolution patterns in many of the thin layers of silicon integrated circuits and to remove masking layers while maintaining high selectivity. Integrated plasma processes consisting of sequential steps such as etch, clean and surface modification, are used in semiconductor industries. The surface in contact with the process plasma is exposed to the fluxes of neutrals, ions, molecules, electrons and photons.

Modeling of surface reaction mechanisms requires the determination of the characterizations of fluxes (e.g. composition, magnitude, energy and angle) and development of the reaction mechanisms of the processes such as adsorption, reflection, bond breaking and etch product evolution, while reproducing the experimental results. When modeling the reaction mechanism for an entirely new material, the experimental data is often fragmentary. Therefore, fundamental principles such as bond energies and volatility of the etch products must be considered to develop the mechanism. In this thesis, results from a computational investigation of porous low- $k$  SiCOH etching in fluorocarbon plasmas, damage during cleaning of  $\text{CF}_x$  polymer etch residue in Ar/ $\text{O}_2$  and He/ $\text{H}_2$  plasmas,  $\text{NH}_3$  plasma pore sealing and low- $k$  degradation due to water uptake, will be discussed. The plasma etching of  $\text{HfO}_2$  gate-stacks is also computationally investigated with an emphasis on the selectivity between  $\text{HfO}_2$  and Si.

Porous dielectric materials offer lower capacitances that reduce RC time delays in integrated circuits. Typical porous, low dielectric (low- $k$ ) materials include SiOCH – silicon dioxide with carbon groups, principally  $-\text{CH}_3$ , lining the pores. Fluorocarbon plasmas are often used to etch such low- $k$  materials. These processes leave a fluorocarbon polymer on

the low- $k$  surface that must be removed, often with oxygen or hydrogen-containing plasmas. Pores open to the surface and which are internally connected, provide pathways for reactive species to enter into the porous network and produce damage. For example, plasma cleaning reactions of O atoms with  $-\text{CH}_3$  groups can increase the  $k$  value by removing C atoms. VUV photons which penetrate into the low- $k$  material, can also play a role in the scission of Si- $\text{CH}_3$  bonds and thus promote removal of  $-\text{CH}_3$  groups. In this thesis, results are presented from a computational investigation of Ar/ $\text{O}_2$  and He/ $\text{H}_2$  plasma damage in porous SiOCH cleaning while including the effects of VUV photons.

Sealing of the pores (up to a few nm in diameter) which blocks water uptake paths, is necessary to preserve *low-k* integrity (that is, maintain a low dielectric constant). Sequential treatment of porous SiOCH by He and  $\text{NH}_3$  plasmas is potentially a means of sealing pores while maintaining the low- $k$  of the dielectric material. The He plasma activates surface sites to accelerate the reactions responsible for pore sealing.  $\text{NH}_3$  plasma treatment completes the sealing through formation of Si-N, C-N and N-N bonds to bridge over the pore. In this thesis, mechanisms for such pore sealing are discussed.

To minimize leakage currents resulting from the thinning of the insulator in the gate-stack of field-effect-transistors, high-dielectric constant (*high-k*) metal oxides and  $\text{HfO}_2$  in particular, are being implemented as a replacement for  $\text{SiO}_2$ . To speed the rate of processing, it is desirable to etch the gate-stack (e.g. metal gate, anti-reflection layers, and dielectric) in a single process while having selectivity to the underlying Si. Plasma etching using Ar/ $\text{BCl}_3$ / $\text{Cl}_2$  mixtures effectively etches  $\text{HfO}_2$  while having good selectivity to Si. In this thesis, results from integrated reactor and feature scale modeling of gate-stack etching in Ar/ $\text{BCl}_3$ / $\text{Cl}_2$  plasmas, preceded by photo-resist trimming in Ar/ $\text{O}_2$  plasmas, will be discussed.

## 1. INTRODUCTION

### 1.1 Plasmas and Applications

Plasmas, in general, are partially ionized gas mixtures where a fraction of the atoms or molecules have lost an electron to produce positively charged ions. Electric and magnetic fields are used to create plasmas and to control their behavior. Plasmas are generated through dissipation of the electrical power supplied to a gas mixture. The power is transferred to electrons and such energetic electrons then undergo collisions with atoms and molecules of the mixture to produce ions, more electrons and radicals by initiating processes such as ionization, excitation and dissociation. Electron impact can ionize an atom or molecule in the plasma or dissociate a molecule producing free radicals. Free radicals may recombine with appropriate gas phase species to reproduce the state they originated from or create other species.[1] Free radicals and ions react with surfaces to modify those species and the surface.[1] Plasmas can be used to deliver required activation energy to a surface to be chemically or physically modified.[2]

Industrial plasmas are partially ionized and contain both neutrals and free radicals.[2] Two types of industrial plasmas are, (a) non-equilibrium, and (b) thermal plasmas.[2] Thermal plasmas have a high operating pressure and the electron and ion temperatures are similar, while non-equilibrium plasmas typically have low operating pressure and the electrons have a higher temperature than ions [2], though atmospheric pressure plasmas can also be non-equilibrium. Plasmas used in industry can be classified as a function of operating pressure. Fig. 1.1 shows a number of such manufacturing techniques. The vertical axis is the log of the operating pressure in Torr, while the horizontal axis describes the general nature of the various processes. When pressure is low, the collision frequency is also low and the charged

plasma particles play a dominant role in material processing, which makes the interaction primarily physical. With a rise in pressure, collisions in the plasma increase, so chemistry then becomes more dominant. When pressure is close to one atmosphere, the temperatures of ions and neutrals are nearly equal and the plasma density is higher.

Thermal plasmas are used as high temperature sources to react with gaseous reactants or solids.[2] The solid may be exposed to the thermal plasmas in the form of bulk matter for processes such as melting and refining.[3] Non-equilibrium plasma processes involve four simultaneous processes: sputtering, etching, polymerization and surface modification.[4] There are many applications of low-pressure non-equilibrium plasmas in semiconductor processing which are required for manufacturing microelectronic devices in integrated circuit industries.[2, 5-13] These applications are known as removal technologies such as etching, sputtering for film deposition, chemical vapor deposition (CVD), photo-resist (PR) stripping and different cleaning processes.[5]

## **1.2 Plasma Processing of Semiconductors**

Any solid that will be processed in plasmas has to be exposed to the plasma mixture. The plasma species interact with the surface of the solid based on their chemical affinity and the surface temperature of the solid. Plasma species can be either chemisorbed by the solid surface or can be adsorbed by the solid through a physisorption mechanism. For the chemisorption process, the reactions between plasma species and the surface generate volatile etch products which will be released into the gas mixture.[2] If the chemisorption reaction products are nonvolatile, such products will form a thin film on the surface of the solid.[2] When some particles of the plasma remain on or just below the solid surface without causing any

modification, it is known as implantation.[2,14] Optimizing operating conditions for plasmas in semiconductor processing requires fine tuning of the plasma composition to generate the required neutral and ion fluxes. The substrate bias has to be controlled in order to produce the required energy distributions for ions (to have certain etch rate or selectivity). The power is regulated to control fluxes of ions and photons and the sample temperature is optimized to control reactivity of the sample with plasma species.

In the earliest applications for semiconductor fabrications, plasmas were only used to strip photo-resist (PR) or for sputtering a target for deposition.[5] Sputtering is done using an inert gas where inert gas atoms are ionized and given a high kinetic energy with a bias power for bombarding a target surface to physically knock-off or sputter the target material atoms or molecules. The other use is in PR stripping.[5] PR layers are used as a mask layer to etch trenches and vias in Si or SiO<sub>2</sub> to delineate patterns. Later such PR layers are removed (unmasked or stripped off) using O<sub>2</sub> plasmas because the O atom is very reactive and can efficiently remove hydrocarbon PR as volatile CO or CO<sub>2</sub>.

Up to the 1970s, patterns in semiconductors were large enough to be created by wet etching.[15] However, as feature sizes in semiconductors became much smaller, dry etching became essential to achieve better control.[5] With time, the dimensions of transistors became smaller and smaller as described by Moore's law which stated that the number density of transistors would double every 18 months (Fig. 1.2). As such, with each technology node the gate length (the distance between source and drain region) in transistors has also reduced. The trend of decrease in gate length with time is shown in Fig. 1.3. This trend has also resulted in a dramatic drop in the per unit cost of computing power for processors.[5] The other advantage of plasma processing of semiconductors is the capability of gaining better con-

trol in producing anisotropic profiles (vertical) as the combined effects of directional ions and diffusive neutrals can create directional profiles, compared to round (isotropic) profiles produced by wet etching, as shown in Fig 1.4. Also, choosing the appropriate plasma mixture, the percentage composition of the mixture and bias allows one material to be etched, with expected selectivity, relative to another.[15,16]

Another major application of plasmas is plasma-enhanced chemical vapor deposition (PECVD).[17,18] In usual chemical vapor deposition (CVD), the deposition of a vapor on a substrate may require activation energies (from the temperature of the substrate) that exceeds the tolerances of the process. To increase the reactivity, the temperature of the substrate must also be increased. However, when a plasma is used, some of the species in the gas phase are excited which increase their reactivity with the heated substrate.[19] Consequently, a better growth rate of desired material can be achieved at a lower temperature than would be possible without using plasmas. For interconnect technology, the CVD technique is applied for atomic layer deposition (ALD) of diffusion barrier metals such as Ti and Ta to prevent the diffusion of Cu into the porous low- $k$  material. Such low- $k$  materials are used to reduce capacitance to enhance signal propagation speed. It has been reported that if plasma-enhanced ALD is used, this kind of deposition process can be done at a much lower temperature, which is vital for the stability of low- $k$  materials used in interconnect technology.[19-22]

Selecting a plasma mixture to etch any material such as Si for semiconductor processing, is primarily based on the volatility of the etch products. However, the selection can be affected by other parameters, such as good directionality or good etch-profile control. For example, etch rate for Si decreases in Cl-based plasmas compared to F-based plasmas and it

decreases even further if Br-based plasmas are used.[23] This is because deposition of Cl or Br compounds on the surface passivates the surface preventing the Cl or Br radical to react with Si. As such, the influence of energetic and directional ions has to increase to etch Si where such protective Cl or Br layers first have to be ablated by energetic ions which will expose Si, again, to etching agents of the plasma. Because of the enhanced influence of directional ions in the etching, Br-based plasmas will create a more vertical trench in Si as compared to F or Cl-based plasmas.

Temperature control can also be a way to improve anisotropy or directionality of etching.[23-26] Lowering temperature decreases the etching reaction probabilities between a radical and the surface. Also, it increases the adsorption reaction probabilities. As such, with a decrease in temperature there is a thicker formation of the passivation layer. In such a process, surface area increases and ion induced reactions with the surface dominate neutral reactions. Since the vertical etching component will dominate the lateral etching component, a directional profile can be achieved by lowering the temperature. However, if the temperature is too low, the passivation layer will be too thick to allow the ions to interact with the material.[23]

In plasma processing of semiconductors, the material to be processed is negatively biased by the external power supply.[23] Thus, positive ions attracted by the negative bias will bombard the wafer. Ions will cause both physical and chemical sputtering of the solid which will enhance the etch rate. Radicals usually have >100 times higher flux than ions and will play the dominant role in etching by chemically interacting with the surface and removing the molecules and atoms as volatile products. Radicals can also passivate the solid surface with polymer like layers if the energy of the ions is not too high to sputter off the protec-

tive polymer coating. Formation of such protective layers, by radicals on a solid, will allow etching of the solid selectively relative to another by controlling the energy of the ions in the plasma so that the ion energy is higher than the etching threshold of the first solid, but lower than the second. Major surface-plasma interaction mechanisms in plasma etching of a solid are shown in Fig. 1.5.

The two main types of reactors used for semiconductor etching are: capacitively coupled plasma (CCP) system and inductively coupled plasma (ICP) system.[23] In a CCP system (Fig. 1.6), bias is applied on the powered electrode so the energy of an ion is a function of the power applied to feed the plasma. As such, ion fluxes and ion energies are not independent parameters.[23] Generation of a high plasma density, which is essential for a high flux of reactive species such as ions and photons, increases the energy of ions. Selective etching of a solid, with a high density plasma, becomes impossible as ion energy increases with the density of the plasma and such ions sputter off the protective passivation layer. On the other hand, low pressure is necessary in plasma semiconductor processing to increase ion bombardment efficiency. However, in a CCP, the electron-neutral collision mean-free path can be of the same order of the gap between the CCP electrodes. As a result, sustaining the plasma in a CCP becomes difficult.

The ICP system allows production of dense plasmas at low pressure without increasing the ion energy.[27] Power is applied to the plasma by an inductive coupling between the plasma and the antenna, through a dielectric window. No bias is applied between the plasma and the chamber wall. The sample to be processed is located on a separate holder. The energy of ions in the plasma can be controlled independently from chamber pressure and plasma density by biasing the substrate. As such, without increasing the ion energy, high plasma

density can be produced at a low pressure which enables formation of passivation layers on sidewalls during trench etching (necessary for a vertical profile) and polymer deposition on a solid to etch it selectively, relative to another solid. A schematic representation of a typical ICP reactor is shown in Fig. 1.7.

### 1.3 Low- $k$ Dielectric Integrity

Porous dielectrics, having a low dielectric constant (*low-k*), are being used to lower the interconnect wiring capacitance in order to limit the  $RC$  time delay in integrated circuits.[28] SiCOH, silicon dioxide with  $\text{CH}_x$  groups lining the pores, is one commonly used material, having porosities as large as 50% with pore diameters of up to a few nm. The pores can also be interconnected, offering pathways for reactive species to enter into the porous network during plasma etching or cleaning steps.[28,29] Such penetrations are thought to compromise the *low-k* nature of the material by removing the hydrophobic  $\text{CH}_n$  groups that surround the pore surface. Once a  $\text{CH}_n$  group is removed, the Si atom attached to it adsorbs moisture from ambient air which increases the  $RC$  time delay because the high  $k$  of water ( $\approx 80$ ) increases the overall dielectric constant of the *low-k*. As a result, a plasma treatment that minimizes  $\text{CH}_n$  group consumption is essential for maintaining porous *low-k* integrity.

In order to maintain the *low-k* values of porous dielectrics and to prevent penetration of plasma species into the material, sealing of the pores at the surface may be necessary.[30] Dielectrics are typically etched in fluorocarbon plasmas in which there is deposition of a  $\text{CF}_x$  polymer. The residual  $\text{CF}_x$  polymer remaining at the end of the etch can, in fact, effectively seal the pores.[31] While  $\text{CF}_x$  polymers have good characteristics because of their low dielectric constant, the fluorine in the polymers might create compatibility issues with diffusion

barriers, including chemically active metals like Ti and Ta.[31] As such, the  $CF_x$  polymer must be removed while then implementing other more integration-compatible treatments for pore sealing.

Due to its reactive nature,  $O_2$  plasmas were traditionally used for  $CF_x$  polymer or PR removal, however, less reactive  $H_2/He$  plasmas can be more beneficial in protecting the surface from damage while also activating the surface, so as to assist the subsequent sealing of the porous surface.  $O_2$  plasmas contain O radicals which are very reactive and remove hydrophobic  $CH_n$  groups efficiently with exothermic reactions. In  $He/H_2$  plasma cleaning, the most reactive radical is H which removes both polymer and PR mildly because the etching reactions are primarily endothermic. It has been reported that  $H_2$  plasmas cause insignificant damage to the  $CH_n$  groups. The other advantage in  $He/H_2$  cleaning is the less significant role of the photons compared to  $O_2$  plasmas.  $O_2$  plasmas contain photons with wavelengths of 130 nm and beyond; such photons can penetrate >100 nm in the low- $k$  causing Si-C bond scission. Once a Si-C bond has been cleaved, adsorbed  $-CH_n$  groups are easily etched by reactive radicals. Thus, photons in  $O_2$  plasmas help O radicals to remove  $-CH_n$  groups from at least 100 nm deep sites.  $He/H_2$  plasmas include photons with wavelengths < 60 nm which do not penetrate more than 20 nm in the low- $k$ . As such, bond scission of Si-C bond in  $He/H_2$  plasma treatment is limited to 20 nm and H radicals can cause damage in the top 20 nm region of the low- $k$ .

Sequential treatment of SiCOH by He and  $NH_3$  plasmas has been shown to seal pores without surface damage while maintaining the low- $k$  values of the SiCOH.[32] He plasmas are thought to create active surface sites which localize and accelerate the chemical reactions responsible for pore sealing.[32] It was found that if  $H_2$  is added to He, hot H atoms can im-

prove the surface activation as energetic H fluxes can remove H from surfaces and pore-interior  $-\text{CH}_n$  groups, thereby producing reactive  $-\text{CH}_{n-1}$  like groups. This is due to the fact that hot H flux is not directional like the  $\text{He}^+$  which is the dominant agent for such activation in He plasmas. Subsequent  $\text{NH}_3$  plasma treatment completes the sealing through formation of Si-N, C-N and N-N bonds resulting from the chemisorption of  $\text{NH}_x$  species.[32] The bridging of these bonds across the opening of the pores effectively seals the pores. Such pore sealing is able to prevent toluene penetration into the profile which validates the blocking of surface pores (Fig. 1.8).[32]

If the low- $k$  is exposed to humidity after cleaning in Ar/ $\text{O}_2$  and He/ $\text{H}_2$  plasmas, adsorption of  $\text{H}_2\text{O}$  molecules by  $-\text{CH}_n$  lost Si sites ( $-\text{CH}_n$  were etched during cleaning) forms Si-OH type products. Si-OH type compounds have a high- $k$  which will increase the overall dielectric constant of the porous material, with treatment time, as shown in Fig. 1.9. After cleaning, if the low- $k$  surface pores are sealed with  $\text{NH}_3$  plasmas, the sealing has been shown to prevent water adsorption from humid air. This is because Si-N and C-N compounds formed during sealing block water uptake pathways as shown in Fig. 1.10. As such, the sealing layer is able to preserve the integrity of the low- $k$  material.

A fully integrated multi-step etch, clean, activation and pore sealing processes using Ar/ $\text{O}_2$  and He/ $\text{H}_2$  plasma cleans was modeled. The sequence begins with etching of an 8:1 aspect ratio trench in porous SiCOH using an Ar/ $\text{C}_4\text{F}_8/\text{O}_2$  CCP. Residual  $\text{CF}_x$  polymers on the sidewalls of the SiCOH were then removed using either Ar/ $\text{O}_2$  or  $\text{H}_2/\text{He}$  inductively coupled plasma (ICP). For Ar/ $\text{O}_2$  clean, subsequent surface activating He ICP followed by sealing Ar/ $\text{NH}_3$  ICP treatments were applied to seal the pores open to the surface. For  $\text{H}_2/\text{He}$

plasma cleaning, surface sites were activated by hot H, He<sup>+</sup> and photons present in the cleaning mixture, an Ar/NH<sub>3</sub> treatment following the clean was sufficient for sealing.

After cleaning, the profile was exposed to humidity and included water in our model resulting in the reactions between –CH<sub>3</sub> free Si sites and H<sub>2</sub>O that form Si-OH type compounds. The  $k$  degradation resulting from water uptake by the cleaned and unsealed profile was numerically investigated. The degradation or rise in the  $k$  value after pore sealing was also computationally investigated to see if sealing pores can preserve the low- $k$  integrity by blocking water uptake.

#### **1.4 High- $k$ Etching With Si Selectivity**

As feature sizes decrease, the gate-silicon dioxide equivalent thickness required for the insulator also decreases.[33] A larger oxide capacitance (thinner oxide layer) is necessary to invert the surface to a sufficient sheet charge density in order to obtain the expected transistor current for a given supply voltage. Continuing to reduce the insulator thickness using SiO<sub>2</sub> is problematic as leakage currents due to tunneling, increase as the thickness approaches a monolayer.[34] Consequently, high dielectric constant (*high-k*) metal oxides and HfO<sub>2</sub> in particular, are being implemented as replacements for SiO<sub>2</sub> in gate-stacks to minimize leakage currents resulting from thinning of the insulator. The larger dielectric constant allows the oxide to be thicker for a given capacitance, thereby decreasing electric fields and leakage currents. The gate length required for an SiO<sub>2</sub> gate insulator as a function of time, as projected by the 2009 International Technology Roadmap for Semiconductors (ITRS), is shown in Fig. 1.3.

A *high-k* dielectric and a poly-Si gate are typically not suitable for high performance

for drive current.[34] Metal gates, having a higher free carrier density, maintain a high mobility at junctions with *high-k* dielectrics and so many advanced designs incorporate metal gates.[34] TiN is one such metal being considered for the gate.[35]

It has been found that HfO<sub>2</sub> gate-stacks can be etched using BCl<sub>3</sub>/Cl<sub>2</sub> plasmas, while having a good selectivity to underlying Si by forming a BCl<sub>n</sub> polymer on the Si which slows its etching.[36] B<sub>n</sub>Cl<sub>m</sub> radicals coming from the plasma reacts with Si and forms a layer of Si<sub>x</sub>B<sub>y</sub> compounds. Formation of such Si<sub>x</sub>B<sub>y</sub> layers is shown in Fig. 1.11. Once such a layer is formed, BCl<sub>n</sub> polymers are deposited and passivate the Si substrate. If the ion energy of BCl<sub>3</sub>/Cl<sub>2</sub> is controlled in such a way that it is higher than the etching threshold of HfO<sub>2</sub> but less than the Si etching threshold, an infinite selectivity for HfO<sub>2</sub>/Si etching can be achieved. Fig. 1.12 shows the control of HfO<sub>2</sub>/Si selectivity by varying bias and BCl<sub>3</sub> percentage in the plasma.

A surface reaction mechanism for HfO<sub>2</sub> etching in Ar/BCl<sub>3</sub>/Cl<sub>2</sub> plasmas was developed and HfO<sub>2</sub>/Si selectivity was computationally investigated. In the model, Hf-O bond breaking was the first step followed by Cl adsorption by Hf atoms that produced solid HfCl<sub>x</sub> and BCl<sub>x</sub> adsorption by bond cleaved O that generated solid B<sub>m</sub>OCl<sub>n</sub>. Later HfCl<sub>x</sub> and B<sub>m</sub>OCl<sub>n</sub> solids were etched as volatile HfCl<sub>x</sub> (x=2-4), BOCl, B<sub>2</sub>OCl<sub>3</sub> and B<sub>2</sub>OCl<sub>4</sub> by ion impact reactions.

## 1.5 Summary

In Chapter 2, a detailed description of the Hybrid Plasma Equipment Model (HPEM), which is the equipment scale model used in this work, is presented. The different modules of the HPEM and the physics used for our simulations are explained. The Plasma Chemistry

Monte Carlo Model (PCMCM) in the HPEM generates the Energy and Angular Distributions (EADs) of the different ions and neutral species on the wafer. Typical results from the HPEM and PCMCM are presented.

In Chapter 3, the Monte Carlo Feature Profile Model (MCFPM) used for the simulations in this work is explained in detail. The MCFPM uses the EADs from the PCMCM as input. Typical results for integrated modeling of semiconductor processes (etch, clean and pore sealing) are presented.

In Chapter 4, the pore sealing mechanisms of porous low- $k$  SiCOH with successive He and NH<sub>3</sub> plasmas are described. Effects of some parameters, such as pore radius, aspect ratio of the trench and plasma treatment time have been described in detail.

In Chapter 5, plasma damage during CF<sub>x</sub> polymer cleaning and PR stripping in Ar/O<sub>2</sub> and He/H<sub>2</sub> plasmas have been summarized and compared. The impact of photons on the damage mechanism has been explained. The degree of plasma damage in the low- $k$  material is estimated by the damage depth or the depth of a SiO<sub>2</sub>-CH<sub>3</sub> site that has lost the -CH<sub>3</sub> group due to its interaction with plasma species.

In Chapter 6, low- $k$  degradation mechanisms or the mechanisms responsible for the increase in dielectric constant of porous SiCOH film have been described. The degradation is compared between Ar/O<sub>2</sub> and He/H<sub>2</sub> plasma cleaning. Preservation of low- $k$  Integrity by pore sealing, after cleaning to block water uptake, has been numerically investigated.

In Chapter 7, reaction mechanisms for a TiN/HfO<sub>2</sub>/SiO<sub>2</sub>/Si gate stack etching in Ar/BCl<sub>3</sub>/Cl<sub>2</sub> plasmas and PR trimming in Ar/O<sub>2</sub> plasmas have been described. Achievement of a high HfO<sub>2</sub>/Si selectivity in the plasma was investigated by varying substrate bias.

## 1.6 Figures

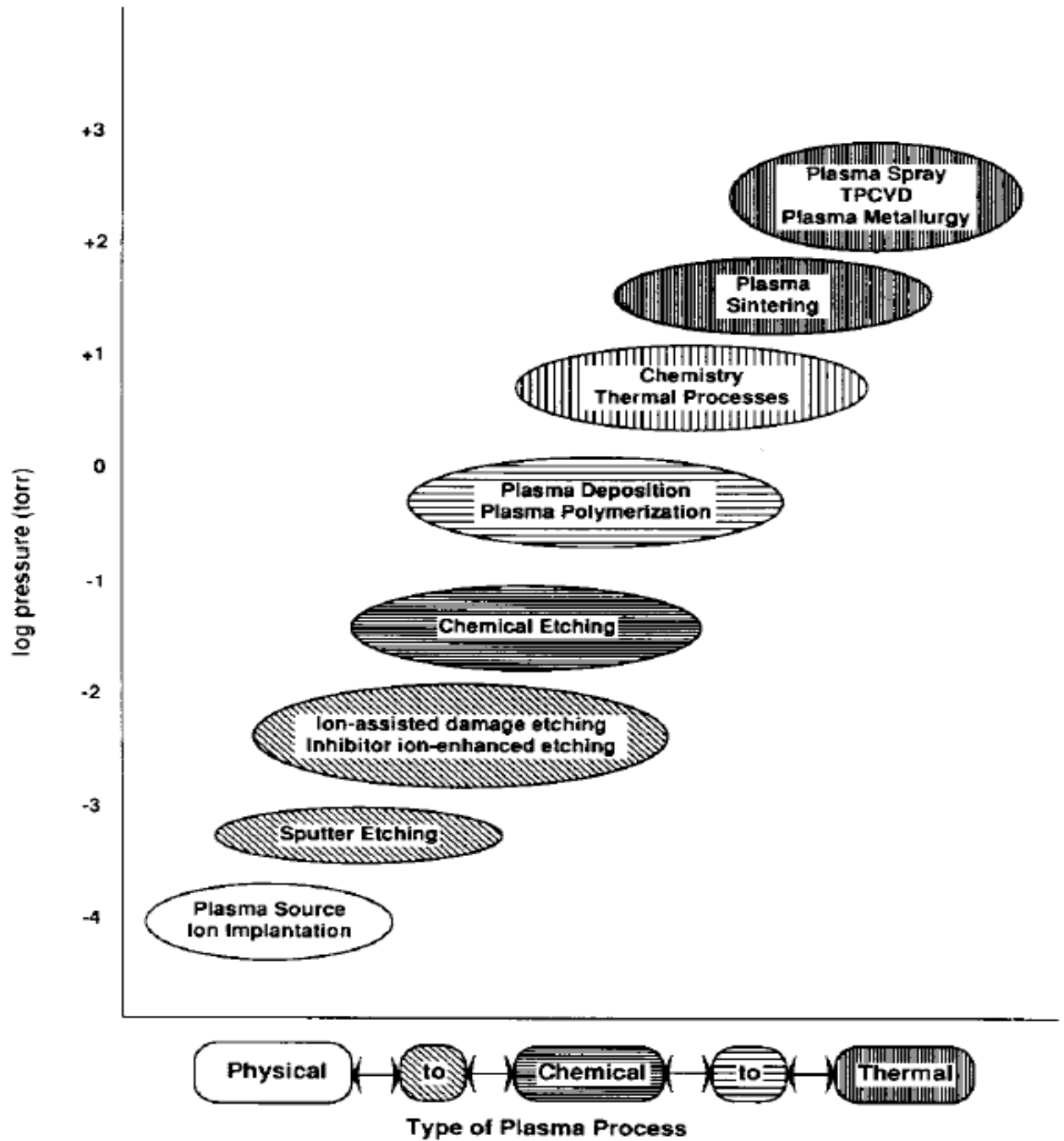


Fig. 1.1 Plasma processes arranged by operating pressure. As the pressure increases, the character of the process tends to move from physical to chemical to thermal in nature.[2]

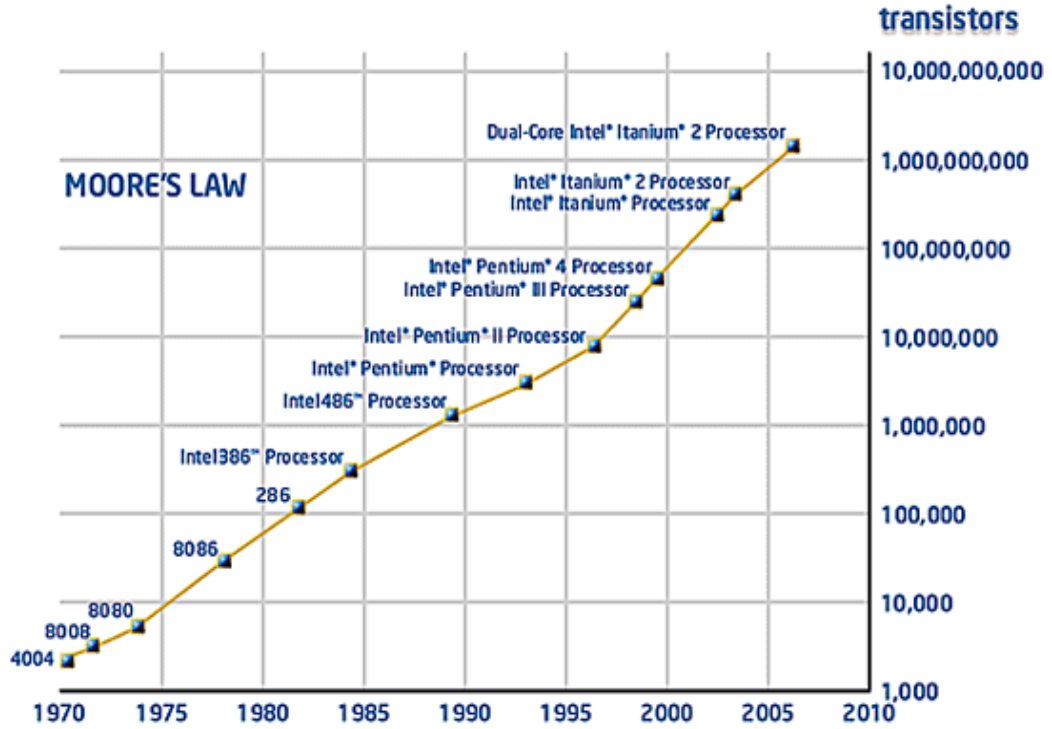


Fig. 1.2 Graphical representation of Moore's Law.

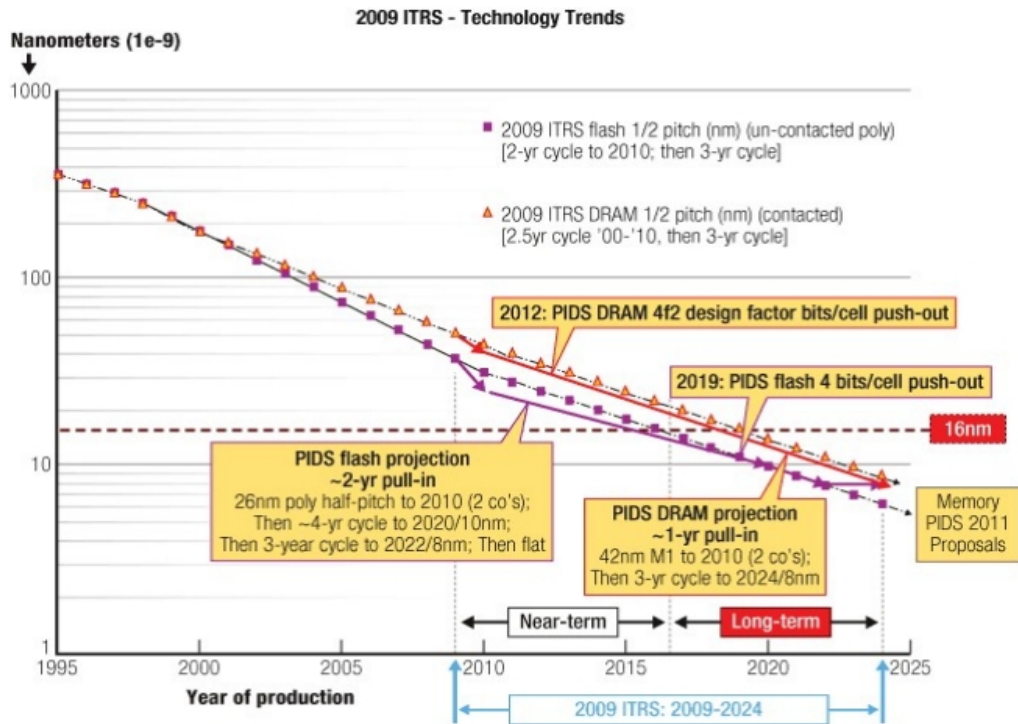


Fig. 1.3 Gate length as a function of time projected by ITRS 2009.

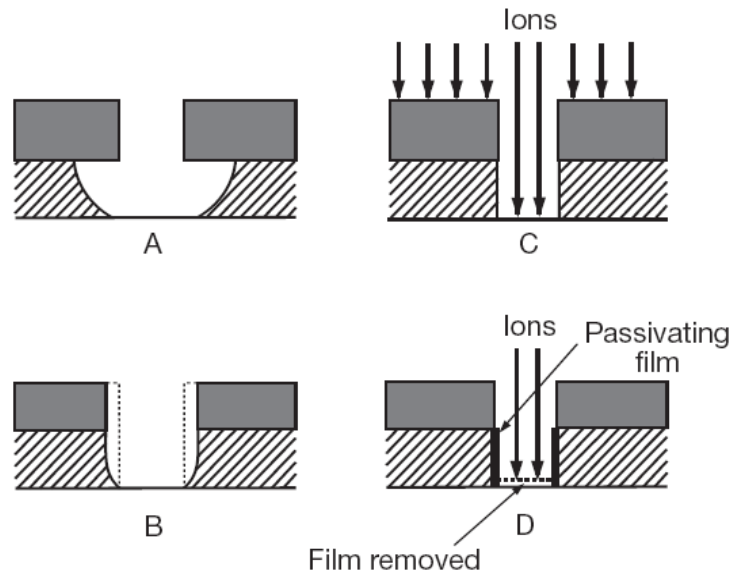


Fig. 1.4 Plasma etching in integrated circuit manufacturing: (a) an example of an isotropic etch; (b) a sidewall etching of the resist mask which leads to a loss of anisotropy in film etch; (c) illustrates the role of bombarding ions in an isotropic etch; (d) illustrates the role of side-wall passivating films in an isotropic etch.[37]

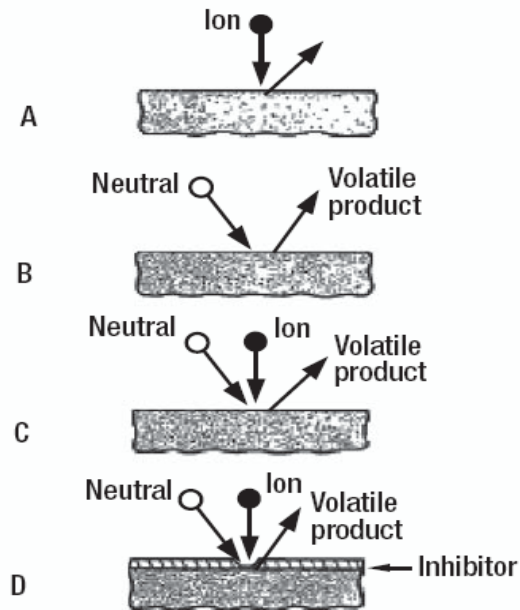


Fig. 1.5 Four basic plasma etching processes: (a) sputtering; (b) pure chemical etching; (c) ion energy-driven etching; (d) ion-enhanced inhibitor etching.[37]

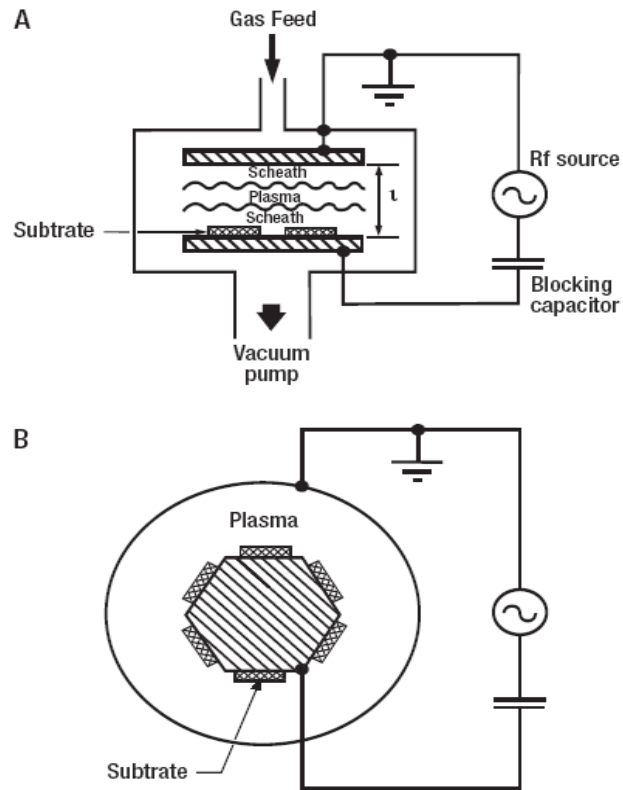


Fig. 1.6 Capacitive RF discharges in (a) plane parallel geometry, and (b) coaxial "hexode" geometry.[37]

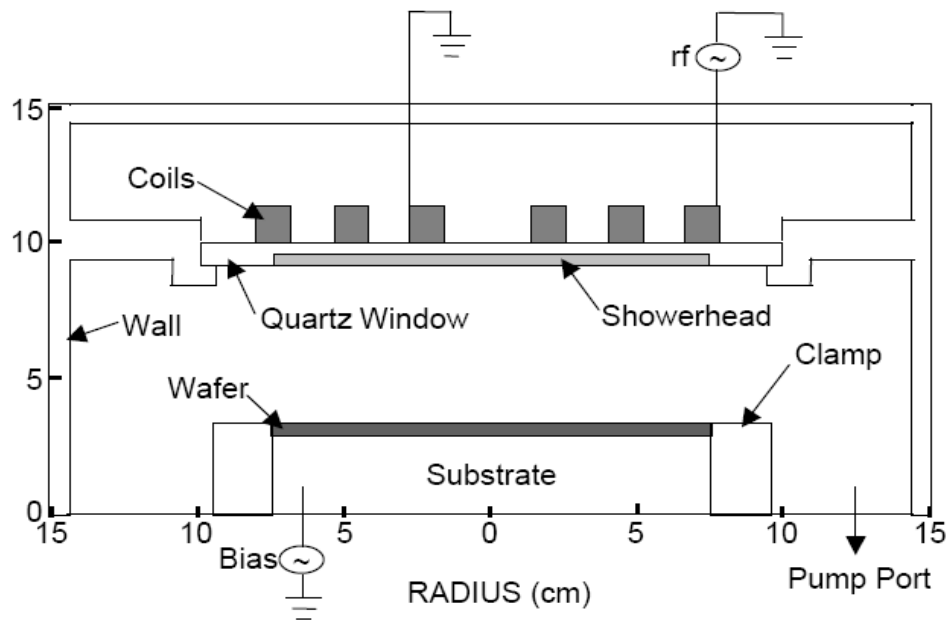


Fig. 1.7 Schematic of a typical ICP reactor.

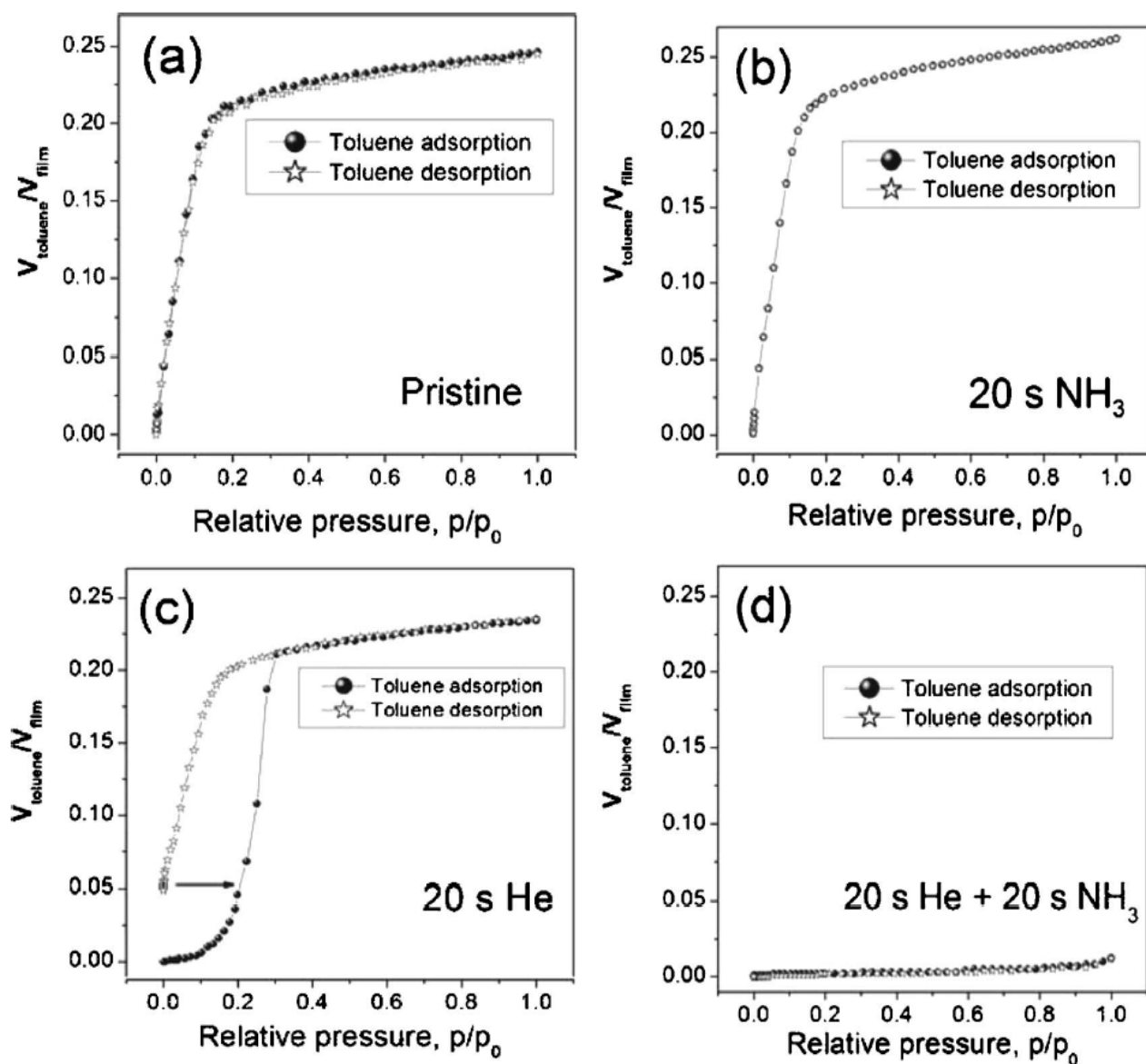


Fig. 1.8 Pore sealing determined by toluene penetration into the porous sample: (a) pristine sample, (b) after  $\text{NH}_3$  plasma, (c) after He plasma, (d) He +  $\text{NH}_3$  plasma.[32]

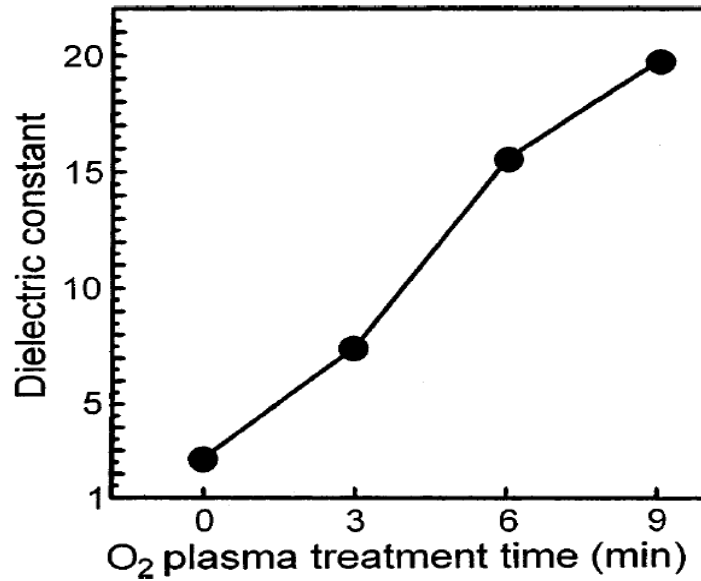


Fig. 1.9 Dielectric constant degradation of porous low- $k$  film with O<sub>2</sub> plasma treatment time (300 mTorr, rf power 300 W, 300 °C).[38]

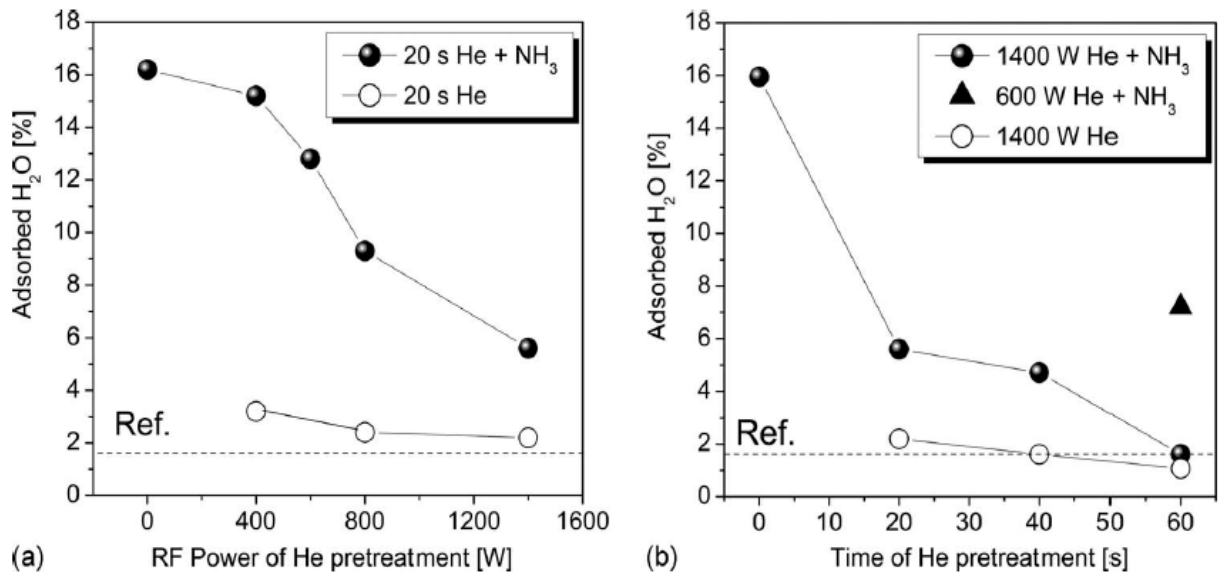


Fig. 1.10 (a) The amount of adsorbed water (as measured by water-based ellipsometric porosimetry) of as-deposited He-plasma-treated and He + NH<sub>3</sub>-plasma-treated low- $k$  films versus rf power during He plasma treatment. (b) The amount of adsorbed water (as measured by water-based ellipsometric porosimetry) of as deposited He-plasma-treated and He + NH<sub>3</sub>-plasma-treated low- $k$  films vs. treatment time.[39]

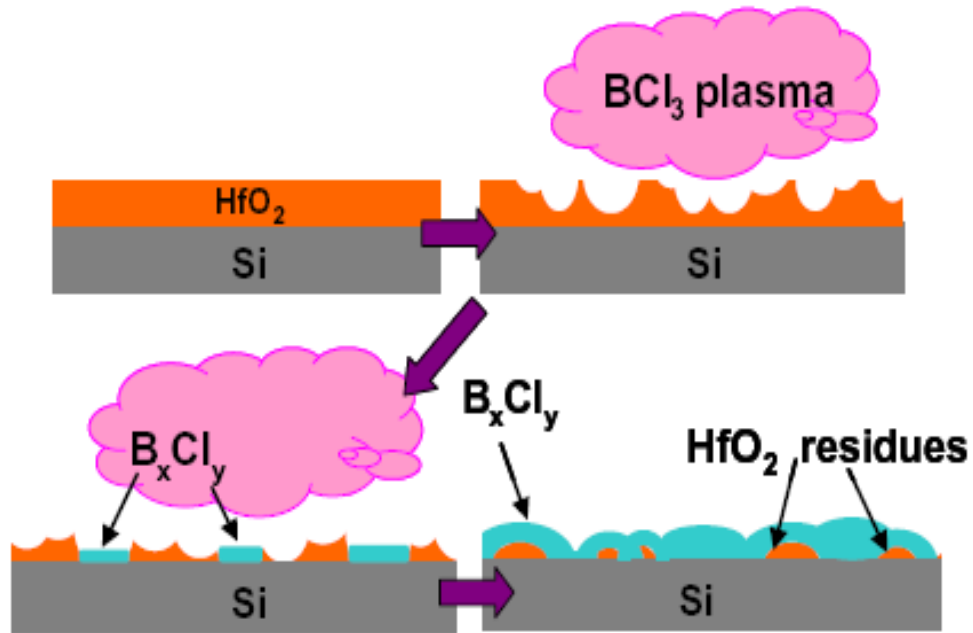


Fig. 1.11 Protective  $B_xCl_y$  layer formation which is essential for a good  $HfO_2/Si$  selectivity.[40]

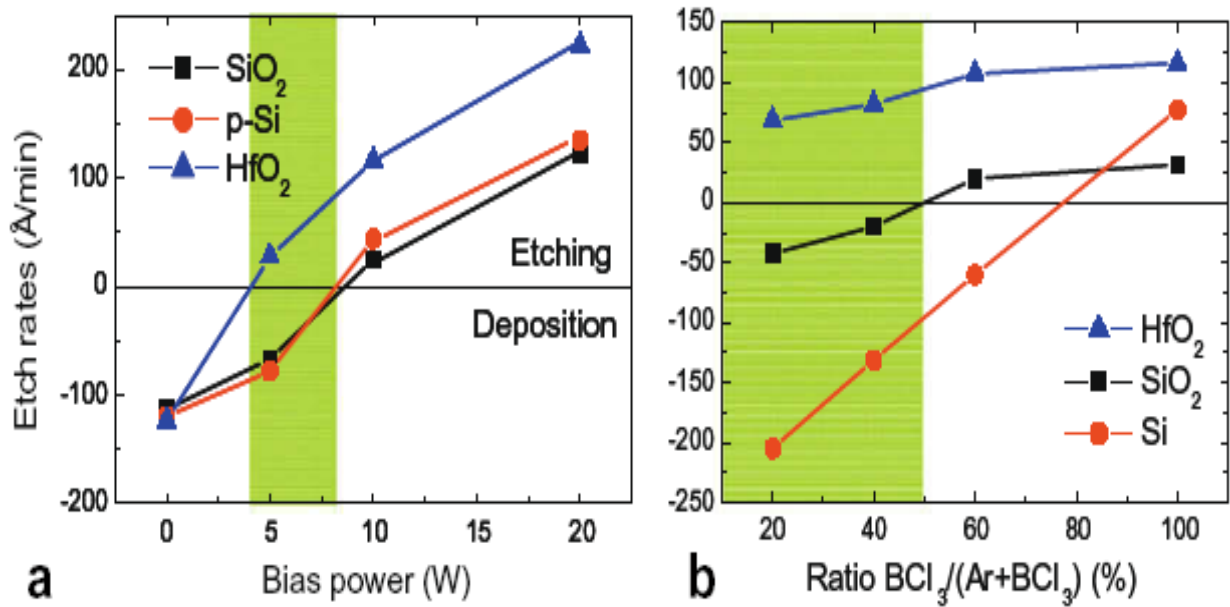


Fig. 1.12 Etch and deposition rates on  $HfO_2$ ,  $SiO_2$  and p-Si as a function of (a) bias power in pure  $BCl_3$  plasma/clean walls, and (b) argon dilution at 10W bias/clean walls. The colored zones represent conditions for which infinite selectivity is achieved.[40]

## 1.7 References

1. L. E. Kline and M. J. Kushner, Crit. Reviews in Solid State and Materials Sci. **16(1)**, 1 (1989).
2. J. L. Shohet, IEEE Trans. Plasma Sci., Vol. **19( 5)**, 725 (1991).
3. Special Issue on Thermal Plasma Processing, Plasma Chem. Plasma Process., vol. 9 (suppl.), 1989.
4. D. M. Manos and D. L. Flamm, in Plasma Etching, D. M. Manos, Ed. San Diego: Harcourt, Brace, Jovanovich, 1989.
5. D. B. Graves, IEEE Trans. Plasma Sci., Vol. **22( 1)**, 31 (1994).
6. D. B. Graves, AIChE J. **35**, 1 (1989).
7. S. M. Rossnagel, J. J. Cuomo, and W. D. Westwood, Eds., Handbook of Plasma Processing Technology. Park Ridge, NJ: Noyes Publications, 1990.
8. J. W. Cobum, Plasma Etching and Reactive Ion Etching, New York: AVS Monograph Series, 1982.
9. B. Chapman, Glow Discharge Processes, New York, Wiley, 1980.
10. T. Sugano, Applications of Plasma Processes to VLSI Technology, New York: Wiley, 1985.
11. N. G. Einspruch and D. M. Brown, Eds., VLSI Electronics Microstructure Science, Plasma Processing for VLSI, Orlando: Academic, vol. 8, 1984.
12. D. Manos and D. Flamm, *Plasma Etching*, San Diego: Academic, 1988.
13. M. Konuma, Film Deposition by Plasma Techniques, Berlin: Springer-Verlag, 1992.
14. P. K. Chu, S. Qin, And C. Chan, N. W. Cheung, And P. K. Ko, IEEE Trans. on Plasma Sci. **26( 1)**, 79 (1998).

15. H. Abe, Y. Sonobe, and T. Enomoto, *Jpn. J. Appl. Phys.* **12**, 287 (1973).
16. F.H. Bell, O. Joubert, G.S. Oehrlein, Y. Zhang, D. Vender, *J. Vac. Sci. Technol. A* **12**, 3095 (1994).
17. *Handbook of Plasma Processing Technology: Fundamentals, Etching, Deposition, and Surface Interactions*, edited by S. M. Rossnagel, J. J. Cuomo, and W. D. Westwood (Noyes, Park Ridge, NJ, 1990).
18. R. Reif and W. Kern, in *Thin Film Process II*, edited by J. L. Vossen and W. Kern (Academic, New York, 1991).
19. S. M. Rossnagel, A. Sherman, and F. Turner, *J. Vac. Sci. Technol. B* **18(4)**, 2016 (2000).
20. H. Kim, *J. Vac. Sci. Technol. B* **21(6)**, 2231 (2003).
21. H. Kim, A. J. Kellock, and S. M. Rossnagel, *J. Appl. Phys.* **92**, 7080 (2002).
22. J.-S. Park, M. J. Lee, C.-S. Lee, and S.-W. Kang, *Electrochem. Solid-State Lett.* **4**, C17 (2001).
23. Christophe Cardinaud, Marie-Claude Peignon, and Pierre-Yves Tessier, *Appl. Sur. Sci.* **164**, 72 (2000).
24. S. Tachi, K. Tsujimoto, S. Arai, T. Kure, *J. Vac. Sci. Technol. A* **9**, 796 (1991).
25. T. Chevolleau, P.-Y. Tessier, Ch. Cardinaud, G. Turban, *J. Vac. Sci. Technol. A* **15**, 2661 (1997).
26. P.-Y. Tessier, T. Chevolleau, Ch. Cardinaud, B. Grolleau, *Nucl. Instrum. Methods B* **155**, 280 (1999).
27. W.L. Johnson, in: O. Popov (Ed.), *High Density Plasma Sources*, Noyes Data Corp., Park Ridge, NJ, 1979.

28. C. M. Whelan, Q. T. Le, F. Cecchet, A. Satta, J. J. Pireaux, P. Rudlof, and K. Maex, *Electrochem. Solid-State Lett.* **7**, F8 (2004). [28]
29. G. Beyer, A. Satta, J. Schuhmacher, K. Maex, W. Besling, O. Kilpela, H. Sprey, G. Tempel, *Microelectron. Eng.* **64**, 233 (2002).
30. T. Abell and K. Maex, *Microelectron. Eng.* **76**, 16 (2004).
31. G. Mannaert, M. R. Baklanov, Q. T. Le, Y. Travaly, W. Boullart, S. Vanhaelemeersch, and A. M. Jonas *J. Vac. Sci. Technol. B* **23**, 2198 (2005).
32. M. Urbanowicz, M. R. Baklanov, J. Heijlen, Y. Travaly, and A. Cockburn, *Electrochem. Solid-State Lett.* **10**, G76 (2007).
33. B. H. Lee, L. Kang, R. Nieh, W.-J. Qi, and J. C. Lee, *Appl. Phys. Lett.* **76**, 1926 (2000).
34. R. Chau, J. Brask, S. Datta, G. Dewey, M. Doczy, B. Doyle, J. Kavalieros, B. Jin, M. Metz, A. Majumdar, and M. Radosavljevic, *Microelectron. Engr.* **80**, 1 (2005).
35. R. Chau, S. Datta, M. Doczy, B. Doyle, J. Kavalieros, and M. Metz, *Elect. Dev. Lett.* **25**, 408 (2004).
36. O. Joubert, E. Sungauer, E. Pargon, X. Mellhaoui, R. Ramos, G. Cunge and L. Valier, *J. Vac. Sci. Technol. B* **25**, 1640 (2007).
37. Pall corporation research, <http://www.pall.com/pdfs/Microelectronics/ABG-106-0405.pdf>.
38. K. Maex, M. Baklanov, D. Shamiryan, F. Iacopi, S. H. Brongersma, K. Maex, and Z. S. Yanovitskaya, *J. Appl. Phys.* **93**, 8793 (2003).
39. A. M. Urbanowicz, D. Shamiryan, A. Zaka, P. Verdonck, S. De Gendt and M. R. Baklanov, *J. Electrochem. Soc.* **157**, H565 (2010).

40. E. Sungauer, X. Mellhaoui, E. Pargon, and O. Joubert, *Microelectron. Eng.* **86**, 965 (2009).

## 2. HYBRID PLASMA EQUIPMENT MODEL

### 2.1 Introduction

The Hybrid Plasma Equipment Model (HPEM) was developed for simulating low-temperature, low-pressure plasma processes such as plasma etching and plasma-assisted deposition.[1-18] The HPEM has been used to predict the reactor scale plasma characteristics and reactant fluxes to surfaces in the ICP reactor.

The HPEM is a two-dimensional (2D), modular model which addresses gas phase and surface kinetics. (See Fig. 2.1) The HPEM addresses plasma physics and plasma chemistry in a modular fashion. There are three main blocks: The Electromagnetic Module (EMM), the Electron Energy Transport Module (EETM) and the Fluid Kinetic Module (FKM). Electromagnetic fields are derived by solving the frequency domain wave equation based on coil currents adjusted to deliver a specified power deposition. The spatially dependent power deposition is used as a source term in obtaining the electron temperature,  $T_e$ , from an electron energy conservation equation. Transport and rate coefficients as function of average electron energy are obtained from a solution of Boltzmann's equation, and a Monte Carlo simulation is used to follow the trajectories of sheath accelerated secondary electrons. The transport coefficients and source functions are used by the FKM to solve separate continuity, momentum, and energy equations for each ion and neutral species, while semi-implicitly solving Poisson's equation for the time varying electrostatic potential. The densities and electrostatic fields from the FKM are then transferred to the other modules. This process is iterated until a converged quasi-steady state solution is obtained.

Several off-line modules of the HPEM have been developed for other specific purposes. The Plasma Chemistry Monte Carlo Simulation (PCMCS) computes energy and angu-

lar dependencies of fluxes at specified surface locations by using outputs from the HPEM [6]. The Monte Carlo Feature Profile Model (MCFPM) uses the results of the PCMCS or the PCMCM to simulate nanoscale feature profile evolution [15]. The physics of these modules contained in the HPEM will be described in the following sections. Also, typical results from the HPEM will be presented.

The Monte Carlo Radiation Transport Module (MCRTM) inputs the gas densities, temperatures, pressures, collision frequencies and rate coefficients for all the gas phase reactions (including radiative reactions), and modifies the rate coefficient for the radiative reactions. The Surface Chemistry Module (SCM) reads in fluxes to the surfaces of interest and returns sticking coefficients and modified gas fluxes from the surface, after the surface reactions are computed. Both MCRTM and SCM will be described in the upcoming chapters.

## 2.2 The Electromagnetic Module

Starting with an initial guess of plasma properties, the EMM computes the inductively coupled electric fields determined by the inductive coils and the magnetostatic fields induced by permanent magnets or dc current loops. These fields are passed to the EETM. The EMM computes time varying electric and magnetic fields for the HPEM.

The EMM module calculates the spatially dependent azimuthal electric fields by solving Maxwell's equation under time harmonic conditions. Assuming azimuthal symmetry, Maxwell's equation for electric fields is reduced to

$$\nabla \cdot \frac{1}{\mu} \nabla E_\phi = \omega^2 \epsilon E_\phi - i \omega J_\phi, \quad (2.1)$$

where  $\mu$  is the permeability,  $E_\phi$  is the azimuthal electric field,  $\omega$  is the frequency of the source current,  $\varepsilon$  is the permittivity, and  $J_\phi$  is the total current consisting of driving and conduction currents. The conduction current  $J_c$  is calculated from  $J_c = \sigma E_\phi$ , where  $\sigma$  is the conductivity. For collisional plasmas, the plasma conductivity is

$$\sigma = \frac{q_e^2 n_e}{m_e} \frac{1}{\nu_{me} + i\omega}, \quad (2.2)$$

where  $q_e$  is the unit electron charge,  $n_e$  represents electron density,  $m_e$  denotes electron mass,  $\nu_{me}$  is the momentum transfer collision frequency of electrons, and  $\omega$  is the driving frequency. Maxwell's equations are solved using the successive over-relaxation (SOR) technique. The weighting coefficient and the convergence criterion for the SOR are adjustable simulation parameters.

The static magnetic fields are solved in the radial and axial directions assuming azimuthal symmetry. DC current loops are used for this calculation. For a mesh that contains a permanent magnet, the code replaces the corresponding grid points with small current loops. The magnetic field can be computed through a vector  $\mathbf{A}$ , which satisfies

$$\nabla \times \mathbf{A} = \mathbf{B}; \quad \nabla \times \frac{1}{\mu} \nabla \times \mathbf{A} = \mathbf{j}; \quad (2.3)$$

where  $\mu$  is the permeability, and  $\mathbf{j}$  is the current density of the source current loops.

### 2.3 The Fluid Kinetics Module

Fluid equations are solved in FKM to obtain plasma species densities and fluxes. The FKM also computes electrostatic fields by either solving Poisson's equation or using an ambipolar field approximation. Transport coefficients and source functions are used by the

FKM to solve separate continuity, momentum, and energy equations for each ion and neutral species, while semi-implicitly solving Poisson's equation for the time varying electrostatic potential.

The continuity equation that describes the density evolution rate for any species is

$$\frac{\partial N_i}{\partial t} = -\nabla \cdot \Gamma_i + S_i, \quad (2.4)$$

where  $N_i$  is the density,  $\Gamma_i$  denotes the flux, and  $S_i$  represents the source term determined by plasma chemical reactions. Rate coefficients for electron impact reactions are obtained from the EETM, and heavy particle reaction coefficients are supplied to the code. These values are used to calculate the source terms. For both electrons and heavy particles, the fluxes can be calculated from the drift-diffusion equation:

$$\Gamma_{\mathbf{k}} = \mu_{\mathbf{k}} q_{\mathbf{k}} N_{\mathbf{k}} \mathbf{E} - D_{\mathbf{k}} \nabla N_{\mathbf{k}}, \quad (2.5)$$

where  $\mu$  is the mobility,  $q$  is the charge,  $N$  is the density, and  $D$  is the diffusion coefficient. The transport properties of electrons are obtained from the EETM results. For ions and neutrals, the transport properties are either taken from a database or calculated from Lenard-Jones parameters.

Ion and neutral fluxes can also be solved from the momentum equation:

$$\frac{\partial \Gamma_i}{\partial t} = -\frac{1}{m_i} \nabla (N_i k T_i) - \nabla \cdot (N_i \mathbf{v}_i \mathbf{v}_j) + \frac{q_i}{m_i} N_i (\mathbf{E} + \mathbf{v}_i \times \mathbf{B}) - \nabla \cdot \bar{\tau} - \sum_j \frac{m_j}{m_i + m_j} N_i N_j (\mathbf{v}_i - \mathbf{v}_j) \nu_{ij}, \quad (2.6)$$

where  $\Gamma_i$ ,  $m_i$ ,  $k$ ,  $N_i$ ,  $T_i$ , and  $\mathbf{v}_i$  denotes the flux, mass, Boltzmann constant, density, temperature, and velocity, respectively, of the species  $i$ ;  $m_j$  and  $N_j$  are the mass and density, respectively, of the species  $j$ ;  $\nu_{ij}$  is the collision frequency between species  $i$  and  $j$ . Here  $\tau$  is the viscosity tensor for neutral species, and it is only used in the neutral momentum equation.

Determination of the time-dependent electrostatic fields is accomplished either by solution of Poisson's equation or based on quasi-neutrality allowing an ambipolar approximation. These are two alternative ways for the FKM to calculate the electrostatic fields. In the first method the time-evolving electrostatic potential  $\phi$  is related to the net charge density as

$$\nabla \cdot \epsilon \nabla \phi = -\rho, \quad (2.7)$$

where  $\epsilon$  is the permittivity,  $\phi$  is the electrostatic potential, and  $\rho$  is the net charge density. To enable an implicit solution, the charge density at the time when  $\phi$  is required is numerically estimated using a first-order Taylor series expansion:

$$\rho^{t+\Delta t} = \rho^t + \Delta t \cdot \left. \frac{\partial \rho}{\partial t} \right|^{t+\Delta t}, \quad (2.8)$$

where  $\rho^{t+\Delta t}$  is the charge density at time  $t+\Delta t$ , and  $\rho^t$  is the charge density at time  $t$ . The evolution rate of the charge density  $\partial \rho / \partial t$  is determined by the gradient of the total current density  $\mathbf{j}$ :

$$\frac{\partial \rho}{\partial t} = -\nabla \cdot \mathbf{j} + S, \quad (2.9)$$

where  $S$  is the source function of charges. In the plasma region,  $\mathbf{j} = \sum_i q_i (-D_i \nabla n_i + q_i \mu_i (-\nabla \phi))$ ; in materials,  $\mathbf{j} = \sigma (-\nabla \phi)$  where  $\sigma$  is the material conductivity.

The second option to compute electrostatic fields in the FKM is to use a quasi-neutrality approximation over the entire plasma region. Under such an assumption, the elec-

tron density is equal to the total ion charge density at all locations. This requires that when using drift-diffusion equations for both electrons and ions, at steady state,

$$\nabla \cdot \Gamma_e + S_e = \sum_i q_i (\nabla \cdot \Gamma_i + S_i), \quad (2.10)$$

or

$$\nabla \cdot (\mu_e n_e \nabla \phi + D_e \nabla n_e) + S_e = \sum_i q_i (\nabla \cdot (-\mu_i n_i \nabla \phi + D_i \nabla n_i) + S_i). \quad (2.11)$$

In the above equations,  $S_e$  and  $S_i$  represent electron and ion source functions, respectively, and the right-hand side of the equations sum over all charged species. From Eq. 2.11, the electrostatic potential can be determined from species densities and species source functions.

## 2.4 The Electron Energy Transport Module

The EETM calculates electron kinetics properties such as the electron energy distribution function, electron temperature, and electron impact rate coefficients. There are two ways for the EETM to calculate the electron energy distribution function. The first method is to solve the 2-D electron energy equation. Electron transport properties are obtained by solving the 0-D Boltzmann equation. The second approach of the EETM is to use an electron Monte Carlo simulation (EMCS). The EEDF is then obtained from the collected statistics.

Under the influence of electric fields, free electrons are accelerated to high energies, on the order of several electron volts. These electrons then inelastically collide with neutrals, leading to neutral dissociation, excitation, and ionization. The electron impact reaction rates strongly depend on the electron temperature  $T_e$ , which is related to the electron energy distribution function (EEDF) as

$$T_e = 1.5 \int f(\varepsilon) \cdot \varepsilon \cdot d\varepsilon, \quad (2.12)$$

where  $\varepsilon$  represents electron energy and  $f(\varepsilon)$  is the electron energy distribution function. Inelastic collisions influence the EEDF by extracting energy from electrons, resulting in a reduction of the high-energy tail of the EEDF. As a result, for collisional plasmas, the EEDF does not behave as a Maxwellian distribution. The EETM was designed to simulate this effect.

#### 2.4.1 The Electron Energy Equation Method

The 0-Boltzmann equation is expressed as

$$\frac{\partial f_e}{\partial t} + \mathbf{v} \cdot \nabla_{\mathbf{r}} f_e - \frac{e(\mathbf{E} + \mathbf{v} \times \mathbf{B})}{m_e} \nabla_{\mathbf{v}} f_e = \left( \frac{\partial f_e}{\partial t} \right)_{collision}, \quad (2.13)$$

where  $f_e = f_e(t, r, v)$  is the electron distribution function,  $\nabla_{\mathbf{r}}$  is the spatial gradient,  $\nabla_{\mathbf{v}}$  is the velocity gradient,  $m_e$  is the electron mass, and  $\left( \frac{\partial f_e}{\partial t} \right)_{collision}$  represents the effect of collisions. The EEEM solves the 0-dimensional Boltzmann equation for a range of E/N (electric field divided by total gas density). The electron temperature and all of its dependent quantities, like electron impact rate coefficients and electron mobility, are derived from the EEDF.

Results of the 0-dimensional Boltzmann equation are then used to solve the electron energy equation:

$$\nabla \kappa \nabla T_e + \nabla \cdot (\Gamma_e T_e) = P_{heating} - P_{loss}, \quad (2.14)$$

where  $k$  is the thermal conductivity,  $T_e$  is the electron temperature,  $\Gamma_e$  is the electron flux,  $P_{heating}$  is the electron heating due to deposition, and  $P_{loss}$  is the power loss due to inelastic collisions.  $P_{heating}$  is computed from the time averaged value of  $\mathbf{j} \cdot \mathbf{E}$ , where  $\mathbf{j}$  is the electron current obtained from the FKM, and  $\mathbf{E}$  is the electric field due to both inductively and capaci-

tively coupled effects. The electric field is both the inductive field computed in the EMM and the capacitively coupled field computed in the FKM.

#### 2.4.2 The Electron Monte Carlo Simulation

The Monte Carlo method is a fully kinetic treatment, which resolves the acceleration of electrons in electric fields and the gyro motion of electrons in magnetic fields using a semi-implicit technique. Non-collisional heating is kinetically resolved by producing electron currents, which are used to correct the assumption of collisional power deposition in the EMM.

The EMCS tracks the trajectories of electron pseudoparticles in the electromagnetic fields obtained from the EMM module and the electrostatic fields obtained from the FKM. Statistics on electron energy distributions are gathered by tracking the particle motion and collisions. The electrons are initially given a Maxwellian distribution and are spatially distributed according to the electron density distribution calculated by the FKM. Electrons are accelerated by the electromagnetic and electrostatic fields in a manner governed by the Lorentz equation:

$$\frac{d\mathbf{v}}{dt} = \frac{q_e}{m_e} (\mathbf{E} + \mathbf{v} \times \mathbf{B}), \quad (2.15)$$

where  $\mathbf{v}$  is the velocity ( $dr/dt = v$  where  $r$  is the location). Collisions can also alter electron energy and location. Energy-dependent collision cross sections and energy losses due to collisions are supplied to the EMCS. EMCS also generates spatially dependent electron temperature, electron impact rate coefficients, and collision frequencies.

## 2.5 The Plasma Chemistry Monte Carlo Module

The PCMCM produces the energy and angular distributions for neutrals and ions striking surfaces in contact with the plasma. The PCMCM launches pseudoparticles representing ions and neutrals based on the electron impact source functions. Using time dependent electric fields from the FKM, their trajectories are integrated while accounting for gas phase collisions. The energy and angular distributions (EADs) of ion (IEADs) and neutral pseudoparticles are recorded as they strike surfaces.

PCMCM module was originally a postprocessor to the HPEM that was later incorporated into the HPEM. It used volumetric sources of plasma species, time-dependent electric fields, and sheath properties exported from the HPEM to obtain the angular and energy distributions of the fluxes using Monte Carlo techniques.[6] The PCMCM functions in a similar manner but also accounts for nonthermal, or in-flight fluxes, resulting from sputter sources in addition to the volumetric sources. Sputtered atoms and neutralized ions which are reflected from the target have kinetic energies of several eV. These species are not initially in thermal equilibrium with the buffer gas, which has a temperature of  $\leq 0.3$  eV. Under certain process conditions, these energetic particles may not thermalize prior to reaching the wafer. The trajectories and energies of these nonequilibrium particles are already tracked by the sputter algorithms in the FKM. Statistics on the energy and angular distributions of the particles as they strike selected surfaces are collected and passed to the PCMCM.

Based on these quantities, a rate of generation of species  $i$  as a function of position,  $GR_i(\vec{r})$  ( $\text{cm}^{-3} \text{s}^{-1}$ ), is computed. This generation term accounts for all sources of species  $i$  on the right- and side of reactions in the mechanism. The rate  $GR_i(\vec{r})$  also includes source functions on surface  $s$  due to, for example, sputtering. In a similar fashion, a consumption rate

$CM_i(\vec{r})$  ( $\text{cm}^{-3} \text{s}^{-1}$ ) is computed based on all reactions containing species  $i$  on the left-hand side of reactions in the mechanism. A local elastic collision frequency with each species is also computed. These elastic frequencies are added to the local consumption frequency  $CM_i(\vec{r})\Delta V(\vec{r})$  where  $\Delta V(\vec{r})$  is the volume of the computational cell at location  $\vec{r}$  to yield a total interaction frequency  $\nu_T(\vec{r})$ . Null collision techniques are used at each spatial location to provide a reactor wide collision frequency  $\nu_i$  for each species  $i$ , which simplifies the random selection of collision times and mean free paths for individual particles.

The Null collision algorithm was proposed by Skullerud.[19-21] For a particle  $i$ , drifting through a gas of density  $N$  under the influence of an electric field where the collision frequency is velocity dependent, the development of the algorithm was driven by the necessity for a simple and fast method to determine the free time  $\Delta t$  between two successive collisions. If the collision frequency  $\nu_i$  is constant, the mean-free time between collisions  $T_{MFT}$  is also constant, and  $\Delta t$  can be obtained from the following relationship:

$$\Delta t = -\frac{1}{\nu_i} \ln(r) \quad (2.16)$$

where  $r$  is a rectangularly distributed random number on the interval  $0 < r < 1$ .

According to Skullerud's null algorithm, a particle at any point in a simulation with an arbitrary energy  $E$  can be assigned a constant trial collision frequency  $\nu_i'$  which is greater than the real collision frequency  $\nu_i$ . [19-21] Simulation of the motion of a particle up to the time of the next collision (associated with  $\nu_i'$ ) can be described as follows. A random number is chosen to determine a free time  $\Delta t$  (evaluated from relationship (2.8) and noting that  $T_{MFT} = 1/\nu_i'$ ) during which the simulated particle is accelerated by the external field. At the end of the interval  $\Delta t$ , another random number  $P$  is chosen. If  $P$  is greater than  $\nu_i/\nu_i'$ , evaluated at

the energy immediately prior to collision, the particle is considered to have suffered a null collision. If a null collision happens, the particle is undeflected and the program returns to choose the next  $\Delta t$ . A real collision involves appropriate calculations for scattering of the particle from the target gas before a subsequent  $\Delta t$  is chosen. After each collision, null or real, a new  $v_i'$  may be chosen. Many such free paths are simulated to obtain statistically significant results, during which time the phase-space coordinates of the particle are sampled in some fashion to determine the transport parameters. It is well established that the above method is faster than performing the integrations required to explicitly determine the free time between collisions for a real cross section.[21]

In the PCMCM, pseudoparticles of species  $i$  are launched from each computational cell at a time randomly chosen in the rf cycle with a weighting (or total number) proportional to  $GR_i(\vec{r})\Delta V(\vec{r})$ . The velocity is randomly chosen from a Maxwell-Boltzmann distribution having a local temperature  $T_i(\vec{r})$  for volumetric sources where the spatially dependent temperature for each species is computed by HPEM. The trajectories of the pseudoparticles are integrated for the time  $\Delta t$  for a random number  $r$  ( $0 < r < 1$ ) using equation 2.16.

At the end of the time step, Monte Carlo techniques are used to determine if the collision is real or null. If real, another random number is used to determine if the collision is elastic or consuming. If consuming, the particle is removed from the simulation. If elastic, the collision partner is identified using another random number and the velocity of the pseudoparticle is changed appropriately using standard elastic collision techniques. The one exception is for charge exchange collisions which are separately accounted for in the sum of collision frequencies. If an ion undergoes a charge exchange collision, its identity is changed to the neutral counterpart and the trajectory is retained. The trajectories are advanced until

the pseudoparticles reach the vicinity of a surface. If the surface is chosen as one for which statistics on incident species are desired, ions are then integrated through the sheath, a computationally expensive process. For surfaces not selected, the particles are removed from the simulation. A similar process is followed for the neutrals, except for integration through the sheath.

## **2.6. Monte Carlo Radiation Transport Model**

The MCRTM in the HPEM is called after each iteration to provide photon fluxes incident onto the SiOCH.[22] The operation of MCRTM is similar to the operation of PCMCM. Source functions for launching of pseudoparticles representing photons are derived from the excited state densities generated by the FKM. The trajectory of a photon is tracked until it is absorbed by a gas phase species or it strikes a surface. The photon absorption probability is obtained from a Voigt line-shape function using the natural lifetime, collisional broadening and Doppler broadening produced by the local gas densities and temperatures. If resonantly absorbed, photons are re-emitted using a partial-frequency redistribution algorithm. The fluxes and spectra of photons are recorded as a function of the material the photons strike, and are exported to the surface kinetics module SCM of the HPEM. The rates of photon absorption and re-emission are recorded for each optical transition, and are used to calculate radiation trapping factors which lengthen the natural lifetime of the emitting species. These factors are exported to the FKM.

The MCRTM has been described in detail in an earlier literature.[22] The MCRTM tracks quanta of energy emitted by plasma excited species as the photon is absorbed and re-emitted while traversing the plasma. As the probability for absorption and re-emission de-

depends on local densities of the absorbing and emitting species, the densities of quenching and lineshape perturbing species and the gas temperature, the MCRTM was interfaced to the HPEM, which provides these quantities. In turn, the MCRTM provides the effective lifetime of emitting excited states for use in the plasma kinetics routines of the HPEM.

The MCRTM directly interfaces with the FKM on each iteration through the HPEM. The parameters provided by the FKM to the MCRTM are species densities, gas temperatures and rate constants, from which the frequencies for perturbing and quenching collisions affecting the species participating in radiative transfer reactions are calculated. The MCRTM produces radiation trapping factors which are used to modify the lifetime of radiating species during the next execution of the FKM. The algorithms used in the MCRTM are similar to those described by Sommerer.[23] Pseudoparticles representing photons are tracked from their site of emission through multiple absorptions and re-emissions until their escape from the plasma or until the quanta of energy is quenched. Although reflection from surfaces can be accounted for, we assumed that all surfaces are absorbing or transmitting and so any photon which strikes a surface is lost from the plasma.

Pseudoparticles are emitted from sites randomly distributed within a numerical mesh cell in proportion to the density of radiators in that cell (obtained from the FKM). As the densities of radiators may vary by orders of magnitude over the plasma region, the number of pseudoparticles released from each cell  $i$  is rescaled to ensure that a statistically relevant number of pseudoparticles is emitted from every cell.

$$n_i = n_{\min} + (n_{\max} - n_{\min}) \left( \frac{\log N_i^* - \log N_{\min}^*}{\log N_{\max}^* - \log N_{\min}^*} \right) \quad (2.17)$$

where  $n_i$  is the number of pseudoparticles emitted from cell  $i$ , and  $n_{\min}$  and  $n_{\max}$  are preselect-

ed minimum and maximum number of pseudoparticles permitted to be emitted and is the density of the radiating species in cell  $i$ .  $N_{\min}^*$  and  $N_{\max}^*$  are the minimum and maximum densities of  $N^*$  in the plasma. These values are dynamically determined during execution of the model. A weighting  $w_i$  is assigned to each pseudoparticle for the purposes of collecting statistics. For a pseudoparticle emitted from cell  $i$ ,

$$w_i = \prod_m w_{m,i} \quad (2.18)$$

where  $w_m$  is a series of subweightings. The first such subweighting is

$$w_{1,i} = \frac{N_i \Delta V_i}{n_i} \quad (2.19)$$

where  $\Delta V_i$  is the volume of cell  $i$ .

The frequency of the photon is then selected from the lineshape function  $g(\nu)$ , the probability of a photon being emitted at a frequency.[24] The likelihood of the photon being emitted near line center can be hundreds to thousands of times higher than being emitted in the far wings of the lineshape. The majority of photons escaping the plasma usually originate from the wings of the lineshape, where absorption probabilities are smaller. Selecting pseudoparticles with probabilities directly proportional to  $g(\nu)$  would, in the absence of using a very large number of pseudoparticles, undersample the wings of the lineshape. Although the assignment of frequency directly proportional to  $g(\nu)$  is the least ambiguous method, the need to avoid sampling problems in 2-dimensions and the desire to obtain frequency resolution throughout the mesh motivates one to try another method. To avoid the statistical under-sampling in the wings of the lineshape profile, we instead uniformly distribute the pseudopar-

ticles over a preselected range of frequencies about the line center  $\nu_0$ , and use an additional weighting factor  $w_2 = g(\nu)$  to account for the likelihood of emission.

## 2.7 Surface Chemistry Model

The capability to address surface reactions in the HPEM was achieved with the creation of the SCM.[25] The SCM addresses surface reactions in the HPEM using a flux in – flux out boundary condition. The physics of this model has already been described in an earlier literature.[25] The SCM implements a modified surface-site balance algorithm along the plasma-surface boundary, and outputs surface coverages, thickness and composition of overlying films, reactive sticking coefficients, and modified fluxes of species returning to the plasma. Aside from the gaseous species being directly available as surface reactants, there is also the possibility (e.g. in fluorocarbon plasmas), of overlying films, through which the gaseous species diffuse to the available surface sites. In addition, the constituents of the film may also react with the gaseous species and the underlying substrate. The SCM is capable of handling all of the above processes.

Reaction probabilities for gas phase species with surfaces are provided by the SCM which computes the composition of surface resident species using a multilayer surface-site-balance model. The reaction mechanism is unique for each surface in contact with the plasma. The PCMCM produces the energy and angular distributions for neutrals and ions striking surfaces in contact with the plasma. The PCMCM launches pseudoparticles representing ions and neutrals based on the electron impact source functions. Using time dependent electric fields from the FKM, their trajectories are integrated while accounting for gas phase collisions. The energy and angular distributions (EADs) of ion (IEADs) and neutral pseudopar-

ticles are recorded as they strike surfaces.

The SCM incorporates energy dependent reaction probabilities based on the EADs obtained from the PCMCM. The probabilities for surface reactions involving energetic species (either ions or hot neutrals) are given by [23]

$$p(E) = p_0 \frac{E^m - E_t^m}{E_r^m - E_t^m} \quad (2.20)$$

where  $p(E)$  is the reaction probability for a particle with energy  $E$ ,  $E_t$  is the threshold energy of the process,  $E_r$  is a reference energy, and  $p_0$  is the reaction probability at the reference energy. We used  $m = 0.5$  for sputtering or ion activated etching.

## 2.8 Typical Results from the HPEM

The results of HPEM simulations include 2-D distributions of fields, species densities, species fluxes, power deposition and source functions. HPEM outputs for an example case are discussed in this section for an ICP discharge sustained in He/H<sub>2</sub> gas mixture. The schematic of the cylindrical reactor used in this simulation is shown in Fig. 2.2a.

The reactor is 13 cm in radius and 17 cm in height. The inductive power is supplied through a three-turn antenna coil above a 0.8 cm thick quartz window. The wafer is on an independently powered substrate 9 cm below the quartz window. The wafer, 15 cm in diameter and 9 cm below the top inside wall, sits on an rf-biased substrate. He/H<sub>2</sub> is supplied through the gas nozzle at a flow rate of 100 sccm. The pressure is stabilized at 10 mTorr. ICP reactor was sustained in a 10 mTorr He/H<sub>2</sub> = 75/25 mixture and was powered at 13.56 MHz with a 10 MHz bias on the substrate. The H<sub>2</sub> and H<sub>2</sub><sup>+</sup> ion densities in the reactor are

shown in Fig. 2.2b and Fig. 2.2c, respectively. The total ion density has a maximum of  $5 \times 10^{10} \text{ cm}^{-3}$  while the H atom density has a maximum of  $2 \times 10^{13} \text{ cm}^{-3}$ , depleted in the center of the reactor due to gas heating (up to 800 K). The IEADs for major ions and the combination of ions is shown in Fig. 2.3. Major fluxes to the wafer are shown in Fig. 2.4a as a function of the reactor radius. The energy and angular distributions of H is shown in Fig. 2.4b. The ion fluxes ( $\approx 10^{16} \text{ cm}^{-2}\text{s}^{-1}$ ) largely responsible for the PR removal in semiconductor processing, have an average energy near 25 eV and an angular spread from the vertical of  $< 35^\circ$ . The H atom fluxes have a nearly isotropic angular distribution and a peak at a maximum at  $< 1000$  K. However, the tail of the energy distribution extends to above 10 eV.

## 2.9 Figures

## HYBRID PLASMA EQUIPMENT MODEL (HPEM)

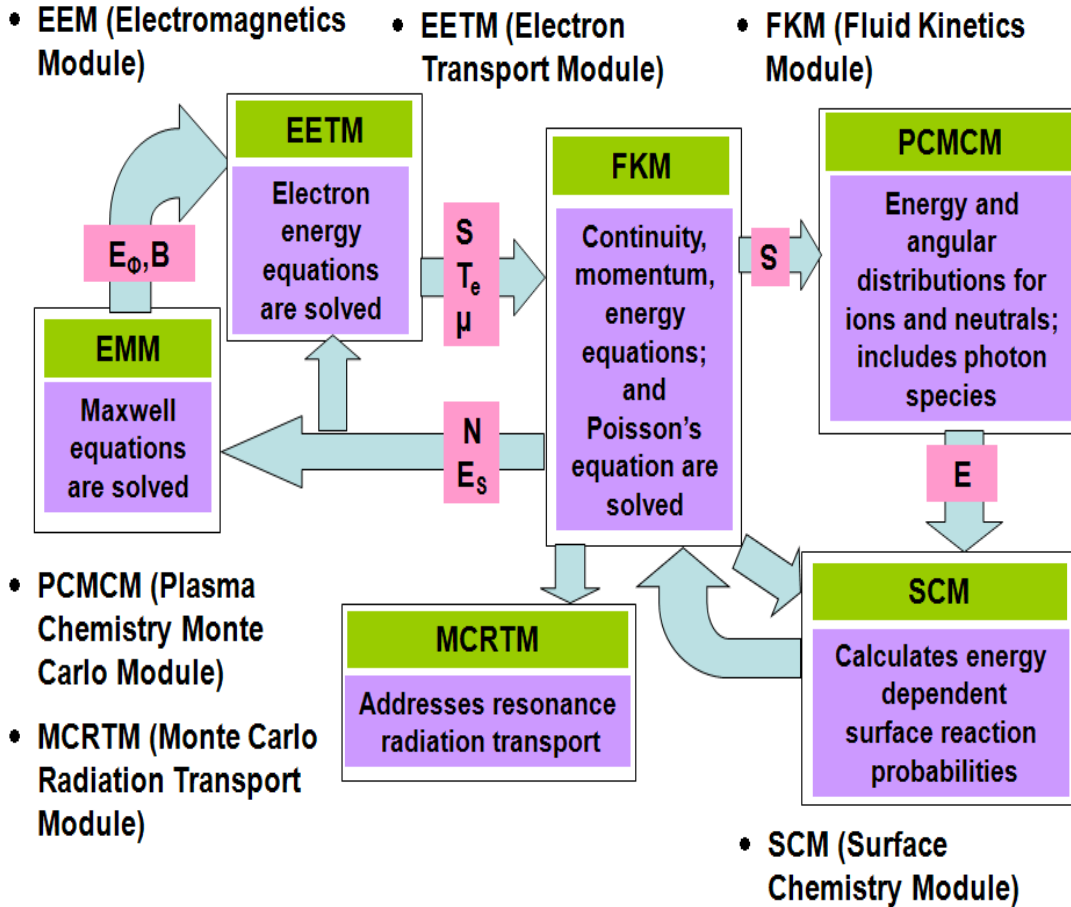


Fig. 2.1 Schematic representation of the HPEM modular model.

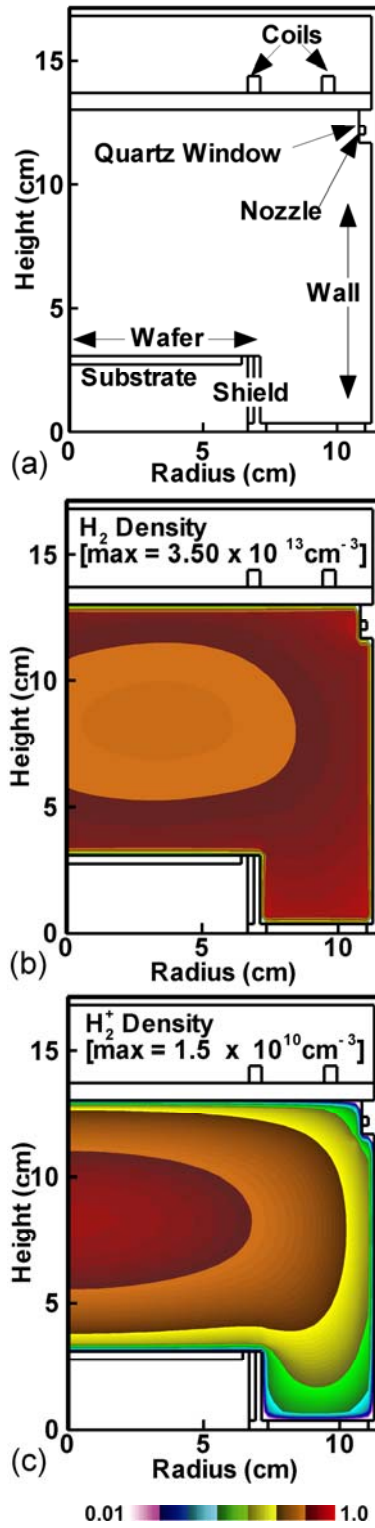


Fig. 2.2 (a) Schematic of the ICP reactor. (b)  $H_2$  density inside the reactor. (c)  $H_2^+$  density distribution inside the reactor.

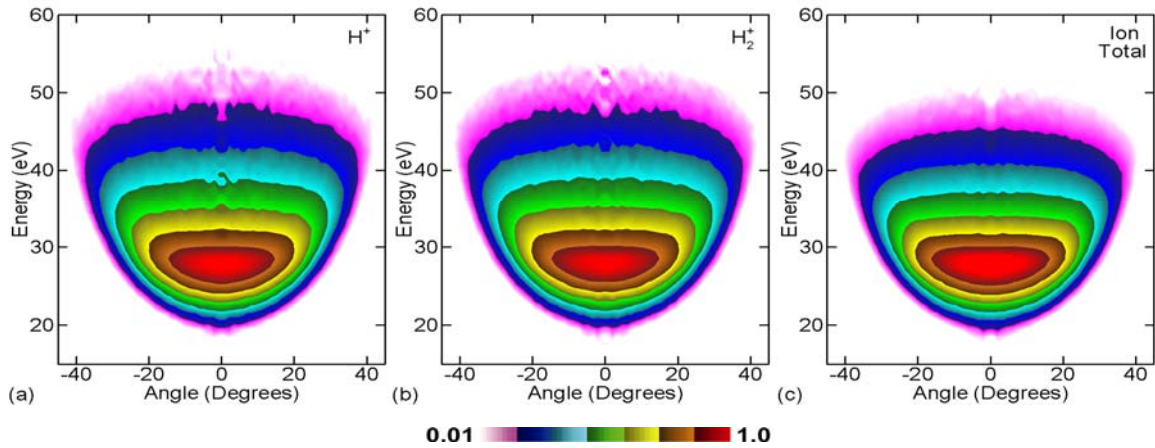


Fig. 2.3 Energy and angular distributions of ions in the He/H<sub>2</sub> plasma: (a) H<sup>+</sup>; (b) H<sub>2</sub><sup>+</sup>; (c) all ions combined.

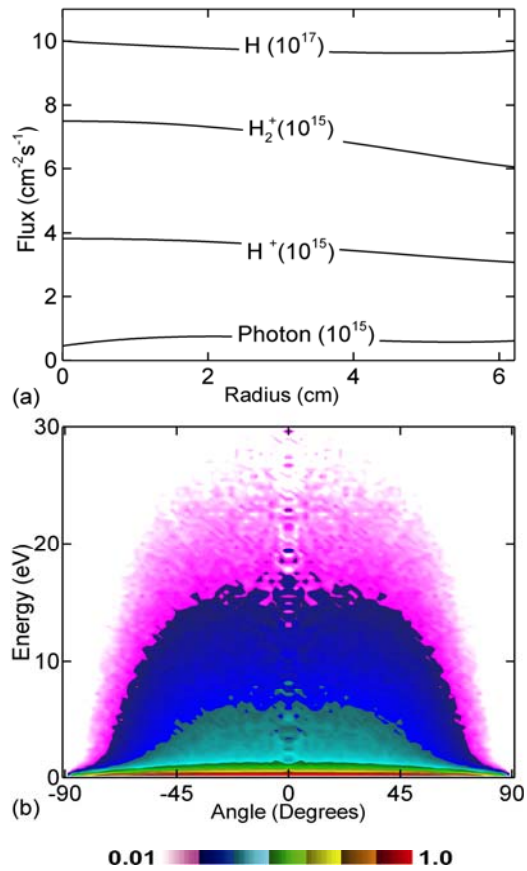


Fig. 2.4 Major fluxes in the He/H<sub>2</sub> plasma and neutral H energy and angular distributions: (a) major radical and ion fluxes; (b) 2-D H energy and angular distribution.

## 2.10 References

1. T. J. Sommerer and M. J. Kushner, *J. Appl. Phys.* **71**, 1654 (1992).
2. P. L. G. Ventzek, R. J. Hoekstra, T. J. Sommerer, and M. J. Kushner, *Appl. Phys. Lett.* **63**, 605 (1993).
3. P. L. G. Ventzek, R. J. Hoekstra, and M. J. Kushner, *J. Vac. Sci. Technol. B* **12**, 461 (1994).
4. P. L. G. Ventzek, M. J. Grapperhaus, and M. J. Kushner, *J. Vac. Sci. Technol. B* **12**, 3118 (1994).
5. F. Y. Huang and M. J. Kushner, *J. Appl. Phys.* **78**, 5909 (1995).
6. R. J. Hoekstra and M. J. Kushner, *J. Appl. Phys.* **79**, 2275 (1996).
7. W. Z. Collison and M. J. Kushner, *Appl. Phys. Lett.* **68**, 903 (1996).
8. H. H. Hwang and M. J. Kushner, *Appl. Phys. Lett.* **68**, 3716 (1996).
9. M. J. Grapperhaus and M. J. Kushner, *J. Appl. Phys.* **81**, 5960 (1997).
10. S. Rauf and M. J. Kushner, *J. Appl. Phys.* **81**, 5966 (1997).
11. M. J. Kushner, *J. Appl. Phys.* **82**, 5312 (1997).
12. M. J. Grapperhaus, Z. Krivokapic, and M. J. Kushner, *J. Appl. Phys.* **83**, 35 (1998).
13. S. Rauf and M. J. Kushner, *IEEE Trans. Semiconductor Manufact.* **11**, 486 (1998).
14. S. Rauf and M. J. Kushner, *J. Appl. Phys.* **83**, 5087 (1998).
15. R. J. Hoekstra and M. J. Kushner, *J. Vac. Sci. Technol. B* **16**, 2102 (1998).
16. S. Rauf and M. J. Kushner, *J. Vac. Sci. Technol. A* **17**, 704 (1999).
17. X. Xu, S. Rauf, and M. J. Kushner, *J. Vac. Sci. Technol. A* **18**, 213 (2000).
18. D. Zhang and M. J. Kushner, *J. Appl. Phys.* **87**, 1060 (2000).
19. H. R. Skullerud, *J. Phys. D.* **1**, 1567 (1968).

20. H. R. Skullerud, J. Phys. B. **6**, 728 (1973).
21. M. J. Brennan, IEEE Trans. Plasma Sci. **19(2)**, 256 (1991).
22. Kapil Rajaraman<sup>1</sup> and Mark J Kushner J. Phys. D: Appl. Phys. **37**, 1780 (2004).
23. T. J. Sommerer, J. Appl. Phys. **74**, 1579 (1993).
24. L. W. Avery, L. L. House, and A. Skumanich, **9**, 519 (1969).
25. D. Zhang and M. J. Kushner, J. Vac. Sci. Technol. A **19**, 524 (2001).
26. C. F. Abrams and D. B. Graves, J. Appl. Phys. **86**, 2263 (1999).

### 3. MONTE CARLO FEATURE PROFILE MODEL

#### 3.1. Introduction

The Monte Carlo Feature Profile Model (MCFPM) can be used to determine and predict topographical feature evolution for semiconductor processing in plasma reactors.[1-3] In this work, the model has been used for predicting profile evolution for porous low- $k$  SiCOH processes. These processes are etching, stripping of PR, polymer cleaning from the low- $k$  after etching, damage in the low- $k$  during plasma treatment, water incorporation into the low- $k$  network, and plasma pore sealing of the low- $k$  surface. Feature profiling for HfO<sub>2</sub> gate-stack etching with HfO<sub>2</sub>/Si selectivity was also investigated. MCFPM also has the capability to include other processes such as plasma enhanced chemical vapor deposition (PECVD) and physical vapor deposition (PVD). The MCFPM is integrated with the Hybrid Plasma Equipment Model (HPEM) through the use of energy and angular distributions (EADs) produced by the Plasma Chemistry Monte Carlo Module (PCMCM) in the HPEM for arbitrary radial location on the substrate.

The MCFPM is described in Section 3.2. The computation mesh used in the MCFPM and the algorithms for particle motions are presented in Section 3.2.1. The physics of the interaction of energetic particles with the surface is captured in Section 3.2.2. Algorithms used in MCFPM to generate porous substrates such as porous SiO<sub>2</sub> and porous SiCOH are discussed in Section 3.2.3. Finally, some results for integrated modeling (etch, strip, cleaning, and pore-sealing) of porous SiCOH processing, and HfO<sub>2</sub> gate-stack etching in the MCFPM are presented in Section 3.3.

## 3.2. Description of the Model

### 3.2.1 Computational Mesh and Particle Motion

The MCFPM can be used to predict feature profile evolution for nano-scale processing. The MCFPM uses statistically weighted pseudoparticles representative of the fluxes of active species to the feature surface. Through ballistic transport and interaction with the mesh delineated surface, time integrated surface evolution is obtained.

The MCFPM resolves the surface topology on a 2D Cartesian mesh to predict etch profiles. In the MCFPM, each cell in the mesh has a material identity. The MCFPM can include plasma surface interactions such as adsorption of radicals and radical-surface reactions. For our porous low- $k$  modeling work we used  $4A \times 4A$  square sized cells to keep the cells compatible with real molecular dimensions of porous low- $k$ . A cell's material identity (e.g., Si, PR, SiO<sub>2</sub>, plasma) may change during the simulation. Also, cells may be removed, added for reactions, etching, and deposition.

In the MCFPM, solid species are represented by the identity of the computational cell. Gas phase species (i.e., radicals, photons and ions) are represented by computational pseudo-particles. Pseudo-particles are launched towards the surface from random locations above the trench with energies and angles sampled from the EADs obtained from the PCMCM of HPEM. The trajectories of the pseudoparticles are tracked until they hit a surface, where a generalized surface reaction mechanism controls the interaction. The identity of the material mesh cell is changed (representing a surface chemical reaction), removed (etching), or a cell is added (deposition) as dictated by the reaction mechanism. Gas phase pseudoparticles are reflected or emitted from the surface consistent with the mechanism.

The EADs produced by the PCMCM are flux weighted probability distribution functions (F). Such distribution functions must be converted and normalized as cumulative distribution functions (f):

$$f(\varepsilon, \theta, r) = \frac{F(\varepsilon, \theta, r)}{\iint F(\varepsilon, \theta) d\varepsilon d\theta} \quad (3.1)$$

The pseudo-particles are launched with a frequency computed from the total flux of radicals or ions incident onto the substrate so that each pseudo-particle represents a fraction of the number of atoms in a mesh cell based on the gas-to-material weighting ratio:

$$W_g = \frac{1}{\gamma} W_s, \quad (3.2)$$

where  $W_g$  is the gas particle weighting,  $W_s$  is the mesh or surface cell weighting, and  $\gamma$  is the gas-to-surface ratio. The pseudo-particle trajectories are advanced in time where the calculation of position and velocity are separated, allowing solution of two linear equations:

$$\mathbf{v}_j = \mathbf{v}_{j-1} + \frac{q\mathbf{E}}{m} \Delta t, \quad (3.3)$$

and

$$\mathbf{x}_j = \mathbf{x}_{j-1} + \mathbf{v}_j \Delta t, \quad (3.4)$$

where  $v$  and  $x$  represent the velocity and position of the particle, and the subscripts indicate the former or current velocity and position;  $q$  and  $m$  indicate the charge and mass of the particle, respectively; and  $\Delta t$  indicates the time-step taken by the particle. This method is used because under the majority of cases the effects of charging are ignored and the electric field  $E$  is set to zero, allowing solution of the linear Eq. (3.4) only.

Particle motion in the MCFPM is described below. The initial time-step of a particle is determined by the time required to move the distance to a surface cell. Based on this time step and the solution to Eq. (3.4), the velocity and position of the particle is determined. At this point the time step is reset to perform the next move. If the distance to a surface cell is still greater than one mesh cell, this new distance is used to calculate the time step for the next move and the previous step is repeated. The particle is moved until a material containing cell is occluded. If the particle is within one mesh cell of a surface cell, the particle is moved back to its previous position, the previous time-step is halved, and the particle is moved again. This process is iterated until the particle moves within a fraction of the material containing cell, generally  $\approx 0.05 \times (\text{Cell width})$ .

Surface charging effects on the profile evolution can also be considered. Surface charging can be an important issue when etching a high aspect ratio trench (aspect ratio  $> 35$ ). In our modeling, our trench aspect ratios were  $< 20$ . As such, we did not include charging effects for porous low- $k$  processing and  $\text{HfO}_2$  gate-stack etching. Electron trajectories can be simulated as low-temperature isotropic fluxes which impinge upon the feature during the low-potential swing of the sheath. This macroscopically balances the current due to the ions. To resolve the electric fields due to the charged surfaces of the feature, an iterative explicit solution of Poisson's equation is determined utilizing successive over-relaxation (SOR) method:

$$\nabla \cdot \epsilon \nabla \phi^{t+\Delta t} = -\rho^t \quad (3.5)$$

SOR is used to accelerate solution by multiplying the calculated  $\Delta\phi$  by an over-relaxation factor greater than one. Neumann boundary conditions are used at the top and bottom of the feature by assuming that the electric field above the feature matches the sheath field from the

FKM of HPEM and that the electric field below the feature is approximately zero. The left and right boundaries are assumed to follow a periodic Dirichlet condition.

### 3.2.2 Energetic Particle Interaction

The generalized reaction probability for a particle of energy  $E$  incident onto a surface at an angle  $\theta$  from the local vertical of the surface is [4,5]

$$p(\theta) = p_0 \left( \frac{E^m - E_{th}^m}{E_r - E_{th}^m} \right) f(\theta) \quad (3.6)$$

where  $E_{th}$  is the threshold energy of the process,  $E_r$  is a reference energy,  $p_0$  is the probability for normal incidence at  $E_r$  and  $f(\theta)$  is the relative probability at angle of incidence  $\theta$ . Based on the work of Graves *et al.*  $f(\theta)$  is an empirical function typical of chemically enhanced sputtering with a maximum value near  $\theta = 60^\circ$ . [5]

EADs will determine the specifics of the interaction of energetic particles with surface species. The source of energetic particles is ions accelerated through the sheath, with energies of up to 100s eV and angular spreads  $<15^\circ$  from the vertical. It was assumed that ions neutralize upon interaction with the surface and so do not distinguish between energetic ions and energetic neutrals. Energetic particles can either specularly or diffusively reflect from surfaces, with an energy loss which is larger for diffusive scattering and small for specular.

Particles reflecting from surfaces were given both specular and diffusive character. To account for surface roughness on spatial scales not resolved by our model, it was specified that a fraction  $f_d = 0.25$  was diffusively scattered. The energy of the specularly reflected

particle was scaled such that forward scattered particles retain the majority of their energy.

The specularly reflected particle energy for incident energy  $E_I$  is

$$E_S = E_I \left( \frac{E_I - E_c}{E_{ts} - E_c} \right) \left( \frac{\theta - \theta_c}{90 - \theta_c} \right) \quad (3.7)$$

for  $\theta > \theta_c$ ,  $E_c < E_I < E_{ts}$ . Particles having  $\theta < \theta_c$  or  $E_I < E_c$  are said to diffusively scatter. Particles having  $E_I > E_{ts}$  are said to retain all of their energy subject to the angular correction. We used  $E_{ts} = 100 \text{ eV}$ ,  $E_c = 0 \text{ eV}$  and  $\theta_c = 60^\circ$ . The final reflected energy of the particle is a weighted sum of the specularly reflected energy and diffusively reflected energy.

MCFPM addresses the energy dependence of a reaction probability and satisfies the requirement that reaction probabilities will add to unity. As such, the construction of the probability arrays for interaction of gas phase with surface cells is a complicated process. This process is facilitated by use of a null process for all combinations of incident gas phase species and surface species. The null process is reflection without reaction. As the probability of energy dependent process changes, the null portion of the probability array is rescaled to ensure that the sum of probabilities is unity. Should an etch yield exceed unity, the null reaction is eliminated and the array rescaled.

### 3.2.3 Porous Material

A porous material can have both isolated and interconnected pores. The interconnectivity of the porous material can be defined as the fraction of pores that are connected to another pore. In the porous material, interconnectivity can vary from 0% to 100%. A porous material having an inter-connectivity of 0% consists of only isolated pores. In a porous material having an inter-connectivity of 100%, every pore is connected to at least one other

pore in a low fractal dimension manner. A porous material having interconnectivity between 0% and 100% consists of both isolated and interconnected pores.

Modeling of two phase porous SiO<sub>2</sub> has been described in an earlier publication.[6] Porous material is modeled as being stoichiometric SiO<sub>2</sub> with vacuum pores.[6] The pore radii and locations are randomly chosen and distributed in the numerical mesh used by the MCFPM with a Gaussian distribution of radii having probability

$$p(r) \sim \exp(-((r-r_0) / \Delta r)^2) \quad (3.8)$$

where  $r$  is the radius of the incorporated pore,  $r_0$  is the average pore radius and  $\Delta r$  is the standard deviation. Algorithms were developed to include the capability of creating both closed and interconnected pore networks. An algorithm was developed to simulate porous SiCOH by replacing SiO<sub>2</sub> cells on the pore-wall with  $-\text{CH}_3$  group in porous SiO<sub>2</sub>. [7]

Generation of an interconnected structure can be described as follows.[6] A pore is randomly chosen to be isolated or connected based on the specified fractional interconnectivity. Pore locations and radii are then chosen randomly. As pores are created in the mesh, the numerical cells which are on the inside of pores are tracked. Pores which overlap result in some fraction of the mesh cells being owned by both pores. For an isolated pore, mesh cells can be owned by only a single pore. For an interconnected pore, at most two pores can own any given mesh cell. If a randomly placed pore overlaps a cell which is already owned by the maximum allowed pores, the placement is disallowed. The end result is that the pores are chainlike with a low fractal dimension. Higher fractal dimensions can be obtained by allowing ownership by additional pores. The pore placement process is repeated until the desired porosity is achieved.

In MCFPM modeling, for etching, computationally solid mesh cells may become isolated from the remainder of the mesh. For nonporous single-phase materials modeling in MCFPM, such cells are dropped or moved vertically to rejoin a solid surface. This is a more difficult challenge when modeling porous material because the unopened vacuum pores must be differentiated from the bulk. During pore creation, the maximum pore dimension in each column of the mesh is stored. As the etch evolves, a solid mesh cell is treated as being isolated if its vertical distance to the closest surface is greater than the maximum pore size in that column. At such time, the isolated solid mesh cell is transitioned to a surface.

### 3.3 Surface Reaction Mechanisms

Surface reaction mechanisms, in general, are an intrinsic property of the gas phase reactant species (incident on the surface) and the surface species. As such, reaction mechanisms should be independent of the process conditions, such as the plasma source or the gas chemistry. The process conditions may determine the energies and magnitudes of the incident reactant fluxes, however the reaction mechanism should not change.

A generalized reaction mechanism applicable for etching of porous SiOCH in Ar/C<sub>4</sub>F<sub>8</sub>/O<sub>2</sub> plasmas was developed.[6] The reaction mechanism was later extended to clean CF<sub>x</sub> polymer layers from the trench sidewalls in both Ar/O<sub>2</sub> and He/H<sub>2</sub> plasmas. The reaction mechanism also addresses surface activation in porous low-*k* in He/H<sub>2</sub> plasmas, surface pore sealing in NH<sub>3</sub> plasmas, photon interactions with the low-*k*, and water reactions with SiO<sub>2</sub> sites having lost -CH<sub>3</sub> .[8-20] A separate surface reaction mechanism for HfO<sub>2</sub> gate-stack etching in Ar/Cl<sub>2</sub>/BCl<sub>3</sub> plasmas with Si selectivity has been developed.[21-27] This reaction mechanism also includes metal gate TiN etching reactions in Ar/Cl<sub>2</sub>/BCl<sub>3</sub> plasmas and PR

trimming reactions in Ar/O<sub>2</sub> plasmas.[28] All these reaction mechanisms will be discussed in the following chapters of the thesis in detail.

### 3.4 Integrated Modeling Using the MCFPM

MCFPM takes IEADs from PCMCM of HPEM and predicts profile evolution for plasma processes. A simple schematic showing the link between HPEM and MCFPM is shown in Fig. 3.1. The MCFPM can take a previously generated profile after a plasma process as input for a successive process. Thus the MCFPM is capable of predicting profile evolution for a multi-step process. Typical profile simulations we used for integrated porous SiCOH modeling included fluorocarbon plasma etching of porous SiCOH, cleaning of residual fluorocarbon polymer and unmasking of PR after the etching, removal of -CH<sub>3</sub> group from the low-*k* during the cleaning, surface pore sealing, and water incorporation in the low-*k*. A schematic of the flow-diagram from generation of energy and angular distribution in HPEM to He plasma activation and NH<sub>3</sub> plasma pore sealing of porous SiCOH in MCFPM is shown in Fig. 3.2. The plasma conditions for such a process are discussed in Chapter 4 in detail. Profiles for a small section of porous SiCOH film near the surface before any treatment, after He plasma activation (to prepare the surface for a better sealing), and successive NH<sub>3</sub> pore sealing are shown in Fig. 3.3.[7] The ICP reactor used for such activation and sealing is explained in Chapter 4.

An integrated process was modeled that included PR trimming and BARC (Bottom Anti-reflection Coating) etching in Ar/O<sub>2</sub> plasmas which was followed by HfO<sub>2</sub> gate-stack etching in Ar/Cl<sub>2</sub>/BCl<sub>3</sub> plasmas with Si selectivity.[29] The flow diagram from generation of IEADs in HPEM for the investigation of feature profile evolution for Ar/O<sub>2</sub> trimming and

BARC etching and the following gate-stack etching in Ar/Cl<sub>2</sub>/BCl<sub>3</sub> plasmas in MCFPM is shown in Fig. 3.4. The initial gate-tack is shown in Fig. 3.5a with a PR width of 80 nm and a BARC thickness of 40 nm. In the first simulation step in the MCFPM, the PR was trimmed down to 32 nm and the BARC was removed with some micro-masking after Ar/O<sub>2</sub> plasma treatment as shown in Fig. 3.5b. In the next step, the MCFPM took the trimmed profile as an initial profile and the gate-stack was etched in Ar/Cl<sub>2</sub>/BCl<sub>3</sub> plasmas that removed TiN and HfO<sub>2</sub> without causing damage to Si substrate due to BCl<sub>x</sub> polymer formation on Si. The etched profile is shown in Fig. 3.5c.

## 3.5 Figures

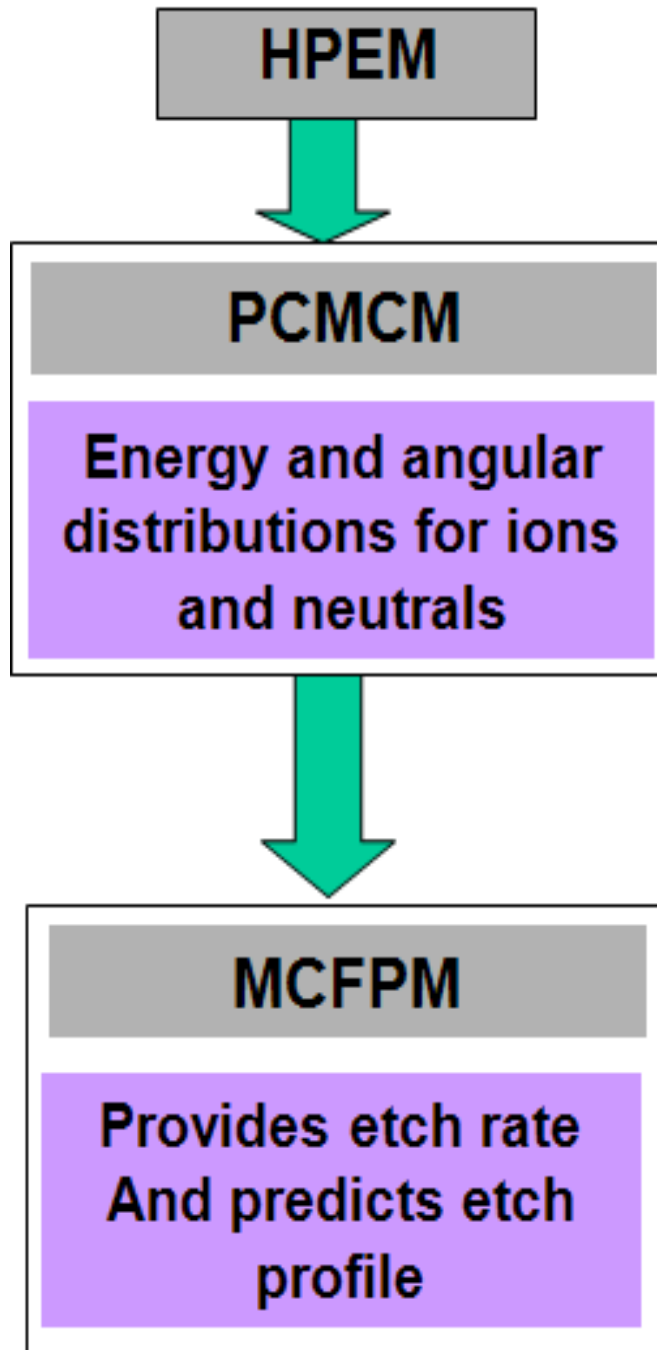
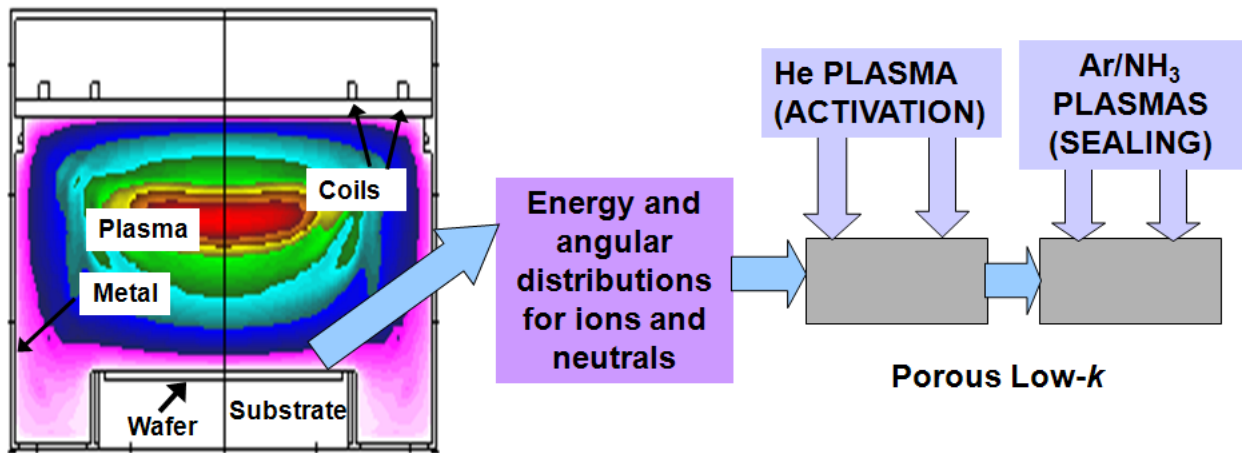


Fig. 3.1 Schematic representation of the link between HPEM and MCFPM.

## MODELING : LOW-*k* PORE SEALING



- **Hybrid Plasma Equipment Model (HPEM)**

- **Plasma Chemistry Monte Carlo Module (PCMCM)**

- **Monte Carlo Feature Profile Model (MCFPM)**

Fig. 3.2 Flow diagram of porous low-*k* SiCOH pore sealing modeling with HPEM and MCFPM. Energy and angular distributions from HPEM were inputted to MCFPM where He activation was followed by NH<sub>3</sub> plasma sealing.

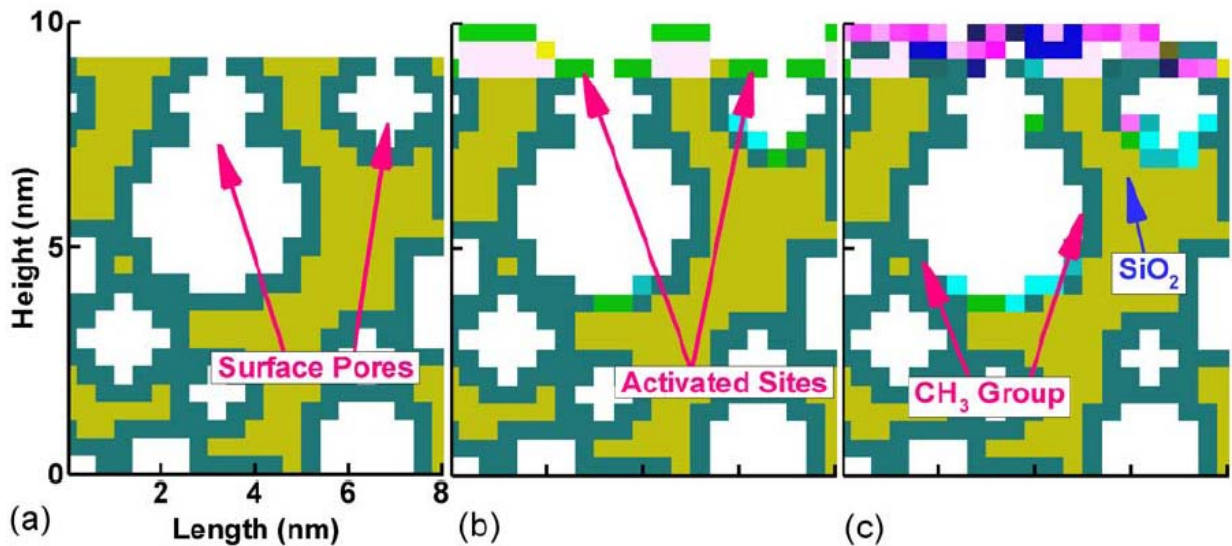


Fig. 3.3 - (a) Initial configuration with CH<sub>3</sub> lining the inside of pores in SiO<sub>2</sub>. (b) Activated sites following He plasma treatment. (c) Sealed pores following Ar/NH<sub>3</sub> plasma treatment.

## MODELING PLASMA ETCHING: HIGH-*k* GATE STACK

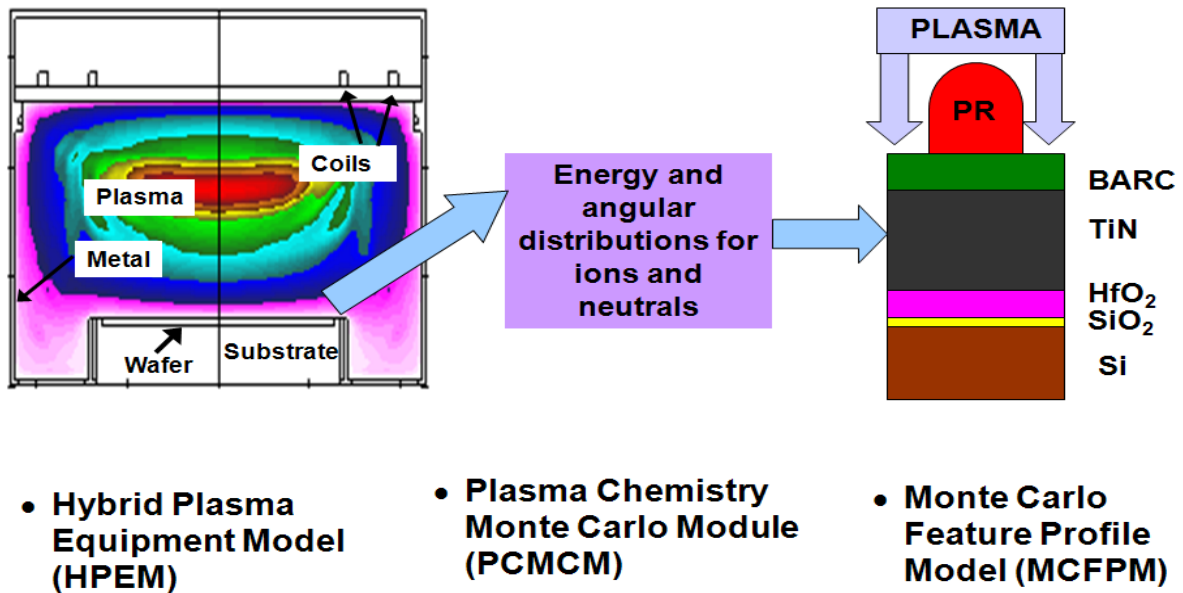


Fig. 3.4 Flow diagram of HfO<sub>2</sub> gate-stack etching with HPEM and MCFPM. Energy and angular distributions from HPEM were inputted to MCFPM where Ar/O<sub>2</sub> trimming was followed by Ar/BCl<sub>3</sub>/Cl<sub>2</sub> etching with Si selectivity.

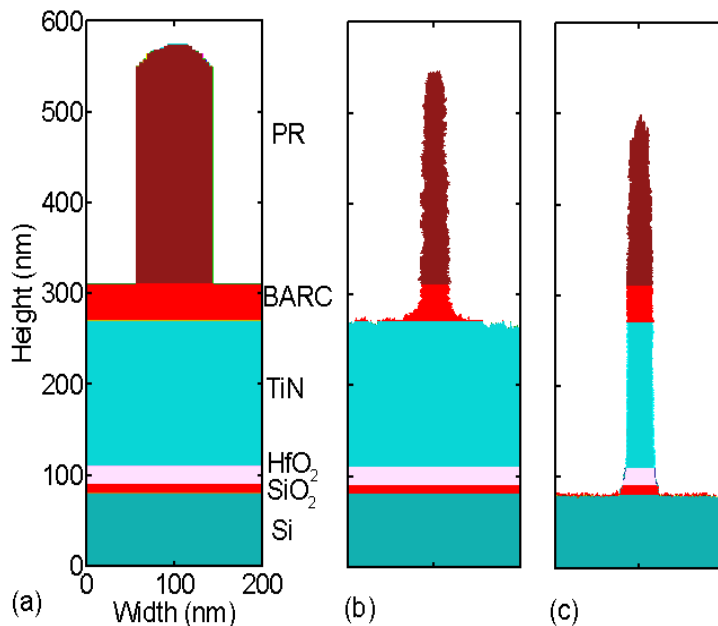


Fig. 3.5 - Multistep HfO<sub>2</sub> gate-stack etching. (a) Initial HfO<sub>2</sub> gate-stack. (b) After Ar/O<sub>2</sub> PR trimming and BARC etching. (c) The profile after Ar/BCl<sub>3</sub>/Cl<sub>2</sub> plasma etching with Si selectivity.

### 3.6 References

1. R. J. Hoekstra, M. J. Grapperhaus, and M. J. Kushner, *J. Vac. Sci. Technol. A* **15**, 1913 (1997).
2. R. J. Hoekstra and M. J. Kushner, *J. Vac. Sci. Technol. B* **16**, 2102 (1998).
3. J. Lu and M. J. Kushner, *J. Vac. Sci. Technol. A* **19**, 2652 (2001).
4. C. C. Cheng, K. V. Guinn, V. M. Donnelly, and I. P. Herman, *J. Vac. Sci. Technol. A* **12**, 2630 (1994).
5. C. F. Abrams and D. B. Graves, *J. Appl. Phys.* **86**, 2263 (1999).
6. A. Sankaran and M. J. Kushner, *J. Vac. Sci. Technol. A* **22**, 1242 (2004).
7. J. Shoeb, M. J. Kushner, *J. Vac. Sci. Technol. A* **29**, 051305 (2011).
8. M. Urbanowicz, M. R. Baklanov, J. Heijlen, Y. Travaly, and A. Cockburn, *Electrochem. Solid-State Lett.* **10**, G76 (2007).
9. A. M. Urbanowicz, D. Shamiryman, A. Zaka, P. Verdonck, S. De Gendt and M. R. Baklanov, *J. Electrochem. Soc.* **157**, H565 (2010).
10. F. N. Dultsev, A. M. Urbanowicz, and M. R. Baklanov, *Mater. Res. Soc. Symp. Proc.* Vol. 1079 (Materials Research Society 1079-N07-03, 2008).
11. K. Vanstreels, and A. M. Urbanowicz, *J. Vac. Sci. Technol. B*, **28**, 173 (2010).
12. F. Ossler, J. Larsson, and M. Alden, *Chem. Phys. Lett.* **250**, 287 (1996).
13. J. Lee and D. B. Graves, *J. Phys. D* **43**, 425201 (2010).
14. B. Jinnai, S. Fukuda, H. Ohtake, and S. Samukawa, *J. Appl. Phys.* **107**, 043302 (2010).
15. M. Chaudhari, J. Du, S. Behera, S. Manandhar, S. Gaddam, and J. Kelber, *Appl. Phys. Lett.* **94**, 204102 (2009).
16. O. V. Braginsky, A. S. Kovalev, D. V. Lopaev, E. M. Malykhin, Yu. A. Mankelevich, T.

- V. Rakhimova, A. T. Rakhimov, A. N. Vasilieva, S. M. Zyryanov, and M. R. Baklanov, *J. Appl. Phys.* **108**, 073303 (2010).
17. M.F.A.M. Van Hest, A. Klaver, D.C. Schram, and M.C.M. Van De Sanden, *Thin Solid Films* **449** 40 (2004).
18. M. A. Worsley, S. F. Bent, S. M. Gates, N. C. M. Fuller, W. Volksen, M. Steen and T. Dalton, *J. Vac. Sci. Technol. B* **23**, 395 (2005).
19. K. Singh, A. A. Kumbhar, and R. O. Dusane, *Materials Letters* **60** 1579 (2006).
20. T. Kikkawa, S. Kuroki, S. Sakamoto, K. Kohmura, H. Tanaka, and N. Hata, *Journal of The Electrochemical Society*, **152(7)**, G560 (2005).
21. O. Joubert , E. Sungauer, E. Pargon, X. Mellhaoui, R. Ramos, G. Cunge and L. Valier , *J. Vac. Sci. Technol. B* **25**, 1640 (2007).
22. L. Sha, and J. P. Chang, *J. Vac. Sci. Technol. A.* **21**, 1915 (2003).
23. L. Sha, and J. P. Chang, *J. Vac. Sci. Technol. A.* **22**, 88 (2003).
24. M. H. Sin, M. S. Park, and N.-E. Lee, *J. Vac. Sci. Technol. A.* **24**, 1373 (2006).
25. C. Wang and V. M. Donnelly, *J. Vac. Sci. Technol. A.* **26**, 597 (2008).
26. K. Nakamura, D. Hamada, Y. Ueda, K. Eriguchi, and K. Ono, *Appl. Phys. Exp.* **2**, 016503 (2009).
27. L. Sha, R. Puthenkovilakam, Y.-S. Lin, and J. P. Chang , *J. Vac. Sci. Technol. B* **21**, 2420 (2003).
28. W. S. Hwang, J. Chen, and W. J. Yoo, *J. Vac. Sci. Technol. A* **23**, 964 (2005).
29. J. Shoeb and M. J. Kushner, *J. Vac. Sci. Technol. A* **27**, 1289 (2009).

## 4. MECHANISMS FOR SEALING OF POROUS LOW-*k* SiOCH BY COMBINED He AND NH<sub>3</sub> PLASMA TREATMENT

### 4.1 Introduction

Porous dielectric materials having a low dielectric constant (*low-k*) are being used to lower the interconnect wiring capacitance to limit the *RC* time delay in integrated circuits.[1] SiOCH, silicon dioxide with CH<sub>x</sub> groups lining the pores, is one commonly used material, having porosities as large as 50% with pore diameters of up to a few nm. The pores can also be interconnected, offering pathways for reactive species to enter into the porous network during plasma etching or cleaning steps.[1,2] Penetration by plasma produced radicals into the interior of the material is thought to compromise its *low-k* nature. These radicals can react with the CH<sub>x</sub> groups to increase the average dielectric constant and so increase the *RC* time delay.

In order to maintain the *low-k* values of porous dielectrics, sealing of the pores at the surface may be necessary to prevent penetration of plasma produced species into the material during subsequent processing steps.[3-7] Dielectrics are typically etched in fluorocarbon plasmas in which there is deposition of a CF<sub>x</sub> polymer. The residual CF<sub>x</sub> polymer remaining at the end of the etch can, in fact, effectively seal the pores.[8] While CF<sub>x</sub> polymers have good sealing characteristics because of their low dielectric constant and hydrophobic properties, the fluorine in the polymers creates compatibility issues with diffusion barriers including chemically active metals like Ti and Ta.[8] As a result, the CF<sub>x</sub> polymer must be removed followed by a more integration compatible treatment for pore sealing.

The removal of the CF<sub>x</sub> layer would ideally be performed using an oxygen containing plasma due to the efficiency of oxidation of the polymer by oxygen radicals.[9-11] Unfortu-

nately, the underlying SiOCH film can also be damaged by the oxygen plasma, primarily by removing methyl groups by oxygen radicals which diffuse into the porous network.[12,13] This damage occurs in downstream effluents of oxygen containing plasmas at room temperature where ion energies are expected to be low and so is likely to be nearly a spontaneous process. Cleaning using oxygen containing plasmas is then a trade-off between treatments that are long enough to fully remove the  $CF_x$  polymer while not producing significant damage to the SiOCH.

Sequential treatment of SiOCH by He and  $NH_3$  plasmas has been shown to seal pores without surface damage while maintaining the *low-k* nature of the SiOCH.[4-6, 14] Pre-treatment with He plasmas is thought to create active surface sites which localize and accelerate the chemical reactions responsible for pore sealing.[5,14] The processes whereby subsequent  $NH_3$  plasma treatment completes the sealing are uncertain but at least two mechanisms have been proposed. The first proposes that  $NH_3$  plasma treatment catalyzes pore collapse and so produces a dense non-porous layer at the surface.[6] The second proposes that chemisorption of  $NH_x$  radicals result in Si-N and C-N bonding which leads to bridging of the opening of the pores.[4,5,14] Recent experimental results favor the latter mechanism.[15]

In this chapter, results from a computational investigation of pore sealing of *low-k* SiOCH, will be discussed on the basis of the bridging mechanism suggested in Refs.[4,5] while varying porosity, interconnectivity, treatment time, pore radius, and aspect ratio. We modeled a fully integrated 4-step etch, clean, activation and pore sealing process. The sequence begins with etching of an 8:1 aspect ratio trench in porous SiOCH using an Ar/ $C_4F_8$ / $O_2$  capacitively coupled plasma (CCP). Residual  $CF_x$  polymers on the sidewalls of the SiOCH were then removed using an Ar/ $O_2$  inductively coupled plasma (ICP). Subse-

quently a He ICP treatment followed by an Ar/NH<sub>3</sub> ICP treatment was applied to seal the pores open to the surface. We found that sealing efficiency is nearly independent of interconnectivity and porosity, but decreases with increasing the pore radius due to the inability for pore-sealing N-bonding to produce long chains. The sealing efficiency in trenches is sensitive to the respective lengths of activation and sealing treatments due to the need for reactive species to penetrate deep into the feature where view angles to the plasma are small. For this reason, sealing efficiency generally decreases with aspect ratio of the trench.

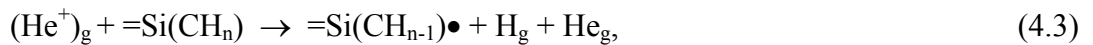
The reaction mechanisms for sealing are discussed in Sec. 4.2 followed by a discussion of sealing efficiency in Sec. 4.3. Our concluding remarks are in Sec. 4.4.

## 4.2 Reaction Mechanisms

A reaction mechanism was developed for plasmas sustained in He and NH<sub>3</sub>/Ar mixtures and their interactions with *low-k* porous SiOCH. The Hybrid Plasma Equipment Model (HPEM) was employed to obtain the energy and angular distributions for charged and neutral species incident onto the surface.[16] The sealing reaction mechanism was implemented in the Monte Carlo Feature Profile Module (MCFPM) with which the evolution of the *low-k* surfaces properties are predicted.[17-19] The MCFPM resolves the porous material with approximately atomic resolution. The cell size in this work is square with 0.4 nm × 0.4 nm dimensions, which is an effective radius of 0.2 nm. This value is smaller by about a factor of 3 than the smallest average pore radius considered in this investigation. The creation of pores in the MCFPM mesh is discussed in Refs. [20, 21]. The internal surfaces of the pores in SiO<sub>2</sub> were lined with a single layer of -CH<sub>3</sub> to approximate the structure of SiOCH.

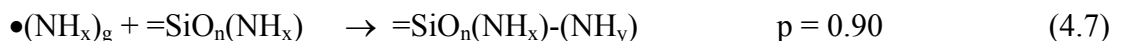
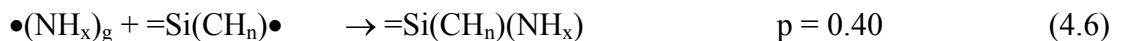
A four step, integrated process was modeled – 1) Etching of SiOCH in a fluorocarbon CCP, 2) cleaning in an oxygen containing ICP, 3) activation in a He ICP and 4) sealing in an NH<sub>3</sub> containing ICP. The reaction mechanism for etching of SiO<sub>2</sub> in Ar/C<sub>4</sub>F<sub>8</sub>/O<sub>2</sub> plasmas is discussed in Refs. [18, 20]. For etching of SiOCH, we additionally included activation reactions wherein H is removed from the CH<sub>3</sub> groups lining the pores creating active sites. This increases the sticking coefficient of, for example, CF<sub>x</sub> radicals resulting in polymerization. We also included the etching of the CH<sub>3</sub> group by O atoms. The polymer deposited on the sidewalls of the trench during the etch step was removed by Ar/O<sub>2</sub> ICP treatment, using the reaction mechanism discussed in Ref. [21]. In addition, the CH<sub>3</sub> group could be activated by ion bombardment and etched by the oxygen radicals and ions as CO/CO<sub>2</sub> during the etch step.

After the cleaning step, He plasma treatment of the SiO<sub>2</sub> and exposed CH<sub>3</sub> groups is thought to create activated sites that assist in pore sealing during a subsequent Ar/NH<sub>3</sub> plasma treatment.[4,5,14] He<sup>+</sup> and VUV photons (whose fluxes are also computed in the plasma equipment model) break Si-O bonds and remove H from CH<sub>3</sub> groups lining the pores to create the active sites. The bond breaking and site activation reactions are summarized as,



where  $=M\bullet$  represents a surface bonded, free radical site, and the subscript g represents a gas phase species. It has been proposed that during He plasma pre-treatment a surface densification process occurs which shrinks the openings to the pores which can then enhance the sealing efficiency by the  $NH_3$  plasmas.[14] This densification produces only a small increase in sealing efficiency, on the order of a few percent, and is less important for pores of 0.8-0.9 nm pore radius.[14,15] As such, densification effects have been excluded in the model for simplicity.

Following He plasma treatment,  $NH_x(x = 1,2)$  species created in an Ar/ $NH_3$  plasma are chemisorbed at activated sites on SiOCH forming Si-N and C-N bonds.[4,5, 22-24] Chemical reactions between  $NH_x$  radicals and activated Si sites produce compounds such as Si- $NH_x$  ( $x=1, 2$ ),  $=Si-NH-Si=$  and  $SiNH_x-NH_y$ . [4,5,22] For porous SiOCH, C-N bonding is also possible forming  $CH_x-NH_y$  compounds which are important to bridging the pore openings.[4,5] The model treats these chemisorbed species as precursors to further adsorption of  $NH_x$  which form N-N bonds linking C or Si atoms from opposite pore walls. This N-N bonding results in, for example,  $=Si(HN)-(NH)(CH_n)Si=$  bridging compounds across pores. These processes and their probabilities are summarized as,



As suggested in Ref. [22],  $\text{NH}_3$  molecules are physisorbed at exposed active surface sites but have limited contributions to sealing.

The probabilities for both surface site activation and sealing reactions have been determined by extensive parameterization of the models to be qualitatively consistent with experimental results available in the literature. Bounds of reaction probabilities are set based on thermodynamic properties and change in enthalpy of reactions, and within those bounds parameterization and comparison to experiments refine the mechanism. Some examples of works that guided the development of the reactions mechanism follow.

It has been reported that a 20s He plasma treatment followed by a 20s  $\text{NH}_3$  plasma treatment can essentially completely seal a porous *low-k* flat surface with 0.8 nm pore radius.[4,14] We parameterized the activation probabilities to determine those values that achieved nearly 100% activation and sealing on flat surfaces for similar fluences of radicals and ions. Si-O bond scission by photons has been reported by Urbanowicz et al.[14] Since the Si-O bond strength is larger than for C-H bond, it is expected similar processing conditions will also produce C-H bond cleavage, and so we included these processes. In this regard, H removal from  $\text{CH}_x$  groups along with Si-O bond scission during He plasma treatment of  $\text{SiOCH}$  has been reported by Dultsev et al.[5] It has been reported that an increase in power for He pretreatment more efficiently blocks water adsorption from air after  $\text{NH}_3$  sealing, which indicates  $\text{He}^+$  ion may play a role in activation that results in a better sealing.[4] We therefore included  $\text{He}^+$  knock-on collisions which sputter H from  $\text{Si-CH}_x$  groups, and used a large substrate bias. Such high energy ions also produce Si-O bond scission. Although other bond-scissions may occur by  $\text{He}^+$  and VUV fluxes, we chose to limit the reaction mechanisms to Si-O and H removal as being representative of those processes. Our

model for N-C bonding was based on analogy to gas phase reactions.[5,22,25]

Operationally, the HPEM is first sequentially run four separate times with the etch, clean, passivation and sealing chemistries to produce fluxes of ions and radicals to the substrate for each of the processing steps. The MCFPM is then sequentially executed using these four sets of fluxes. The initial conditions for the first etch step is the masked but otherwise untreated SiOCH. The ending conditions from the MCFPM from the etch step are then used as the initial conditions for the clean step. This sequence is repeated for the activation and sealing steps. Each result for sealing efficiency discussed here is the average of 20 integrated processing sequences (80 MCFPM runs) where the initial distributions for pore size and distribution are determined by the choice of a different random number seed, as discussed in Refs. [20, 21].

The first etch step was performed using a CCP sustained in  $\text{Ar}/\text{C}_4\text{F}_8/\text{O}_2 = 80/15/5$ , 40 mTorr, and powered at 10 MHz. The remaining steps were performed in an ICP reactor treating a wafer 15 cm in diameter. The coil was powered at 13.56 MHz with a 10 MHz bias on the substrate. The reactor was 26 cm in diameter with a wafer-to-coil height of 10 cm. The conditions for the polymer removal step were  $\text{Ar}/\text{O}_2 = 5/95$ , 10 mTorr, 100 sccm with 300 W ICP power. He treatment was also at 10 mTorr and 300 W. The ion density for the  $\text{Ar}/\text{O}_2$  plasmas was  $2.6 \times 10^{10} \text{ cm}^{-3}$  and  $3.8 \times 10^{10} \text{ cm}^{-3}$  for the He plasmas. For both plasmas, a 250 V rf bias, produced ions incident on the substrate with average energy near 400 eV and with an angular spread from the vertical of  $<15^\circ$ . For the sealing step, the process conditions were 10 mTorr of  $\text{Ar}/\text{NH}_3 = 25/75$  and 300 W. No substrate bias was applied.  $\text{NH}_4^+$  had the highest ion density ( $2.9 \times 10^{10} \text{ cm}^{-3}$ ), followed by  $\text{NH}_3^+$  ( $2.6 \times 10^{10} \text{ cm}^{-3}$ ). The major radical

densities were  $\text{NH}_2$  ( $2.4 \times 10^{13} \text{ cm}^{-3}$ ) and  $\text{NH}$  ( $1.6 \times 10^{13} \text{ cm}^{-3}$ ). The flux of  $\text{NH}_2$  was  $4 \times 10^{17} \text{ cm}^{-2} \text{ s}^{-1}$  and that of  $\text{NH}$  was  $2 \times 10^{16} \text{ cm}^{-2} \text{ s}^{-1}$ .

In the discussion that follows, we characterize the sealing process using *sealing efficiency*,  $\eta$ . The sealing efficiency is the fraction of pores that were initially open to the plasma that are sealed.  $\eta$  was determined for each set of conditions by running 20 separate simulations while varying the random number seeds that determine the geometrical layout of the pores and the random fluxes striking the substrate. The fractions of pores that are sealed are then averaged over these trials to produce  $\eta$ .

The measure of what is a good or acceptable sealing efficiency is ultimately determined by the subsequent processing steps and procedures. For example, water exposure of porous SiOCH produces Si-OH bonding which increases the dielectric constant  $k$  of the material. A good sealing efficiency might then be defined as the value that will prevent water during air exposure from entering the pores and increasing the  $k$  value. Ideally a sealing efficiency of 100% will prevent such damage. However, even partial sealing that reduces the average pore opening size will reduce water uptake by the porous network. In our own computational studies, we have found that  $\eta > 70\%$  is effective at reducing water vapor uptake when porous SiOCH is exposed to humid air. With the caveat that the goodness of sealing is determined by the subsequent process steps, for purposes of discussion in this paper,  $\eta \geq 70\%$  is likely a good criterion for acceptable sealing.

### 4.3 Sealing Efficiency

The base case conditions for this study used an average pore radius in the SiOCH of

0.8 nm with a standard deviation of 0.1 nm. Both the porosity and interconnectivity were 30%. These parameters correspond to a  $k$ -value of about 2.5.  $-\text{CH}_3$  groups line the pores of otherwise  $\text{SiO}_2$  material, where  $\text{CH}_3$  groups are connected to Si atom. A typical region of the  $\text{SiOCH}$  (as represented in the MCFPM) at the top of the feature with an open pore is shown in Fig. 4.1a. The entire feature after the four integrated steps is shown in Fig. 4.2 – (4.2a) after fluorocarbon plasma etching, (4.2b) after removal of the polymer, (4.2c) after hard mask removal and He plasma activation, and (4.2d) after  $\text{Ar}/\text{NH}_3$  plasma sealing. A typical pore after He plasma treatment is shown in Fig. 1b during which surface sites were activated by fluxes of  $\text{He}^+$  and VUV photons. The pore after sealing by the  $\text{Ar}/\text{NH}_3$  plasma is shown in Fig. 4.1c. The pore openings were bridged by a short chain of, for example,  $\text{Si-N-N-Si}$ ,  $\text{C-N-N-C}$  or  $\text{Si-N-N-C}$  bonding, thereby sealing the pore.

After plasma etching, a  $\text{CF}_x$  polymer layer about 1.5 nm thick remains on the surface of the  $\text{SiOCH}$ . The length of the  $\text{Ar}/\text{O}_2$  plasma cleaning is a compromise between fully removing the  $\text{CF}_x$  polymer (longer times) and minimizing the removal of the  $-\text{CH}_3$  groups by penetration of O atoms into the porous network (shorter times). Some residual  $\text{CF}_x$  remains in this tradeoff while a few pores have been opened or expanded by etching of their  $-\text{CH}_3$  groups. Since activation by the He plasma is largely line-of-sight by directional photons and ions, the sidewalls of the trench are activated slowly compared to the top surfaces, and the interior surfaces of open pores are often not activated. After the sealing step, there is  $-\text{NH}_x$  functionalization on all exposed surfaces whose sites were activated by the He plasma to saturation.

The purpose of the He plasma is to create reactive sites that are amenable to chemisorption by  $\text{NH}_x$  ( $x=1,2$ ). Site activation consists of loss of an H atom if the site is occupied

by a  $-\text{CH}_x$  group or Si-O bond breaking if the site is  $\text{SiO}_2$ . The fraction of surface sites that are activated by  $\text{He}^+$  and photons is shown in Fig. 4.3 as a function of time of He plasma treatment. Results are shown for different probabilities of bond breaking per incident  $\text{He}^+$  ion. For probabilities from 0.01 to 0.9, there is initially a rapid activation of sites corresponding to those that have direct view angles to the plasma. After this initial activation there is a slower asymptotic approach to activation of all sites that have any view angle to the plasmas. Sites that are shadowed from direct line of site to the plasmas due to the roughness of the porous surface must rely upon favorable reflection and backscatter of hot atoms for activation. Although the majority of surface sites can be activated on the top surface, within the trench, the small view angle to the plasma combined with shadowing by surface roughness allows a maximum of 80% surface sites to be activated. High probabilities for activation, for example,  $p = 0.8$  and  $0.9$  in Fig. 3, asymptote to this same value.

An interesting situation occurs when site activation for  $p=0.1$  is higher than that for  $p=0.2$  at times  $< 50\text{s}$ , as shown in Fig. 4.3. This is likely a consequence of the higher reaction probability initially producing additional surface roughness which then shadows adjacent sites. However, as the activation time increases, the increase in probability of site activation dominates over the shadowing caused by the small increase in surface roughness.

$\eta$  (the fraction of all pores open to the surface that are sealed) as a function of He plasma treatment time is shown in Fig. 4.4a for 30 s of  $\text{Ar}/\text{NH}_3$  plasma treatment. Typical profiles with bridging sealing groups displayed are shown in Fig. 4.5. Without He plasma pre-treatment, some activation of surface sites is accomplished by the  $\text{Ar}/\text{NH}_3$  plasma and so some sealing does occur. However, the efficiency of activation is small compared to He plasmas and only 40% of the pores are ultimately sealed. For a flat low- $k$  surface, as on the

top of the surface of the feature,  $\eta$  increases with He plasma treatment time for up to 10 s as an increasing fraction of the Si-O surface bonds are broken and H is removed from surface -CH<sub>3</sub> groups.  $\eta$  then saturates when at about 95% when the majority of Si-O bonds and -CH<sub>3</sub> sites have been activated.

For the interior sidewalls of the trench, a longer He plasma time is required to activate sites deep in the trench to enable sealing. For instance, a 200 s He plasma pretreatment followed by a 30 s Ar/NH<sub>3</sub> plasma treatment seals 75% of the surface pores on the 8:1 aspect ratio trench sidewalls (shown in Fig. 4.2d, 4.5b and 4.6b). Overall  $\eta$ , which combines both flat surface and sidewall sealing, is 82%. The surface sites on sidewalls deeper in the trench require more time to be activated due to their smaller view-angles to the plasma. This dependence on depth in the trench is most critical for the directed or line-of-sight fluxes (ions and photons) which activate the surface sites. The passivating neutral NH<sub>x</sub> neutral fluxes are less sensitive to view-angle to the plasma as there will be some diffusive reflection off the sidewalls, however these fluxes may be depleted by reactions as they diffuse into the trench.

$\eta$  as a function of Ar/NH<sub>3</sub> plasma treatment time is shown in Fig. 4.4b for 200s of He plasma pretreatment. Ignoring the possibility of densification during He plasma treatment, in the absence of the Ar/NH<sub>3</sub> plasma treatment, there is no sealing. Sealing efficiency increases for the first 10 s on flat surfaces and for the first 20 s on trench sidewalls, and then saturates as the majority of the activated sites are passivated. It takes a longer time for NH<sub>x</sub> radicals to passivate the active sites on sidewalls deep inside the trench compared to the flat top surface due to the smaller view-angle to the plasma, achieving only 75% sealing.

The lower fraction of sealed sites on the sidewalls is more a function of the lack of activation by the He plasma than the inability of  $\text{NH}_x$  radicals to reach a site. For example, the sidewall sealing efficiency  $\eta$  was computed as a function of the length of  $\text{NH}_3$  plasma treatment for short (8 s) and long (200 s) He plasma pretreatment times. The results are shown in Fig. 4.5 along with profiles for the two cases. In both cases,  $\eta$  first increases and then saturates as the  $\text{NH}_3$  plasma treatment time increases. The short pretreatment time results in incomplete activation and  $\eta$  asymptotes to about 42%. The longer pretreatment time, able to activate more sites lacking direct view angles to the plasma, asymptotes to a higher sealing efficiency, about 75%. The incomplete sealing is shown by the profile in Fig. 4.5a where larger pores, lacking activated sites along the edges of the pore, are left open. The otherwise identical profile having longer He plasma pretreatment, has many of these larger pores sealed over.

The sealing efficiency decreases with increasing pore size as shown in Fig. 4.4c. Since  $\text{NH}_x$  compounds do not form long chains, sealing relies on the formation of C-N, Si-N and single N-N bonds to bridge the pore opening. The limited range for the bonding of these surface species sets the maximum pore size that can be sealed. Overall  $\eta$  decreases nearly linearly with pore size, to below 60%, as the pore radius exceeds 1.1 nm. These results are somewhat skewed by the persistence of a small amount of  $\text{CF}_x$  polymer on the sidewalls that provides about 5-10% of sealing (which does not occur on the top surface). This is due to the afore-mentioned limited exposure to Ar/ $\text{O}_2$  cleaning plasmas to minimize the likelihood of removing  $-\text{CH}_3$  groups. These results are also sensitive to the standard deviation of the distribution of the pore radii. Larger standard deviations for a given pore radius have a higher

proportion of pores larger than the critical pore size that can be sealed. The end result is less sealing of those pores for the same average pore size. These trends are shown in Fig. 4.6 where profiles are shown of sealed SiOCH for different aspect ratios. Small pores or pores with a limited opening are efficiently sealed. Statistically larger pore openings cannot be bridged.

The activation of surface sites generally decreases with depth into the trench due to the decreasing view angle to the plasma. Truly shadowed features are not activated by photons – whereas such shadowed features are only activated by reflected hot neutrals or ions. As a result of this depth dependence, we found that for same He and Ar/NH<sub>3</sub> plasma treatment times, the sealing efficiency  $\eta$  on the sidewalls is inversely proportional to the trench aspect ratio as shown in Fig. 4.6d. For example, with a smaller aspect ratio of 4, similar He and Ar/NH<sub>3</sub> plasma treatments sealed 90% of sidewall surface pores. For a larger aspect of 15, less than 50% of the sidewall pores were sealed.

We found that  $\eta$  is nearly independent of porosity and interconnectivity for a constant pore radius. With higher porosity for a fixed pore radius, the number of surface pores increases but the likelihood of sealing any given pore depends dominantly on its radius. A longer time may be required to seal the pores with increasing porosity but the final fraction of pores being sealed is the same. For a fixed porosity, increasing connectivity in principle only affects the geometrical relationship of pores to each other but should not affect the radii of individual pores. As a result,  $\eta$  is not sensitive to connectivity.

It has been experimentally shown that flat porous SiOCH having 0.8-0.9 nm pore radii can be completely sealed by combined He and NH<sub>3</sub> plasma treatment.[14] Our results for

a flat low- $k$  surface predict that such combined treatment provides a sealing efficiency of  $> 95\%$ . Although our process conditions are different than reported in the literature, the scaling laws are generally applicable. Sealing of pores in SiOCH can be achieved by pretreating with He plasmas having sufficient VUV and  $\text{He}^+$  fluences to activate sites, and treating with Ar/ $\text{NH}_3$  plasmas having sufficient  $\text{NH}_x$  radical fluences to passivate the activated sites. This assumes that pore radii are not too large (generally  $\leq 1$  nm) and substrate biases are sufficiently low during the sealing step that  $-\text{CH}_x-\text{NH}_y$  and  $-\text{Si}-\text{NH}_x$  sealing compounds are not sputtered by energetic ions. As discussed in Refs. [4] and [5], if bridging is the dominant sealing mechanism, the bridging network will have a limited extent, and there should be a sensitivity of  $\eta$  on pore radius, as our results have shown. It has also been suggested that the small coverage of  $-\text{NH}_x$  groups responsible for pore sealing reside only on the surface and so are not likely to dominate IR absorption spectra.[4] In our model, only 1-2 monolayers of  $-\text{NH}_x$  radicals are adsorbed on the low-  $k$  which either bridge pore openings or form  $\text{Si}-\text{NH}_y/\text{CH}_x-\text{NH}_y$  compounds.

#### 4.4 Concluding Remarks

Integrated processing of high aspect ratio trenches in porous SiOCH using Ar/ $\text{C}_4\text{F}_8/\text{O}_2$  plasmas for etching, Ar/ $\text{O}_2$  plasmas for polymer removal, and successive He and  $\text{NH}_3$  plasma treatments for activation and pore sealing were computationally investigated. To avoid diffusion of O species into the porous network which would remove  $-\text{CH}_3$  groups, limited Ar/ $\text{O}_2$  plasma exposure time was allowed, which resulted in traces of polymer to persist on the sidewalls. However, with He pretreatment these polymer sites were activated, en-

abling the polymer traces to be covered by C-N compounds during Ar/NH<sub>3</sub> sealing. Pore sealing was achieved by formation of Si-N and C-N bonds at He plasma activated sites followed by one N-N bond linking C or Si atoms from opposite pore walls. Pore sealing efficiency is nearly independent of porosity and interconnectivity, while being dependent on He and NH<sub>3</sub> plasma treatment time, pore radius, and aspect ratio. The efficiency of pore sealing decreases with increasing pore size due to the limited extent of these bonding configurations.

## 4.5 Figures

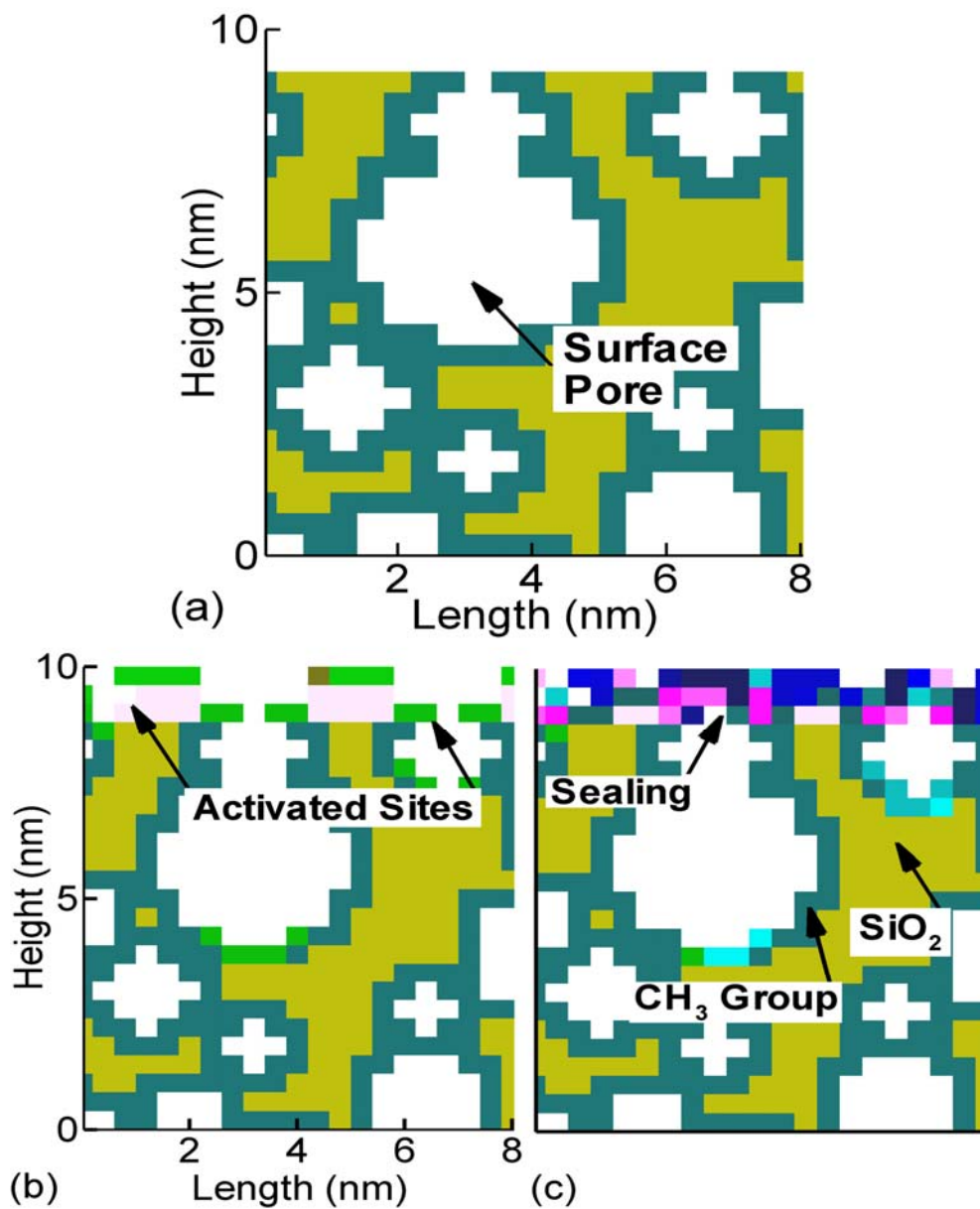


Fig. 4.1 Activation of pores open to the surface by He plasmas and sealing by Ar/NH<sub>3</sub> plasmas. (a) Typical initial conditions with CH<sub>3</sub> groups lining pores in SiO<sub>2</sub>, an approximation to SiOCH. (b) Activated surface sites following He plasma treatment. (c) Sealed pores following Ar/NH<sub>3</sub> plasma treatment.

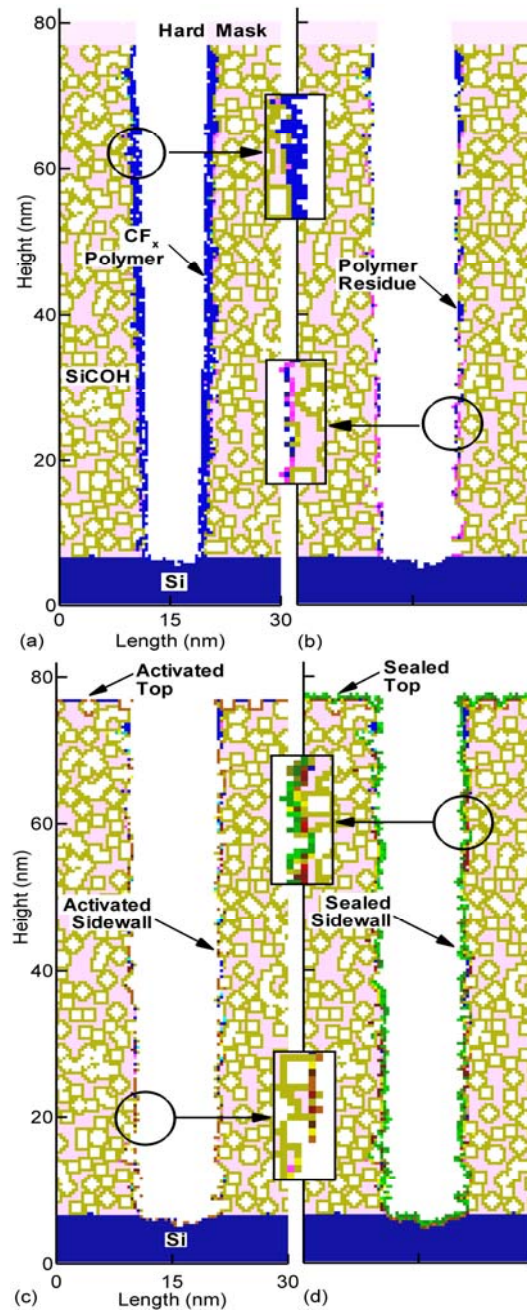


Fig. 4.2 Profiles of porous low- $k$  SiOCH during integrated etch, clean, activation and sealing of an 8:1 aspect ratio trench. (a) After Ar/C<sub>4</sub>F<sub>8</sub>/O<sub>2</sub> plasma etching where sidewalls are covered with fluorocarbon polymers. (b) CF<sub>x</sub> polymers are removed from sidewalls by Ar/O<sub>2</sub> plasma cleaning. (c) He plasma activated porous surfaces by Si-O bond breaking and H removal from CH<sub>3</sub> group. (d) Surface pores are sealed in Ar/NH<sub>3</sub> plasmas by NH<sub>x</sub> adsorption at reactive surface sites forming Si-N and C-N bonds. (Color coding: dark pink – SiO<sub>2</sub>, light pink – hard mask, olive – CH<sub>3</sub> groups, blue-CF<sub>x</sub> polymer, brown – activated sites, green – N-containing bridging compounds.)

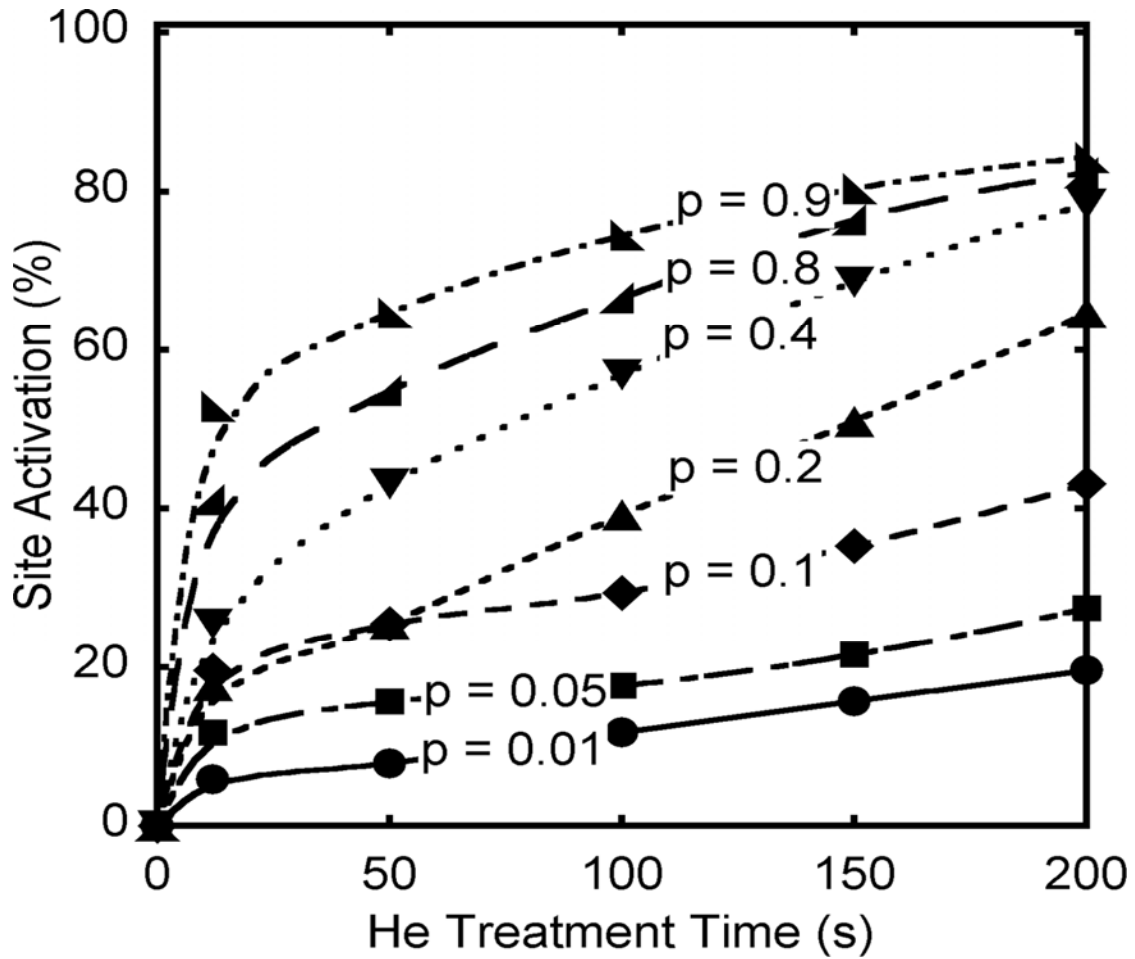


Fig. 4.3 Fraction of surface sites in a HAR trench activated in a He plasma as a function of treatment time. Values are shown for different probabilities for site activation by  $\text{He}^+$  ion impact. The small view angle to the plasma and sites shadowed by surface roughness limits the percentage of sidewall surface sites that can be activated to about 80%. A higher surface activation probability reaches this saturated value faster but does not change the asymptotic value.

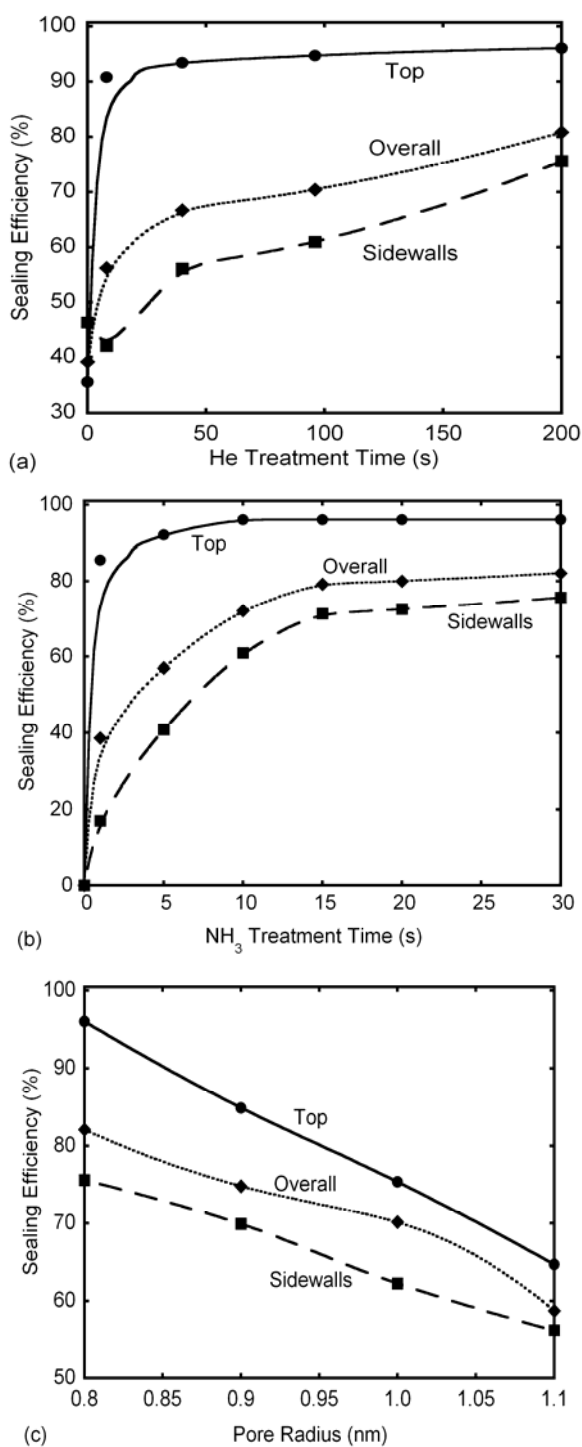


Fig. 4.4 Sealing efficiency as a function of (a) He plasma exposure time, (b) Ar/NH<sub>3</sub> plasma exposure time and (c) pore radius. For both surface site activation and sealing efficiency, sidewalls require more time for sealing due to their smaller view angle to the plasma and ultimately have a lower asymptotic value. Sealing efficiency decreases with increasing pore radius as the N-N bonding has a limited extent.

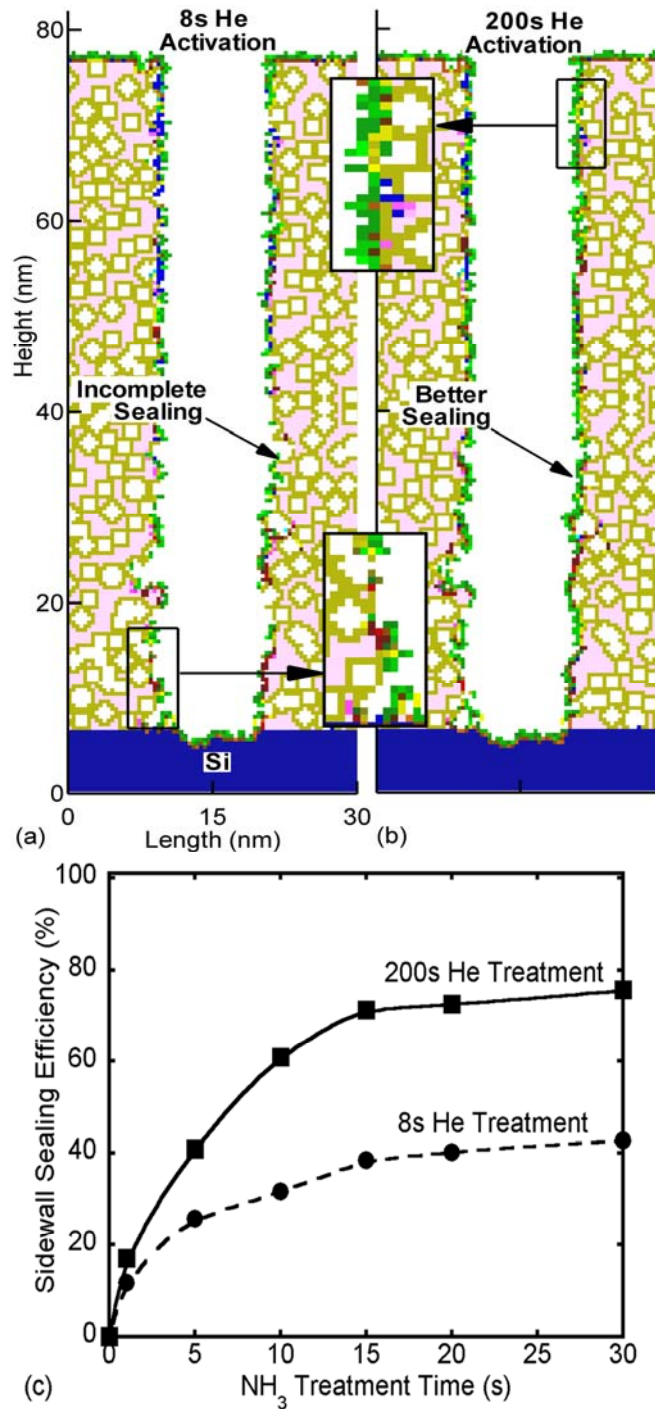


Fig. 4.5 Effect of He pretreatment time on sidewall sealing. Profiles of the trench after Ar/ $\text{NH}_3$  sealing for He pretreatment time of (a) 8 s and (b) 200 s. (c) Sealing efficiency as a function of  $\text{NH}_3$  plasma treatment time after 8 s and 200 s of He pretreatment. As the He pretreatment time increases the sealing efficiency as a function of  $\text{NH}_3$  plasma treatment time saturates to a higher value. (Color coding: dark pink –  $\text{SiO}_2$ , olive –  $\text{CH}_3$  groups, blue- $\text{CF}_x$  polymer, brown – activated sites, green – N-containing bridging compounds.)

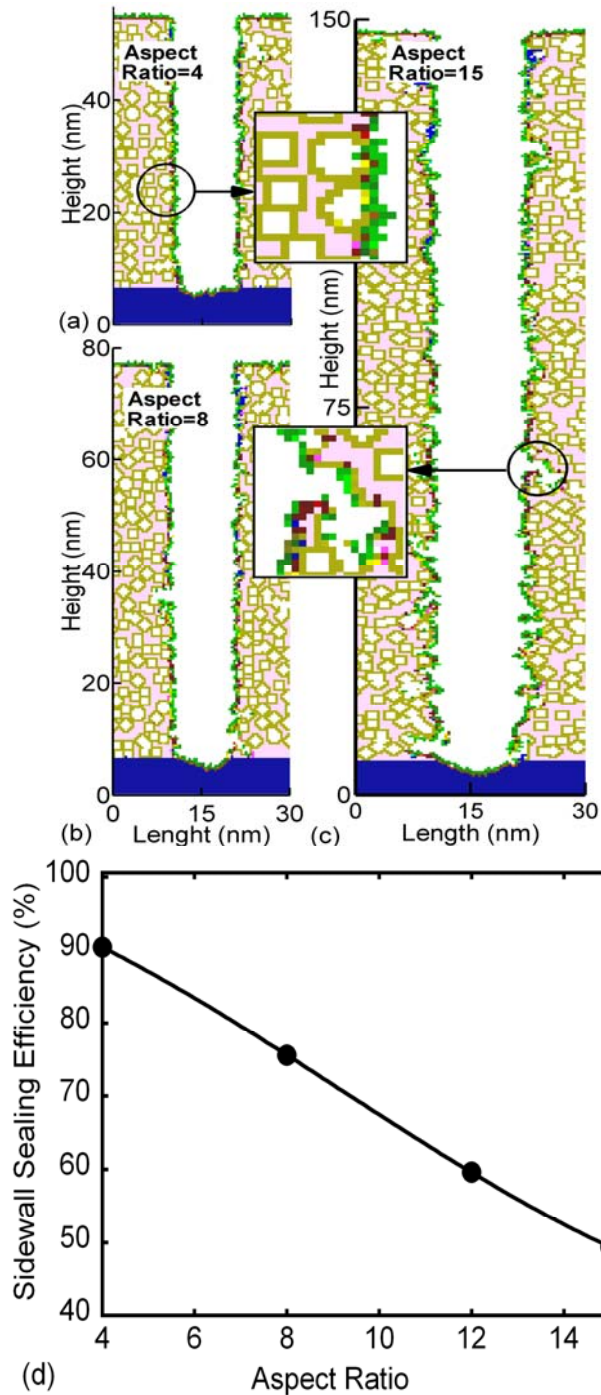


Fig. 4.6 Effect of aspect ratio effect on pore sealing. Profiles of trench after Ar/NH<sub>3</sub> plasma sealing for aspect ratios of (a) 4:1, (b) 8:1, and (c) 15:1. (d) Sealing efficiency as a function of aspect ratio. With equal times for He activation and NH<sub>3</sub> sealing, sidewall sealing efficiency is inversely proportional to the trench aspect ratio. (Color coding: dark pink – SiO<sub>2</sub>, light pink – hard mask, olive – CH<sub>3</sub> groups, blue – CF<sub>x</sub> polymer, brown – activated sites, green – N-containing bridging compounds.)

#### 4.6 References

1. C. M. Whelan, Q. T. Le, F. Cecchet, A. Satta, J. J. Pireaux, P. Rudlof, and K. Maex, *Electrochem. Solid-State Lett.* **7**, F8 (2004).
2. G. Beyer, A. Satta, J. Schuhmacher, K. Maex, W. Besling, O. Kilpela, H. Sprey, G. Tempel, *Microelectron. Eng.* **64**, 233 (2002).
3. T. Abell and K. Maex, *Microelectron. Eng.* **76**, 16 (2004).
4. A. M. Urbanowicz, D. Shamiryan, A. Zaka, P. Verdonck, S. De Gendt and M. R. Baklanov, *J. Electrochem. Soc.* **157**, H565 (2010).
5. F. N. Dultsev, A. M. Urbanowicz, and M. R. Baklanov, *Mater. Res. Soc. Symp. Proc.* Vol. 1079 © 2008 Materials Research Society 1079-N07-03.
6. H.-G. Peng, D.-Z. Chi, W.-De Wang, J.-H. Li, K.-Y. Zeng, R. S. Vallery, W. E. Frieze, M. A. Skalsey, D. W. Gidley, and A. F. Yee, *J. Electrochem. Soc.* **154**, G85 (2007).
7. K. Hamioud, V. Arnal, A. Farcy, V. Jousseau, A. Zenasni, B. Icard, J. Pradelles, S. Manakli, Ph. Brun, G. Imbert, C. Jayet, M. Assous, S. Maitrejean, D. Galpin, C. Monget, J. Guillan, S. Chhun, E. Richard, D. Barbier, M. Haond, *Microelectron. Eng.* **87**, 316 (2010).
8. G. Mannaert, M. R. Baklanov, Q. T. Le, Y. Travaly, W. Boullart, S. Vanhaelemeersch, and A. M. Jonas *J. Vac. Sci. Technol. B* **23**, 2198 (2005).
9. H. Seo, S. B. Kim, J. Song, Y. Kim, H. Soh, Y. C. Kim, and H. Jeon, *J. Vac. Sci. Technol. B* **20**, 1548 (2002).
10. K. Sakuma, K. Machida, K. Kamoshida, Y. Sato, K. Imai, and E. Arai, *J. Vac. Sci. Technol. B* **13**, 902 (1995)

11. M. A. Hartney, D. W. Hess, and D. S. Soane, *J. Vac. Sci. Technol. B* **7**, 1 (1989).
12. D. Shamiryany, M. R. Baklanov, S. Vanhaelemeersch and K. Maex, *J. Vac. Sci. Technol. B* **20**, 1923 (2002).
13. O. V. Braginsky, A. S. Kovalev, D. V. Lopaev, E. M. Malykhin, Yu. A. Mankelevich, T. V. Rakhimova, A. T. Rakhimov, A. N. Vasilieva, S. M. Zyryanov and M. R. Baklanov, *J. Appl. Phys.* **108**, 073303 (2010).
14. M. Urbanowicz, M. R. Baklanov, J. Heijlen, Y. Travalay, and A. Cockburn, *Electrochem. Solid-State Lett.* **10**, G76 (2007).
15. Private communication with M. Urbanowicz, IMEC, Belgium, 2011.
16. M. J. Kushner, *J. Phys. D* **42**, 194013 (2009).
17. A. Agarwal and M. J. Kushner, *J. Vac. Sci. Technol. A* **27**, 37 (2009).
18. D. Zhang and M. J. Kushner, *J. Vac. Sci. Technol. A* **19**, 524 (2001).
19. J. Lu and M. J. Kushner, *J. Vac. Sci. Technol. A* **19**, 2652 (2001).
20. A. Sankaran and M. J. Kushner, *J. Vac. Sci. Technol. A* **22**, 1242 (2004).
21. A. Sankaran and M. J. Kushner, *J. Vac. Sci. Technol. A* **22**, 1260 (2004).
22. J. L. Bischoff, F. Lutz, D. Bolmont and L. Kubler, *Surf. Sci.* **251/252**, 270 (1991).
23. H.-W. Guo, L. Zhu, L. Zhang, S.-J. Ding, D. W. Zhang, R. Liu, *Microelectron. Eng.* **85**, (2114) 2008.
24. S. Behera, J. Lee, S. Gaddam, S. Pokharel, J. Wilks, F. Pasquale, D. Graves, and J. A. Kelber, *Appl. Phys. Lett.* **97**, (034134) 2010.
25. M. S. Foster, A. D. Williamson, and J. L. Beauchamp, *International Journal of Mass Spectrometry and Ion physics*, **15** (429) 1974.

## 5. DAMAGE BY RADICALS AND PHOTONS DURING CLEANING OF POROUS LOW- $k$ SiOCH USING Ar/O<sub>2</sub> AND He/H<sub>2</sub> PLASMAS

### 5.1 Introduction

The lower dielectric constant (low- $k$ ) and lower capacitance of porous materials used for the interlayer dielectric in integrated circuits reduces signal propagation delays. Typical low- $k$  materials include porous SiO<sub>2</sub> with methyl groups (CH<sub>3</sub>) lining the pores – SiOCH. Such pristine low- $k$  materials are essentially hydrophobic (because of the presence of hydrophobic -CH<sub>3</sub> groups) and do not absorb more than a few percent of water when exposed to air even when the humidity is high.[1] This moisture can be driven out of the porous network by heating to 200 C without detrimentally affecting the stability of the porous material.[2] However, when porous low- $k$  SiOCH is exposed to oxygen and hydrogen containing plasmas –CH<sub>3</sub> groups are etched and the nature of the dielectric changes from hydrophobic towards hydrophilic as unbonded Si atoms can adsorb water from the environment which increases the dielectric constant.[1]

Fluorocarbon containing plasmas are often used to etch SiOCH, a process that deposits CF<sub>x</sub> polymers on the sidewalls of the features and inside surface lining pores. Although the polymer can effectively seal the surface pores to block moisture uptake,[1] these CF<sub>x</sub> polymers are usually removed as they can cause compatibility issues in subsequent processing steps. For example, halogen containing polymers can react with the diffusion barrier metals Ti and Ta.[3] Also, these polymers can introduce hydrophilic properties since, on a relative basis, they are not as hydrophobic as –CH<sub>x</sub> groups.[1] It has been reported that after a fluorocarbon etch, porous SiOCH can adsorb water from the ambient air to volume

fractions as high as 8%, which questions the hydrophobicity and sealing efficiency introduced by  $\text{CF}_x$  polymers.[1]

The removal of the  $\text{CF}_x$  layer is ideally performed using an oxygen containing plasma due to the efficiency of etching the polymer by oxygen radicals.[4-6] As such,  $\text{O}_2$  containing plasmas have often been used for such post-etch cleaning and photoresist removal.[7] However,  $\text{O}_2$  plasma cleaning can also remove hydrophobic groups (such as  $-\text{CH}_3$  from  $-\text{SiO}_2-\text{CH}_3$  and  $-\text{Si}-\text{H}$  groups) from  $\text{SiOCH}$ , replacing them with hydrophilic groups (such as  $-\text{SiO}_2-\text{OH}$ ) which can initiate further adsorption of  $\text{H}_2\text{O}$  molecules that increases the dielectric constant.[7-11] The presence of  $-\text{SiO}_2-\text{OH}$  can result in further water uptake by creating  $-\text{SiO}_2-\text{OH}-\text{H}_2\text{O}$  like compounds through hydrogen bonding.[9-11] It has been reported that with the high dielectric constant of water ( $k \approx 80$ ), loss of hydrophobic  $-\text{CH}_3$  groups and incorporation of water from humid air can increase the dielectric constant  $k$  from 2.5 to 20 within 10 minutes of  $\text{O}_2$  plasma treatment.[2]

The hydrophilic nature of  $\text{SiOCH}$  has a nearly linear relationship with carbon depletion.[1] As a result, a cleaning process that minimizes C depletion will also help to maintain the hydrophobic properties of the film.  $\text{SiOCH}$  is relatively stable when  $\text{H}_2$  plasmas are used for cleaning compared to the use of  $\text{Ar}/\text{O}_2$  plasma cleaning.[12] The addition of He to the  $\text{H}_2$  plasma aids in preconditioning the surface to improve pore sealing in subsequent treatment using  $\text{NH}_3$  containing plasmas.[13-15] It has also been reported that He/ $\text{H}_2$  plasmas are an attractive option for photoresist (PR) mask removal due to there being a small increase of the dielectric constant of low- $k$  films during the ashing process.[16]

These processes are complicated by the presence of VUV radiation from the plasma coincident to the fluxes of radicals and ions. VUV photons can produce scission of nearly all

bonds in the SiOCH films and of Si-C bond in  $-\text{SiO}_2\text{-CH}_3$  in particular. Such bond scissioning has the potential of accelerating damage by generating sites that react with plasma produced species at locations that would otherwise be nonreactive with the same species. These sites are more likely to react with or hydrogen bond with water, which further increases the dielectric constant.

In this chapter, we discuss reaction mechanisms and computationally analyze damage of porous SiOCH during cleaning with Ar/O<sub>2</sub> and He/H<sub>2</sub> plasmas when considering the consequences of VUV photon fluxes from the plasma. The Hybrid Plasma Equipment Model (HPEM) was used to obtain the ion energy and angle distributions of reactive fluxes from inductively coupled plasmas with capacitive substrate biases for cleaning, and from capacitively coupled plasmas for etching.[17] These distributions were then used as input to the Monte Carlo Feature Profile Model (MCFPM) to predict profiles and composition of the SiOCH.[18] Damage of the porous SiOCH was characterized by the depth at which removal of  $-\text{CH}_3$  is observed – the demethylation depth. For pores which are not in the line-of-sight to the plasma, diffusion of reactive species into the porous SiOCH is required for damage to occur in the absence of VUV photons. We have also found that deeply penetrating plasma-produced-photons can produce Si-C bond scissioning which accelerates the removal of  $-\text{CH}_3$  groups. Results will be discussed for the cleaning of pores as a function of treatment time, interconnectivity, and photon fluxes.

In Chapter 6, we concentrate on degradation or increase in dielectric constant resulting from water incorporation after the cleaning damage.[19]  $-\text{CH}_3$  groups are etched from  $-\text{SiO}_2\text{-CH}_3$  during cleaning and such removal generates  $-\text{SiO}_2\bullet$  which has a dangling bond. Water attacks such site and form  $-\text{SiO}_2\text{-OH}$  type products. For the high  $k$  ( $\approx 80$ ) of water,

such products have a high  $k$  and it increases the overall  $k$  of the porous low- $k$ . In Chapter 6, we model the degradation of  $k$  as a function of water volume incorporation in the porous SiCOH. O<sub>2</sub> plasmas for its aggressive etching nature remove more –CH<sub>3</sub> groups and will cause more water adsorption from air after the damage compared to He/H<sub>2</sub> clean. As such, Ar/O<sub>2</sub> clean is more harmful to the low- $k$  in terms of preservation of low- $k$  integrity, than He/H<sub>2</sub> clean.

The reaction mechanisms for plasma damage of SiOCH are discussed in Sec. 5.2, followed by a discussion of plasma properties in Sec. 5.3. Removal of hydrophobic –CH<sub>3</sub> and its dependence on interconnectedness, porosity and photon fluxes is discussed in Sec. 5.4. Consequences of VUV photon fluxes are discussed in Sec. 5.5 and a comparison of our computed trends with prior works is discussed in Sec. 5.6. Our concluding remarks are in Sec. 5.7.

## 5.2 Surface Reaction Mechanisms

A reaction mechanism was developed for plasmas sustained in He/H<sub>2</sub> and Ar/O<sub>2</sub> mixtures and their interactions with *low-k* porous SiOCH. The HPEM was employed to obtain the energy and angular distributions for charged and neutral species incident onto the surface.[17] The HPEM has been previously described and so is only briefly summarized here. The HPEM is a two-dimensional, modular model which addresses gas phase and surface kinetics. Electromagnetic fields are derived by solving the frequency domain wave equation based on coil currents adjusted to deliver a specified power deposition. The spatially dependent power deposition is used as a source term in obtaining the electron temperature,  $T_e$ , from an electron energy conservation equation. Transport and rate coefficients as func-

tion of average electron energy are obtained from a solution of Boltzmann's equation, and a Monte Carlo simulation is used to follow the trajectories of sheath accelerated secondary electrons. The transport coefficients and source functions are used by the fluid kinetics module (FKM) to solve separate continuity, momentum, and energy equations for each ion and neutral species, while semi-implicitly solving Poisson's equation for the time varying electrostatic potential. The densities and electrostatic fields from the FKM are then transferred to the other modules. This process is iterated until a converged quasi-steady state solution is obtained.

Reaction probabilities for gas phase species with surfaces are provided by the surface chemistry module (SCM) which computes the composition of surface resident species using a multilayer surface-site-balance model. The reaction mechanism is unique for each surface in contact with the plasma. The plasma chemistry Monte Carlo module (PCMCM) produces the energy and angular distributions for neutrals and ions striking surfaces in contact with the plasma. The PCMCM launches pseudo-particles representing ions and neutrals based on the electron impact source functions. Using time dependent electric fields from the FKM, their trajectories are integrated while accounting for gas phase collisions. The energy and angular distributions (EADs) of neutral and ion pseudo-particles are recorded as they strike surfaces.

The SCM and MCFPM incorporate energy dependent reaction probabilities based on the EADs obtained from the PCMCM. The probabilities for surface reactions involving energetic species (either ions or hot neutrals) are given by [17]

$$p(E) = p_0 \frac{E^m - E_t^m}{E_r^m - E_t^m} \quad (5.1)$$

where  $p(E)$  is the reaction probability for a particle with energy  $E$ ,  $E_t$  is the threshold energy

of the process,  $E_r$  is a reference energy, and  $p_o$  is the reaction probability at the reference energy. We used  $m = 0.5$  in this work.

The Monte Carlo Radiation Transport Module (MCRTM) in the HPEM is called after each iteration to provide photon fluxes incident onto the SiOCH.[18] The operation of MCRTM is similar to the operation of PCMCM. Source functions for launching of pseudo-particles representing photons are derived from the excited state densities generated by the FKM. The trajectory of a photon is tracked until it is absorbed by a gas phase species or it strikes a surface. The photon absorption probability is obtained from a Voight line-shape function using the natural lifetime, collisional broadening and Doppler broadening produced by the local gas densities and temperatures. If resonantly absorbed, photons are re-emitted using a partial-frequency redistribution algorithm. The fluxes and spectra of photons are recorded as a function of the material the photons strike, and are exported to the surface kinetics module SCM of the HPEM. The rates of photon absorption and re-emission are recorded for each optical transition, and are used to calculate radiation trapping factors which lengthen the natural lifetime of the emitting species. These factors are exported to the FKM.

The damage mechanism for SiOCH to be discussed below was implemented in the MCFPM with which the evolution of the SiOCH and damage are predicted.[20] The MCFPM resolves the porous material with approximately atomic resolution. The numerical cell size in this work is  $0.4 \text{ nm} \times 0.4 \text{ nm}$ , which is an effective radius of  $0.2 \text{ nm}$ . The creation of pores in the MCFPM mesh is discussed in Ref. [21]. The internal surfaces of the pores in  $\text{SiO}_2$  were lined with a single layer of  $-\text{CH}_3$  to approximate the structure of SiOCH.

Using the angular distribution of fluxes provided by the MCRTM, the MCFPM then addresses photon penetration into the SiOCH. In principle, the MCFPM treats photons simi-

larly to radicals or ions. Based on the magnitude and angular distribution of photons of different wavelengths, a pseudoparticle representing a photon is randomly directed towards the substrate. For each material in the mechanism an absorption length is specified. The probability that a photon  $m$  will be absorbed by material  $j$  crossing cell  $i$  is  $p_{imj} = 1 - \exp(-\lambda_{mj}\ell_i)$ , where  $\lambda_{mj}$  is the absorption length in material  $j$  for photon  $m$  and  $\ell_i$  is the traversal distance of the photon across the cell  $i$ . When a photon enters into a material cell, this probability is evaluated. If  $r \leq p_{imj}$ , where  $r$  is a random number distributed on (0, 1), the photon is absorbed. Otherwise, the photon continues along its trajectory. When absorbed, the material identity of the solid cell is changed based on the reaction mechanism.

For the Ar/O<sub>2</sub> plasmas of interest, the UV and VUV fluxes are dominated by emission from oxygen species.[22] Electron impact excitation of O atoms generates O(3s), O(5s), and O(5p) states. The O(3s) emits 130 nm photons and O(5s) emits 136 nm photons in relaxing to ground state. O(5p) also emits 777 nm photons in relaxing to O(5s). To simplify the reaction mechanism in the MCFPM we considered only radiation transport into solid materials of the 130 nm photons. The penetration distance of 130 nm photons into porous SiOCH is  $\lambda \approx 100$  nm.[23-25] In low pressure He/H<sub>2</sub> plasmas, damaging VUV fluxes are dominated by resonance radiation from He(2<sup>1</sup>p) at 58.4 nm having a penetration depth of  $\approx 20$  nm in the porous SiOCH.[13, 24] The damage mechanisms of these VUV photons are dominantly bond breaking. For example, the 130 nm and 58.4 nm photons have enough energy to break both Si-C and Si-O bonds. In the former case, the dissociated •CH<sub>3</sub> remains physisorbed. In the latter case, the Si-O is converted to a free radical site (denoted as SiO<sub>2</sub><sup>\*</sup> here).

It is believed that reactions of O radicals with CH<sub>3</sub> groups of SiOCH are the primary mechanism for C depletion during Ar/O<sub>2</sub> plasma processing of porous low-*k* films.[8,26] With interconnected porous SiOCH, oxygen atoms can diffuse into the porous network and react with the hydrophobic –CH<sub>3</sub> groups in –SiO<sub>2</sub>-CH<sub>3</sub> located on the pore-walls well below the surface.[27] The carbon in the –CH<sub>3</sub> groups is likely removed as CO or CO<sub>2</sub>. [27-29] Reactions of O atoms can also abstract H from –SiO<sub>2</sub>-CH<sub>3</sub> leaving –SiO<sub>2</sub>-CH<sub>2</sub>. [27] O radicals having an energy >0.1 eV can break the Si-C bond of –SiO<sub>2</sub>-CH<sub>2</sub> that eventually leads to the formation of CO and H<sub>2</sub>O leaving behind an unpassivated Si atom on the surface of the pore.[26,27] Si-C bond scission in –SiO<sub>2</sub>-CH<sub>3</sub> by VUV photons, leaves behind adsorbed •CH<sub>3</sub> which can be later etched by O atom.[23,25,26] We note that O<sub>2</sub> plasmas do not significantly etch SiO<sub>2</sub>, and so their primary reactions are with the carbon contained in CH<sub>3</sub> groups.[28]

The probabilities in the following reactions for both surface site modification and –CH<sub>3</sub> etching in Ar/O<sub>2</sub> and He/H<sub>2</sub> plasmas have been determined by extensive parameterization of the models to be qualitatively consistent with experimental results available in the literature. Bounds of reaction probabilities are set based on thermodynamic properties and the change in enthalpy of reactions. Within those bounds parameterization and comparison to experiments refine the mechanism. Some examples of works that guided the development of the reactions are discussed in Sec. 5.6.

The reactions for removal of –CH<sub>3</sub>, or demethylation of SiOCH, in plasmas containing O<sub>2</sub> are listed in Table. 5.1.[23, 25-29] In these mechanisms, the subscript *g* denotes a gas phase species, subscript *a* denotes an adsorbed species, the number of symbol • represents number of dangling bonds or free radical site, and – (or =) represents bonding to the solid.

(A complete reaction mechanism consisting of many hundreds of reactions can be obtained by request from the authors.)

Oxygen radicals, O, can directly and exothermically reaction with  $-\text{SiO}_2\text{-CH}_3$  through H abstraction to form OH and a free radical site, or O atoms with energy  $> 0.1$  eV can produce Si-C bond scission as suggested in Ref. [26], in turn producing  $\bullet\text{CH}_3$  on the surface. Both of these outcomes are vulnerable to further O radical or  $\text{O}_2$  attack that eventually remove methyl groups. To etch  $-\text{CH}_3$  groups in Ar/ $\text{O}_2$  plasmas, Si-C bond breaking caused by VUV photons is not essential. However, if photons are present, Si-C bond scission occurs which can accelerate removal of  $-\text{CH}_3$  groups. Etch products of such  $-\text{CH}_3$  removal reactions include CO,  $\text{CO}_2$  and  $\text{H}_2\text{O}$ . Such internally generated  $\text{H}_2\text{O}$  during  $-\text{CH}_3$  etching can react with  $-\text{SiO}_2\bullet$  sites forming  $-\text{SiO}_2\text{-OH}$  which can contribute to an increase in the dielectric constant.

He/ $\text{H}_2$  plasmas remove  $-\text{CH}_3$  groups from  $\text{SiOCH}$  at a slower rate compared to  $\text{O}_2$  containing plasmas primarily due to the higher threshold energies for these reactions involving H atoms. In addition, the reactions responsible for  $-\text{CH}_3$  removal in He/ $\text{H}_2$  plasmas likely produce less volatile products, such as  $\text{CH}_4$ , which are less likely to continue reacting with the  $\text{SiOCH}$ . He plasma pretreatment of  $\text{SiOCH}$  has been found to produce surface modifications that can minimize damage of the low- $k$ . [13-15]  $\text{He}^+$  and photons from He/ $\text{H}_2$  plasmas can remove H from the  $-\text{CH}_3$  groups of  $-\text{SiO}_2\text{-CH}_3$  producing  $-\text{SiO}_2\text{-CH}_n$  ( $n = 0-2$ ) that have lower etch rates. This is because H is only efficient in removing C from  $-\text{SiO}_2\text{-CH}_3$  among all  $-\text{SiO}_2\text{-CH}_n$  ( $n = 0-3$ ) products as volatile  $\text{CH}_4$ . Since the activation energy to remove C from  $-\text{SiO}_2\text{-CH}_3$  increases as  $n$  decreases, the rate of C removal from  $-\text{SiO}_2\text{-CH}_n$  by thermal H atoms decreases as H is removed. Although hot H atoms are able to produce this etching,

H\* are only energetically above threshold near the surface. By the time H atoms diffuse into the pores, their energy has largely been thermalized to below the threshold energies required to etch  $-\text{SiO}_2\text{-CH}_n$  ( $n < 3$ ). To etch these compounds, they would first need to be saturated back to  $-\text{SiO}_2\text{-CH}_3$  through H adsorption, followed by H atom etching  $-\text{CH}_3$  as volatile  $\text{CH}_4$ . The end result is that generation of  $-\text{SiO}_2\text{-CH}_n$  ( $n < 3$ ) by photons or ions could slow  $-\text{CH}_3$  removal.

In certain parameter spaces of operating of low pressure He/ $\text{H}_2$  plasmas, it is possible to produce significant fluxes of hot H atom fluxes to the substrate. The dominant mechanism for hot H generation is the dissociation of vibrationally excited  $\text{H}_2$  ( $v \geq 2$ ) by electron impact. Such reactions can generate H atoms with energies sufficient to remove both  $\text{CF}_x$  polymers and PR. Charge exchange reactions between  $\text{H}_2$  ( $v$ ) and  $\text{H}^+$ , or  $\text{H}^+$  and H can generate H atoms and  $\text{H}_2$  with energies as high as the energy of  $\text{H}^+$ . Such charge exchange reactions also occur between  $\text{H}_2$  ( $v$ ) and  $\text{H}_2^+$  producing translationally hot  $\text{H}_2$  ( $v$ ). Vibrational-translational (VT) reactions of H atoms with  $\text{H}_2$  ( $v$ ) also can produce hot H. In these collisions,  $\text{H}_2$  ( $v$ ) molecules are relaxed to a state  $\text{H}_2$  ( $v' < v$ ), and the H atoms carries away the energy difference as translational energy. A more detailed hot H generation mechanism is discussed in Sec. 5.3.

Hot H atoms in this context have translational energies of up to or exceeding a few tenths of an eV. H atoms with energies  $> 0.4$  eV are able to abstract H from  $-\text{SiO}_2\text{-CH}_3$  producing  $-\text{SiO}_2\text{-CH}_n$  ( $n = 1, 2$ ) which slows the rate of carbon removal. Cleaving of Si-C bonds by photons produces adsorbed  $\bullet\text{CH}_{3a}$  groups that can be later etched by H atom as  $\text{CH}_4$ . [13,14,29] After  $-\text{CH}_3$  removal from  $-\text{SiO}_2\text{-CH}_3$ , H atoms can passivate the resulting  $-\text{SiO}_2\bullet$  site by forming  $-\text{SiO}_2\text{-H}$  which is hydrophobic in nature and can also block subsequent water update. [30] However,  $\text{He}^+$  can break Si-O bond in  $-\text{SiO}_2\bullet$  and generate free radical site

$-\text{SiO}\bullet\bullet$ , and a successive strike can produce  $-\text{Si}\bullet\bullet\bullet$ . H can passivate  $-\text{Si}\bullet\bullet\bullet$  forming  $-\text{Si-H}_n$  ( $n= 1-3$ ). Such Si-H bond compounds are also hydrophobic in nature and can block water uptake. As such, even after the  $-\text{CH}_3$  group removal, He/ $\text{H}_2$  plasma treatment may be able to maintain some hydrophobic properties of the  $\text{SiOCH}$ .

Reactions during interaction between He/ $\text{H}_2$  plasmas and  $\text{SiCOH}$  are listed in Table 5.2.[13,14,25,29,30] Among these reactions, H reactions that involve removal of  $-\text{CH}_3$  groups or demethylation (Reactions 6 and 13) and abstraction of H from  $-\text{CH}_n$  ( $x=1-3$ ) (Reactions 15-35) are endothermic, and require hot H atoms or vibrationally excited  $\text{H}_2$  to quickly proceed. However,  $-\text{CH}_3$  removal reactions are less endothermic than H abstraction reactions and H passivation of  $-\text{SiO}_2\text{-CH}_n$ .  $-\text{Si}\bullet\bullet\bullet$  and  $-\text{Si-H}_n$  ( $n=1, 2, 3$ ) reactions with H (Reactions 10-12) are exothermic in nature.

PR which is dominantly a hydrocarbon, can be removed by O atoms from Ar/ $\text{O}_2$  plasmas by forming compounds such as CHO, while hot H atoms ( $> 0.5 - 1$  eV) and vibrationally excited  $\text{H}_2(v>2)$  produced in He/ $\text{H}_2$  plasmas can remove PR by forming compounds such as  $\text{CH}_4$ . O containing ions such as  $\text{O}^+$  and  $\text{O}_2^+$  can etch PR as CHO. H containing ions  $\text{H}^+$ ,  $\text{H}_2^+$  and  $\text{H}_3^+$  chemically etch PR as  $\text{CH}_4$ . Energetic ions such as  $\text{Ar}^+$  and  $\text{He}^+$  can physically sputter PR. The mechanism for removal of PR in Ar/ $\text{O}_2$  and He/ $\text{H}_2$  plasmas is listed in Table 5.3. PR etching reactions that involve O species (Reactions 1-3) are exothermic. H atom or  $\text{H}_2(v>3)$  etching reactions (Reactions 4-10) are endothermic.  $\text{SiO}_2^*$  (bond cleaved  $\text{SiO}_2$ ) which is generated by VUV photons are not believed to be chemically active in  $\text{H}_2$  or  $\text{O}_2$  plasmas. It has been reported that  $\text{SiO}_2^*$  can only adsorb O in Ar/ $\text{O}_2$  plasmas forming a  $\text{SiO}_2$  like layer (without showing any etching of  $\text{SiO}_2$ ).[29] Similarly, H is adsorbed by  $\text{SiO}_2^*$  without causing any Si consumption in He/ $\text{H}_2$  plasmas. Given these trends, since the empha-

sis of this study is on demethylation, we excluded  $\text{SiO}_2^*$  reactions in Ar/O<sub>2</sub> or He/H<sub>2</sub> plasmas for simplicity.[29,31]

### 5.3 Plasma Properties

For purposes of this investigation, plasma cleaning processes were modeled as performed in inductively coupled plasmas. The test reactor treated a wafer 15 cm in diameter. The reactor was 26 cm in diameter with a wafer-to-coil height of 10 cm. (See Fig. 5.1a.) The conditions for both Ar/O<sub>2</sub> and He/H<sub>2</sub> plasma treatment were 10 mTorr with a flow rate of 100 sccm. For the base case, the coil delivered 300 W at 10 MHz with a pressure of 10 mTorr and flow rate of 100 sccm. The gas mixtures were He/H<sub>2</sub> = 75/25 and Ar/O<sub>2</sub> = 5/95. The substrate was biased with at 10 MHz

Typical plasma properties for a power of 300 W are shown in Fig. 5.1 and reactive fluxes to the substrate are shown in Fig. 5.2. For Ar/O<sub>2</sub> plasmas, the peak O-atom density is  $9.5 \times 10^{13} \text{ cm}^{-3}$  and the peak total ion density is  $6 \times 10^{11} \text{ cm}^{-3}$ . O(3s), which emits 130 nm photons, has a peak density of  $3.5 \times 10^7 \text{ cm}^{-3}$ , a small density due to its short radiative lifetime that produces, when integrated over the reactor, reasonably large VUV fluxes to the substrate. With a 20 V substrate bias, ions have an average energy near 30 eV and a total flux of  $2.3 \times 10^{16} \text{ cm}^{-2}\text{s}^{-1}$  at the center of the wafer. The individual fluxes include  $1.5 \times 10^{16} \text{ cm}^{-2}\text{s}^{-1}$  for O<sup>+</sup>,  $0.6 \times 10^{16} \text{ cm}^{-2}\text{s}^{-1}$  for O<sub>2</sub><sup>+</sup>, and  $2.1 \times 10^{15} \text{ cm}^{-2}\text{s}^{-1}$  for Ar<sup>+</sup>. O atoms, the dominant agent for -CH<sub>3</sub> removal, has a flux of  $1.5 \times 10^{18} \text{ cm}^{-2}\text{s}^{-1}$ . The flux of VUV photons is  $2.5 \times 10^{13} \text{ cm}^{-2}\text{s}^{-1}$ .

In He/H<sub>2</sub> plasmas, the peak ion density is  $3.5 \times 10^{10} \text{ cm}^{-3}$  while H atoms have a maximum density of  $1.8 \times 10^{13} \text{ cm}^{-3}$ . The ion fluxes ( $1.8 \times 10^{16} \text{ cm}^{-2}\text{s}^{-1}$ ) largely responsible for the PR removal had an average energy near 30 eV for a 20 V bias and an angular spread from the vertical of  $< 15^\circ$ . He(2<sup>1</sup>p) which emits 58.4 nm photons has a peak density of  $1.5 \times 10^8 \text{ cm}^{-3}$ . The individual fluxes include  $4 \times 10^{15} \text{ cm}^{-2}\text{s}^{-1}$  for H<sup>+</sup>,  $7 \times 10^{15} \text{ cm}^{-2}\text{s}^{-1}$  for H<sub>2</sub><sup>+</sup>,  $1 \times 10^{15} \text{ cm}^{-2}\text{s}^{-1}$  for H<sub>3</sub><sup>+</sup>, and  $6 \times 10^{15} \text{ cm}^{-2}\text{s}^{-1}$  for He<sup>+</sup>. The VUV flux is  $6 \times 10^{14} \text{ cm}^{-2}\text{s}^{-1}$  and that for H atoms is  $1 \times 10^{18} \text{ cm}^{-2}\text{s}^{-1}$ .

Hot H atoms (H\*) have temperatures (or energies) that exceed that of the average gas temperature. The EADs of H atoms incident onto the wafer are shown in Fig. 5.3 for He/H<sub>2</sub> mixtures for pressures of 10-80 mTorr. H\* fluxes to the wafer are also shown as a function of pressure. The EADs are dominated by a thermal isotropic component corresponding to the gas temperature of  $\approx 800 \text{ K}$ . At lower pressures, a significant population of H\* is produced, in general also having an isotropic angular distribution. As the pressure increases, the fraction of H\* decreases, however, its angular distribution narrows.

The dominant H\* generation mechanism is by Frank-Condon heating through the dissociation excitation of H<sub>2</sub>( $v \geq 2$ ) by electron impact.[32] Although such reactions cannot generate H atoms with energies  $>4 \text{ eV}$ , the energy is sufficient to initiate endothermic polymer cleaning or PR removal reactions. Charge exchange reactions between H<sub>2</sub>( $v$ ) and H<sup>+</sup>, or H<sup>+</sup> and H can generate H atoms with energies as high as the energy of H<sup>+</sup> ions in the plasma. Charge exchange reactions can also occur between H<sub>2</sub>( $v$ ) and H<sub>2</sub><sup>+</sup> producing translationally hot H<sub>2</sub>( $v$ ) having sufficient energies to initiate endothermic polymer cleaning or PR etching

reactions. As the rate of charge exchange is small compared to dissociative excitation, a small fraction of  $H^*$  is produced in this manner.

$H^*$  can also be produced through vibrational-translational (VT) reactions of H atoms with  $H_2(v)$ . [33] In these collisions  $H_2(v)$  molecules are quenched to a state  $H_2(v' < v)$ , and the H atoms carries away the energy difference as translational energy, 0.5 eV per vibrational level. These VT reactions can give H atoms enough energy to broach the endothermic barrier to clean  $CF_x$  polymer or PR.

Optimizing the collisionality of He/ $H_2$  plasmas by changing pressure enables a high rate of  $H^*$  production while also allowing these  $H^*$  to reach the wafer. The total H atom flux, and fluxes of H atoms with energies  $>0.5$  eV and  $>1$  eV as a function of pressure are shown in Fig. 5.3b. For pressures  $>20$  mTorr the  $H^*$  fluxes decrease in large part due to thermalization of initially produced  $H^*$  before those atoms reach the surface. With an increase in pressure from 10 mTorr to 200 mTorr, total H flux rises from  $10^{18}$  to  $10^{19}$   $cm^{-2}s^{-1}$  while the energy of H atoms decreases. At 10 mTorr, roughly 1% of the H atoms have energies  $>0.5$  eV which is above the threshold energy to etch PR and remove  $CF_x$  polymers. At 30 mTorr, only 0.1 % of H atoms have energies  $>0.5$  eV. At pressures of  $>80$  mTorr, the fraction of H atoms with energy  $>0.5$  eV is only 0.006%. Since  $H^*$  fluxes are required to efficiently remove the  $CF_x$  polymer that remains on trench sidewalls after fluorocarbon plasma etching, operating at pressures of less than tens of mTorr is preferred.

#### 5.4 Demethylaton

For the base case the pore size is 0.8 nm in diameter with a 10% standard deviation and the porosity is 30% with 100% interconnected pores.  $-CH_3$  groups initially line the pore-

walls. The calculated dielectric constant is approximately  $k = 2.5$ , based on the relationship between film dielectric constant, and volume of each element in the porous film ( $\text{CH}_3$  group,  $\text{SiO}_2$  and air gap) and their individual dielectric constants.[34]

Trenches were etched into  $\text{SiOCH}$  with a capacitively coupled plasma using an  $\text{Ar}/\text{C}_4\text{F}_8/\text{O}_2 = 80/15/5$  gas mixture at 40 mTorr.[20,35] The end result of the etching includes a  $\text{CF}_x$  polymer layer, approximately 1.5 nm thick, on the etched  $\text{SiOCH}$  surface, as shown in Fig. 5.4a. The simulation was run for a sufficiently long time to completely erode the PR mask to investigate the damage during the cleaning step. The trench profile following 850s of treatment by the  $\text{Ar}/\text{O}_2$  plasma is shown in Fig. 5.4b. Damage in these profiles is interpreted primarily as the removal of  $-\text{CH}_3$  (demethylation) and to a secondary degree by the formation of  $\text{SiO}_2^*$ . In this Monte Carlo based model, the removal of  $-\text{CH}_3$  from the inside of pores results in the appearance of an increase in the pore-size, as a layer of molecules have been removed from the surface of the pore. In reality, there is likely a collapse of the pores, a process that is not resolved in these simulations.

The mask and polymer are essentially fully removed during the cleaning process. We found that demethylation (removal of  $-\text{CH}_3$  groups from  $-\text{SiO}_2-\text{CH}_3$  in porous  $\text{SiOCH}$ ) is a diffusion dominated process, as suggested by Goldman et al.[8] The maximum depth of demethylation increases linearly with time at short times and scales with  $t^{1/2}$  at longer times, as shown in Fig. 5.4c.[8] Pores which are open or line-of-sight connected to the plasma have their  $-\text{CH}_3$  groups more rapidly removed by photons, ions and O radicals. Interconnected pores deeper into the material are demethylated only after diffusion of O atoms through the porous network and, if near the surface, catalyzed by VUV bond scission.

VUV Photons have a finite penetration depth into solid SiO<sub>2</sub>. Photons that are absorbed by –SiO<sub>2</sub>-CH<sub>3</sub> likely produce Si-C bond scission, which then produces free radical sites, –SiO<sub>2</sub>• and bond cleaved and surface adsorbed •CH<sub>3a</sub>. These sites speed the demethylation process, as discussed below. Bond cleaved •CH<sub>3a</sub> can be etched by O as CO and H<sub>2</sub>O, and can be removed by H radicals as CH<sub>4</sub>. In these situations, even O<sub>2</sub> can promote such demethylation once the Si-C bond has been broken and •CH<sub>3a</sub> produced.[23] One of the products of O-atom reactions with –SiO<sub>2</sub>-CH<sub>3</sub> and •CH<sub>3a</sub> is OH, which can itself react with SiOCH, which tends to perpetuate the demethylation process.[27]

For both Ar/O<sub>2</sub> and He/H<sub>2</sub> plasmas photon fluxes increase with power as shown in Fig. 5.5. The VUV photon fluxes from Ar/O<sub>2</sub> plasmas are 10-100 times smaller than for comparably powered He/H<sub>2</sub> plasmas. To decouple heavy particle kinetics and photon fluxes in the assessment of demethylation, we held the heavy particle fluxes constant at their base case values and varied the fluxes of VUV photons. As the photon fluxes increase so does the demethylation depth, shown in Fig. 5.5c for a treatment time of 900 s. Since O atoms are exothermically reactive with SiOCH there is significant demethylation even in the absence of VUV fluxes for Ar/O<sub>2</sub> plasmas. For He/H<sub>2</sub> plasmas, there is little demethylation in the absence of VUV fluxes. In both cases, increasing the VUV fluxes increases the amount of Si-C scission in –SiO<sub>2</sub>-CH<sub>3</sub> (producing either •CH<sub>3a</sub> or –SiO<sub>2</sub>-CH<sub>2</sub>•), which enables more rapid reactions which lead to demethylation. The demethylation depth increases linearly with photon flux up to about 10<sup>14</sup> cm<sup>-2</sup>s<sup>-1</sup> and then increases with flux<sup>1/2</sup> for the range 10<sup>14</sup>-10<sup>15</sup> cm<sup>-2</sup>s<sup>-1</sup>. This dependence is similar to diffusion limited damage, as suggested by the results in Fig. 5.4c.[8,24] The demethylation depth increases to nearly 30 nm in the Ar/O<sub>2</sub> plasma with in-

creasing photon flux for fixed exposure time (or increasing fluence) and up to 11 nm in the He/H<sub>2</sub> plasma.

To compare the impact of VUV photons on damage of the SiOCH, the top layer of SiOCH is shown in Fig. 5.6 for Ar/O<sub>2</sub> plasma cleaning and in Fig. 5.7 for He/H<sub>2</sub> plasma cleaning without photons and with increasing photon fluxes. The demethylation is represented by the depth of removal of (olive colored) –CH<sub>3</sub> groups after plasma treatment. The change in color from pink (SiO<sub>2</sub>) to purple represents the formation of SiO<sub>2</sub><sup>\*</sup>, the free radical state of SiO<sub>2</sub> due to Si-O bond breaking by photons. Although SiO<sub>2</sub><sup>\*</sup> can be etched in plasmas containing Cl and F radicals, radicals produced in Ar/O<sub>2</sub> or He/H<sub>2</sub> plasmas generally do not react with SiO<sub>2</sub><sup>\*</sup> as etchants though these plasmas may passivate the free radical site.[29,31] As Worsely et al. suggested, Ar/O<sub>2</sub> plasmas can remove the entire carbon content from SiOCH but do not remove SiO<sub>2</sub> and leave a SiO<sub>2</sub> like layer.[29] On the other hand, He/H<sub>2</sub> plasmas less aggressively remove carbon but leave SiO<sub>2</sub> primarily unaffected with only some H incorporation.

Increasing VUV fluxes increases the depth of demethylation and also increases the proportion of SiO<sub>2</sub><sup>\*</sup> sites. Although many of these free radical sites likely reconnect to reform SiO<sub>2</sub> without long term damage to the SiOCH, some fraction of SiO<sub>2</sub><sup>\*</sup> also likely remains in the long term, making the SiOCH more sensitive to damage in other processing steps. Note that in those regions of the SiOCH where, statistically, there are more pores and so more damage, the VUV penetration depth is greater. This is due to there being more line-of-sight pathways for the photons to penetrate or there being smaller line averaged mass density.

The demethylation depth is larger for flat surfaces than for the sidewalls, as shown in Fig. 4b. This is due, in part, to the additional role that directional ions and photons play in the demethylation process. Due to their either line-of-sight reactivity or anisotropic trajectories, ions and photons make larger contributions to demethylation to horizontal surfaces than vertical surfaces. The average angle of incidence of ions and photons is more normal on the flat surfaces, and so the penetration is deeper perpendicular to the surface. Finally, there is also a time-lag issue. Additional time is required by O atoms, the dominant demethylation agent, to statistically enter into pores at the bottom of the trench where their fluxes are smaller than on the top surfaces, which may result in a reduced demethylated depth.

As the interconnectivity of the SiOCH increases, there are, on the average, longer average pathways from the surface for the diffusion of plasma produced species into the SiOCH. This ultimately produces more damage (demethylation) in the porous material compared to a smaller interconnectivity.[8] For example, demethylation depth as a function of interconnectivity during Ar/O<sub>2</sub> and He/H<sub>2</sub> plasma cleaning is shown in Fig. 5.8 after 900 s of treatment. For both without and with photons, demethylation depth increases nearly linearly with interconnectivity. The increase in interconnectivity for a given porosity increases the likelihood of having a line-of-site path through the porosity from the plasma. Even though photon penetration on the average should depend only on porosity (or the average mass density), statistically, increasing porosity does increase the likelihood of having pores aligned that enable deeper photon penetration. We did find that the maximum photon penetration depth increases with interconnectivity, as shown in Fig. 5.8c. The deeper photon penetration then facilitates greater rates of demethylation deeper into the SiOCH. As a result, damage is more sensitive to interconnectivity when including photon fluxes. Since a reasonable large

porosity ( $\approx 20\text{-}30\%$ ) is achieved a low  $k$ -value, minimizing interconnectivity can be helpful in minimizing the damage of the network.[8]

SiOCH profiles for interconnectivities of 10, 40 and 100% for following treatment with Ar/O<sub>2</sub> and He/H<sub>2</sub> plasmas are shown in Figs. 5.9 and 5.10. (The penetration depth of photons is shown by the change in color: brown -CH<sub>3</sub> groups turn green after photon produced Si-C bond scission, and light pink SiO<sub>2</sub> turns dark pink to represent SiO<sub>2</sub>\*). During He/H<sub>2</sub> plasma cleaning, reactive H atoms also diffuse inside the material through interconnected pathways. Although H atoms being lighter than O atoms can diffuse more rapidly and so possibly deeper into the SiOCH, reactions of H atoms with SiOCH are slower and produce less volatile and reactive products than reactions with O atoms.[12,29] So for otherwise identical conditions, diffusion of O atoms through interconnected pores will produce more damage than diffusion of H atoms.

The demethylation process is facilitated by Si-C bond scission by VUV photons. In Ar/O<sub>2</sub> plasmas, demethylation by O atoms is an exothermic process. As a result, demethylation is enhanced though not dependent on bond scission by VUV photons. The profile of demethylation is therefore more diffusive, a consequence of O atoms diffusion into the pores. In He/H<sub>2</sub> plasmas, Si-C bond scission significantly enhances the rate of demethylation, and so its depth is more closely correlated to that of the photon penetration. As a result, the demethylation depths as a function of interconnectivity in He/H<sub>2</sub> plasma are approximately 3 times smaller than in Ar/O<sub>2</sub> plasmas.

Increasing porosity increases the depth of damage in SiOCH as shown in Figs. 5.11 for porosities of 30% and 40% in Ar/O<sub>2</sub> plasmas. We found that the depth of damage increases nearly linearly with porosity as shown in Fig. 5.11c.[1,29] At first glance, a more

porous network should enable more rapid diffusion of radicals throughout the volume of the SiOCH and so increase the likelihood of damage at a deeper site. There is a secondary effect of photon transport – the less dense the SiOCH due to increasing porosity, the longer the penetration depth of photons due to the lower mass density of the material. These results are not independent of interconnectivity, as discussed below.

### 5.5 Consequences of VUV Photon Fluxes

VUV photons from Ar/O<sub>2</sub> and He/H<sub>2</sub> plasmas penetrating into SiOCH produce Si-C bond scission which generates •CH<sub>3a</sub> radicals on the surface of pores. These photons also produce SiO<sub>2</sub><sup>\*</sup> through Si-O bond cleavage.[23-25] These Si-C bond cleaved •CH<sub>3a</sub> groups are thought to remain as adsorbed surface species.[23] Since the •CH<sub>3a</sub> groups are no longer chemisorbed, they are vulnerable to rapid reaction with O, O<sub>2</sub> or H to produce volatile CO, CO<sub>2</sub> or CH<sub>4</sub> to complete the -CH<sub>3</sub> removal process. Molecular oxygen is unable to etch –CH<sub>3</sub> when bonded to Si, however after Si-C bond cleavage, •CH<sub>3a</sub> is etchable by O<sub>2</sub> ultimately producing CO and H<sub>2</sub>O.[23] Fluxes of VUV photons from plasma can therefore significantly increase the rate of demethylation compared to fluxes of only O or H atoms. The 130 nm photons from O atoms in Ar/O<sub>2</sub> plasmas have a penetration depth of ≈100 nm into SiOCH and so can increase demethylation to at least this depth provided the interconnectivity enables penetration of plasma produced radicals into the network.[23,25] The 58 nm photons produced by He\* in He/H<sub>2</sub> plasmas have penetration depths of only ≈20 nm, and are energetic enough to break both Si-O and Si-C bonds.[24] Due to the less reactive nature of H radicals with –SiO<sub>2</sub>-CH<sub>x</sub> groups, Si-C bond cleavage by photons from He/H<sub>2</sub> plasmas is a more important precursor to the removal of hydrophobic –CH<sub>3</sub> groups by H atoms than oxygen

containing plasmas where the carbon removal step is exothermic.[25]

The depths of demethylation shown in Figs. 5.6 and 5.7 as a function of photon flux are consistent with experimentally measured ranges of damage of SiOCH for photon fluxes of  $10^{14}$ - $10^{15}$   $\text{cm}^{-2}\text{s}^{-1}$ . [25] Damage of the SiOCH increases in depth as the photon fluxes increase. This is in large part due to saturation of the scission of the Si-C bonding in  $-\text{SiO}_2\text{-CH}_3$ . The maximum demethylation depth is to a large degree determined by the penetration depth of the particular wavelength into the SiOCH. The actual demethylation depth is then determined by the degree of Si- $\text{CH}_3$  scission within that maximum depth. In some ways, damage is a matter of fluence of photons ( $\text{photons}/\text{cm}^2$ ) as opposed to simply flux ( $\text{photons}/\text{cm}^2\text{-s}$ ). A longer treatment time for a given flux of photons will produce a deeper demethylation. Damage of SiOCH for the same fluence of VUV photons (keeping VUV photon flux  $\times$  time = constant) is shown in Fig. 5.12 for He/ $\text{H}_2$  and Ar/ $\text{O}_2$  plasma cleans. With the same fluence, SiOCH was treated in Ar/ $\text{O}_2$  plasmas with photon fluxes of  $5 \times 10^{14}$  and  $10^{15}$   $\text{cm}^{-2}\text{s}^{-1}$ . The amount of Si-C bond scission was essentially the same in both cases. However, O radicals had twice the time to diffuse into the network for the lower photon flux, and so produced somewhat deeper damage. Similarly, in He/ $\text{H}_2$  plasmas for equal photon fluence, H radicals having more time to diffuse into the network caused more damage to the SiOCH with the lower photon flux.

Fluorocarbon plasma etched trenches in porous SiCOH producing  $\text{CF}_x$  polymer covered sidewalls were cleaned in Ar/ $\text{O}_2$  and He/ $\text{H}_2$  plasmas. The resulting profiles are shown in Fig. 5.13 with and without photon fluxes. During the over-etch required to remove all of the  $\text{CF}_x$  polymers,  $\text{O}_2$  containing plasmas caused significant demethylation by removing  $-\text{CH}_3$  groups. (Damage is shown as pink sites indicating a  $\text{SiO}_2$  site that has lost  $-\text{CH}_3$ ). On the

other hand, H radicals remove  $-\text{CH}_3$  less aggressively in large part because hot H atoms are required for efficient removal of  $-\text{CH}_3$ , and as H atoms diffuse into the pores, they thermalize and so lose reactivity. In the absence of VUV illumination, He/H<sub>2</sub> may clean porous SiCOH without causing significant damage, only modifying the surface which sees larger fluxes of hot H atoms, as suggested by others.[12,16]

However, with 58 nm photon fluxes in He/H<sub>2</sub> plasmas, the resulting Si-C bond scission enables damage, both on the sidewalls and on the top of the feature. Due to the grazing view-angle to the plasma deep in the trench, the depth of the damaged layer due to photon absorption perpendicular to the surface is less than on the top of the feature. As the absorption length of the photons produced in Ar/O<sub>2</sub> plasmas is longer than in He/H<sub>2</sub> plasmas the extent of the damage perpendicular to the sidewalls is correspondingly thicker. During He/H<sub>2</sub> plasma cleaning, Si-C bond scission which causes the removal of  $-\text{CH}_3$  from Si-CH<sub>3</sub> as CH<sub>4</sub> eventually leads to the formation of hydrophobic =Si-H<sub>x</sub> which additionally protects the Si from moisture adsorption. [29]

## 5.6 Comparison of Trends With Prior Works

As reported by Goldman et al. [8] and, Vanstreels and Urbanowicz [16], we found that diffusion of O atoms is the dominant process for producing damage by Ar/O<sub>2</sub> plasmas in porous SiOCH. We also found that, as suggested by Jinnai et. al. [25], and Lee and Graves [23] scission of Si-C bonds by VUV fluxes can increase the rate of damage. We found that in the absence of VUV fluxes, He/H<sub>2</sub> plasmas modify the low-*k* surface but do not efficiently remove C atoms which agrees with reports that found little damage in SiOCH after processing in a downstream He/H<sub>2</sub> plasma reactor where the flux of VUV photons is negli-

ble.[12,16] However, the 58 nm photons produced in He/H<sub>2</sub> plasmas can cause Si-C bond scission and so likely act as a precursor to damage, as concluded by Jinnai et al.[25] We found that the depth of damage (-CH<sub>3</sub> removal) for Ar/O<sub>2</sub> plasma treatment when treated for the same duration is approximately 3 times larger than He/H<sub>2</sub> plasma cleaning. These results align with those reported by Worsley et al.[29], albeit for plasma damage produced in a capacitively coupled system. They found deeper damage of SiOCH in Ar/O<sub>2</sub> mixtures compared to Ar/H<sub>2</sub> mixtures but deeper non-damaging modification in Ar/H<sub>2</sub> mixtures, perhaps due to the higher mobility of H atoms in the SiOCH. They also found etch rates and the rate of carbon removal were significantly higher in the Ar/O<sub>2</sub> plasmas due to the highly reactive O atom fluxes. Based on the  $\Delta H$  of the reaction, Worsley et al. estimated that CH<sub>3</sub> removal by O atoms is more than two times energetically favorable compared to removal by H atoms. [29]

## 5.7 Concluding Remarks

Ar/O<sub>2</sub> and He/H<sub>2</sub> plasma damage of porous SiOCH was investigated and mechanisms discussed. While diffusion of radicals into the network is likely the primary cause for damage of porous SiOCH, the presence of photons can accelerate the rate of damage. Plasmas that can remove -CH<sub>3</sub> by virtue of exothermic reactions will cause more damage to SiOCH than plasmas that remove such groups relying on endothermic reactions, and this in large part explains the higher damage potential of Ar/O<sub>2</sub> plasmas compared to He/H<sub>2</sub> plasmas. The wavelength of photons present in the plasmas is important as the penetration depth of photons increases with wavelength in the VUV and deep UV, and energies of photons decrease with wavelength. Photons having wavelengths <140 nm have enough energy (>9 eV) to

cause Si-C and Si-O bond scission and play a major role in the damage of SiOCH. The interconnectivity of the pores enables radicals to etch methyl groups deep in the SiOCH by diffusing through the network. If pores are relatively isolated (less interconnected), reactive species will not find a well-connected path to diffuse and remove  $-\text{CH}_3$  groups located on deeper pore-walls. As such, SiOCH with low interconnectivity, cleaned by a plasma producing fluxes containing small fractions of O atoms and producing photons which do not penetrate deeply into the material may be a way to maintain low- $k$  integrity.

## 5.8 Tables

Table 5.1 Reaction Mechanisms for Porous SiCOH Damage in Ar/O<sub>2</sub> Plasmas

Species:

M <sub>g</sub>	Gas phase species
M	Surface site
=M/-M	Surface site bonded to a solid
M•	Active surface site with dangling bond
M <sub>a</sub>	Adsorbed surface site
M <sub>g</sub> <sup>+</sup>	Ion

<u>No.</u>	<u>Reaction<sup>a-c</sup></u>	<u>Probability</u>
1	$O_g + -SiO_2-CH_3 \rightarrow -SiO_2-CH_2\bullet + OH_g$	0.005, d
2	$O_g + -SiO_2-CH_3 \rightarrow -SiO_2\bullet + \bullet CH_{3a} + O_g$	0.005, d
3	$OH_g + -SiO_2-CH_3 \rightarrow -SiO_2-CH_2\bullet + H_2O_g$	0.004, d
4	$h\nu(130\text{ nm}) + -SiO_2-CH_3 \rightarrow -SiO_2\bullet + \bullet CH_{3a}$	0.800
5	$O_g + -SiO_2-CH_2 \rightarrow -SiO_2\bullet + CH_2O\bullet_a$	0.004
6	$O_g + \bullet CH_{3a} \rightarrow CH_2O\bullet_a + H_g$	0.004
7	$O_g + CH_2O\bullet_a \rightarrow CO_g + H_2O_g$	0.004
8	$O_{2g} + \bullet CH_{3a} \rightarrow CH_2O\bullet_a + OH_g$	0.004
9	$O_{2g} + CH_2O\bullet_a \rightarrow CO_g + H_2O_g$	0.004
10	$H_2O_g + -SiO_2\bullet \rightarrow -SiO_2-OH + H_g$	$1.5 \times 10^{-5}$
11	$O_g^+ + -SiO_2-CH_3 \rightarrow -SiO_2\bullet + CH_{3g} + O_g$	$10^{-4}$ , e
12	$O_g^+ + -SiO_2-CH_3 \rightarrow -SiO_2\bullet + -CH_2\bullet + OH_g$	$10^{-4}$ , e
13	$O_g^+ + -SiO_2-CH_2\bullet \rightarrow -SiO_2\bullet + CH_{2g} + O_g$	$10^{-4}$ , e

Table 5.1 (Continued)

14	$O_g^+ + -SiO_2-CH_2\bullet \rightarrow -SiO_2\bullet + -CH\bullet\bullet + OH_g$	$10^{-4}, e$
15	$O_2^+_g + -SiO_2-CH_3 \rightarrow -SiO_2\bullet + CH_3g + O_{2g}$	$10^{-4}, e$
16	$O_2^+_g + -SiO_2-CH_3 \rightarrow -SiO_2\bullet + CH_2O\bullet_a + OH_g$	$10^{-4}, e$
17	$O_2^+_g + -SiO_2-CH_2\bullet \rightarrow -SiO_2\bullet + CH_2g + O_{2g}$	$10^{-4}, e$
18	$O_2^+_g + -SiO_2-CH_2\bullet \rightarrow -SiO_2\bullet + CH_2O\bullet_a + O_g$	$10^{-4}, e$
19	$O_g^+ + \bullet CH_{3a} \rightarrow CH_3g + O_g$	$10^{-4}, e$
20	$O_2^+_g + \bullet CH_{3a} \rightarrow CH_3g + O_{2g}$	$10^{-4}, e$

- a. Unless specified, all ions neutralize on surfaces, returning as their neutral counterparts.
- b. Gas phase species have units of flux ( $cm^{-2} s^{-1}$ ). Surface species have units of fractional coverage.
- c. In reactions with no chemical change, the gas species are reflected off the surface. These reactions are not shown.
- d.  $E_r=3.5$  eV,  $E_t=0.18$  eV, probability is at  $E_r$ .
- e.  $E_r=100$  eV,  $E_t=10$  eV, probability is at  $E_r$ .

Table 5.2 Reaction Mechanisms for Porous SiCOH Damage in He/H<sub>2</sub> Plasmas

Species:

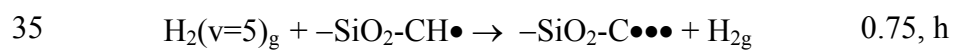
M <sub>g</sub>	Gas phase species
M	Surface site
=M/-M	Surface site bonded to a solid
M•	Active surface site with dangling bonds
M <sub>a</sub>	Adsorbed surface site
M <sub>g</sub> <sup>+</sup>	Ion

<u>Reaction</u>	<u>Reaction</u> <sup>a-c</sup>	<u>Probability</u>
1	$h\nu (\approx 58 \text{ nm}) + \text{-SiO}_2\text{-CH}_3 \rightarrow \text{-SiO}_2\bullet + \bullet\text{CH}_3\text{a}$	0.9
2	$\text{He}_g^+ + \text{-SiO}_2\text{-CH}_3 \rightarrow \text{-SiO}_2\text{-CH}_2\bullet + \text{H}_g + \text{He}_g$	0.4, d
2	$\text{He}_g^+ + \text{-SiO}_2\text{-CH}_2\bullet \rightarrow \text{-SiO}_2\text{-CH}\bullet\bullet + \text{H}_g + \text{He}_g$	0.4, d
3	$\text{He}_g^+ + \text{-SiO}_2\text{-CH}\bullet\bullet \rightarrow \text{-SiO}_2\text{-C}\bullet\bullet\bullet + \text{H}_g + \text{He}_g$	0.4, d
4	$\text{He}_g^+ + \text{-SiO}_2\bullet \rightarrow \text{=SiO}\bullet\bullet + \text{-O}\bullet + \text{He}_g$	0.4, d
5	$\text{He}_g^+ + \text{=SiO}\bullet\bullet \rightarrow \text{-Si}\bullet\bullet\bullet + \text{-O}\bullet + \text{He}_g$	0.4, d
6	$\text{H}_g + \text{-SiO}_2\text{-CH}_3 \rightarrow \text{-SiO}_2\bullet + \text{CH}_4\text{g}$	10 <sup>-5</sup> , e
7	$\text{H}_g + \text{-SiO}_2\text{-C}\bullet\bullet\bullet \rightarrow \text{-SiO}_2\text{-CH}\bullet\bullet$	10 <sup>-5</sup>
8	$\text{H}_g + \text{-SiO}_2\text{-CH}\bullet\bullet \rightarrow \text{-SiO}_2\text{-CH}_2\bullet$	10 <sup>-5</sup> , e
9	$\text{H}_g + \text{-SiO}_2\text{-CH}_2\bullet \rightarrow \text{-SiO}_2\text{-CH}_3$	10 <sup>-5</sup> , e
10	$\text{H}_g + \text{-SiO}_n\bullet \rightarrow \text{-SiO}_n\text{-H}$	0.1
11	$\text{H}_g + \text{-Si}\bullet\bullet\bullet \rightarrow \text{-Si-H}\bullet\bullet$	0.01
12	$\text{H}_g + \text{-Si-H}_x\bullet \rightarrow \text{-Si-H}_{x+1}$	0.001
13	$\text{H}_g + \bullet\text{CH}_3\text{a} \rightarrow \text{CH}_4\text{g}$	0.03, f
14	$\text{H}_g + \text{-O}\bullet \rightarrow \text{-OH}$	0.01

Table 5.2 (Continued)

15	$\text{H}_g + -\text{SiO}_2\text{-CH}_3 \rightarrow -\text{SiO}_2\text{-CH}_2\bullet + \text{H}_{2g}$	0.75, g
16	$\text{H}_g + -\text{SiO}_2\text{-CH}_2\bullet \rightarrow -\text{SiO}_2\text{-CH}\bullet\bullet + \text{H}_{2g}$	0.75, g
17	$\text{H}_g + -\text{SiO}_2\text{-CH}\bullet \rightarrow -\text{SiO}_2\text{-C}\bullet\bullet + \text{H}_{2g}$	0.75, g
18	$\text{H}_2(\text{v}=0)_g + -\text{SiO}_2\text{-CH}_3 \rightarrow -\text{SiO}_2\text{-CH}_2\bullet + \text{H}_{2g}$	0.75, h
19	$\text{H}_2(\text{v}=0)_g + -\text{SiO}_2\text{-CH}_2\bullet \rightarrow -\text{SiO}_2\text{-CH}\bullet\bullet + \text{H}_{2g}$	0.75, h
20	$\text{H}_2(\text{v}=0)_g + -\text{SiO}_2\text{-CH}\bullet\bullet \rightarrow -\text{SiO}_2\text{-C}\bullet\bullet\bullet + \text{H}_{2g}$	0.75, h
21	$\text{H}_2(\text{v}=0)_g + -\text{SiO}_2\text{-CH}_3 \rightarrow -\text{SiO}_2\text{-CH}_2\bullet + \text{H}_{2g}$	0.75, h
22	$\text{H}_2(\text{v}=1)_g + -\text{SiO}_2\text{-CH}_2\bullet \rightarrow -\text{SiO}_2\text{-CH}\bullet\bullet + \text{H}_{2g}$	0.75, h
23	$\text{H}_2(\text{v}=1)_g + -\text{SiO}_2\text{-CH}\bullet\bullet \rightarrow -\text{SiO}_2\text{-C}\bullet\bullet\bullet + \text{H}_{2g}$	0.75, h
24	$\text{H}_2(\text{v}=2)_g + -\text{SiO}_2\text{-CH}_3 \rightarrow -\text{SiO}_2\text{-CH}_2\bullet + \text{H}_{2g}$	0.75, h
25	$\text{H}_2(\text{v}=2)_g + -\text{SiO}_2\text{-CH}_2\bullet \rightarrow -\text{SiO}_2\text{-CH}\bullet\bullet + \text{H}_{2g}$	0.75, h
26	$\text{H}_2(\text{v}=2)_g + -\text{SiO}_2\text{-CH}\bullet\bullet \rightarrow -\text{SiO}_2\text{-C}\bullet\bullet\bullet + \text{H}_{2g}$	0.75, h
27	$\text{H}_2(\text{v}=3)_g + -\text{SiO}_2\text{-CH}_3 \rightarrow -\text{SiO}_2\text{-CH}_2\bullet + \text{H}_{2g}$	0.75, h
28	$\text{H}_2(\text{v}=3)_g + -\text{SiO}_2\text{-CH}_2\bullet \rightarrow -\text{SiO}_2\text{-CH}\bullet\bullet + \text{H}_{2g}$	0.75, h
29	$\text{H}_2(\text{v}=3)_g + -\text{SiO}_2\text{-CH}\bullet\bullet \rightarrow -\text{SiO}_2\text{-C}\bullet\bullet + \text{H}_{2g}$	0.75, h
30	$\text{H}_2(\text{v}=4)_g + -\text{SiO}_2\text{-CH}_3 \rightarrow -\text{SiO}_2\text{-CH}_2\bullet + \text{H}_{2g}$	0.75, h
31	$\text{H}_2(\text{v}=4)_g + -\text{SiO}_2\text{-CH}_2\bullet \rightarrow -\text{SiO}_2\text{-CH}\bullet\bullet + \text{H}_{2g}$	0.75, h
32	$\text{H}_2(\text{v}=4)_g + -\text{SiO}_2\text{-CH}\bullet\bullet \rightarrow -\text{SiO}_2\text{-C}\bullet\bullet\bullet + \text{H}_{2g}$	0.75, h
33	$\text{H}_2(\text{v}=5)_g + -\text{SiO}_2\text{-CH}_3 \rightarrow -\text{SiO}_2\text{-CH}_2\bullet + \text{H}_{2g}$	0.75, h
34	$\text{H}_2(\text{v}=5)_g + -\text{SiO}_2\text{-CH}_2\bullet \rightarrow -\text{SiO}_2\text{-CH}\bullet\bullet + \text{H}_{2g}$	0.75, h

Table 5.2 (continued)



- a. Unless specified, all ions neutralize on surfaces, returning as their neutral counterparts.
- b. Gas phase species have units of flux ( $\text{cm}^{-2} \text{s}^{-1}$ ). Surface species have units of fractional coverage.
- c. In reactions with no chemical change, the gas species are reflected off the surface. These reactions are not shown.
- d.  $E_r=100.0 \text{ eV}$ ,  $E_t=10.0 \text{ eV}$ , probability is at  $E_r$ .
- e.  $E_r=3.5 \text{ eV}$ ,  $E_t=0.5 \text{ eV}$ , probability is at  $E_r$ .
- f.  $E_r=3.5 \text{ eV}$ ,  $E_t=0.03 \text{ eV}$ , probability is at  $E_r$ .
- g.  $E_r=3.5 \text{ eV}$ ,  $E_t=1.0 \text{ eV}$ , probability is at  $E_r$ .
- h.  $E_r=3.5 \text{ eV}$ ,  $E_t=0.3 \text{ eV}$ , probability is at  $E_r$ .

Table 5.3 Reaction Mechanisms for PR removal in Ar/O<sub>2</sub> and He/H<sub>2</sub> Plasmas

Species:

M <sub>g</sub>	Gas phase species
M	Surface site
=M/-M	Surface site bonded to a solid
M•	Active surface site with dangling bond
M <sub>a</sub>	Adsorbed surface site
M <sub>g</sub> <sup>+</sup>	Ion

<u>Reaction</u>	<u>Reaction</u> <sup>a-c</sup>	<u>Probability</u>
1	O <sub>g</sub> + PR → CHO <sub>g</sub>	0.002
2	O <sub>g</sub> <sup>+</sup> + PR → CHO <sub>g</sub>	0.002
3	O <sub>2g</sub> <sup>+</sup> + PR → CHO <sub>g</sub>	0.002
4	H <sub>g</sub> + PR → CH <sub>4g</sub>	0.010, d
5	H <sub>g</sub> <sup>+</sup> + PR → CH <sub>4g</sub>	0.010, d
6	H <sub>2g</sub> <sup>+</sup> + PR → CH <sub>4g</sub>	0.010, d
7	H <sub>3g</sub> <sup>+</sup> + PR → CH <sub>4g</sub> ,	0.010, d
8	H <sub>2(v=3)g</sub> + PR → CH <sub>4g</sub>	0.010, d
9	H <sub>2(v=4)g</sub> + PR → CH <sub>4g</sub>	0.010, d
10	H <sub>2(v=5)g</sub> + PR → CH <sub>4g</sub>	0.010, d
11	He <sub>g</sub> <sup>+</sup> + PR → PR <sub>g</sub> + He <sub>g</sub>	10 <sup>-5</sup> , e
12	Ar <sub>g</sub> <sup>+</sup> + PR → PR <sub>g</sub> + Ar <sub>g</sub>	10 <sup>-5</sup> , e

<sup>a.</sup> Unless specified, all ions neutralize on surfaces, returning as their neutral counterparts.

<sup>b.</sup> Gas phase species have units of flux (cm<sup>-2</sup> s<sup>-1</sup>). Surface species have units of fractional coverage.

- c. In reactions with no chemical change, the gas species are reflected off the surface. These reactions are not shown.
- d.  $E_r=100$  eV,  $E_t=1.4$  eV, probability is at  $E_r$ .
- e.  $E_r=100$  eV,  $E_t=10$  eV, probability is at  $E_r$ .

## 5.9 Figures

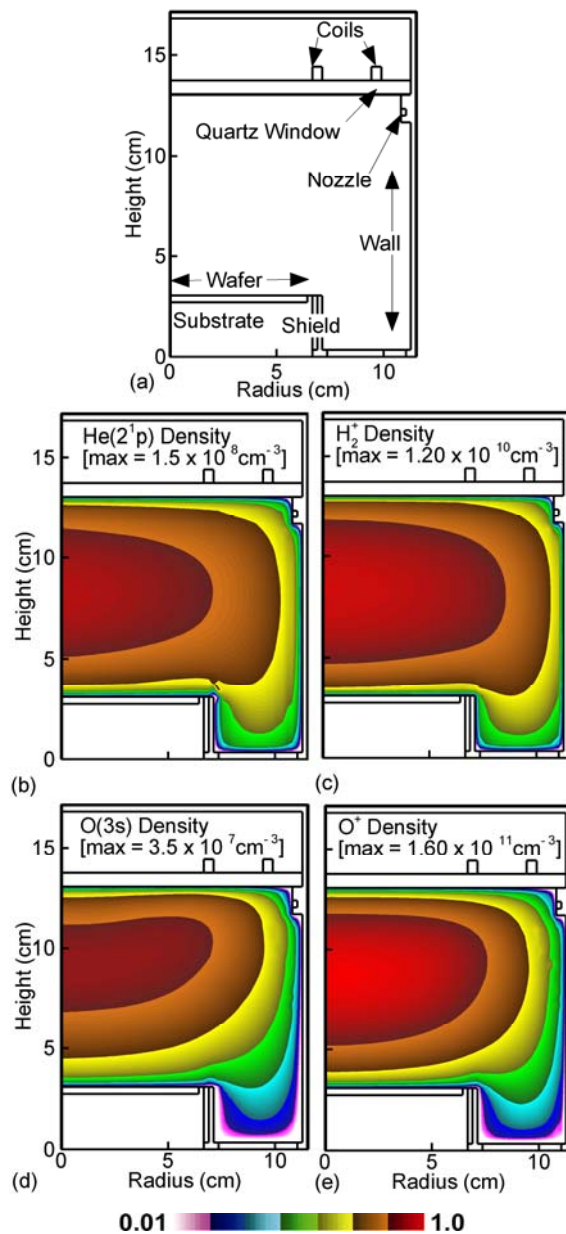


Fig. 5.1 Properties of the plasma cleaning reactors. (a) Schematic of the reactor. Properties of He/H<sub>2</sub> = 75/25 plasmas showing (b) He(2<sup>1</sup>p) which emits 58.4 nm photons having a peak density of  $1.5 \times 10^8 \text{ cm}^{-3}$ , and (c) dominant ion H<sub>2</sub><sup>+</sup> (maximum  $1.2 \times 10^{10} \text{ cm}^{-3}$ ). Properties of Ar/O<sub>2</sub> = 5/95 plasmas showing (d) O(3s) density (maximum  $3.5 \times 10^7 \text{ cm}^{-3}$ ) which is responsible for 130 nm photon emission, and (e) dominant ion O<sup>+</sup> density (maximum  $1.60 \times 10^{11} \text{ cm}^{-3}$ ). Plasma conditions are 300 W ICP, 10 mTorr, 100 sccm.

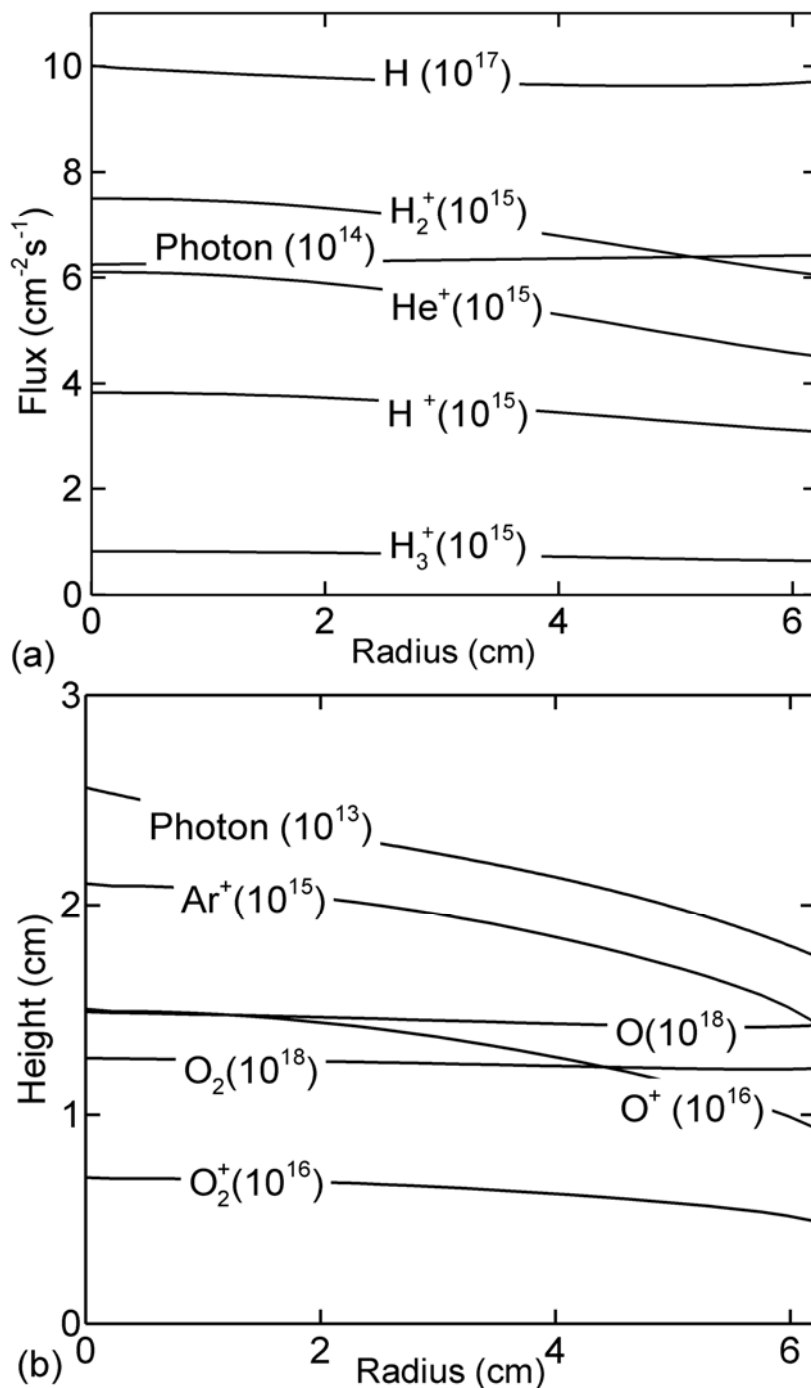


Fig. 5.2 Fluxes to the wafer. (a) Ion, photon, and neutral fluxes for He/H<sub>2</sub> plasmas as a function of radius. (b) Ion, photon, and neutral fluxes for Ar/O<sub>2</sub> plasmas. The scaling for fluxes is indicated in the figure. (He/H<sub>2</sub>=75/25, 300 W ICP, 10 mTorr, 100 sccm; Ar/O<sub>2</sub>=05/95, 300 W ICP, 10 mTorr, 100 sccm).

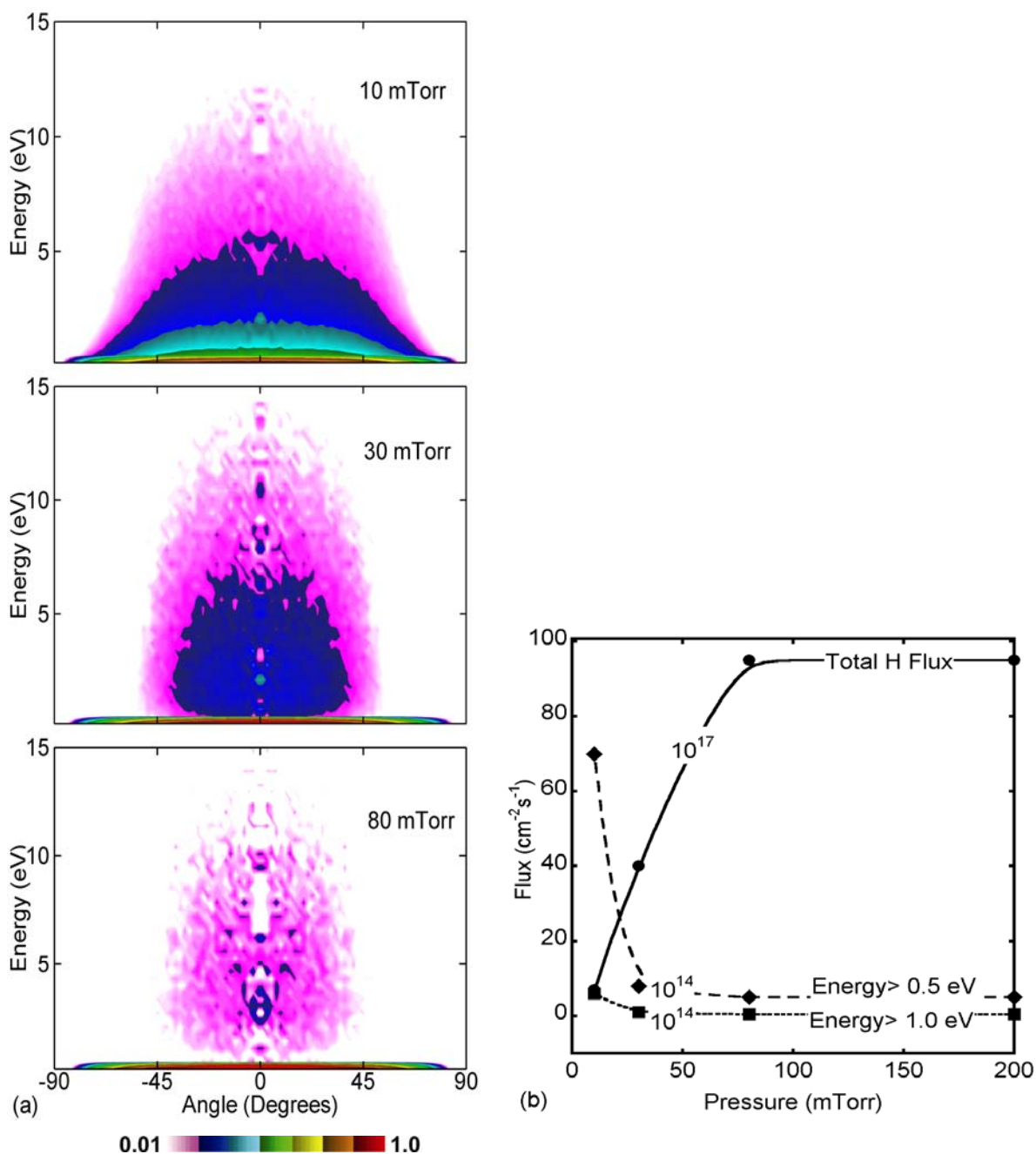


Fig. 5.3 Optimization of hot H (energy > 0.5 eV) fluxes to the wafer by varying pressure (He/H<sub>2</sub>=75/25, 300 W ICP, 100 sccm). (a) Energy and angular distribution of H atoms for pressures of 10 mTorr, 30 mTorr, and 80 mTorr. (b) Total H flux, and hot H flux (energy > 0.5 eV and energy > 1.0 eV) as a function of pressure. The scaling for fluxes is indicated in the figure.

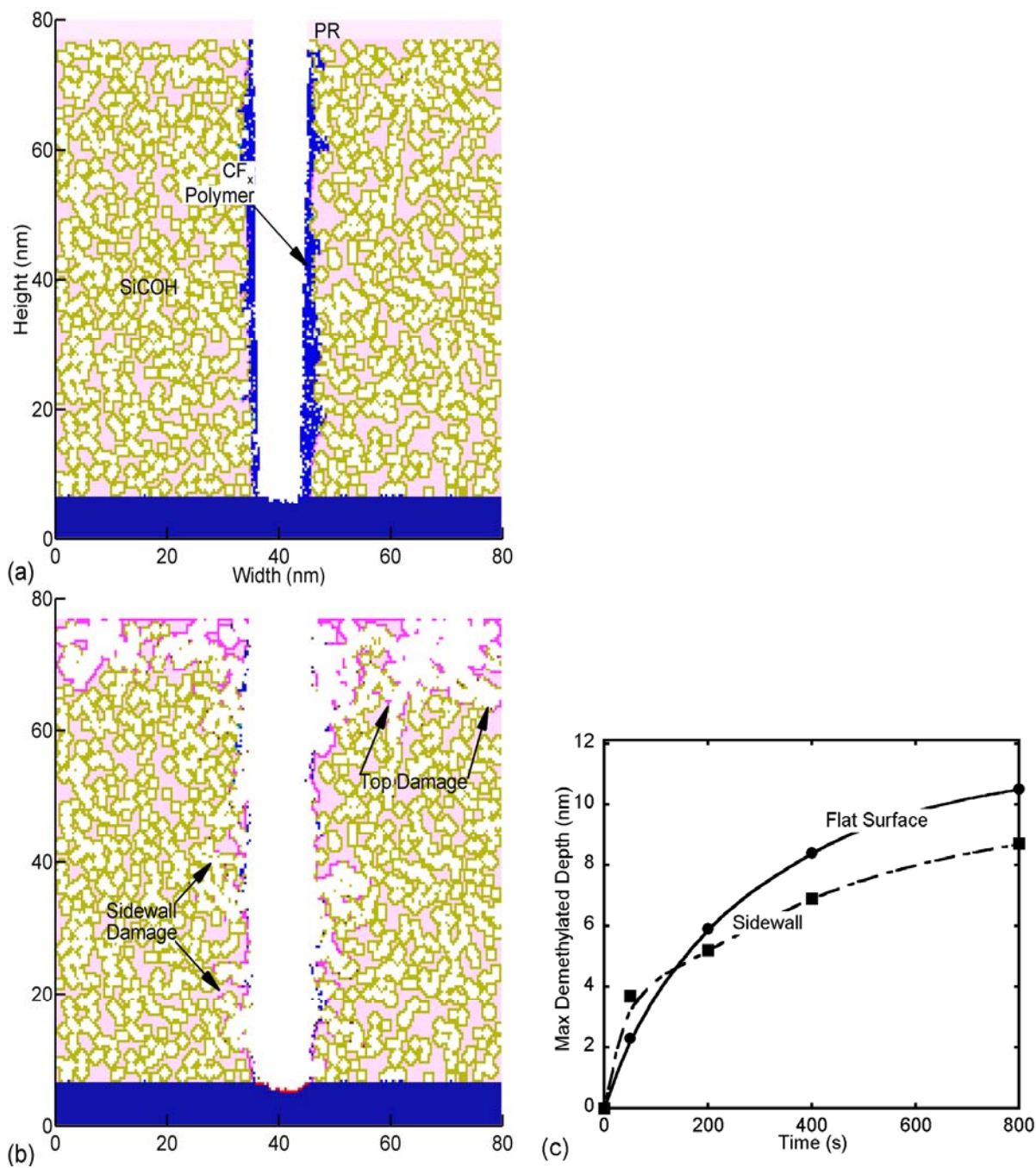


Fig. 5.4 Properties of plasma etched and cleaned porous SiOCH. (a) After fluorocarbon plasma etching leaving a CF<sub>x</sub> polymer. (b) After cleaning the fluorocarbon polymers with an Ar/O<sub>2</sub> plasma. (c) Progression of demethylation depth in the sidewalls and top flat surface with time. (Color coding: light pink – SiO<sub>2</sub>; olive – CH<sub>3</sub>; light blue – CF<sub>x</sub>; bright pink – cleaved SiO<sub>2</sub>\*; green – •CH<sub>3a</sub> sites after Si-C scission; brown – Si bonded-CH<sub>x</sub> (x<3) groups.)

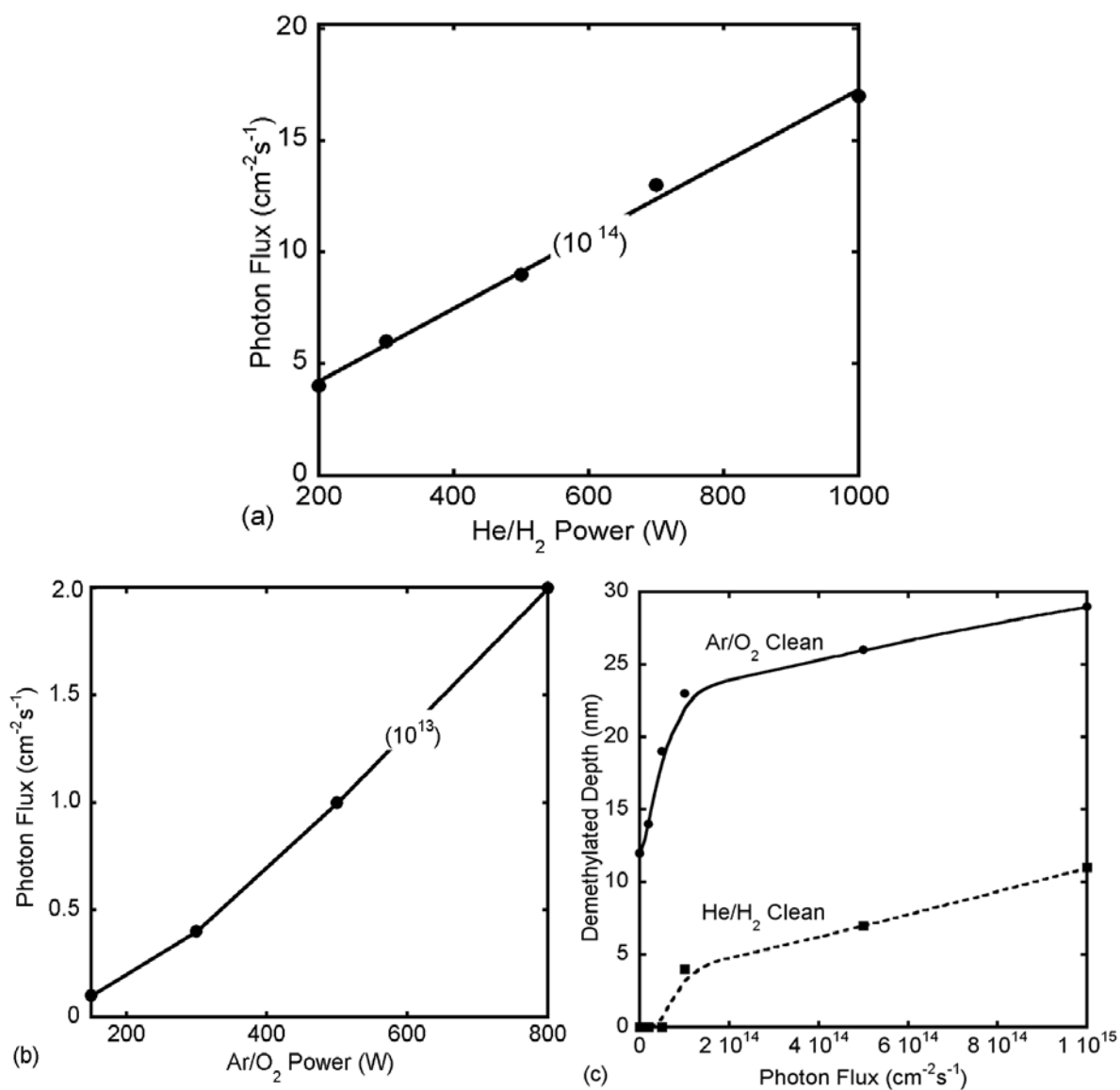


Fig. 5.5 Photon flux as a function of power and demethylation depth as a function of photon flux. VUV photon flux in: (a) He/ $\text{H}_2$ , and (b) Ar/ $\text{O}_2$  plasmas as a function of ICP power. (c) Damage depth in SiOCH as a function of photon flux. The damage depth is initially linear with photon flux but later the rate of damage decreases as most of the Si- $\text{CH}_3$  sites are within the absorption depth of the photons have undergone scission.

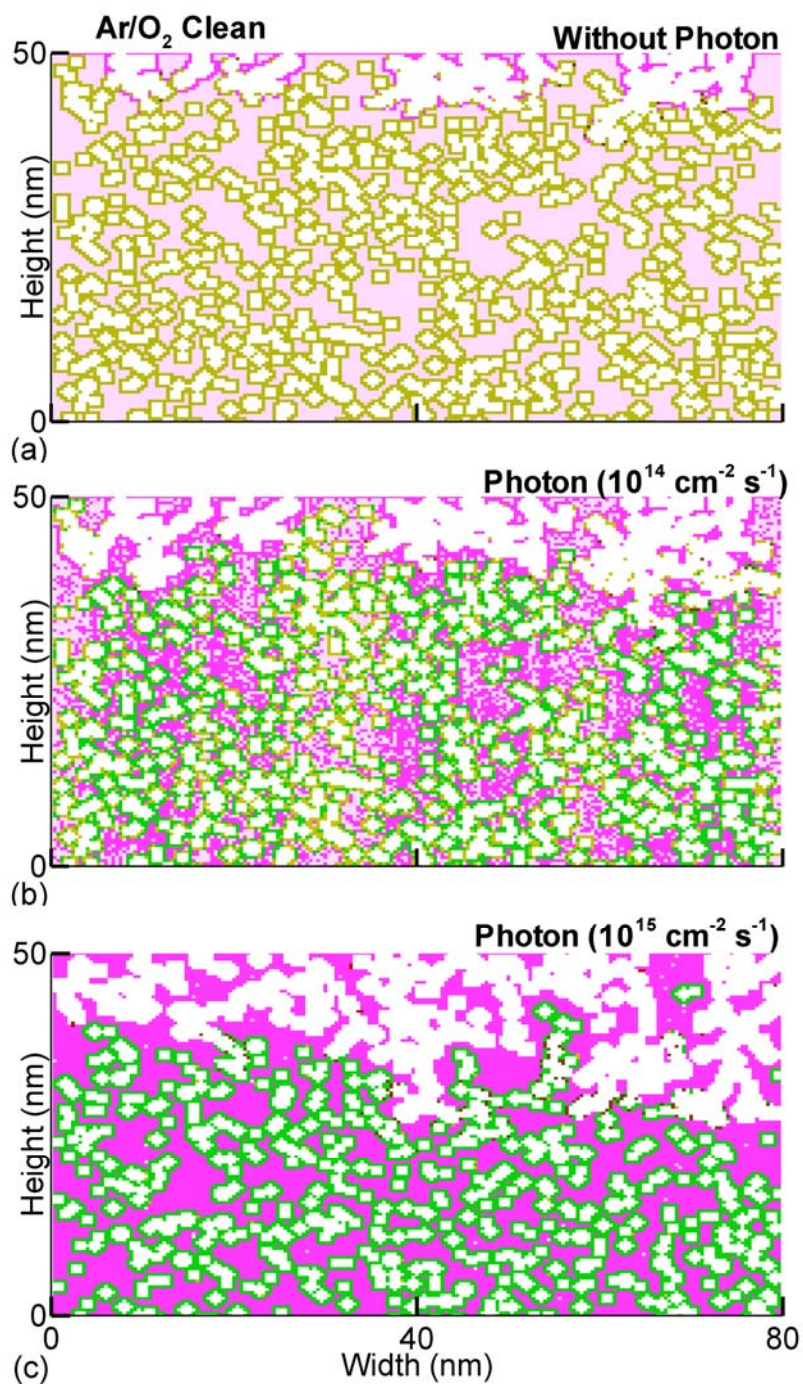


Fig. 5.6 SiOCH profiles showing the impact of VUV photon fluxes on demethylation during Ar/O<sub>2</sub> cleaning. (a) Without photons. (b) With a photon flux of  $10^{14} \text{ cm}^{-2} \text{ s}^{-1}$ , and (c) with a photon flux of  $10^{15} \text{ cm}^{-2} \text{ s}^{-1}$ . Penetration of 130 nm photons in Ar/O<sub>2</sub> plasmas is about 100 nm and accelerates demethylation depth to at least this depth. (Color coding: light pink – SiO<sub>2</sub>; olive – CH<sub>3</sub>; light blue – CF<sub>x</sub>; bright pink – cleaved SiO<sub>2</sub>\*; green – •CH<sub>3a</sub> sites after Si-C scission; brown – Si bonded–CH<sub>x</sub> (x<3) groups.)

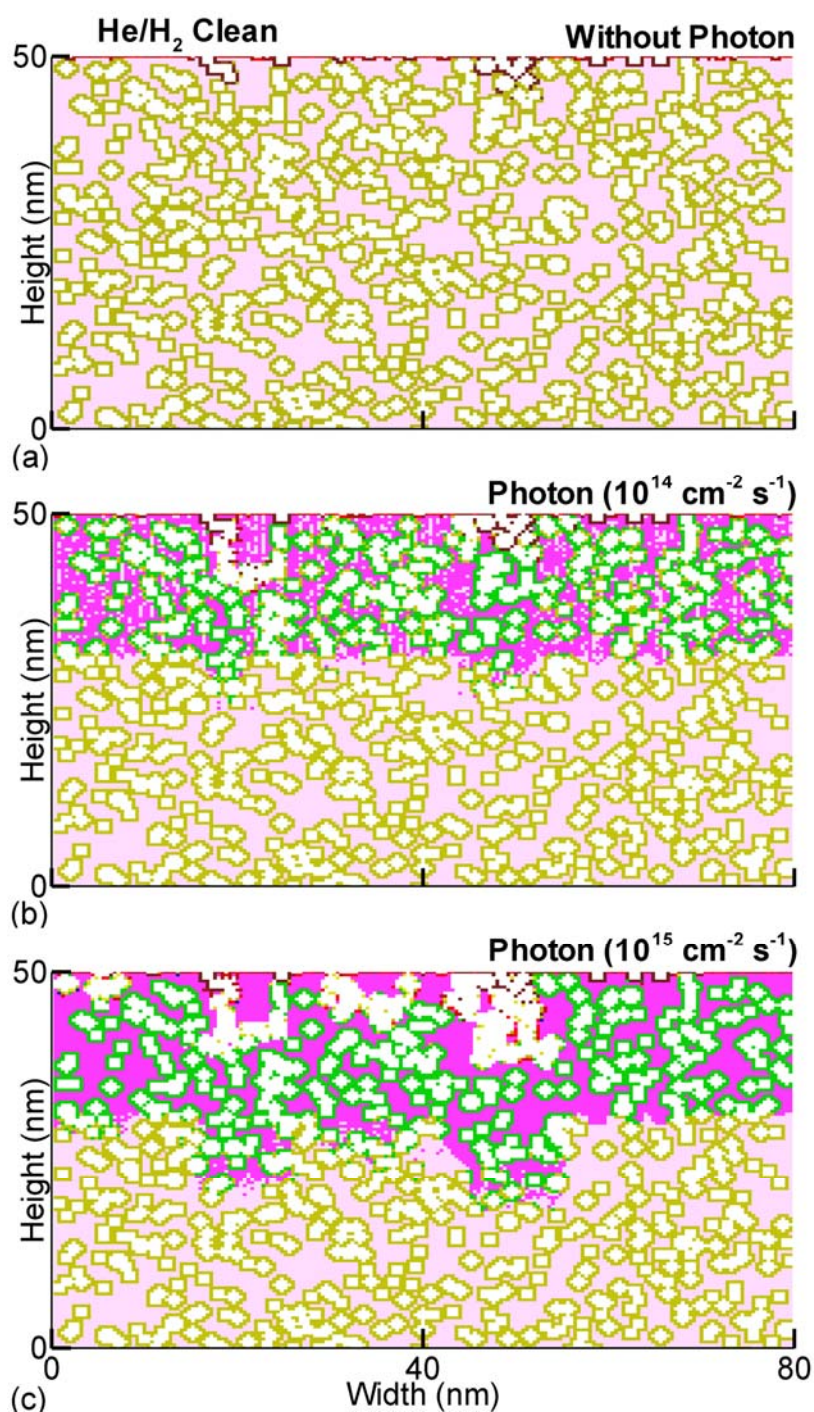


Fig. 5.7 SiOCH profiles showing the impact of VUV photon fluxes on demethylation during He/H<sub>2</sub> cleaning. (a) Without photons. (b) With a photon flux of  $10^{14} \text{ cm}^{-2} \text{ s}^{-1}$ , and (c) with a photon flux of  $10^{15} \text{ cm}^{-2} \text{ s}^{-1}$ . Penetration of 58 nm photons in He/H<sub>2</sub> plasmas is about 20-30 nm and accelerates demethylation depth to at least this depth. (Color coding: light pink – SiO<sub>2</sub>; olive – CH<sub>3</sub>; light blue – CF<sub>x</sub>; bright pink – cleaved SiO<sub>2</sub>\*; green – •CH<sub>3a</sub> sites after Si-C scission; brown – Si bonded-CH<sub>x</sub> (x<3) groups.)

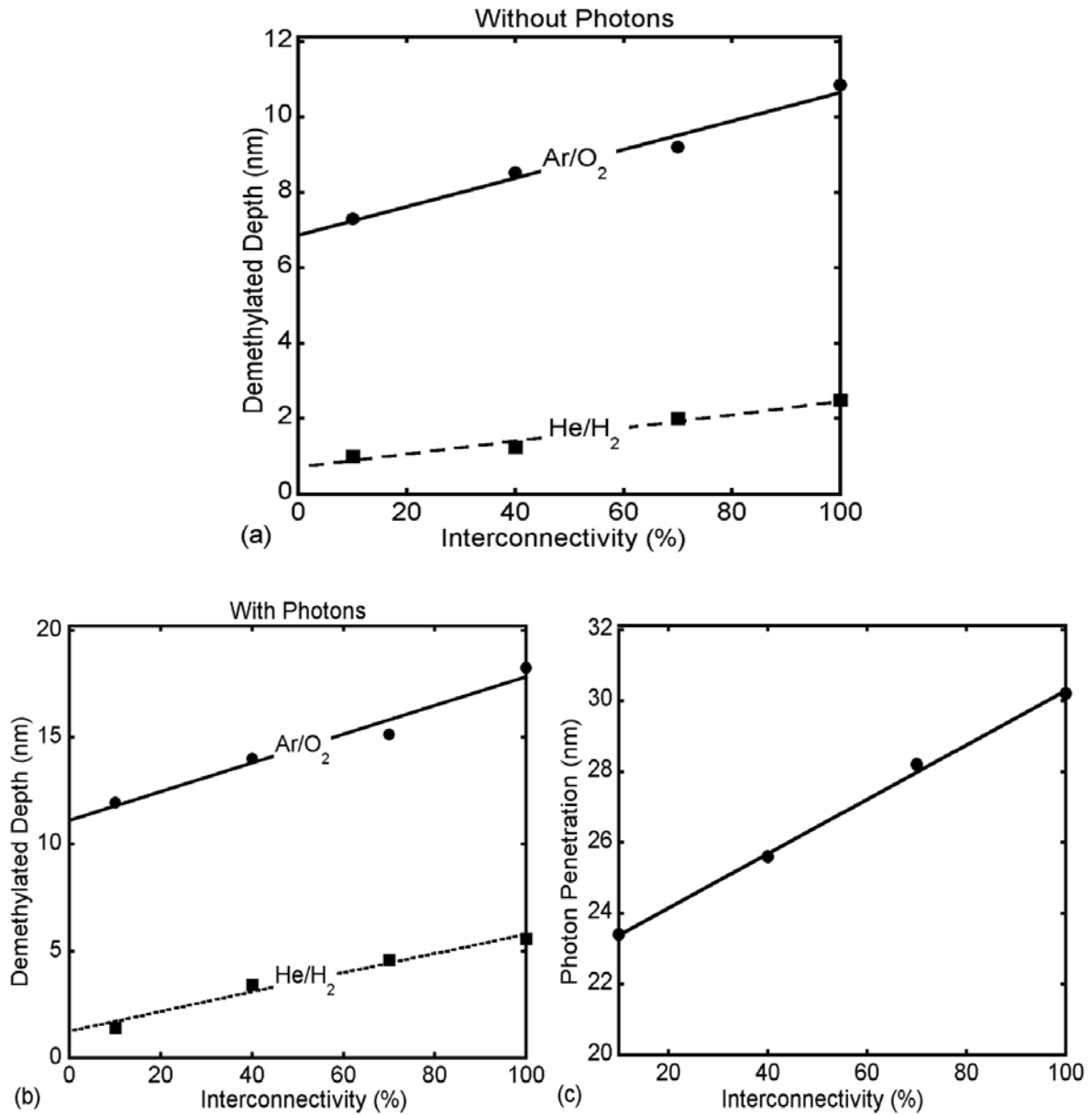


Fig. 5.8 Demethylation depth as a function of interconnectivity. Results are shown for Ar/O<sub>2</sub> and He/H<sub>2</sub> plasma cleaning, (a) without photons and, (b) with photons for an interconnectivity range of 10%-100%. (c) Penetration depth of 130 nm photons from Ar/O<sub>2</sub> plasmas and 58.4 nm photons from He/H<sub>2</sub> plasmas. Interconnected pores provide more pathways for radicals to diffuse into the SiOCH and facilitate deeper penetration of photons which produce more Si-CH<sub>3</sub> bond scission that speeds the demethylation process. (Color coding: light pink – SiO<sub>2</sub>; olive – CH<sub>3</sub>; light blue – CF<sub>x</sub>; bright pink – cleaved SiO<sub>2</sub>\*; green – •CH<sub>3a</sub> sites after Si-C scission; brown – Si bonded-CH<sub>x</sub> (x<3) groups.)

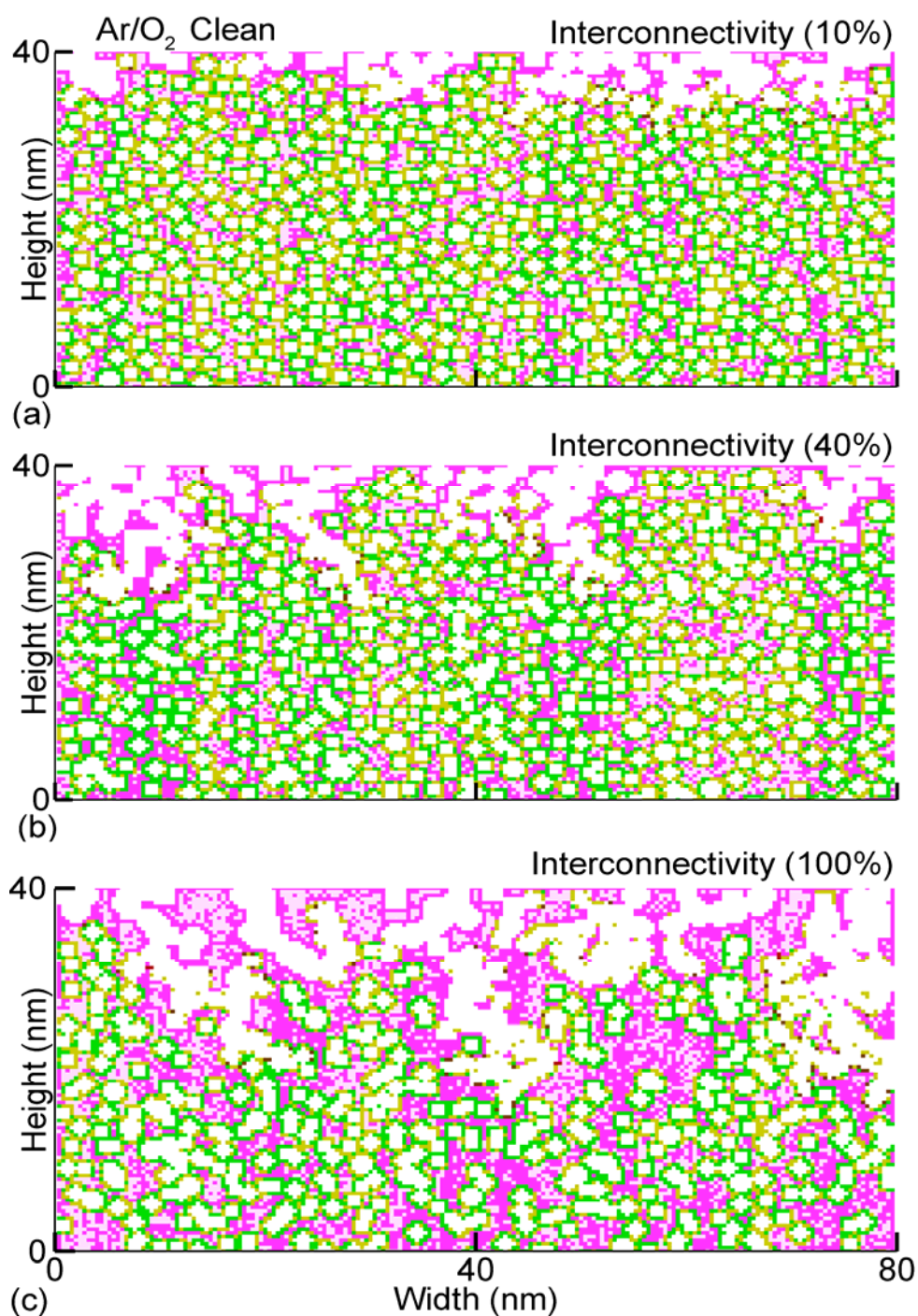


Fig. 5.9 Profiles showing the effects of interconnectivity on demethylation during Ar/O<sub>2</sub> cleaning. Profiles are shown for interconnectivities, (a) 10%, (b) 40%, and (c) 100%. Demethylated depth increases almost linearly with interconnectivity. (Color coding: light pink – SiO<sub>2</sub>; olive – CH<sub>3</sub>; light blue – CF<sub>x</sub>; bright pink – cleaved SiO<sub>2</sub>\*; green – •CH<sub>3a</sub> sites after Si-C scission; brown – Si bonded–CH<sub>x</sub> (x<3) groups.)

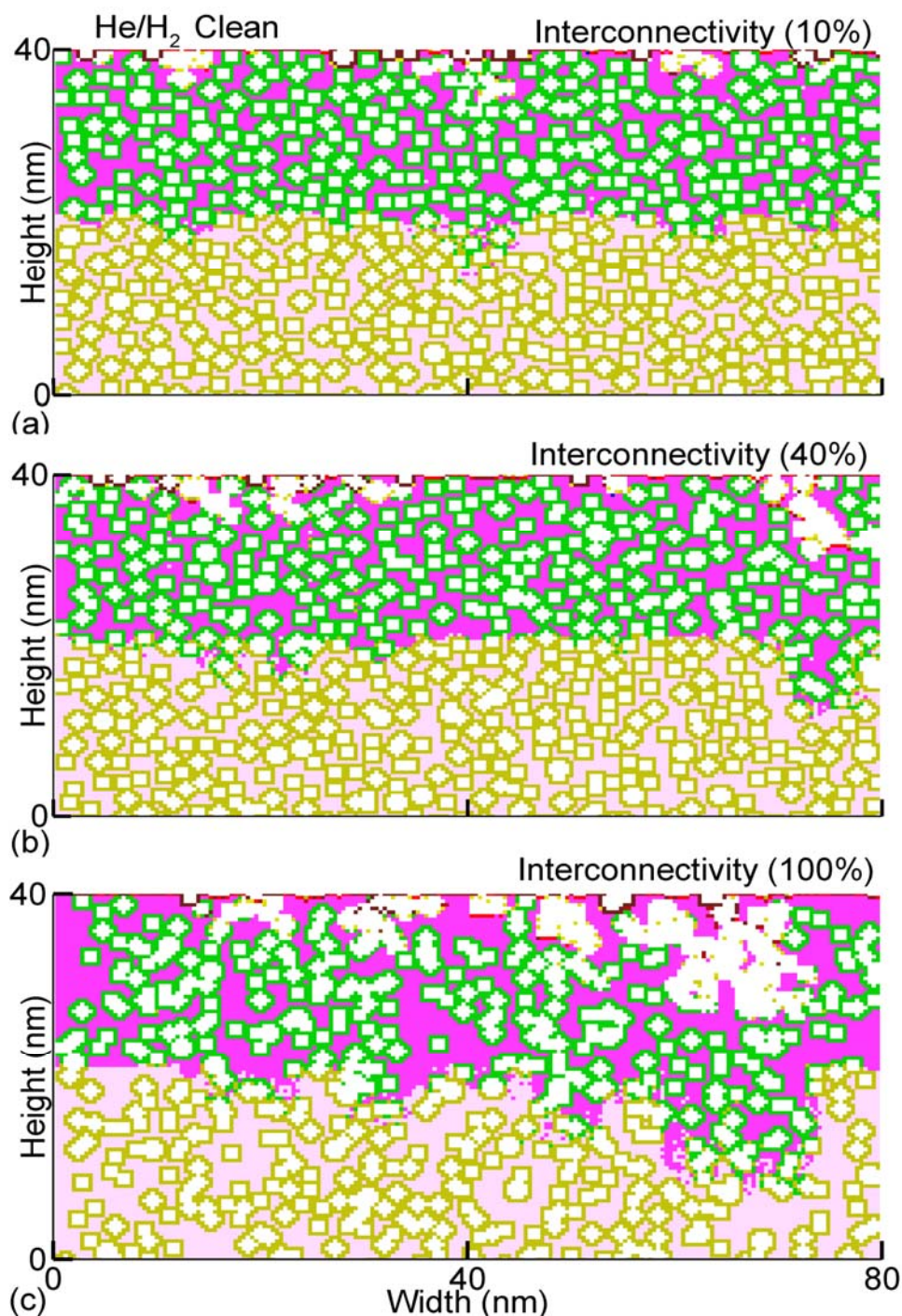


Fig. 5.10 Profiles showing interconnectivity effects on demethylation during He/H<sub>2</sub> cleaning. Profiles are shown for interconnectivities, (a) 10%, (b) 40%, and (c) 100%. Damage depth increases almost linearly with interconnectivity as for Ar/O<sub>2</sub> plasma cleaning. (Color coding: light pink – SiO<sub>2</sub>; olive – CH<sub>3</sub>; light blue – CF<sub>x</sub>; bright pink – cleaved SiO<sub>2</sub>\*; green – •CH<sub>3a</sub> sites after Si-C scission; brown – Si bonded–CH<sub>x</sub> (x<3) groups.)

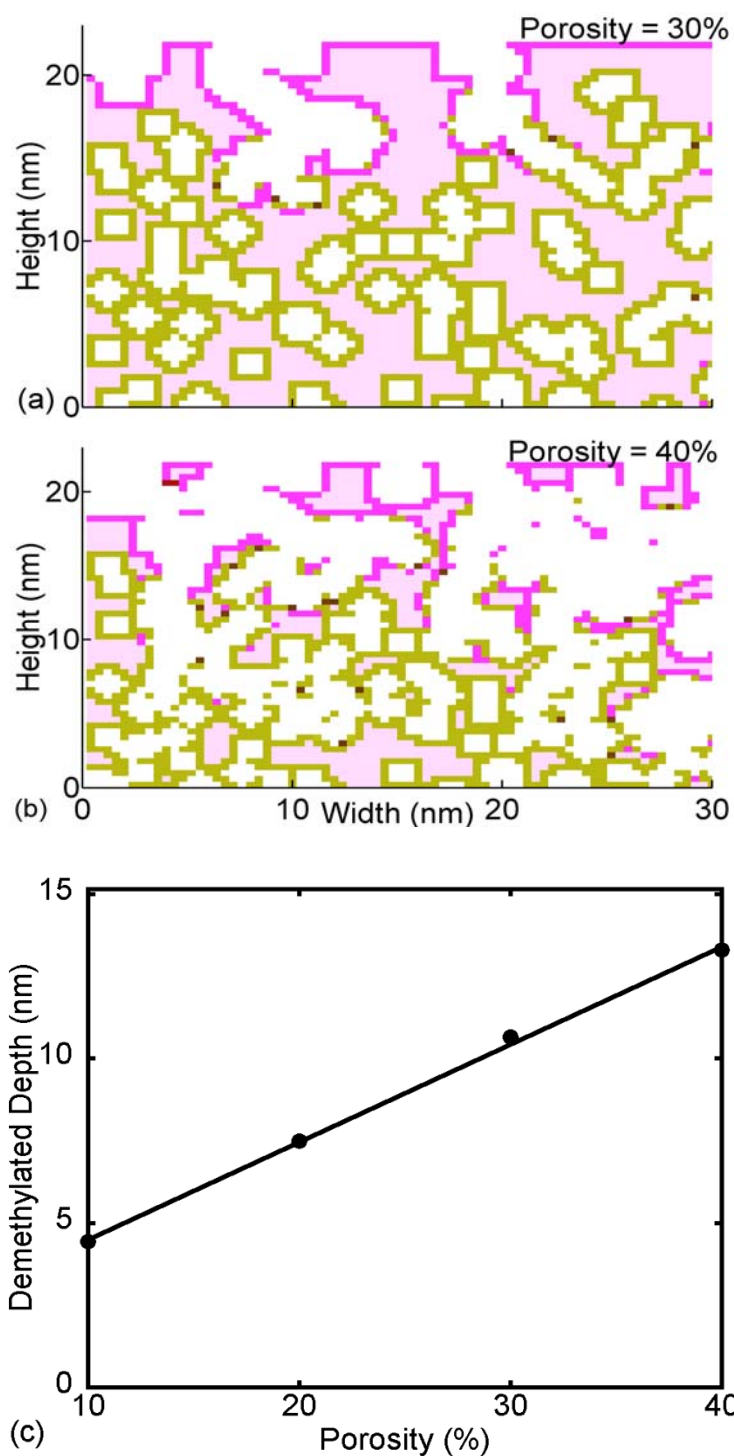


Fig. 5.11 Effects of porosity on damage of SiOCH. Profile for damage of (a) 30% porous SiOCH after 900s of Ar/O<sub>2</sub> plasma treatment without photons and (b) 40% porosity. (c) Demethylation depth as a function of porosity. The damage depth increases linearly with porosity. (Color coding: light pink – SiO<sub>2</sub>; olive – CH<sub>3</sub>; light blue – CF<sub>x</sub>; bright pink – cleaved SiO<sub>2</sub>\*; green – •CH<sub>3a</sub> sites after Si-C scission; brown – Si bonded-CH<sub>x</sub> (x<3) groups.)

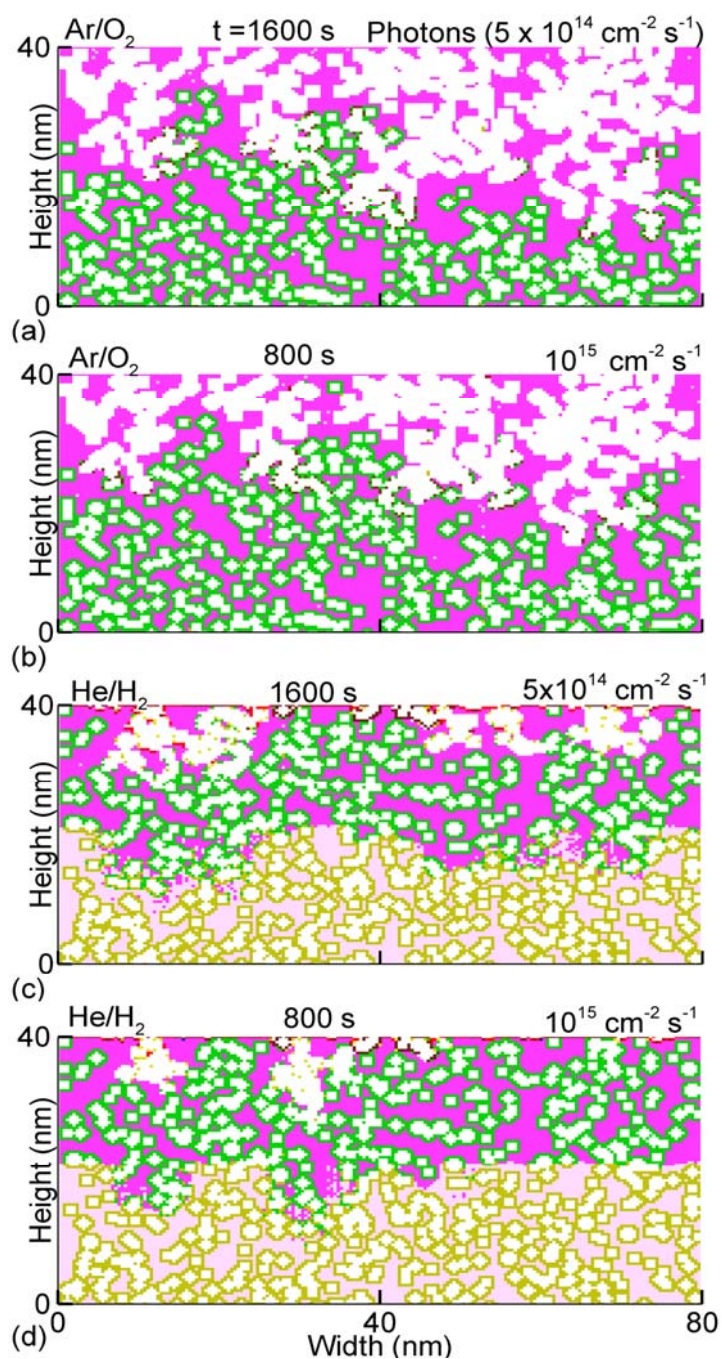


Fig. 5.12 SiOCH treated with different fluxes of VUV photons for the same fluence. Ar/O<sub>2</sub> plasma clean with a  $5 \times 10^{14} \text{ cm}^{-2} \text{ s}^{-1}$  photon flux treated for 1600s, and (b)  $10^{15} \text{ cm}^{-2} \text{ s}^{-1}$  flux treated for 800s. (c) He/H<sub>2</sub> plasma clean with a  $5 \times 10^{14} \text{ cm}^{-2} \text{ s}^{-1}$  photon flux treated for 1600s and (b)  $10^{15} \text{ cm}^{-2} \text{ s}^{-1}$  flux treated for 800s. For a constant fluence, the amount of Si-C bond scission is essentially same but for longer treatment times, there is more opportunity for radical fluxes to diffuse into the SiOCH and so cause more damage. (Color coding: light pink – SiO<sub>2</sub>; olive – CH<sub>3</sub>; light blue – CF<sub>x</sub>; bright pink – cleaved SiO<sub>2</sub>\*; green – •CH<sub>3a</sub> sites after Si-C scission; brown – Si bonded –CH<sub>x</sub> (x<3) groups.)

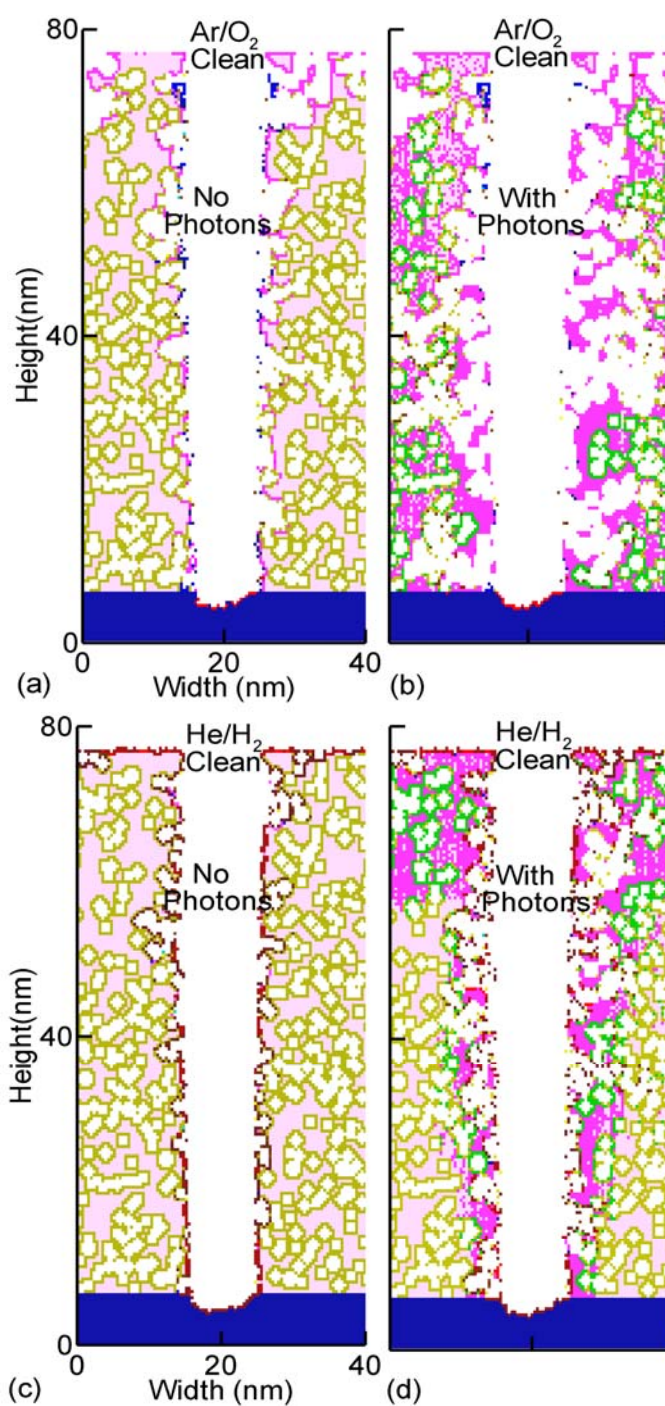


Fig. 5.13 Trenches in SiOCH following cleaning of CF<sub>x</sub> polymer. Cleaning by Ar/O<sub>2</sub> plasmas (a) without and (b) with VUV photons. Cleaning by He/H<sub>2</sub> plasmas (c) without and (d) with VUV photons. Presence of photons accelerates damage by Si-C bond scission for gas mixtures. (Color coding: light pink – SiO<sub>2</sub>; olive – CH<sub>3</sub>; light blue – CF<sub>x</sub>; bright pink – cleaved SiO<sub>2</sub>\*; green – •CH<sub>3a</sub> sites after Si-C scission; brown – Si bonded-CH<sub>x</sub> (x<3) groups.)

## 5.10 References

1. M. R. Baklanov, K. P. Mogilnikov, and Q. T. Le, *Microelectron. Eng.* **83** 2287 (2006).  
K. Maex, M. Baklanov, D. Shamiryman, F. Iacopi, S. H. Brongersma, K. Maex, and Z. S. Yanovitskaya, *J. Appl. Phys.* **93**, 8793 (2003).
2. G. Mannaert, M. R. Baklanov, Q. T. Le, Y. Travaly, W. Boullart, S. Vanhaelemeersch, and A. M. Jonas *J. Vac. Sci. Technol. B* **23**, 2198 (2005).
3. H. Seo, S. B. Kim, J. Song, Y. Kim, H. Soh, Y. C. Kim, and H. Jeon, *J. Vac. Sci. Technol. B* **20**, 1548 (2002).
4. K. Sakuma, K. Machida, K. Kamoshida, Y. Sato, K. Imai, and E. Arai, *J. Vac. Sci. Technol. B* **13**, 902 (1995).
5. M. A. Hartney, D. W. Hess, and D. S. Soane, *J. Vac. Sci. Technol. B* **7**, 1 (1989).
6. E. Kondoh, T. Asano, A. Nakashima, and M. Komatu, *J. Vac. Sci. Technol. B* **18**, 1276 (2000).
7. M. A. Goldman, D. B. Graves, G. A. Antonelli, S. P. Behera, and J. A. Kelber, *J. Appl. Phys.* **106**, 013311 (2009).
8. H. Shi, J. Bao, R. S. Smith, H. Huang, J. Liu, P. S. Ho, M. L. McSwiney, M. Moinpour, and G. M. Kloster, *Appl. Phys. Lett.* **93**, 192909 (2008).
9. J. Proost, E. Kondoh, G. Vereecke, M. Heyns, and K. Maex, *J. Vac. Sci. Technol. B* **16**, 2091 (1998).
10. J. Proost, M. Baklanov, K. Maex, and L. Delaey, *J. Vac. Sci. Technol. B* **18**, 303 (2000).
11. D. Shamiryman, M. R. Baklanov, S. Vanhaelemeersch, and K. Maex, *J. Vac. Sci. Technol. B* **20**, 1923 (2002).
12. M. Urbanowicz, M. R. Baklanov, J. Heijlen, Y. Travaly, and A. Cockburn, *Electrochem.*

- Solid-State Lett. **10**, G76 (2007).
13. A. M. Urbanowicz, D. Shamiryan, A. Zaka, P. Verdonck, S. De Gendt and M. R. Baklanov, J. Electrochem. Soc. **157**, H565 (2010).
  14. F. N. Dultsev, A. M. Urbanowicz, and M. R. Baklanov, Mater. Res. Soc. Symp. Proc. Vol. 1079 (Materials Research Society 1079-N07-03, 2008).
  15. K. Vanstreels, and A. M. Urbanowicz, J. Vac. Sci. Technol. B, **28**, 173 (2010).
  16. M. J. Kushner, J. Phys. D **42**, 194013 (2009).
  17. K. Rajaraman<sup>1</sup> and M. J. Kushner J. Phys. D: Appl. Phys. **37**, 1780 (2004).
  18. J. Shoeb and M. J. Kushner, "Damage by Radicals and Photons during Plasma Cleaning of Porous Low-*k* SiOCH Part II: Water Uptake and Change in Dielectric Constant".
  19. A. Agarwal and M. J. Kushner, J. Vac. Sci. Technol. A **27**, 37 (2009).
  20. A. Sankaran and M. J. Kushner, J. Vac. Sci. Technol. A **22**, 1242 (2004).
  21. F. Ossler, J. Larsson, and M. Alden, Chem. Phys. Lett. **250**, 287 (1996).
  22. J. Lee and D. B. Graves, J. Phys. D **43**, 425201 (2010).
  23. J. R. Woodworth, M. E. Riley, V. A. Amatucci, T. W. Hamilton, and B. P. Aragon, J. Vac. Sci. Technol. A **19**, 45 (2001).
  24. B. Jinnai, S. Fukuda, H. Ohtake, and S. Samukawa, J. Appl. Phys. **107**, 043302 (2010).
  25. M. Chaudhari, J. Du, S. Behera, S. Manandhar, S. Gaddam, and J. Kelber, Appl. Phys. Lett. **94**, 204102 (2009).
  26. O. V. Braginsky, A. S. Kovalev, D. V. Lopaev, E. M. Malykhin, Yu. A. Mankelevich, T. V. Rakhimova, A. T. Rakhimov, A. N. Vasilieva, S. M. Zyryanov, and M. R. Baklanov, J. Appl. Phys. **108**, 073303 (2010).

27. M.F.A.M. Van Hest, A. Klaver, D.C. Schram, and M.C.M. Van De Sanden, *Thin Solid Films* **449** 40 (2004).
28. M. A. Worsley, S. F. Bent, S. M. Gates, N. C. M. Fuller, W. Volksen, M. Steen and T. Dalton, *J. Vac. Sci. Technol. B* **23**, 395 (2005).
29. K. Singh, A. A. Kumbhar, and R. O. Dusane, *Materials Letters* **60** 1579 (2006).
30. J. Pelletier and M. J. Cooke, *J. Vac. Sci. Technol. B* **7**, 59 (1989).
31. K. Hassouni, T. A. Grotjohn, and A. Gicquel, *J. Appl. Phys.* **86** 134 (1999).
32. G. D. Billing and E. R. Fisher, *J. Chem. Phys.* **18**, 225, (1976).
33. T. Kikkawa, S. Kuroki, S. Sakamoto, K. Kohmura, H. Tanaka, and N. Hata, *Journal of The Electrochemical Society*, **152(7)**, G560 (2005).
34. M. Wang and M. J. Kushner, *J. Appl. Phys.* **107**, 023309 (2010).

## 6. NUMERICAL INVESTIGATION OF LOW-*k* DEGRADATION BY HUMID AIR

### 6.1 Introduction

Low dielectric constant (*low-k*) materials are now used for the inter-layer dielectric in the fabrication of microelectronics devices to lower the *RC* time constant for signal propagation.[1] One such *low-k* material is porous SiO<sub>2</sub> with hydrophobic methyl groups (–CH<sub>3</sub>) lining the pores – SiOCH. Such pristine *low-k* materials are essentially hydrophobic because of the presence of these hydrophobic –CH<sub>3</sub> groups on the pore walls which prevent SiO<sub>2</sub> from adsorbing water from humid air. As a result SiOCH usually does not contain more than a few percent of physisorbed water in its volume even when the humidity is high.[2] Even if this water does get inside the SiOCH by transport through the interconnected network,[2] this physisorbed water can be driven out with mild heating (200-300 C) without harming the integrity of the SiOCH.[1] If the hydrophobic –CH<sub>3</sub> groups are etched creating free radical sites, –SiO<sub>2</sub>•, (or chemically reactive sites), reactions can occur with water vapor through chemisorption forming, for example, –SiO<sub>2</sub>-OH. These sites cause the SiOCH to lose its hydrophobic nature by more easily enabling hydrogen bonding with additional water vapor. With the high dielectric constant of water (≈80), such reactions potentially increase the *k* value of SiOCH. As such, preservation of –CH<sub>3</sub> groups on pore walls is desired for maintaining the *low-k* integrity of SiOCH.

The CF<sub>x</sub> polymers which are deposited during the etching of SiOCH in fluorocarbon plasmas must be removed as these compounds may cause compatibility issues in subsequent processing steps.[3] Such polymers can also introduce some hydrophilic properties to SiOCH as they are not as hydrophobic as –CH<sub>x</sub> groups.[2] The removal of the CF<sub>x</sub> layer

would ideally be performed using an oxygen containing plasma due to the efficiency of oxidation of the polymer by oxygen radicals.[4-6] However, O<sub>2</sub> plasma cleaning can also remove the hydrophobic methyl groups from SiOCH that will, as described above, make the SiOCH less hydrophobic and possible lead to an increase in its *k*-value. SiOCH is relatively stable when H<sub>2</sub> plasmas are used for cleaning with minimal removal of –CH<sub>3</sub> groups.[7] When correlating SiOCH etch rates with damaged produced by plasma cleaning, He/H<sub>2</sub> plasma cleaning has been reported to result in one third etch the etch rate produced by Ar/O<sub>2</sub> plasma etching plasmas under similar conditions.[8] Given that He/H<sub>2</sub> plasma cleaning is relatively benign to the underlying SiOCH, these systems are being investigated for photo-resist (PR) mask removal.[9]

An unavoidable outcome of plasma cleaning of SiOCH is illumination with UV and VUV photons. For example, plasmas containing O<sub>2</sub> produce photon fluxes in the 130-145 nm range which have penetration distances >100 nm. In He/H<sub>2</sub> plasmas, the resonance radiation for He at 58.4 nm penetrates only ≈20 nm.[10] These UV/VUV photons can produce Si-C bond scission in –SiO<sub>2</sub>-CH<sub>3</sub> which can accelerate the –CH<sub>3</sub> removal process.[11,12] Since the –CH<sub>3</sub> removal process by O atoms is exothermic, demethylation is enhanced by VUV fluxes, but is not a prerequisite for demethylation. However, the deeper penetration depth into SiOCH of photons from Ar/O<sub>2</sub> plasmas magnifies the influence they have. On the other hand, demethylation by the intrinsically less reactive He/H<sub>2</sub> plasmas is greatly enhanced by the Si-C bond scission produced by VUV photons. However, the shorter penetration depth of VUV fluxes produced in He/H<sub>2</sub> plasmas limits the range of this enhancement.

Exposure of SiOCH to humid air results in water uptake due to reaction of H<sub>2</sub>O with free radical sites –SiO<sub>2</sub>• resulting from oxidation or bond-scission that removes –CH<sub>3</sub>. The

end result is formation of hydrophilic  $-\text{SiO}_2\text{-OH}$ . That is, hydrophobic  $-\text{CH}_3$  group from  $-\text{SiO}_2\text{-CH}_3$  is replaced by hydrophilic  $-\text{OH}$  group. The presence of  $-\text{SiO}_2\text{-OH}$  enables further water uptake, creates  $-\text{SiO}_2\text{-OH}(\text{H}_2\text{O})$  type compounds through hydrogen bonding.[13-15] Given the high dielectric constant of water ( $\approx 80$ ), loss of hydrophobic  $-\text{CH}_3$  groups after  $\text{O}_2$  plasma cleaning of  $\text{SiOCH}$  and incorporation of water from humid air can cause an increase in the dielectric constant from 2.5 to 20 within 9 minutes.[1]

One of the strategies to reduce or eliminate the increase in dielectric constant resulting from water intake is to seal the pores. A number of different techniques have been developed for pore sealing, including densification of the surface with a plasma treatment and formation of a sealing layer of Si-N and C-N compounds with a  $\text{NH}_3$  plasma treatment. Pre-treatment with He plasmas is thought to create active surface sites which localize and accelerate the chemical reactions responsible for pore sealing.[16-18] The processes whereby subsequent  $\text{NH}_3$  plasma treatment completes the sealing are uncertain but at least two mechanisms have been proposed. The first proposes that  $\text{NH}_3$  plasma treatment catalyzes pore collapse and so produces a dense non-porous layer at the surface.[19] The second proposes that chemisorption of  $\text{NH}_x$  radicals result in Si-N and C-N bonding which leads to bridging of the opening of the pores.[16-18]

The He ions produced in  $\text{He}/\text{H}_2$  plasma cleaning also aids in preconditioning the surface which improves pore sealing by subsequent treatment using  $\text{NH}_3$  containing plasmas.[16-18] The preconditioning promotes formation of Si-N and C-N bonding which produces a 1-2 monolayer thick sealing layer. The protective layer helps prevent water molecules from humid air from entering the porous network. Due to  $\text{He}/\text{H}_2$  plasmas being less reactive with  $-\text{CH}_3$  groups and also able to precondition the  $\text{SiOCH}$  for subsequent pore

sealing in  $\text{NH}_3$  plasmas,  $\text{He}/\text{H}_2$  plasmas are attractive candidates for cleaning  $\text{SiOCH}$  and helping to maintain its low- $k$  nature.

In this chapter, we discuss reaction mechanisms and computationally investigate the change in dielectric constant due to water uptake from humid air after polymer cleaning from  $\text{SiOCH}$  with  $\text{Ar}/\text{O}_2$  and  $\text{He}/\text{H}_2$  plasmas. This study is a follow-on to a more general investigation of damage mechanisms of  $\text{SiOCH}$  by plasma cleaning (including VUV photons) discussed in Chapter 5.[20] Change in the dielectric constant of the  $\text{SiOCH}$   $k$  value was assessed using the amount of water adsorbed with exposure to humid air after cleaning.

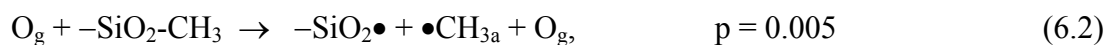
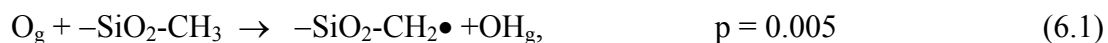
The reaction mechanism for damage of  $\text{SiOCH}$  in  $\text{Ar}/\text{O}_2$  and  $\text{He}/\text{H}_2$  is discussed in Chapter 5, and so will be only briefly discussed in Sec. 6.2 along with mechanism for water uptake and increase in dielectric constant. A comparison of low- $k$  degradation (that is, increase in dielectric constant of  $\text{SiOCH}$ ) after  $\text{Ar}/\text{O}_2$  and  $\text{He}/\text{H}_2$  plasma cleaning is discussed in Sec. 6.3 and preservation of low- $k$  properties by pore sealing are discussed in Sec. 6.4. Comparison of our results with experiments is in Sec. 6.5 and our concluding remarks are in Sec. 6.6.

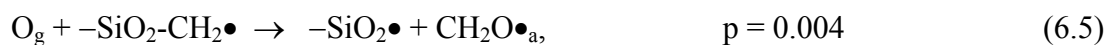
## 6.2 Surface Reaction Mechanisms

Reaction mechanisms were developed for plasmas sustained in  $\text{He}/\text{H}_2$  and  $\text{Ar}/\text{O}_2$  mixtures and their interactions with low- $k$  porous  $\text{SiOCH}$ , and is discussed in detail in Chapter 5.[20] In this chapter, the uptake of  $\text{H}_2\text{O}$  molecules coming from humid air was included and an assessment of the change in low- $k$  properties of the  $\text{SiOCH}$  made based on the amount of water in the pores. As in Chapter 5, the Hybrid Plasma Equipment Model (HPEM) was em-

ployed to obtain the energy and angular distributions of fluxes of charged and neutral species, and of photon fluxes, incident onto the surface.[21] These fluxes and the reaction mechanism was implemented in the Monte Carlo Feature Profile Model (MCFPM) with which the evolution of the SiOCH properties are predicted.[22] The MCFPM resolves the porous material with approximately atomic resolution. The cell size in this work is square with  $0.4 \text{ nm} \times 0.4 \text{ nm}$  dimensions, which is an effective radius of 0.2 nm. The creation of pores in the MCFPM mesh is discussed in Ref. [23]. The internal surfaces of the pores in SiO<sub>2</sub> were lined with a single layer of  $-\text{CH}_3$  to approximate the structure of SiOCH as discussed in Ref. [24].

When SiOCH is processed in an O<sub>2</sub> containing plasma, the  $-\text{CH}_3$  groups of the porous low- $k$  are etched as CO/CO<sub>2</sub> from deeper sites below the surface which O atoms reach by diffusion through the interconnected porous network.[8,25,26] Photons produced by the plasma having wavelength of <145 nm and penetrating into the SiOCH can break the Si-C bond and initiate a series of reactions starting with production of an adsorbed  $\bullet\text{CH}_{3a}$  radical which is removed by further reaction with O and O<sub>2</sub>. [11,12] The dominant reactions for methyl group removal or demethylation in O<sub>2</sub> plasmas is described in Chapter 5 and is summarized as [8,11,20, 25-27],

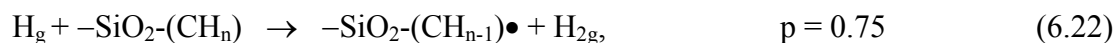
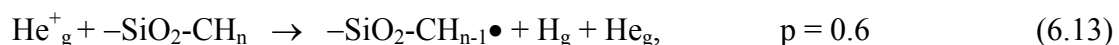




Subscript g denotes a gas phase species, subscript a denotes an adsorbed species, the symbols  $\bullet$  represent a dangling bond or free radical site, and  $-$  (or  $=$ ) represents bonding to the solid. Note that there is a chain reaction where H abstraction by O or OH from  $-\text{SiO}_2\text{-CH}_3$  produces OH or  $\text{H}_2\text{O}$  which can further react in the demethylation process.

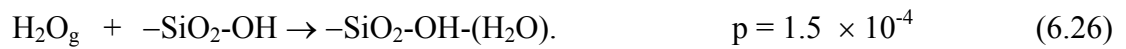
He/ $\text{H}_2$  plasmas remove  $-\text{CH}_3$  groups from  $\text{SiOCH}$  at a slower rate primarily because the reactions for  $-\text{CH}_3$  removal in He/ $\text{H}_2$  plasmas are either endothermic or proceed at a slower rate than in Ar/ $\text{O}_2$  plasmas, and the reaction products are themselves less reactive. As a result, photons from He/ $\text{H}_2$  plasmas which produce Si-C bond cleavage to separate  $-\text{CH}_3$  from Si can greatly accelerate the demethylation by enabling the  $\bullet\text{CH}_3a$  to be removed by H atoms as  $\text{CH}_4$ . [16,17, 27] After  $-\text{CH}_3$  removal from  $-\text{SiO}_2\text{-CH}_3$ , H atoms can passivate the free radical site  $-\text{SiO}_2\bullet$  forming  $-\text{SiO}_2\text{-H}$  where Si is bonded to H with a Si-H bond. However,  $\text{He}^+$  can break Si-O bonding in  $-\text{SiO}_2\bullet$  and generate free radical site  $-\text{SiO}\bullet\bullet$ , and a successive strike can produce  $-\text{Si}\bullet\bullet\bullet$ . H can passivate  $-\text{Si}\bullet\bullet\bullet$  as  $-\text{Si-H}_n$  ( $n = 1-3$ ). Such compounds with Si-H bonds are hydrophobic in nature and can block water uptake. [28] The

analogous process in Ar/O<sub>2</sub> plasmas produce hydrophilic –SiO<sub>2</sub>-OH sites. The interaction between He/H<sub>2</sub> plasmas and SiCOH is discussed in Part I and is summarized as [8,11,16,17,28],



After Ar/O<sub>2</sub> or He/H<sub>2</sub> plasma cleaning and upon exposure to humid air, free radical (–SiO<sub>2</sub>•) or passivated (–SiO<sub>2</sub>-OH) sites formed after –CH<sub>3</sub> removal can react with water. Any remaining •CH<sub>3</sub>a generated by photon produced Si-C bond scission in –SiO<sub>2</sub>-CH<sub>3</sub> can also be etched by H<sub>2</sub>O to form CH<sub>4</sub> and OH, which can then produce more demethylation. The general sequence of events is that –SiO<sub>2</sub>• on the pore-walls react with H<sub>2</sub>O to form hy-

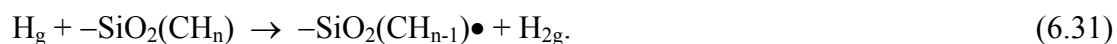
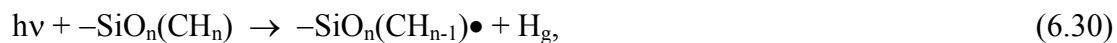
drophilic  $-\text{SiO}_2\text{-OH}$ . Additional water uptake can occur by reaction of  $-\text{SiO}_2\text{-OH}$  with  $\text{H}_2\text{O}$  to form hydrogen bonded  $-\text{SiO}_2\text{-OH-(H}_2\text{O)}$ . The volume averaged uptake of  $\text{H}_2\text{O}$  with its dielectric constant of 80, results in an increase of the dielectric constant of the SiOCH and a degradation of the low- $k$  properties. These reactions are summarized as [11, 13-15],



Computationally, water exposure was addressed in the following manner. Fluxes of  $\text{H}_2\text{O}$  and  $\text{O}_2$  commensurate with humid air were directed towards the surface of the SiOCH with trajectories randomly chosen isotropically in angle and from a Maxwellian velocity distribution for room temperature. Gas phase collisions were included but are unimportant for the size of porosity we are addressing. The method of computation was otherwise identical to that for low pressure processing.

During the He/ $\text{H}_2$  plasma cleaning step, active sites SiOCH are produced that assist in pore sealing during a subsequent Ar/ $\text{NH}_3$  plasma treatment.[16-18]  $\text{He}^+$  and VUV photons break Si-O bonds and remove H from  $-\text{CH}_3$  groups lining the pores to create the active sites. The bond breaking and site activation reactions are summarized as [16-18, 24],





Following He/H<sub>2</sub> plasma treatment, NH<sub>n</sub> (n = 1, 2) species created in Ar/NH<sub>3</sub> plasmas are chemisorbed at activated sites on SiOCH forming Si-N and C-N bonds.[16-18, 24] Chemical reactions between NH<sub>x</sub> radicals and activated Si sites produce compounds such as Si-NH<sub>n</sub> (n=1, 2), =Si-NH-Si= and SiNH<sub>x</sub>-NH<sub>y</sub>. [16-18, 24] In SiOCH, C-N bonding is also possible forming =CH<sub>x</sub>-NH<sub>y</sub> compounds which are important in bridging and sealing the pore openings.[16-18, 24] The model treats these chemisorbed species as precursors to further adsorption of NH<sub>x</sub> which form N-N bonds linking C or Si atoms from opposite pore walls. This N-N bonding results in, for example, =Si(HN)-(NH)(CH<sub>n</sub>)Si= bridging compounds across pores. Our reaction mechanisms for sealing SiOCH is discussed in detail in Ref. [24], and are summarized as [16-18, 24],



Such a sealing layer can prevent H<sub>2</sub>O molecules from entering the porous network and so reduce the degree of low-k degradation. Experimentally, it has been observed that after such sealing, humid air exposure does not significantly increase the water volume percentage compared to pristine SiOCH.[17] This results indicates that H<sub>2</sub>O molecules from humid air do not react with –NH<sub>x</sub> compounds to remove the sealing layer. As such, the –NH<sub>x</sub> sealing layer essentially blocks water uptake.

Prior to plasma exposure, pristine SiOCH contains < 2% of physisorbed H<sub>2</sub>O which can be removed by moderate heating (≈200 C) without otherwise detrimentally affecting the material.[1,2,17] As a result, in our model, there is no adsorbed water nor hydrophillic groups present in the porous volume before plasma treatment. Consequences of water uptake is measured by the effective dielectric constant of SiOCH,  $k'$ , which accounts for the volume fraction of the water and the porosity,[29]

$$k_p = k_w \frac{2k_A + \frac{V_W}{V_P}(k_W - k_A)}{2k_W - \frac{V_W}{V_P}(k_W - k_A)}, \quad (6.36)$$

$$k' = k_S \frac{k_S + k_P + V_P(k_P - k_S)}{k_S + k_P - V_P(k_P - k_S)}, \quad (6.37)$$

where dielectric constants are  $k_W$  for water (80),  $k_A$  for air (1.0),  $k_P$  for a pore and  $k_S$  for non-porous SiOCH (≈3.2).  $V_P$  is the volume fraction of pores and  $V_W$  is the volume fraction of water.  $k'$  as a function of water volume  $V_W$  is shown in Fig. 1a for a porosity  $V_P = 30\%$ . An increase in  $V_W$  of even a few percent for a given porosity increases  $k'$  by significant amounts,

in this case to a dielectric constant of 5 for  $V_W = 6\%$ , due to the large dielectric constant of water.

The plasma conditions are the same as in Chapter 5. The inductively coupled plasmas treated a wafer 15 cm in diameter. The reactor was 26 cm in diameter with a wafer-to-coil height of 10 cm. The gas mixture were  $\text{Ar}/\text{O}_2 = 5/95$  and  $\text{He}/\text{H}_2 = 75/25$  at a pressure of 10 mTorr, flow rate of 100 sccm and ICP power of 300 W applied at 10 MHz. An rf bias at 10 MHz with amplitude of 20 V was used. The base case properties of the SiOCH are a porosity of 30%, pore radius of 0.8 nm with standard deviation of 10% and interconnectivity of 100%. This result in a dielectric constant of  $k = 2.55$ .

The probabilities for surface site modification,  $-\text{CH}_3$  etching reactions and sealing have been determined by extensive parameterization of the models to be qualitatively consistent with experimental results available in the literature. The mechanism for demethylation is described in Part I and for sealing in Ref. [24]. Bounds of reaction probabilities are set based on thermodynamic properties and change in enthalpy of reactions, and within those bounds parameterization and comparison to experiments refine the mechanism. Although the majority of these reactions have a dependence on substrate temperature, our mechanism assumes a fixed substrate temperature of 27 C while including energy dependencies for gas phase radicals. Some examples of works that guided the development of the reactions are discussed in section 6.6 to validate our mechanisms and reaction probabilities.

### **6.3 Low- $k$ Degradation: Ar/O<sub>2</sub> and He/H<sub>2</sub> Cleaning**

We treated the pristine porous SiOCH of Fig. 6.2a separately with 800 s exposure to Ar/O<sub>2</sub> and He/H<sub>2</sub> plasmas. The Ar/O<sub>2</sub> plasma etched the  $-\text{CH}_3$  groups to  $\approx 30$  nm depth while

the maximum etching depth for He/H<sub>2</sub> plasmas was ≈10 nm. After each clean, the SiOCH was exposed to air exposure with 2% for 120 s. The profiles of the pristine SiOCH, after plasma exposure and after humid air exposure are shown in Fig. 6.2. Water uptake and dielectric constant as a function of air exposure time are shown in Fig. 6.3. After 120 s of humid air exposure, the total  $V_W$  is 9% after Ar/O<sub>2</sub> plasma cleaning, and 2% after He/H<sub>2</sub> plasma cleaning.

After a critical amount of water adsorption, the increase in  $V_W$  as a function of time slows. This is due to the blocking of pore openings by  $-\text{SiO}_2\text{-OH-(H}_2\text{O)}$  compounds. The  $V_W$  is composed to two components, chemisorbed  $-\text{SiO}_2\text{-OH}$  and hydrogen bonded H<sub>2</sub>O. In  $-\text{SiO}_2\text{-OH}$ , the  $-\text{OH}$  is chemically bonded to  $-\text{SiO}_2$  (bond strength 8.3 eV) and so is not removable by heating without damaging the SiOCH.[1] On the other hand, physisorbed hydrogen bonded H<sub>2</sub>O can be driven out from the SiOCH with heating to 200-300 C without damaging the substrate.[1] The water uptake after Ar/O<sub>2</sub> plasma exposure is roughly half chemisorbed and half physisorbed. After He/H<sub>2</sub> plasma exposure, the majority is chemisorbed. The higher volume of water addition after Ar/O<sub>2</sub> treatment than He/H<sub>2</sub> treatment is because  $-\text{CH}_3$  groups are more lost in the first treatment compared to the second. The more reactive nature of O<sub>2</sub> plasmas is primarily responsible for such increase in  $-\text{CH}_3$  consumption in Ar/O<sub>2</sub> plasmas. Since  $-\text{CH}_3$  removal from  $-\text{SiO}_2\text{-CH}_3$  is the precondition for water uptake or  $-\text{SiO}_2\text{-OH}$  formation, the amount of water adsorbed is directly related to the number of  $-\text{CH}_3$  groups lost. As such, for more etching of  $-\text{CH}_3$  groups in Ar/O<sub>2</sub> plasmas than He/H<sub>2</sub> cleaning, Ar/O<sub>2</sub> cleaned profile adsorbed more water than He/H<sub>2</sub> cleaned profile.

With the increase in  $V_W$ , the increase in dielectric constant following Ar/O<sub>2</sub> plasma cleaning is 2.5 to 5.5 for Ar/O<sub>2</sub> clean and; and 2.5 to 3.5 for He/H<sub>2</sub> plasma cleaning. The proportion of this increase which is apportioned between chemisorbed –SiO<sub>2</sub>-OH and hydrogen bonded –H<sub>2</sub>O is shown in Fig. 6.3c. About 60% of the increase in the dielectric constant (to 4.5) following Ar/O<sub>2</sub> plasma exposure is attributable to chemisorption. The remaining increase is due to hydrogen bonded –H<sub>2</sub>O, which is in principle reversible by heating. Of the increase in  $k$  to 3.5 for He/H<sub>2</sub> plasma cleans, the increase attributable to –SiO<sub>2</sub>-OH is to 3.25. As such, the irreversible increase in  $k$  rise is only 0.25.

We deposited a  $\approx 10$  nm thick CF<sub>x</sub> polymer layer on the top surface of SiOCH using a capacitively coupled plasma sustained in an Ar/C<sub>4</sub>F<sub>8</sub>/O<sub>2</sub> = 80/15/5 mixture at 40 mTorr, as shown in Fig. 6.1b and Fig. 6.4a. The conditions are the same as in Chapter 5 except at a lower bias to prevent etching. The polymer layer was then removed with a 20 s short exposure to either the Ar/O<sub>2</sub> and or He/H<sub>2</sub> plasmas. The short cleaning was long enough to clean the polymer layer but not long enough to produce deep damage into the SiOCH by diffusion of radicals to enable investigation of the surface layers. However, a flux of  $10^{16}$  cm<sup>-2</sup>s<sup>-1</sup> photons from the plasmas produces Si-C bond scission deeper into the SiOCH than plasma damage produced by O or H radicals. Later, during lengthy humid air exposure, H<sub>2</sub>O molecules can etch adsorbed •CH<sub>3a</sub> and passivate the –SiO<sub>2</sub>• free radical sites to form –SiO<sub>2</sub>-OH-(H<sub>2</sub>O) as shown in Fig. 6.4, which increases the dielectric constant  $k$ . This is an example of where photon penetration into the SiOCH, even in the absence of further reactions with radicals from the plasma, can lead to *low-k* degradation by humid air exposure.

#### 6.4 Low $k$ Integrity by Pore Sealing

We investigated the consequences on water uptake of pore sealing using Ar/NH<sub>3</sub>

plasmas in preserving low- $k$  integrity.[16-18, 24] The procedure and processes for pore sealing using Ar/NH<sub>3</sub> plasmas is discussed in Sec. 6.2 and Ref. [24]. After an Ar/O<sub>2</sub> plasma clean, we treated the SiOCH with a He plasma for  $\approx 30$  s to activate surface sites (Reaction 6.27-6.30) and then to an Ar/NH<sub>3</sub> plasma for 30s to seal the pores (Reaction 6.31-6.35). Ar/O<sub>2</sub> treated SiOCH profiles after surface activation and sealing are shown in Fig. 6.5a. Surface pore blocking olive-green sites in Fig. 6.5a are Si-N and C-N compounds which are formed during NH<sub>3</sub> plasma sealing. For He/H<sub>2</sub> plasma cleaning of the polymers, the photons and He<sup>+</sup> present in the plasma were able to activate the surface. Its important to note that He/H<sub>2</sub> cleaning plasmas have all the species present in He plasma which are required for surface activation (Reaction 6.27-6.31) to prepare the surface for the sealing. Moreover, He/H<sub>2</sub> plasmas have energetic H atoms which are capable of abstracting H from  $-\text{SiO}_2(\text{CH}_n)$  producing  $-\text{SiO}_2(\text{CH}_{n-1})\bullet$  with dangling bonds (Reaction 6.31 and also discussed in detail in Chapter 5). As such, He/H<sub>2</sub> cleaning will activate the surface during polymer cleaning so a successive He plasma treatment after He/H<sub>2</sub> cleaning is unnecessary (unlike the Ar/O<sub>2</sub> clean). Therefore, we used the Ar/NH<sub>3</sub> sealing plasma treatment right after He/H<sub>2</sub> cleaning for the pore sealing. The Ar/NH<sub>3</sub> sealing plasma after He/H<sub>2</sub> cleaning formed C-N and Si-N compounds to seal surface pores, shown in Fig. 6.5b. For Ar/O<sub>2</sub> cleaning, the Ar/NH<sub>3</sub> plasma sealed  $\approx 70\%$  of the surface pores, while for He/H<sub>2</sub> plasma cleaning  $\approx 90\%$  of the surface pores were sealed.

After pore sealing by the Ar/NH<sub>3</sub> plasma, Si-N and C-N compounds which bridge the pore openings block the pathways through which water molecules diffuse to enter the Si-OCH. As such, after sealing, the volume of water adsorbed in the SiOCH when using both of the cleaning methods, as shown in Fig. 6.5, was minimal. As a result, the low- $k$  degradation

after pore sealing was not significant, as shown in Fig. 6.6. The dielectric constant increased from 2.5 to no more than 2.7 for both of the cleaning methods. The small increase in the  $k$ -value resulted from incomplete sealing as the C-N and Si-N compounds are unable to bridge all of the pore openings. Although the average pores size is 0.8 nm which is sealable by this method, the statistical variation in pore size produces some pores having sizes that exceed the sealable limit (about 1.1 nm). Also, during cleaning of polymers, the plasmas remove  $-CH_3$  groups from surface pore-entrance which enlarge the pore opening. As a result, there are a few pores (in this case, about 30% for Ar/O<sub>2</sub> clean and 10 % for He/H<sub>2</sub> clean) which remain unsealed which provide a pathway for H<sub>2</sub>O molecules to diffuse into the SiOCH.[24] This effect will become more severed as the pore size increase and the fraction of pores that are sealed decreases.

## 6.5 Comparison with Experimental Trends

The details of water uptake and increase in dielectric constant following humid air exposure of plasma damaged SiOCH depend on the precise processing steps and properties of the SiOCH (e.g., structure, porosity, interconnectivity). As a result, direct comparisons with experiments are difficult. However, trends from the experiments are useful for qualitative validation of the model. The general trends observed in experiments are that oxygen containing plasma exposure of SiOCH followed by exposure to air can produce significant increases in the  $k$ -value of the SiOCH. For example, Maex et al [1] exposed SiOCH to an O<sub>2</sub> plasma (300 mTorr, rf power 300 W, 300 °C) for 9 min long O<sub>2</sub>, and upon exposure to air (humidity not specified), the  $k$ -value increased from 2 to 20.[1] This is a larger increase that we predict, perhaps attributable to the elevated substrate temperature during plasma expo-

sure, 300 C, which may accelerate S-C bond scission by O atoms. Our computed trends of more water uptake following Ar/O<sub>2</sub> plasma exposure compared to He/H<sub>2</sub> plasma exposure correlate with experimental observations of damage in these systems. C depletion in Ar/O<sub>2</sub> plasmas, which is the precursor to water adsorption, is 3-5 times more severe compared to He/H<sub>2</sub> plasmas.[8] Urbanowicz et al. found that He plasma pretreatment followed by a NH<sub>3</sub> plasma was able to seal SiOCH pores to sufficient degree to block water uptake from humid air – no low-*k* degradation was observed.[17] We also found after plasma sealing, for both of the cleaning methods, the uptake of water was insignificant.

It has been reported, for a porous film of  $\approx 30\%$  porosity, adsorbed water volume percentage at first increases with increase in humidity for a humidity range of 0-15% and then the rate of increase slows down when water volume is  $>10\%$ . [29] We varied the humidity for a range 0-7.5% and found the water volume first rises and then settle down at  $\approx 7.25\%$  as shown in Fig. 6.7a. In literature, for a humidity of 0-10%, the dielectric constant of the low *k* became  $> 4$ . [29] In our model, the *k* increased from 2.55 to 5.55 for the humidity range of 0-7.5% (shown in Fig. 6.7b). As shown in the plots of Ref. 29, the relationships for water volume and *k* with increase in humidity is initially linear but later rise in water volume and *k* slow down with increase in humidity which agrees with our observations that surface pore blocking by  $-\text{SiO}_2\text{-OH-H}_2\text{O}$  compounds may eventually limit the amount of water uptake and *k* degradation.

## 6.6 Concluding Remarks

Low-*k* degradation by humid air after Ar/O<sub>2</sub> and He/H<sub>2</sub> plasma cleaning of porous

SiOCH was investigated. Both of these cleans can remove hydrophobic  $-\text{CH}_3$  groups from  $-\text{SiO}_2-\text{CH}_3$  compounds exposing  $-\text{SiO}_2$  to  $\text{H}_2\text{O}$  molecules coming from humid air that increases  $k$  value by forming  $-\text{SiO}_2-\text{OH}$  which later adsorbs another  $\text{H}_2\text{O}$  molecule to form  $-\text{SiO}_2-\text{OH}-\text{H}_2\text{O}$ . While hydrogen bonded  $\text{H}_2\text{O}$  can be removed applying a moderate temperature (200-300 C), the rise of  $k$  because of  $-\text{SiO}_2-\text{OH}$  formation cannot be reversed because Si-OH is tightly bonded. A cleaning such as He/ $\text{H}_2$  that etches  $-\text{CH}_3$  groups not so severely compared to Ar/ $\text{O}_2$  plasmas will adsorb less amount of water and degrade the  $k$  value less aggressively. If a short exposure of these cleaning plasmas is used, the reactive radicals do not have enough time to etch  $-\text{CH}_3$  groups significantly but photons were able to cause Si-C bond scission to create adsorbed  $-\text{CH}_{3a}$  group which is separated from Si. As such, even after a short exposure,  $\text{H}_2\text{O}$  of humid air will etch  $-\text{CH}_{3a}$  as  $\text{CH}_4$ . A sealing layer formation by  $\text{NH}_3$  plasma exposure can form a thin layer of Si- $\text{NH}_x$  and C- $\text{NH}_x$  compounds that can prevent water from entering the network. Such a sealing layer can preserve the low- $k$  integrity by blocking water uptake.

## 6.7 Figures

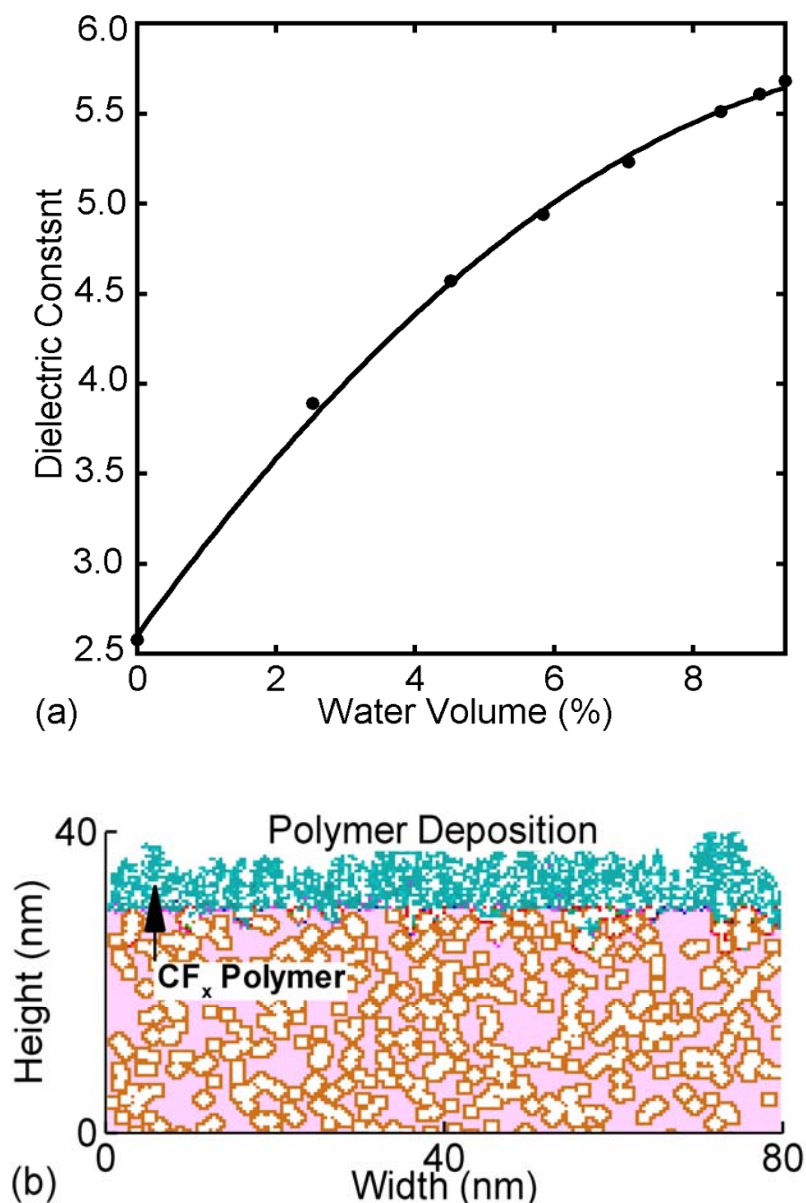


Fig. 6.1 Computed dielectric constant of the porous low- $k$  as a function of water volume and polymer deposited low- $k$  profile used for the investigation of low- $k$  degradation. (a) Relationship between adsorbed water volume in the low- $k$  and overall dielectric constant. (b) Porous SiCOH with deposited CF<sub>x</sub> polymer at the top to investigate the  $k$  degradation for such polymer cleaning in Ar/O<sub>2</sub> and He/H<sub>2</sub> plasmas. (Color coding: light pink – SiO<sub>2</sub>; brown – CH<sub>3</sub>; cyan – CF<sub>x</sub> polymers.)

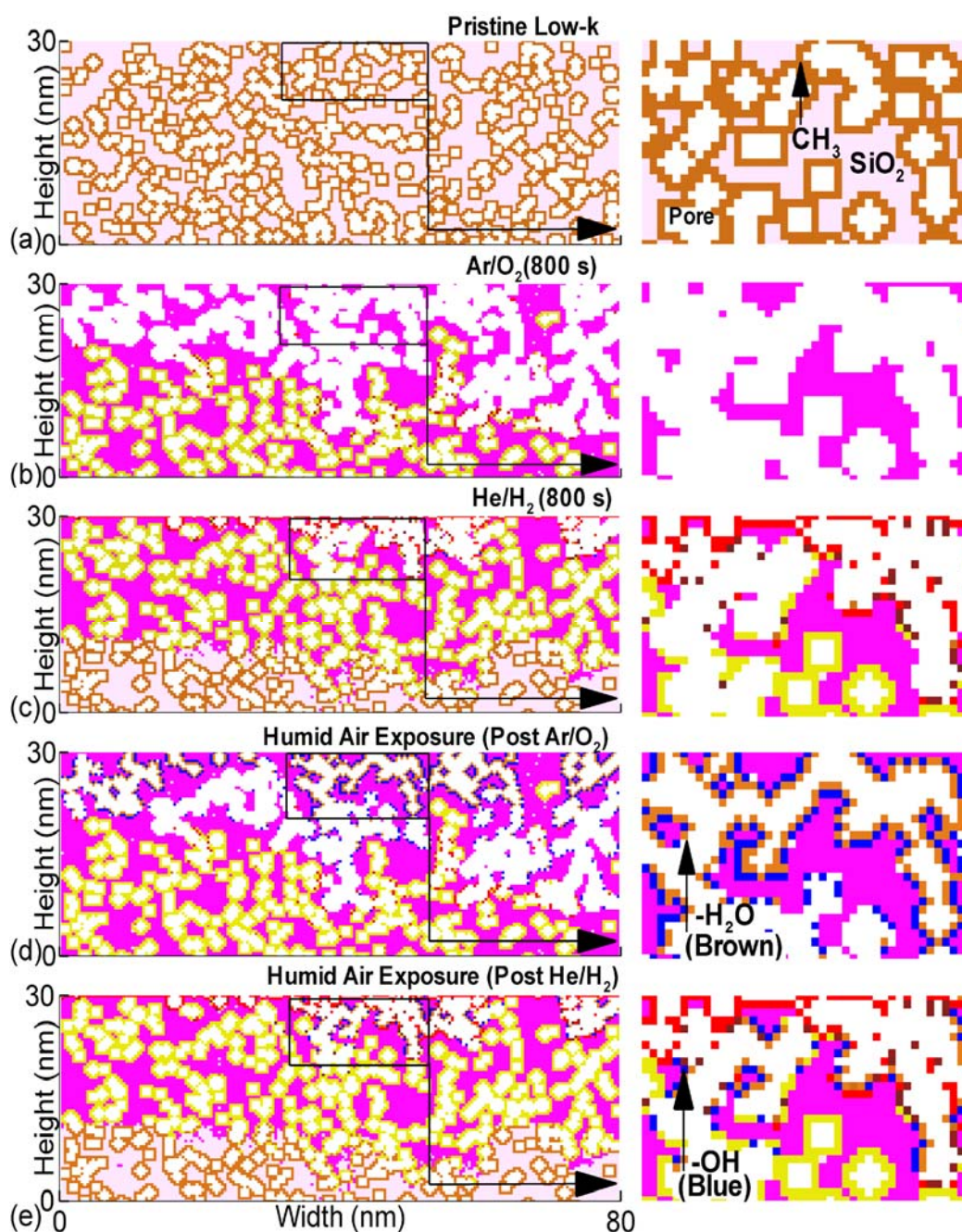


Fig. 6.2 Demethylation in porous low- $k$  SiOCH during Ar/O<sub>2</sub> and He/H<sub>2</sub> plasma treatment and water uptake following the treatments. (a) Pristine porous SiCOH. (b) After 800s treatment of Ar/O<sub>2</sub> plasmas. (c) After 800s He/H<sub>2</sub> plasma treatment. (d) The Ar/O<sub>2</sub> treated profile after 120s exposure in 2% humid air. (e) He/H<sub>2</sub> treated profile after 120s exposure in 2% humid air. -CH<sub>3</sub> lost SiO<sub>2</sub> sites adsorbed water when exposed to humid air and formed -SiO<sub>2</sub>-OH-H<sub>2</sub>O. (Color coding: light pink - SiO<sub>2</sub>; brown (not attached to blue sites) -CH<sub>3</sub>; bright pink - cleaved SiO<sub>2</sub>\*; olive - •CH<sub>3a</sub> sites after Si-C scission; blue -OH; brown (attached to blue -OH sites) - hydrogen bonded -H<sub>2</sub>O.)

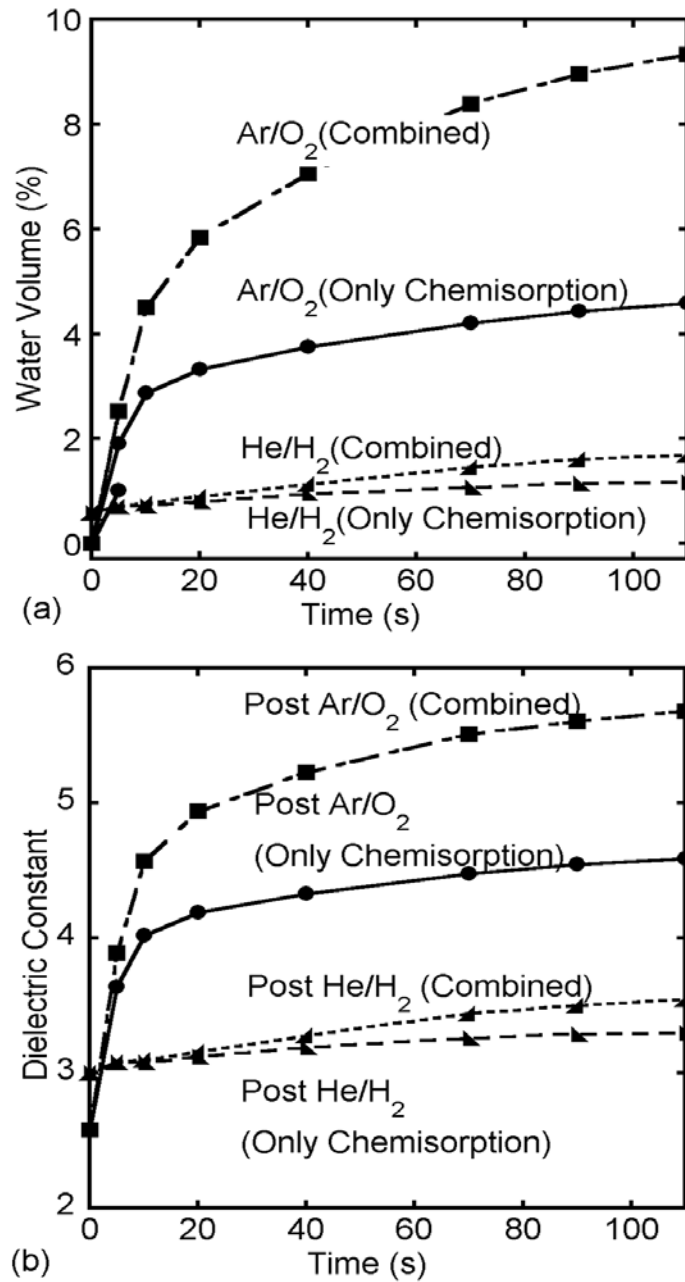


Fig. 6.3 Classification of adsorbed water in the low- $k$  based on if such water adsorption causes reversible or irreversible  $k$  increase. (a) Adsorbed water volume after cleaning as a function of time. (b) Increase in dielectric constant  $k$  as a function of time because of  $-\text{SiO}_2\text{-OH-H}_2\text{O}$  formation. Chemisorbed water is  $-\text{OH}$  while  $-\text{H}_2\text{O}$  part is hydrogen bonded. Hydrogen bonded  $\text{H}_2\text{O}$  can be removed by applying  $\sim 300\text{C}$  but  $-\text{OH}$  removal requires  $>400\text{C}$  which will make porous low- $k$  unstable. Increase in water volume and  $k$  slows down with time as  $-\text{SiO}_2\text{-OH-H}_2\text{O}$  compounds block the pore openings.

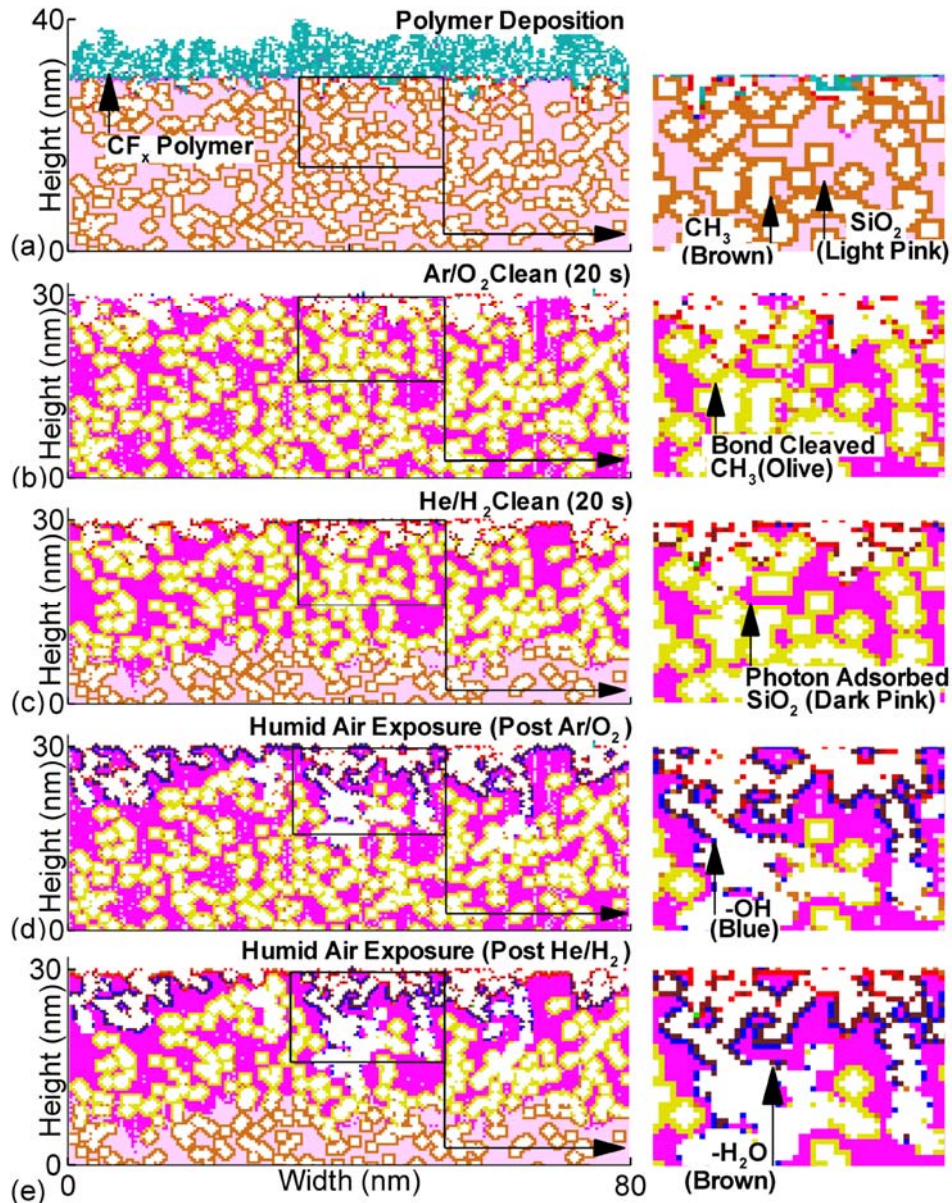


Fig. 6.4  $\text{CF}_x$  polymer cleaning from flat porous low- $k$  with a cleaning plasma; the cleaning time was not long enough to etch  $-\text{CH}_3$  group significantly but photons in the plasmas caused Si-C bond scission to generate Si-C bond cleaved and adsorbed  $\bullet\text{CH}_{3a}$  sites. (a) Deposited  $\text{CF}_x$  polymer on top of porous  $\text{SiCOH}$ . (b)  $\text{CF}_x$  polymer removal with 20 s  $\text{Ar}/\text{O}_2$  cleaning. (c)  $\text{CF}_x$  polymer removal with 20 s  $\text{He}/\text{H}_2$ . (d) Post  $\text{Ar}/\text{O}_2$  cleaned low- $k$  with 120 s of 2% humid air exposure. (e) Post  $\text{He}/\text{H}_2$  cleaned low- $k$  with 120 s of 2% humid air exposure. When low- $k$  was exposed to humid air,  $\text{H}_2\text{O}$  molecules of the air first etched bond cleaved and adsorbed  $\bullet\text{CH}_{3a}$  sites and later reacted with  $-\text{CH}_3$  free  $\text{SiO}_2$  sites to produce  $\text{SiO}_2\text{-OH-H}_2\text{O}$  which degraded the  $k$  value. (Color coding: light pink –  $\text{SiO}_2$ ; brown (not attached to blue sites)  $-\text{CH}_3$ ; bright pink – cleaved  $\text{SiO}_2^*$ ; olive –  $\bullet\text{CH}_{3a}$  sites after Si-C scission; blue –  $-\text{OH}$ ; brown(attached to blue  $-\text{OH}$  sites) – hydrogen bonded  $-\text{H}_2\text{O}$ ; cyan –  $\text{CF}_x$  polymers.)

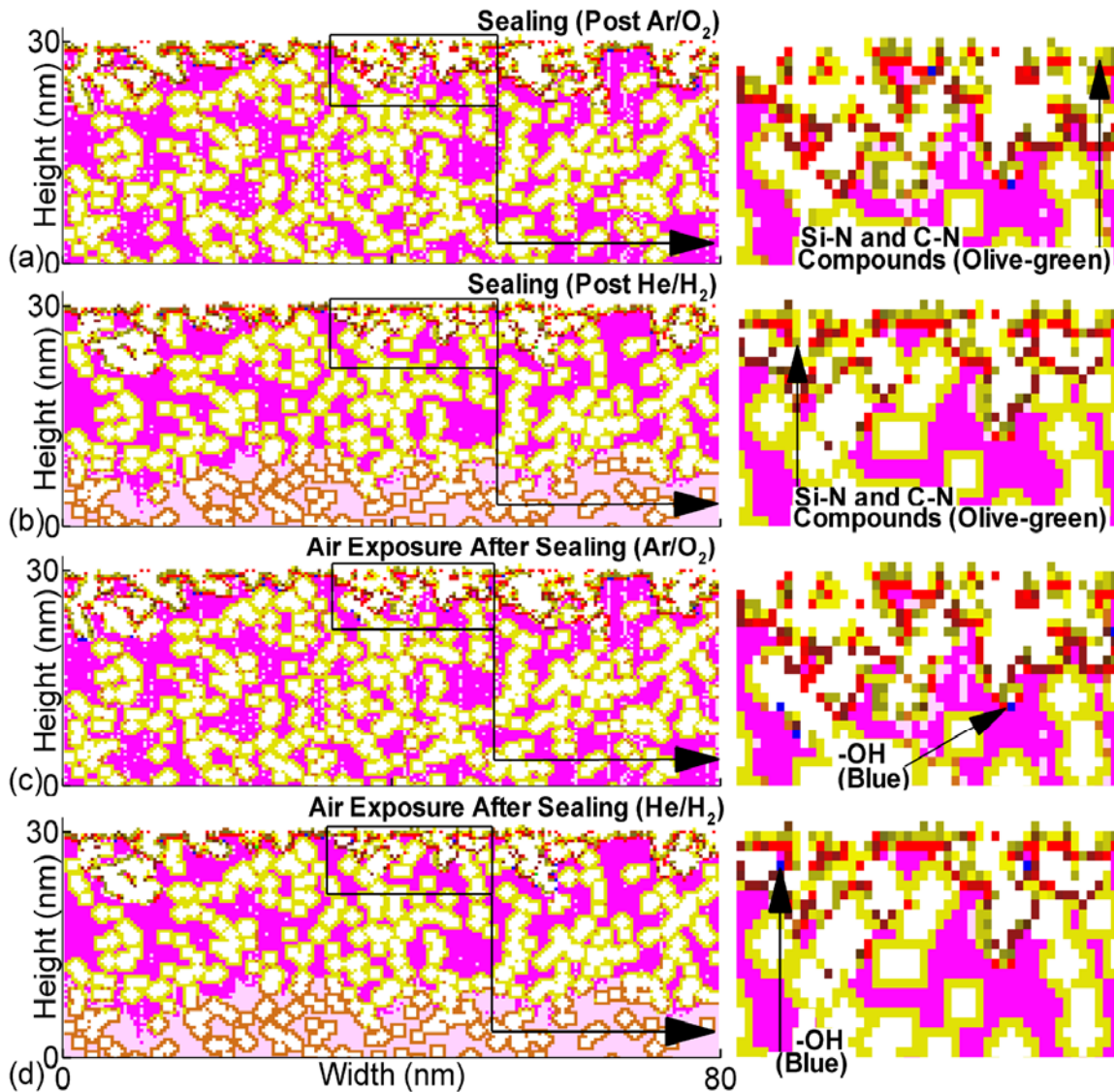


Fig. 6.5 Preservation of the integrity of the low- $k$  by surface pore sealing with Ar/NH<sub>3</sub> plasmas. (a) NH<sub>3</sub> plasma sealed Ar/O<sub>2</sub> cleaned profile where a 30s He plasma pre-treatment was used for surface activation before the sealing step. (b) NH<sub>3</sub> plasma sealed He/H<sub>2</sub> cleaned profile. (c) Ar/O<sub>2</sub> cleaned, He activated and NH<sub>3</sub> sealed profile after 120s of 2% humid air exposure. (d) NH<sub>3</sub> sealed He/H<sub>2</sub> cleaned profile after 120s of 2% humid air exposure. Ar/O<sub>2</sub> plasma cleaned profile needs the He treatment before sealing but He/H<sub>2</sub> plasma clean can itself activate the surface during the cleaning so no separate He pretreatment was required before sealing. After sealing, most of the pore openings in the surface were blocked by Si-N or C-N compounds and no significant water uptake was observed (blue sites indicate -OH) during humid air exposure. (Color coding: light pink – SiO<sub>2</sub>; brown (not attached to blue sites) – CH<sub>3</sub>; bright pink – cleaved SiO<sub>2</sub>\*; olive – •CH<sub>3</sub><sub>a</sub> sites after Si-C scission; blue -OH; brown(attached to -OH blue sites) – hydrogen bonded -H<sub>2</sub>O; cyan – CF<sub>x</sub> polymers; olive-green (near porous surface) – Si-N and C-N compounds responsible for pore sealing.)

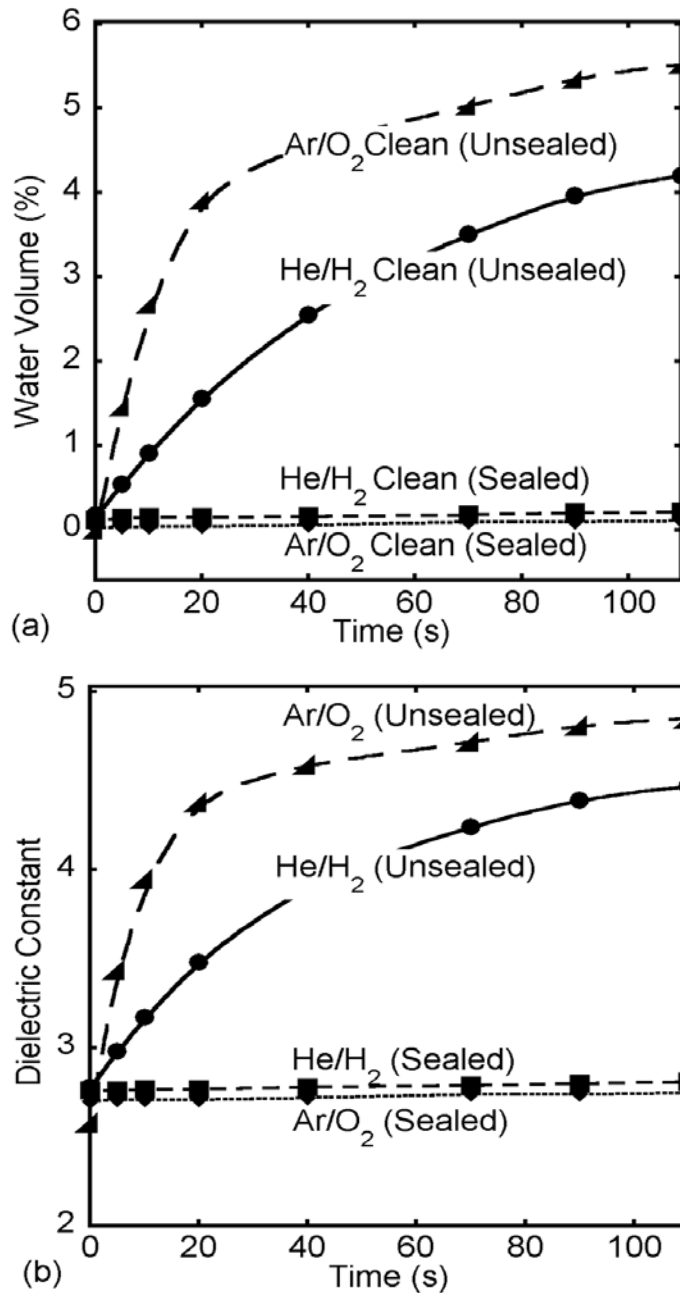


Fig. 6.6 Water uptake and  $k$  degradation by humid air in post-cleaned low- $k$  for sealed and unsealed low- $k$ . (a) Adsorbed water volume for sealed and unsealed low- $k$  when exposed to humid air after the 20s polymer cleaning. (b) Degradation of low- $k$  with time for sealed and unsealed profile as the 20s cleaned low- $k$  was exposed to humid air.  $\text{NH}_3$  plasma sealing was able to block the pathways needed for the diffusion of  $\text{H}_2\text{O}$  molecules of humid air; there was no significant water uptake and no significant low- $k$  degradation after sealing.

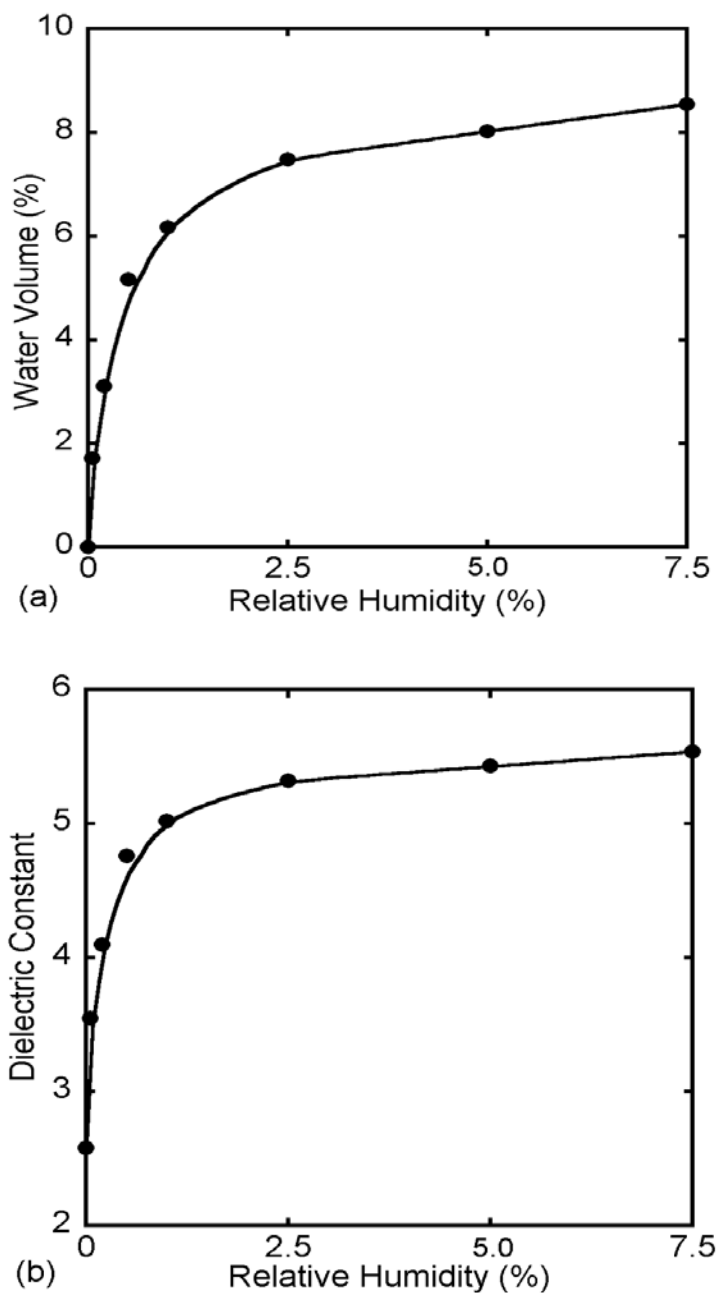


Fig. 6.7 Low- $k$  degradation as a function of humidity when 800s Ar/O<sub>2</sub> treated low- $k$  was exposed to air with variable relative humidity. (a) Adsorbed water volume in the post Ar/O<sub>2</sub> treated low- $k$  as a function of humidity, (b) low- $k$  degradation as a function of humidity. Both water volume and  $k$  increases linearly with humidity initially and then both of them slow down because of the blocking of pore-openings by  $-\text{SiO}_2\text{-OH-H}_2\text{O}$  compounds.

## 6.8 References

1. K. Maex, M. Baklanov, D. Shamiryman, F. Iacopi, S. H. Brongersma, K. Maex, and Z. S. Yanovitskaya, *J. Appl. Phys.* **93**, 8793 (2003).
2. M. R. Baklanov, K. P. Mogilnikov, and Q. T. Le, *Microelectron. Eng.* **83** 2287 (2006).
3. G. Mannaert, M. R. Baklanov, Q. T. Le, Y. Travaly, W. Boullart, S. Vanhaelemeersch, and A. M. Jonas *J. Vac. Sci. Technol. B* **23**, 2198 (2005).
4. H. Seo, S. B. Kim, J. Song, Y. Kim, H. Soh, Y. C. Kim, and H. Jeon, *J. Vac. Sci. Technol. B* **20**, 1548 (2002).
5. K. Sakuma, K. Machida, K. Kamoshida, Y. Sato, K. Imai, and E. Arai, *J. Vac. Sci. Technol. B* **13**, 902 (1995).
6. M. A. Hartney, D. W. Hess, and D. S. Soane, *J. Vac. Sci. Technol. B* **7**, 1 (1989).
7. D. Shamiryman, M. R. Baklanov, S. Vanhaelemeersch, and K. Maex, *J. Vac. Sci. Technol. B* **20**, 1923 (2002).
8. M. A. Worsley, S. F. Bent, S. M. Gates, N. C. M. Fuller, W. Volksen, M. Steen and T. Dalton, *J. Vac. Sci. Technol. B* **23**, 395 (2005).
9. K. Vanstreels, and A. M. Urbanowicz, *J. Vac. Sci. Technol. A*, **28**, 173 (2010).
10. J. R. Woodworth, M. E. Riley, V. A. Amatucci, T. W. Hamilton, and B. P. Aragon, *J. Vac. Sci. Technol. A* **19**, 45 (2001).
11. B. Jinnai, S. Fukuda, H. Ohtake, and S. Samukawa, *J. Appl. Phys.* **107**, 043302 (2010).
12. J. Lee and D. B. Graves, *J. Phys. D* **43**, 425201 (2010).
13. H. Shi, J. Bao, R. S. Smith, H. Huang, J. Liu, P. S. Ho, M. L. McSwiney, M. Moinpour, and G. M. Kloster, *Appl. Phys. Lett.* **93**, 192909 (2008).
14. J. Proost, E. Kondoh, G. Vereecke, M. Heyns, and K. Maex, *J. Vac. Sci. Technol. B* **16**,

- 2091 (1998).
15. J. Proost, M. Baklanov, K. Maex, and L. Delaey, *J. Vac. Sci. Technol. B* **18**, 303 (2000).
  16. M. Urbanowicz, M. R. Baklanov, J. Heijlen, Y. Travalay, and A. Cockburn, *Electrochem. Solid-State Lett.* **10**, G76 (2007).
  17. A. M. Urbanowicz, D. Shamiryan, A. Zaka, P. Verdonck, S. De Gendt and M. R. Baklanov, *J. Electrochem. Soc.* **157**, H565 (2010).
  18. F. N. Dultsev, A. M. Urbanowicz, and M. R. Baklanov, *Mater. Res. Soc. Symp. Proc. Vol. 1079* © 2008 Materials Research Society 1079-N07-03.
  19. H.-G. Peng, D.-Z. Chi, W.-De Wang, J.-H. Li, K.-Y. Zeng, R. S. Vallery, W. E. Frieze, M. A. Skalsey, D. W. Gidley, and A. F. Yee, *J. Electrochem. Soc.* **154**, G85 (2007).
  20. J. Shoeb and M. J. Kushner, "Damage by Radicals and Photons during Cleaning of Porous Low-*k* SiOCH Part I: Demethylation in Ar/O<sub>2</sub> and He/H<sub>2</sub> Plasmas".
  21. M. J. Kushner, *J. Phys. D* **42**, 194013 (2009).
  22. A. Agarwal and M. J. Kushner, *J. Vac. Sci. Technol. A* **27**, 37 (2009).
  23. A. Sankaran and M. J. Kushner, *J. Vac. Sci. Technol. A* **22**, 1242 (2004).
  24. J. Shoeb and M. J. Kushner, *J. Vac. Sci. Technol. A* **29**, 051305 (2011).
  25. O. V. Braginsky, A. S. Kovalev, D. V. Lopaev, E. M. Malykhin, Yu. A. Mankelevich, T. V. Rakhimova, A. T. Rakhimov, A. N. Vasilieva, S. M. Zyryanov, and M. R. Baklanov, *J. Appl. Phys.* **108**, 073303 (2010).
  26. M.F.A.M. Van Hest, A. Klaver, D.C. Schram, and M.C.M. Van De Sanden, *Thin Solid Films* **449** 40 (2004).

27. M. Chaudhari, J. Du, S. Behera, S. Manandhar, S. Gaddam, and J. Kelber, *Appl. Phys. Lett.* **94**, 204102 (2009).
28. K. Singh, A. A. Kumbhar, and R. O. Dusane, *Materials Letters* **60** 1579 (2006).
29. T. Kikkawa, S. Kuroki, S. Sakamoto, K. Kohmura, H. Tanaka, and N. Hata, *Journal of The Electrochemical Society*, **152(7)**, G560 (2005).

## 7. MECHANISMS FOR PLASMA ETCHING OF HfO<sub>2</sub> GATE-STACKS WITH Si SELECTIVITY AND PHOTORESIST TRIMMING

### 7.1 Introduction

SiO<sub>2</sub> has long served as the gate insulator for field-effect-transistors in very-large-scale integrated circuits.[1] As feature sizes decrease, the gate-silicon dioxide equivalent thickness required for the insulator also decreases.[2] A larger oxide capacitance (thinner oxide layer) is necessary to invert the surface to a sufficient sheet charge density to obtain the desired transistor current for a given supply voltage. Continuing to reduce the insulator thickness using SiO<sub>2</sub> is problematic as leakage currents due to tunneling increase as the thickness approaches a monolayer.[1] Consequently, high dielectric constant (*high-k*) metal oxides, and HfO<sub>2</sub> in particular, are being implemented as replacements for SiO<sub>2</sub> in gate-stacks to minimize leakage current resulting from thinning of the insulator. The larger dielectric constant allows the oxide to be thicker for a given capacitance, thereby decreasing electric fields and leakage currents.

A *high-k* dielectric and a poly-Si gate are typically not suitable for high performance logic as the combination has a higher threshold voltage and lower channel mobility, and so a poor drive current.[1] Metal gates, having a higher free carrier density, maintain a high mobility at junctions with *high-k* dielectrics and so many advanced designs incorporate metal gates.[1] TiN is one such metal being considered for the gate.[3] Given other technology requirements, such as back-anti-reflection coatings (BARC) to maintain critical dimensions (CD) during lithography, the gate-stack prior to etching can contain many layers and materials, as schematically shown in Fig. 7.1.

To speed the plasma processing of gate-stacks, it is desirable to etch the entire stack using a single process. This requires a high selectivity for the oxide, in this case  $\text{HfO}_2$ , with respect to the underlying Si layer. (That is, the  $\text{HfO}_2$  will be etched but the underlying Si will not be etched.) It has been found that similar gate-stacks can be etched using  $\text{BCl}_3/\text{Cl}_2$  plasmas while having a good selectivity to underlying Si by forming a  $\text{BCl}_n$  polymer on the Si which slows its etching.[4]

In this chapter, the plasma etching of  $\text{HfO}_2$  gate-stacks is computationally investigated with an emphasis on the selectivity between  $\text{HfO}_2$  and Si. The model gate-stack consists of photoresist (PR), BARC, TiN,  $\text{HfO}_2$ ,  $\text{SiO}_2$  and the underlying Si. (See Fig. 7.1.) This gate-stack is based on industrial test structures. Reaction mechanisms for etching of TiN and  $\text{HfO}_2$  were developed for plasmas sustained in Ar/ $\text{BCl}_3/\text{Cl}_2$  mixtures. Trimming of the PR to achieve narrower linewidths was also addressed. The Hybrid Plasma Equipment Model (HPEM) was employed to simulate the reactor scale and surface kinetics for inductively and capacitively coupled plasma tools. The model reactor is an inductively coupled plasma (ICP) having a radio frequency (rf) bias on the substrate. The mechanisms were then implemented in the Monte Carlo Feature Profile Model (MCFPM) with which etch profiles are predicted. Validation was performed with data from literature.

We found that  $\text{BCl}_n$  species produced by electron impact in the plasma react with  $\text{HfO}_2$ , which, under ion impact, form volatile etch products such as  $\text{B}_m\text{OCl}_n$  and  $\text{HfCl}_n$ . Selectivity to Si is achieved by creating Si-B bonding as a precursor to the deposition of a  $\text{BCl}_n$  polymer, which slows the etch rate relative to  $\text{HfO}_2$ . The low ion energies required to achieve this selectivity then challenge one to obtain highly anisotropic profiles in the metal gate portion of the stack.

The models used in this investigation are briefly described in Sec. 7.2, followed by a discussion of the reaction mechanisms in Sec. 7.3. Photoresist trimming and BARC etching are discussed in Sec. 7.4. Plasma properties and  $\text{HfO}_2$  etch characteristics are discussed in Sec. 7.5 followed by our concluding remarks in Sec. 7.6.

## 7.2 Description of the Models

The HPEM was used to predict the reactor scale plasma characteristics and reactant fluxes to surfaces in the ICP reactor. The HPEM has been previously described and so is only briefly summarized here.[5] The HPEM is a two-dimensional (2d), modular model which addresses gas phase and surface kinetics. Electromagnetic fields are derived by solving the frequency domain wave equation based on coil currents adjusted to deliver a specified power deposition. The spatially dependent power deposition is used as a source term in obtaining the electron temperature,  $T_e$ , from an electron energy conservation equation. Transport and rate coefficients as function of average electron energy are obtained from a solution of Boltzmann's equation, and a Monte Carlo simulation is used to follow the trajectories of sheath accelerated secondary electrons. The transport coefficients and source functions are used by the fluid kinetics module (FKM) to solve separate continuity, momentum, and energy equations for each ion and neutral species, while semi-implicitly solving Poisson's equation for the time varying electrostatic potential. The densities and electrostatic fields from the FKM are then transferred to the other modules. This process is iterated until a converged quasi-steady state solution is obtained.

Reaction probabilities for gas phase species with surfaces are provided by the surface chemistry module (SCM) which computes the composition of surface resident species using

a multilayer surface-site-balance model. The reaction mechanism is unique for each surface in contact with the plasma. The plasma chemistry Monte Carlo module (PCMCM) produces the energy and angular distributions for neutrals and ions striking surfaces in contact with the plasma. The PCMCM launches pseudoparticles representing ions and neutrals based on the electron impact source functions. Using time dependent electric fields from the FKM, their trajectories are integrated while accounting for gas phase collisions. The energy and angular distributions (EADs) of ion (IEADs) and neutral pseudoparticles are recorded as they strike surfaces.

The SCM and MCFPM incorporate energy dependent reaction probabilities based on the EADs obtained from the PCMCM. The probabilities for surface reactions involving energetic species (either ions or hot neutrals) are given by [6]

$$p(E) = p_0 \frac{E^m - E_t^m}{E_r^m - E_t^m} \quad (7.1)$$

where  $p(E)$  is the reaction probability for a particle with energy  $E$ ,  $E_t$  is the threshold energy of the process,  $E_r$  is a reference energy, and  $p_0$  is the reaction probability at the reference energy. We used  $m = 0.5$  for sputtering or ion activated etching.

The 2d MCFPM has been previously described and so is briefly summarized here.[7] The MCFPM predicts the evolution of surface morphology and profiles based on the fluxes and EADs from the HPEM. The MCFPM resolves surface materials using a 2d rectilinear mesh where each cell in the mesh is assigned a material identity. Gas phase species are represented by pseudoparticles and surface species are represented by computational mesh cells.

Pseudoparticles are launched towards the surface from random locations above the wafer with energies and angles sampled from the EADs. The trajectories of the pseudoparticles are tracked until they hit a surface, where a generalized surface reaction mechanism controls the interaction. The identity of the material mesh cell is changed (representing a surface chemical reaction), removed (etching) or a cell is added (deposition) as dictated by the reaction mechanism. Gas phase pseudoparticles are reflected or emitted from the surface consistent with the mechanism.

The ICP reactor used in this study is schematically shown in Fig. 7.2(a). The cylindrical chamber is 13 cm in radius and 17 cm in height. The inductive power is supplied through a three-turn antenna coil above a 0.8-cm-thick quartz window. The wafer is on an independently powered substrate 9 cm below the quartz window. For gate-stack etching, the 300 W ICP was sustained in  $\text{Ar}/\text{BCl}_3/\text{Cl}_2 = 5/40/55$  at 5 mTorr with a flow rate of 100 sccm. The gas phase reaction mechanism is listed in Table 7.1. The wafer size used in this simulation was 150 mm, however, the etching mechanisms discussed here are independent of wafer size.

The *high-k* gate-stack used for the simulation, as shown in Fig. 7.1, consists of a 290 nm thick erodible photoresist mask, 40 nm thick BARC layer, 160 nm thick TiN, 20 nm  $\text{HfO}_2$ , 10 nm  $\text{SiO}_2$  (to improve carrier mobility in the channel) and the Si substrate. The substrate bias voltage was varied to investigate the effect of ion energy on the selectivity of  $\text{HfO}_2$  with respect to Si.[4,8] Extensive parameterizations were performed to determine the effects of the probabilities of polymer formation, polymer sputtering and Si-B bond formation on selectivity. Parameterizations were also performed to determine whether the proposed mechanism is sensitive to the device layout. For example, the default gate-stack pitch (the full dis-

tance between the center of gate-stacks) of 200 nm was decreased to 150 nm and increased to 300 nm. The scaling laws discussed here were insensitive to those variations.

### 7.3 Surface Reaction Mechanism for Gate-stack Etching

#### 7.3.1 Etching of HfO<sub>2</sub>

Previous investigations of the plasma etching of metal oxides were used to develop our reaction mechanism. Sha *et. al* investigated the etching of *high-k* ZrO<sub>2</sub> in BCl<sub>3</sub>/Cl<sub>2</sub> plasmas which shares many etch characteristics with HfO<sub>2</sub>. [8] They concluded that BCl<sub>2</sub><sup>+</sup> ions play an important role in removing O atoms from ZrO<sub>2</sub>, as volatile B<sub>2</sub>OCl<sub>4</sub>, B<sub>3</sub>O<sub>2</sub>Cl<sub>5</sub> and (BOCl)<sub>3</sub>. These processes, with the formation of a Si-B passivation layer, enabled a ZrO<sub>2</sub> to Si selectivity of 10 at ion energies near but above the threshold for ZrO<sub>2</sub> etching. They also found that in BCl<sub>3</sub>/Cl<sub>2</sub> plasmas, HfO<sub>2</sub> and ZrO<sub>2</sub> etch rates are dependent on the BCl<sub>2</sub><sup>+</sup> density that is responsible for O-atom removal, the Cl density which is responsible for Hf passivation to eventually remove Hf as HfCl<sub>n</sub> (n = 2-4), and on the bond strength of the metal-oxygen bond. [9] By operating with ion energies slightly above the etching threshold for the metal oxide, HfO<sub>2</sub> to Si selectivity can be obtained.

TaN/HfO<sub>2</sub> gate-stacks have been etched employing Ar/BCl<sub>3</sub>/O<sub>2</sub> plasmas to obtain high TaN/HfO<sub>2</sub> selectivity. [10] However with the presence of oxygen species in these plasmas, the Si-B passivation layer thought to be responsible for high HfO<sub>2</sub>/Si selectivity is difficult to maintain. This results in a lower HfO<sub>2</sub>/Si selectivity as compared to etching in Ar/BCl<sub>3</sub>/Cl<sub>2</sub> plasmas. Wang *et. al* investigated etching of HfO<sub>2</sub> and poly-Si in BCl<sub>3</sub> plasmas as a function of substrate temperature as a function of source power in a helicon reactor. [11] BCl<sub>2</sub> and Cl were found to be the dominant gas phase radicals at all powers investigated,

which is consistent with our findings. They found that selectivity of  $\text{HfO}_2$  over Si was enhanced at low power and low substrate temperature. Nakamura *et. al* etched  $\text{HfO}_2$  films in  $\text{BCl}_3$ -containing plasmas employing an electron cyclotron resonance (ECR) reactor without rf biasing.[12] For  $\text{BCl}_3/\text{Cl}_2 = 40/60$  mixtures, a  $\text{HfO}_2/\text{Si}$  selectivity of approximately 10 and an etch rate of 1000 Å/min were obtained. Our simulation results are in reasonable agreement with their findings.

When modeling plasma etching of new materials such as  $\text{HfO}_2$ , the fundamental experimental data base required to develop the mechanism is often fragmentary. When both mechanisms and rates are not available, modeling and developing a reaction mechanism begins with examining the current databases for experimental results for etch rates and selectivity, material thermodynamic properties, and mechanisms and reaction probabilities for analogous processes, as well as theoretical expressions for general scaling laws. Based on these analyses, a sequence of reactions is proposed and probabilities assigned for bond breaking, adsorption and etching reactions (that is, the mechanism is built). Extensive parameterizations and sensitivity analyses are then required to refine the mechanism to well represent the etch rates, threshold energies and selectivities available from the literature. This is done while acknowledging that there are always risk of uncertainties in building such a mechanism.

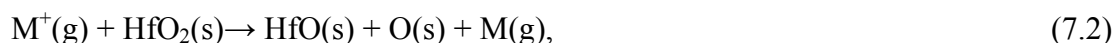
Following these procedures while benefiting from the insights provided by previous works, a mechanism was developed for etching  $\text{HfO}_2$  in  $\text{Ar}/\text{BCl}_3/\text{Cl}_2$  plasmas. In our mechanism the etching of  $\text{HfO}_2$  incorporates two distinct steps – removal of Hf and of O. While  $\text{Cl}_2$  plasmas can etch  $\text{HfO}_2$  forming volatile  $\text{HfCl}_n$  and  $\text{ClO}$  species as a result of Cl adsorption and ion impact, selectivity for  $\text{HfO}_2$  with respect to Si cannot necessarily be insured.[13]

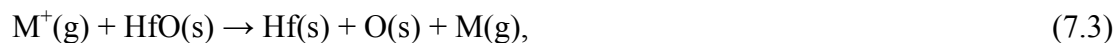
This is the fundamental motivation for using  $\text{BCl}_3/\text{Cl}_2$  plasmas. Electron impact dissociation of  $\text{BCl}_3$  produces  $\text{BCl}_n$  ( $n = 1,2$ ) species which have the ability to form volatile etch products such as  $\text{B}_2\text{OCl}_3$ ,  $\text{B}_2\text{OCl}_4$ ,  $\text{BOCl}$ ,  $(\text{BOCl})_3$  and  $\text{B}_3\text{O}_2\text{Cl}_5$ . These species also have the ability to inhibit Si etching through formation of a  $\text{BCl}_n$  polymer.

In our mechanism,  $\text{HfO}_2$  etching is initiated by the breaking of the Hf-O bonds, each having bond strength of approximately 8.3 eV. By analogy with other processes and through parametric studies, a threshold energy of 14 eV was assigned to the Hf-O bond breaking step. The first such process breaks one Hf-O bond in  $\text{HfO}_2$ , and so generates  $\text{HfO}(s)$  and  $\text{O}(s)$ , where (s) denotes a surface resident species. A second above threshold ion can break the remaining Hf-O bond in  $\text{HfO}(s)$  to produce  $\text{O}(s)$  and  $\text{Hf}(s)$ . The exposed  $\text{Hf}(s)$  sites are subsequently passivated by Cl to produce  $\text{HfCl}_n(s)$  ( $n = 1-4$ ) and ultimately a volatile etch product  $\text{HfCl}_n(g)$  following ion impact. (Note that at low temperatures,  $\text{HfCl}_4$  may be formed as a loosely adhered non-volatile product that requires ion activation for removal.)

Exposed  $\text{HfO}(s)$  sites are passivated by  $\text{Cl}(g)$  leading to the formation of  $\text{HfOCl}(s)$  and  $\text{HfOCl}_2(s)$ . The Hf atom in  $\text{HfOCl}(s)$  and  $\text{HfOCl}_2(s)$  can be removed in a single step by ion impact as volatile  $\text{HfCl}_n(g)$  leaving behind  $\text{O}(s)$  with a dangling bond on the surface. Although the probability is small,  $\text{Cl}(g)$  can adsorb on  $\text{HfO}_2(s)$  forming solids such as  $\text{HfO}_2\text{Cl}(s)$  and  $\text{HfO}_2\text{Cl}_2(s)$ . The first Hf-O bond in these species can be broken by ion bombardment producing nonvolatile  $\text{HfOCl}(s)$  and  $\text{HfOCl}_2(s)$ .

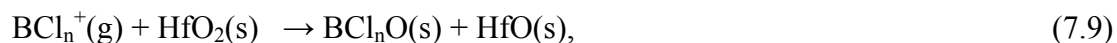
The full reaction mechanism for  $\text{Hf}(s)$  removal is listed in Table 7.2 and, in summary, is





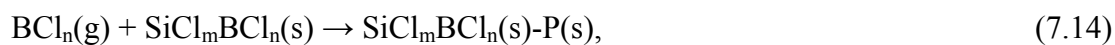
where  $M^+(g)$  represents an ion.

To remove bonded oxygen on the surface, the site can adsorb  $BCl_n(g)$  ( $n=1,2$ ) forming  $OBCl_n(s)$ . These complexes can then be removed by ion bombardment. The bonded oxygen can also be removed directly by  $BCl_n^+(g)$  ( $n=1,2$ ) bombardment as either as  $B_2OCl_4(g)$  or  $B_2OCl_3(g)$ . A second process for removing bonded O is initiated by  $BCl_n^+(g)$  directly striking  $HfO_2(s)$  producing  $OBCl_2(s)$  and  $OBCl(s)$ . The  $OBCl(s)$  can be etched by energetic ions as volatile  $BOCl(g)$ , and producing  $OBCl_2(s)$ . The latter can be removed by the previously described mechanism. The full reaction mechanism for O(s) removal is listed in Table 7.2 and in summary is



One of the motivations to include  $BCl_3$  in the gas mixture is to improve the selectivity for  $HfO_2$  with respect to Si. Formation of a  $BCl_n$  passivation layer on the Si is believed to play an important role in obtaining this selectivity by slowing the Si etch rate. The pas-

sivation layer is proposed to form in two steps. The first is forming Si-B bonds by adsorption of  $\text{BCl}_n$  to create a base layer. The second is polymer deposition by  $\text{BCl}_n(\text{g})$  on the base layer.[4]. The polymerization reaction mechanism is listed in Table 7.3, and is summarized as,

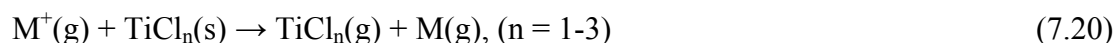
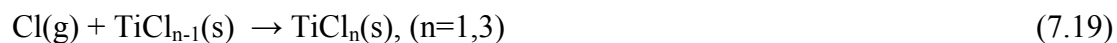


where  $\text{P}(\text{s})$  is the polymer and  $\text{P}^*(\text{s})$  is an activated state of the polymer generated by low energy ion bombardment with enhanced deposition rates. Although not strictly stoichiometrically correct, sputtering of the polymer produces  $\text{BCl}_2(\text{g})$  which can redeposit. As such there are two competing processes – higher ion energies increase the rate of etching of the  $\text{HfO}_2$  while also increasing the rate of sputtering of  $\text{P}(\text{s})$  on the Si which decreases selectivity.

### 7.3.2 TiN Etching

TiN(s) etching begins with ion bombardment to break the Ti-N bond and liberate N atoms. The Ti(s) site then adsorbs Cl(g) leading to the formation of  $\text{TiCl}_n(\text{s})$  ( $n= 1\text{-}3$ ). Ion bombardment removes these compounds as  $\text{TiCl}_n(\text{g})$ . [26] TiN(s) can itself adsorb Cl(g) to produce  $\text{TiNCl}(\text{s})$  followed by energetic ion bombardment containing Cl to directly remove

Ti from TiNCl(s) as volatile TiCl<sub>n</sub>(g). In an integrated gate-stack etching process, the PR may be trimmed and BARC removed in plasmas producing O atoms. When the TiN surface is exposed to both energetic ions and O atoms, Ti-N bond breaking followed by O atom adsorption can form nonvolatile TiO(s). When then etching the gate-stack in Ar/BCl<sub>3</sub>/Cl<sub>2</sub> plasmas, TiO(s) adsorbs Cl(g) forming TiOCl<sub>n</sub>(s) (n=1, 2). Ions striking these oxichlorides can then be removed as volatile TiOCl<sub>n</sub>(g) (n=1, 2) by ion bombardment. The reaction mechanism for TiN(s) etching is listed in Table 7.4 and is summarized as,



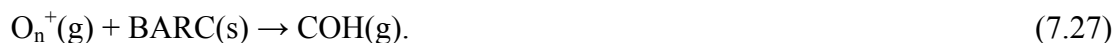
### 7.3.3 Photo-resist trimming, BARC etching and PR erosion

As gate length shrinks below 50 nm, 193 nm lithography is challenged to directly define the features.[27-29] Consequently, when the width of the PR line after lithography is larger than the desired dimensions, trimming of the PR is often employed. For organically based PR, controlled exposure to an O<sub>2</sub> containing plasma will etch back the PR to a smaller dimension. Such plasmas may also reduce the sidewall roughness of the PR. For example, Sin *et. al* investigated trimming of PR and etching of BARC in an integrated step employing CF<sub>4</sub>/O<sub>2</sub> plasmas.[26] The oxygen provided a high PR removal rate while the polymerizing CF<sub>4</sub> maintained a vertical PR/BARC profile after trimming.[27] Although the trim rate is higher for CF<sub>4</sub>/O<sub>2</sub> plasmas compared to Cl<sub>2</sub>/O<sub>2</sub> and HBr/O<sub>2</sub> plasmas, the amount of oxygen

found on the PR sidewall after trimming is higher.[28] In spite of its slow trim rate, precise control of the CD during trimming has been obtained using  $\text{Cl}_2/\text{O}_2$  plasmas. [28,29] It has also been shown that  $\text{Ar}/\text{O}_2$  plasmas generate a vertical and uniform PR profile with a high PR removal rate.[30]

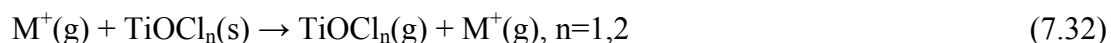
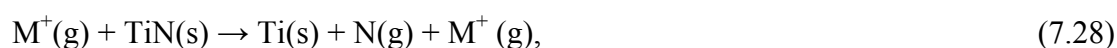
To simulate the full gate-stack etching process, we included a PR-trim step prior to exposure to the  $\text{Ar}/\text{BCl}_3/\text{Cl}_2$  plasma. The PR-trim step was performed in an  $\text{Ar}/\text{O}_2$  plasma which also served to remove the BARC layer. The intent of the trim process was to reduce the initial photo-resist having a height of 290 nm and width of 58 nm to a width of 32 nm.

As both BARC and PR are primarily hydrocarbons, they can be chemically etched by plasma produced oxygen species such as,  $\text{O}(\text{g})$ ,  $\text{O}^+(\text{g})$  and  $\text{O}_2^+(\text{g})$  and chemically sputtered by the ions. The reaction mechanism for  $\text{Ar}/\text{O}_2$  plasma etching of the organic PR and BARC is listed in Table 7.5, and is summarized as follows. (Note that  $\text{COH}(\text{g})$  is a *generic* PR and BARC etch product which can redeposit as a PR or BARC species but is otherwise unreactive in the plasma.)



If the BARC is completely cleared during the PR-trim, ions in the  $\text{Ar}/\text{O}_2$  plasma can

break Ti-N bonds to produce Ti(s) sites which then adsorb O(g) to produce TiO(s). During the gate-stack etch in Ar/BCl<sub>3</sub>/Cl<sub>2</sub> plasmas, the TiO(s) sites can further adsorb Cl(g) to produce TiOCl(s) and TiOCl<sub>2</sub>(s). Ions in the Ar/BCl<sub>3</sub>/Cl<sub>2</sub> plasma remove these species as volatile TiOCl(g) and TiOCl<sub>2</sub>(g). A summary of the reactions for TiO(s) and TiOCl<sub>n</sub>(s) (n = 1,2) formation and removal are (See Table 7.4),



There will be a tradeoff between fully removing the BARC and exposing the TiN to the oxygen plasma and leaving a thin BARC later that must be removed during the gate-stack etch.

The process conditions for the PR-trimming and BARC etching were 5 mTorr, Ar/O<sub>2</sub>=5/95 gas mixture with a flow rate of 100 sccm. The coil delivered 300 W at 10 MHz. A bias of 18 V was applied to the substrate. Probabilities for BARC and PR etching were varied to determine the values required to maintain an acceptable CD while also trimming the PR. It was found that when the BARC etch rate is 1.5 times higher than the PR etch rate, these goals are met. For example, post-trim gate-stack profiles with relative etching probabilities between the BARC and PR of 1.5, 1.0 and 0.5 are shown in Fig. 7.3. With the BARC etch rate 1.5 times that of the PR, a good CD was obtained however a small amount of BARC was left on the TiN which produced micro-masking during the etch steps. When the

PR and BARC etch rates are equal, the PR width shrank below 25 nm and a 5-10 nm layer of BARC micro-masking was left on the TiN. Leaving this layer would require more time in the gate-stack etch step to clear the BARC due to the absence of O species in the Ar/BCl<sub>3</sub>/Cl<sub>2</sub> plasma. To totally clear the BARC during the trim would produce an unacceptably narrow PR.

#### 7.4. Plasma and HfO<sub>2</sub> Etch Properties

The process conditions for the gate-stack etch were a 5 mTorr Ar/BCl<sub>3</sub>/Cl<sub>2</sub>=5/40/55 gas mixture with a flow rate of 100 sccm. The coil delivered 300 W at 10 MHz. The amplitude of the 13.56 MHz rf bias on the substrate was varied. The total ion density was  $3.2 \times 10^{11} \text{ cm}^{-3}$ . BCl<sub>2</sub><sup>+</sup> has the highest density ( $1.6 \times 10^{11} \text{ cm}^{-3}$ ) followed by Cl<sup>+</sup> ( $1.0 \times 10^{11} \text{ cm}^{-3}$ ). Cl is the radical with the largest density ( $1.0 \times 10^{14} \text{ cm}^{-3}$ ) followed by BCl<sub>2</sub> ( $1.3 \times 10^{13} \text{ cm}^{-3}$ ). (See Fig. 7.2.) Fluxes of the major ions and neutral radicals to the substrate are shown in Fig. 7.4 for the base case with a 32 V substrate bias. The dominant radical fluxes are Cl ( $1 \times 10^{18} \text{ cm}^{-2}\text{s}^{-1}$ ) and BCl<sub>2</sub> ( $7.5 \times 10^{16} \text{ cm}^{-2}\text{s}^{-1}$ ). Cl is produced by both electron impact dissociation of Cl<sub>2</sub> and BCl<sub>3</sub>, the latter yielding BCl<sub>2</sub> and Cl. Electron-impact ionization of BCl<sub>3</sub> dominantly produces BCl<sub>2</sub><sup>+</sup> and Cl. The major ion fluxes are BCl<sub>2</sub><sup>+</sup> ( $8 \times 10^{15} \text{ cm}^{-2}\text{s}^{-1}$ ), Cl<sup>+</sup> ( $4 \times 10^{15} \text{ cm}^{-2}\text{s}^{-1}$ ), Cl<sub>2</sub><sup>+</sup> ( $4 \times 10^{14} \text{ cm}^{-2}\text{s}^{-1}$ ) and Ar<sup>+</sup> ( $4 \times 10^{13} \text{ cm}^{-2}\text{s}^{-1}$ ). The low flux of Ar<sup>+</sup> results from the low mole fraction of Ar but also from rapid charge exchange reactions to other species. With a 32 V bias, the average energy for all ions incident on the substrate is near 30 eV with an angular spread from the vertical of  $< 15^\circ$ , as shown by the IEADs in Fig. 7.5.

## 7.5 HfO<sub>2</sub> Etch Rate vs. Bias Voltage

Bias voltage affects the properties of the gate-stack etch through rate, profile and selectivity of HfO<sub>2</sub> to Si. The post-etch gate-stack profiles for biases of 32, 60 and 100 V are shown in Fig. 7.6a for equal etch times corresponding to when the 32 V bias removes the SiO<sub>2</sub> layer. Etch rate and selectivity as a function of bias voltage are shown in Fig. 7.6b. The etch rate of HfO<sub>2</sub> has a threshold bias of 27 V increasing from 100 Å/min at 32 V to 650 Å/min at 200 V. The increase in etch rate slows above 100 V as the rates of increase in ion activated reaction probabilities begin to saturate. The increase in etch rate comes at the expense of selectivity. The selectivity is as large as 12 at a bias of 32 V, decreasing monotonically to 2 for a bias of 200 V. The decrease in selectivity is largely a consequence of the removal of polymer on the Si by sputtering.

Our predicted threshold of 27 V for HfO<sub>2</sub> etching is in agreement with the experimentally measured threshold of 28 V.[9,13] The predicted high selectivity near the etching-threshold is corroborated by experimental results where highly selective etching of HfO<sub>2</sub> layer over Si was achieved by control of the substrate bias.[4,13] The predicted decrease in selectivity as a function of increasing bias is also in general agreement with experiment, though our decrease in selectivity is more gradual.[13]. Predicted HfO<sub>2</sub> etch rates for biases of 32-200 V bias are also in general agreement with experiment, with differences attributable to differences in the total fluxes of reactants in the reactors used by different researchers.[4,12,13]

The increase in bias voltage also produces undercutting of the TiN. In spite of a narrowing of the IEAD with increasing bias, there is still sufficient width to produce some lateral etching due to the open field on both sides of the feature. This is an affect that would not

be as apparent in trench or via etching where at higher aspect ratios the ions at broader angles are shadowed.

Gate-stack profiles at the time when the  $\text{SiO}_2$  layer is cleared for each bias are shown in Fig. 7.7a for 32, 60 and 100 V. Using a qualitative assessment of maintaining CD (that is, a vertical profile) while minimizing Si damage, the best profiles obtained for 32, 60 and 100 V biases as a function of over-etch time are shown in Fig. 7.7b. The high  $\text{HfO}_2/\text{Si}$  selectivity afforded by the 32 V bias allows a sufficient over-etch to produce a largely uniform gate-stack width. There is little damage to the Si substrate although there is a small narrowing of the TiN. The lower selectivity obtained with a 60 V bias produced some damage to Si layer while the gate-stack has less narrowing. This damage is, in part, due to the initial micro-masking of the TiN by the BARC and TiO which ultimately produces different clearing times to the Si at different locations. Those TiN sites that are micro-masked have a delayed start to etching corresponding to when the masking material (BARC or TiO) is removed. Although the BARC and TiO that produce micro-masking are more rapidly removed with the higher bias, thereby reducing the negative aspects of micro-masking, the etch rates of the TiN,  $\text{HfO}_2$  and  $\text{SiO}_2$  are also more rapid with increasing bias. This leads to over-etching at random sites on the Si that were not micro-masked. Further etching to remove the tapering in the gate-stack then produces more Si damage. These trends are intensified with the 100 V bias; as both the  $\text{HfO}_2/\text{Si}$  selectivity decreases and the CD worsens (narrowing of the gate-stack.).

Both an acceptable CD and  $\text{HfO}_2/\text{Si}$  selectivity were obtained with a 32 V bias where the TiN and  $\text{HfO}_2$  had a nearly consistent width of 32 nm. A slight tapering of the TiN and  $\text{HfO}_2$  occurred for the 60 V bias with a small amount of damage to the Si. The profile could not be optimized for both width and lack of damage to the Si at 100 V. For example, the TiN

narrowed to a width of below 25 nm, with there being significant erosion of the Si substrate.

As discussed above, depending on the ratio of the PR to BARC etch rates during the PR-trim step, there may be micro-masking on the TiN at the end of the trim step due to incomplete removal of the BARC. In practice, the remaining BARC layer is often removed with an intermediate plasma etching step prior to the gate-stack etch to eliminate the possibility of micro-masking. In the absence of the BARC removal step, the micro-masking material is dominantly removed by sputtering reactions during the gate-stack etch, which also serves to further erode the PR. For example, while clearing the micro-masking layer and etching the gate-stack in the base case, the PR width was further reduced by a few nm. Sites underneath the micro-masking etch more slowly due to the prior need to remove the BARC by sputtering. For example, time sequences of the gate-stack profile with biases of 32 and 100 V are shown in Fig. 7.8 with BARC micro-masking remaining from the PR-trim. If the selectivity of  $\text{HfO}_2/\text{Si}$  is high enough, as with the 32 V bias, the different clearing times of the TiN and  $\text{HfO}_2$  laterally across the feature due to micro-masking are not detrimental to either the final CD or selectivity. For low selectivity conditions, as with the 100 V bias, the micro-masking is problematic as the over-etch results in local sites on the Si being damaged.

A quantitative measure of CD is the slope of the gate-stack profile where  $90^\circ$  would indicate a vertical profile. The slope of the gate-stack profile is shown in Fig. 7.9 for different biases as a function of over-etch time. The beginning of the over-etch is when the  $\text{SiO}_2$  on top of Si substrate is cleared. The asymptotic slope at long over-etch is  $80^\circ$ - $90^\circ$  with higher biases both achieving a slope nearer the vertical and achieving that slope with shorter over-etch times. These more optimum slopes are obtained at the expense of poor selectivity.

### 7.5.1 Selectivity: Si-B Bond Formation

The selectivity of  $\text{HfO}_2$  to Si depends on the formation and persistence of the  $\text{BCl}_n$  polymer layer. To determine the sensitivity of selectivity to rates of Si-B bond formation, polymer deposition and polymer sputtering, the probabilities for these processes were parameterized in the model.

Selectivity while varying the probability of the Si-B bond formation that initiates the deposition of polymer is shown in Fig. 7.10a for different bias voltages. The corresponding gate-stack profiles are shown in Fig. 7.11a. In the absence of Si-B bond formation, the polymer does not deposit, and so the selectivity is based only on the intrinsic etch rates of the  $\text{HfO}_2$  and the Si, which for the base case conditions are nearly equal. As the probability for Si-B bond formation increases from 0 to 0.4, the rate of etching of Si slows and the selectivity improves to 10 for a bias of 32 V. At this probability, the majority of the available sites are passivated and covered by  $\text{BCl}_n$  polymer. Although selectivity increases with increasing bond formation probability for all biases, as the bias voltage and sputtering rates increase, the residence time of Si-B bonding decreases and so the rate of polymer formation also decreases. The end result is a decrease in selectivity with bias voltage. For example, for a bias of 100 V, only 45% of the Si sites are, on the average, passivated.

The gate-stack profile prior to reaching the Si layer is essentially independent of the Si-B bond formation probability for a given etch time. The consequences of Si-B bonding are only felt once the  $\text{SiO}_2$  layer is cleared. With a low Si-B bond formation probability, sites on the Si are periodically exposed to the plasma, producing roughness and damage, as shown in Fig. 7.11a. Increasing the bond formation probability insures that these sites are nearly continuously passivated, thereby reducing the propensity for damage.

### 7.5.2 Selectivity: Polymer Deposition

Provided that Si-B bonds are present,  $\text{BCl}_n(\text{g})$  species adsorb on top of Si-B compounds to form  $\text{BCl}_n$  polymers.[4] Selectivity as a function of polymer deposition probability and interface properties for different bias voltages are shown in Fig. 7.10b and Fig. 7.11b. As the probability for polymer deposition is increased from 0 to 0.5, the selectivity improves from 3 to 10 for a bias of 32 V. The selectivity is almost constant at probabilities higher than 0.5. Selectivity is above 2 for all biases even in the absence of polymer formation as the Si etch rate is slowed by the base layer of Si-B bonding. As the bias voltage increases, the rates of sputtering of the polymer and Si-B bond breaking increase resulting in a lower selectivity. Increasing the bias to 100 V reduces selectivity by nearly half at all deposition probabilities. Again, the gate-stack profile is independent of the polymer formation rate, though the roughness and damage to the Si layer increases with increasing bias, as shown in Fig. 7.11b.

### 7.5.3 Selectivity: Polymer Sputtering

As the polymer is deposited, it is also necessary that the polymer be sustained in order to obtain high selectivity. Higher polymer sputtering rates produce thinner polymer layers and so results in lower selectivity. For example, selectivity as a function of the polymer sputtering probability (this is the probability at the reference energy of 140 eV) is shown in Fig. 7.10c for biases of 40, 100 and 150 V bias. Gate-stack profiles for different polymer sputtering probabilities are shown in Fig. 7.12. Selectivity decreases with increasing polymer sputtering probability while the Si roughness and damage increase.

## 7.6 Concluding Remarks

PR/BARC/TiN/SiO<sub>2</sub>/Si gate-stack etching employing Ar/BCl<sub>3</sub>/Cl<sub>2</sub> plasmas preceded by an Ar/O<sub>2</sub> plasma PR-trim and BARC removal was computationally investigated. HfO<sub>2</sub> etching likely requires breaking of Hf-O bonds and separate removal of Hf(s) and O(s) atoms by Cl(g) adsorption and ion assisted etching. Etching of TiN likely includes breaking of Ti-N bonds and chlorination of Ti(s) to be removed as TiCl<sub>n</sub>(g). The model confirms that HfO<sub>2</sub>/Si selectivity can be achieved by deposition of a BCl<sub>n</sub> polymer on the Si, preceded by Si-B bond formation. With low biases, selective etching of HfO<sub>2</sub> with respect to Si can be achieved while minimizing undercutting of the TiN gate due to the persistence of the polymer layer. A significant over-etch, however, is required to achieve the optimum etch profile (that is, closest to 90°). While higher bias voltages require less time to achieve a profile slope close to 90°, this is achieved at the cost of selectivity. The role of Si-B bond formation and growth of BCl<sub>n</sub> polymer were parametrically investigated. We found that both Si-B bond formation and polymer deposition are necessary to achieve high selectivity though some nominal selectivity is afforded by the Si-B bonding.

Optimizing the PR-trim prior to the gate-stack etch involves a tradeoff between maintaining the CD of the PR and total removal of the BARC. This tradeoff results from the PR and BARC both typically being organics having similar etch rates in oxygen containing plasmas. Parameterization showed that a BARC etch rate 1.5 times higher than that of the PR provides the best post-trim profile. A thin layer of BARC left on the TiN produces micro-masking which must first be removed during the gate-stack etch. At low bias voltages, this micro-masking was not necessarily detrimental to the final gate-stack profile and did not significantly contribute to damaging the Si due to the need to over-etch. These trends result-

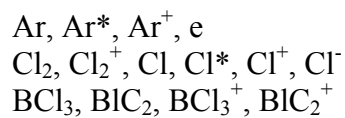
ed from the high  $\text{HfO}_2/\text{Si}$  selectivity at low bias voltages that protects the Si substrate sites during even a long over-etch.

Although the reaction mechanism we developed does reproduce experimental trends, there are uncertainties in both the sequence of reactions and in reaction probabilities. For example, our studies have shown the range of probabilities for important processes, such as for sputtering and polymer deposition, over which predicted etch rates and selectivity are most sensitive. The test of the mechanism is whether it provides accurate predictions for process conditions considerably different from that used to help create the mechanisms. As such refinement of the mechanism will benefit from further comparisons to experiments.

## 7.7 Tables

Table 7.1 Ar/BCl<sub>3</sub>/Cl<sub>2</sub> Gas Phase Reaction Mechanism

Species:



Reaction	Rate Coefficient	Reference
$\text{e} + \text{Ar} \rightarrow \text{Ar} + \text{e}$	$f(\varepsilon)^a$	14
$\text{e} + \text{Ar} \rightarrow \text{Ar}^* + \text{e}$	$f(\varepsilon)^a$	15
$\text{e} + \text{Ar} \rightarrow \text{Ar}^+ + \text{e} + \text{e}$	$f(\varepsilon)^a$	16
$\text{e} + \text{Ar}^* \rightarrow \text{Ar}^+ + \text{e} + \text{e}$	$f(\varepsilon)^a$	17
$\text{e} + \text{Ar}^* \rightarrow \text{Ar} + \text{e}$	$f(\varepsilon)^a$	18
$\text{e} + \text{Cl}_2 \rightarrow \text{Cl}_2 + \text{e}$	$f(\varepsilon)^a$	19
$\text{e} + \text{Cl}_2 \rightarrow \text{Cl}_2(\text{v}) + \text{e}$	$f(\varepsilon)^a$	19, c
$\text{e} + \text{Cl}_2 \rightarrow \text{Cl} + \text{Cl}^-$	$f(\varepsilon)^a$	19
$\text{e} + \text{Cl}_2 \rightarrow \text{Cl} + \text{Cl} + \text{e}$	$f(\varepsilon)^a$	19
$\text{e} + \text{Cl}_2 \rightarrow \text{Cl}_2^+ + \text{e} + \text{e}$	$f(\varepsilon)^a$	19
$\text{e} + \text{Cl} \rightarrow \text{Cl} + \text{e}$	$f(\varepsilon)^a$	19
$\text{e} + \text{Cl} \rightarrow \text{Cl}^* + \text{e}$	$f(\varepsilon)^a$	19
$\text{e} + \text{Cl} \rightarrow \text{Cl}^+ + \text{e} + \text{e}$	$f(\varepsilon)^a$	19
$\text{e} + \text{Cl}^* \rightarrow \text{Cl}^* + \text{e}$	$f(\varepsilon)^a$	19
$\text{e} + \text{Cl}^* \rightarrow \text{Cl} + \text{e}$	$f(\varepsilon)^a$	19

Table 7.1 (Continued)

$e + Cl^* \rightarrow Cl^+ + e + e$	$f(\epsilon)^a$	19
$e + Cl^- \rightarrow Cl + e + e$	$f(\epsilon)^a$	19
$e + Cl_2^+ \rightarrow Cl + Cl$	$1 \times 10^{-7}/T_e^{0.5}$	b
$e + BCl_3 \rightarrow BCl_3 + e$	$f(\epsilon)^a$	b
$e + BCl_3 \rightarrow BCl_3(v) + e$	$f(\epsilon)^a$	20
$e + BCl_3 \rightarrow BCl_2 + Cl^-$	$f(\epsilon)^a$	20
$e + BCl_3 \rightarrow BCl_2 + Cl + e$	$f(\epsilon)^a$	21
$e + BCl_3 \rightarrow BCl_3^+ + e + e$	$f(\epsilon)^a$	21
$e + BCl_3 \rightarrow BCl_2^+ + Cl + e + e$	$f(\epsilon)^a$	21
$e + BCl_3^+ \rightarrow BCl_2 + Cl$	$1 \times 10^{-7}/T_e^{0.5}$	22, b
$e + BCl_2 \rightarrow BCl_2 + e$	$f(\epsilon)^a$	d
$e + BCl_2 \rightarrow BCl_2(v) + e$	$f(\epsilon)^a$	c, d
$e + BCl_2 \rightarrow BCl_2^+ + e + e$	$f(\epsilon)^a$	23
$e + BCl_2^+ \rightarrow BCl_2$	$1 \times 10^{-7}/T_e^{0.5}$	22
$Cl^* \rightarrow Cl$	$1 \times 10^5$	b
$Cl^- + Cl^+ \rightarrow Cl + Cl$	$1 \times 10^{-7}$	b
$Cl^- + Cl_2^+ \rightarrow Cl_2 + Cl$	$1 \times 10^{-7}$	b
$Cl^- + Ar^+ \rightarrow Cl + Ar$	$1 \times 10^{-7}$	b
$Cl^- + BCl_2^+ \rightarrow BCl_2 + Cl$	$1 \times 10^{-7}$	b
$Cl^- + BCl_3^+ \rightarrow BCl_3 + Cl$	$1 \times 10^{-7}$	b

Table 7.1 (Continued)

$\text{Ar}^* + \text{Ar}^* \rightarrow \text{Ar}^+ + \text{e} + \text{Ar}$	$5 \times 10^{-10}$	b
$\text{Ar}^* + \text{Cl}_2 \rightarrow \text{Cl}_2^+ + \text{Ar} + \text{e}$	$7.1 \times 10^{-10}$	b
$\text{Ar}^* + \text{Cl} \rightarrow \text{Cl}^* + \text{Ar}$	$0.7 \times 10^{-11}$	b
$\text{Ar}^* + \text{BCl}_3 \rightarrow \text{BCl}_2 + \text{Cl} + \text{Ar}$	$1 \times 10^{-11}$	b
$\text{Ar}^* + \text{BCl}_2 \rightarrow \text{BCl}_2^+ + \text{Ar} + \text{e}$	$1 \times 10^{-11}$	b
$\text{Ar}^+ + \text{Cl}_2 \rightarrow \text{Cl}_2^+ + \text{Ar}$	$0.84 \times 10^{-10}$	24
$\text{Ar}^+ + \text{Cl}_2 \rightarrow \text{Cl}^+ + \text{Cl} + \text{Ar}$	$0.64 \times 10^{-10}$	24
$\text{Ar}^+ + \text{Cl} \rightarrow \text{Cl}^+ + \text{Ar}$	$2 \times 10^{-10}$	24
$\text{Ar}^+ + \text{BCl}_3 \rightarrow \text{BCl}_2^+ + \text{Cl} + \text{Ar}$	$5 \times 10^{-10}$	b
$\text{Ar}^+ + \text{BCl}_2 \rightarrow \text{BCl}_2^+ + \text{Ar}$	$1 \times 10^{-10}$	b
$\text{Cl}^+ + \text{Cl}_2 \rightarrow \text{Cl}_2^+ + \text{Cl}$	$5.4 \times 10^{-10}$	b
$\text{Cl}^+ + \text{BCl}_3 \rightarrow \text{BCl}_2^+ + \text{Cl}_2$	$6.2 \times 10^{-10}$	b
$\text{Cl}^* + \text{BCl}_3 \rightarrow \text{BCl}_2 + \text{Cl} + \text{Cl}$	$1 \times 10^{-11}$	b
$\text{Cl}^* + \text{BCl}_3 \rightarrow \text{BCl}_2^+ + \text{Cl} + \text{e}$	$1 \times 10^{-11}$	b
$\text{Cl}_2^+ + \text{BCl}_3 \rightarrow \text{BCl}_2^+ + \text{Cl}_2$	$1 \times 10^{-10}$	b
$\text{Cl} + \text{Cl} + \text{Ar} \rightarrow \text{Cl}_2 + \text{Ar}$	$1.28 \times 10^{-32}$	24
$\text{Cl} + \text{Cl} + \text{Cl}_2 \rightarrow \text{Cl}_2 + \text{Cl}_2$	$5.4 \times 10^{-32}$	24

- a. Rate coefficients are calculated from electron energy distribution obtained in the EMCS.  $T_e$  is the electron temperature ( $eV$ ).
- b. Estimated.
- c. Energy loss due to vibrational excitation is included in the solution of Boltzmann's equation however the density of vibrationally excited species is not tracked in the model.
- d. Estimated by analogy to  $\text{BCl}_3$ .

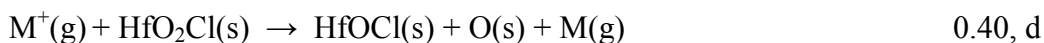
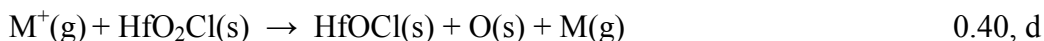
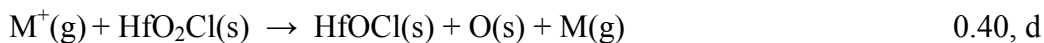
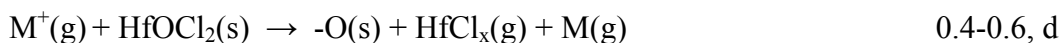
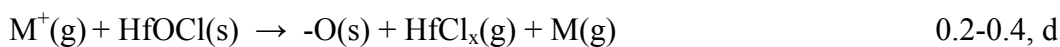
Table 7.2 Reaction Mechanism for HfO<sub>2</sub> Etching in Ar/BCl<sub>3</sub>/Cl<sub>2</sub> Plasmas.

Species:

M(g) Gas phase species  
M(s) Surface site  
M<sup>+</sup> Ion

<u>Reaction</u> <sup>a-c</sup>	<u>Probability</u>
<i>HfO<sub>2</sub>: Bond Breaking</i>	
M <sup>+</sup> (g) + HfO <sub>2</sub> (s) → HfO(s) + O(s) + M(g)	0.40, d
M <sup>+</sup> (g) + HfO(s) → Hf(s) + O(s) + M(g)	0.40, d
<i>Hf(s) Passivation</i>	
Cl(g) + Hf(s) → HfCl(s)	0.20
Cl(g) + HfCl(s) → HfCl <sub>2</sub> (s)	0.50
Cl(g) + HfCl <sub>2</sub> (s) → HfCl <sub>3</sub> (s)	0.20
Cl(g) + HfCl <sub>3</sub> (s) → HfCl <sub>4</sub> (s)	0.20
<i>HfCl<sub>x</sub>: Etching</i>	
M <sup>+</sup> (g) + HfCl <sub>2</sub> (s) → HfCl <sub>2</sub> (g) + M(g)	0.30, d
M <sup>+</sup> (g) + HfCl <sub>3</sub> (s) → HfCl <sub>3</sub> (g) + M(g)	0.40, d
M <sup>+</sup> (g) + HfCl <sub>4</sub> (s) → HfCl <sub>4</sub> (g) + M(g)	0.90, d
<i>HfO<sub>n</sub> Passivation</i>	
Cl(g) + HfO <sub>2</sub> (s) → HfO <sub>2</sub> Cl(s)	0.10
Cl(g) + HfO <sub>2</sub> Cl(s) → HfO <sub>2</sub> Cl <sub>2</sub> (s)	0.06
Cl(g) + HfO(s) → HfOCl(s)	0.20
Cl(g) + HfOCl(s) → HfOCl <sub>2</sub> (s)	0.20

Table 7.2 (Continued)

*HfO<sub>2</sub>Cl<sub>x</sub>: Bond Breaking:**HfOCl<sub>n</sub>: Etching:**OBCl<sub>n</sub> Formation**O Etching*

- a. Unless specified, all ions neutralize on surfaces, returning as their neutral counterparts.
- b. Gas phase species have units of flux ( $\text{cm}^{-2} \text{s}^{-1}$ ). Surface species have units of fractional coverage.
- c. In reactions with no chemical change, the gas species are reflected off the surface. These reactions are not shown.
- d. See Eq. (1).  $E_r=100 \text{ eV}$ ,  $E_i=10 \text{ eV}$ , probability is at  $E_r$ .

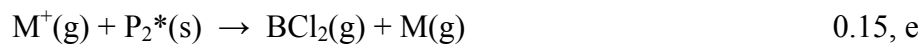
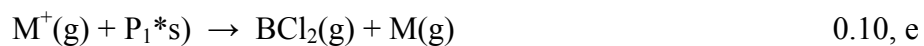
Table 7.3 Si-B Bond Formation and Polymerization Reactions

Species:

M(g) Gas phase species  
M(s) Surface site  
M<sup>+</sup> Ion

Reaction <sup>a-c</sup>	Probability
<i>Si-B Bond Formation</i>	
$\text{BCl}_n(\text{g}) + \text{Si}(\text{s}) \rightarrow \text{SiBCl}_n(\text{s}), n = 1,2$	0.40
$\text{BCl}_n(\text{g}) + \text{SiCl}(\text{s}) \rightarrow \text{SiClBCl}_n(\text{s}), n = 1,2$	0.40
$\text{BCl}_n(\text{g}) + \text{SiCl}_2(\text{s}) \rightarrow \text{SiCl}_2\text{BCl}_n(\text{s}), n = 1,2$	0.40
$\text{BCl}_n(\text{g}) + \text{SiCl}_3(\text{s}) \rightarrow \text{SiCl}_3\text{BCl}_n(\text{s}), n = 1,2$	0.40
<i>Polymer Formation on SiBCl Sites</i>	
$\text{BCl}_n(\text{g}) + \text{SiBCl}_n(\text{s}) \rightarrow \text{SiBCl}_n(\text{s}) + \text{P}_1(\text{s}), n = 1,2$	0.70
$\text{BCl}_n(\text{g}) + \text{SiClBCl}_n(\text{s}) \rightarrow \text{SiClBCl}_n(\text{s}) + \text{P}_1(\text{s}), n=1,2$	0.70
$\text{BCl}_n(\text{g}) + \text{SiCl}_2\text{BCl}_n(\text{s}) \rightarrow \text{SiCl}_2\text{BCl}_n(\text{s}) + \text{P}_1(\text{s}), n=1,2$	0.70
$\text{BCl}_n(\text{g}) + \text{SiCl}_3\text{BCl}_n(\text{s}) \rightarrow \text{SiCl}_3\text{BCl}_n(\text{s}) + \text{P}_1(\text{s}), n=1,2$	0.70
<i>Polymer Formation on Activated sites</i>	
$\text{BCl}_2(\text{g}) + \text{P}_1^*(\text{s}) \rightarrow \text{P}_1(\text{s}) + \text{P}_2(\text{s})$	0.70
$\text{BCl}(\text{g}) + \text{P}_1^*(\text{s}) \rightarrow \text{P}_1(\text{s}) + \text{P}_2(\text{s})$	0.70
$\text{BCl}_2(\text{g}) + \text{P}_2^*(\text{s}) \rightarrow \text{P}_2(\text{s}) + \text{P}_2(\text{s})$	0.70
$\text{BCl}_2(\text{g}) + \text{P}_2^*(\text{s}) \rightarrow \text{P}_2(\text{s}) + \text{P}_2(\text{s})$	0.70
<i>Polymer Activation and Sputtering</i>	
$\text{M}^+(\text{g}) + \text{P}_1(\text{s}) \rightarrow \text{P}_1^*(\text{s}) + \text{M}(\text{g})$	0.10, d
$\text{M}^+(\text{g}) + \text{P}_2(\text{s}) \rightarrow \text{P}_2^*(\text{s}) + \text{M}(\text{g})$	0.15, d

Table 7.3 (Continued)



- a. Unless specified, all ions neutralize on surfaces, returning as their neutral counterparts.
- b. Gas phase species have units of flux ( $\text{cm}^{-2} \text{s}^{-1}$ ). Surface species have units of fractional coverage.
- c. In reactions with no chemical change, the gas species are reflected off the surface. These reactions are not shown.
- d.  $p(E) = \text{Max}[p_0(1-E/E_c), 0]$ , where  $E_c$  is the cut-off energy for polymer activation.  $p_0 = 0.1$  and  $E_c = 45 \text{ eV}$ .
- e. See Eq. (1).  $E_r = 140 \text{ eV}$ ,  $E_t = 45 \text{ eV}$ .

Table. 7.4 Reaction Mechanism for TiN Etching and PR/BARC Sputtering in Ar/BCl<sub>3</sub>/Cl<sub>2</sub> Plasmas

Species:

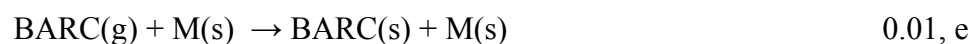
M(g) Gas phase species  
 M(s) Surface site  
 M<sup>+</sup> Ion

<u>Reaction<sup>a-c</sup></u>	<u>Probability</u>
<i>Bond Breaking</i>	
M <sup>+</sup> (g) + TiN(s) → Ti(s) + N(g) + M(g)	0.51, d
<i>Passivation</i>	
Cl(g) + Ti(s) → TiCl(s)	0.89
Cl(g) + TiCl(s) → TiCl <sub>2</sub> (s)	0.65
Cl(g) + TiCl <sub>2</sub> (s) → TiCl <sub>3</sub> (s)	0.65
Cl(g) + TiN(s) → TiNCl(s)	0.51
O(g) + Ti(s) → TiO(s)	0.51
Cl(g) + TiO(s) → TiOCl(s)	0.60
Cl(g) + TiOCl(s) → TiOCl <sub>2</sub> (s)	0.60
<i>Etching</i>	
Cl(g) + TiCl <sub>3</sub> (s) → TiCl <sub>4</sub> (g)	0.02
M <sup>+</sup> (g) + TiCl(s) → TiCl(g) + M(g)	0.35, d
M <sup>+</sup> (g) + TiCl <sub>2</sub> (s) → TiCl <sub>2</sub> (g) + M(g)	0.45, d
M <sup>+</sup> (g) + TiCl <sub>3</sub> (s) → TiCl <sub>3</sub> (g) + M(g)	0.65, d
M <sup>+</sup> (g) + TiNCl(s) → TiCl <sub>x</sub> (g) + M(g)	0.35, d
M <sup>+</sup> (g) + TiOCl(s) → TiOCl(g) + M(g)	0.60, d

Table 7.4 (Continued)



*PR and BARC: Sputtering and redeposition*



- a. Unless specified, all ions neutralize on surfaces, returning as their neutral counterparts.
- b. Gas phase species have units of flux ( $\text{cm}^{-2} \text{s}^{-1}$ ). Surface species have units of fractional coverage.
- c. In reactions with no chemical change, the gas species are reflected off the surface. These reactions are not shown.
- d. See Eq. (1).  $E_r=100$  eV,  $E_{\bar{r}}=10$  eV, probability is at  $E_r$ .
- e. PR(g) and BARC(g) can redeposit on all surfaces. The redeposited material has the same characteristics as the original PR and BARC.

Table 7.5 Reaction Mechanism for PR-trimming and BARC Etching

Species:

M(g) Gas phase species  
M(s) Surface site  
M<sup>+</sup> Ion

<u>Reaction<sup>a-c</sup></u>	<u>Probability</u>
<i>PR Sputtering</i>	
M <sup>+</sup> (g) + PR(s) → PR(g) + M(g)	0.020, d
<i>PR etching:</i>	
O(g) + PR(s) → COH(g)	0.010
O <sup>+</sup> (g) + PR(s) → COH(g)	0.010
O <sub>2</sub> <sup>+</sup> (g) + PR(s) → COH(g)	0.010
<i>BARC Sputtering</i>	
M <sup>+</sup> (g) + BARC(s) → BARC(g) + M(g)	0.050, d
<i>BARC etching</i>	
O(g) + BARC(s) → COH(g)	0.015
O <sup>+</sup> (g) + BARC(s) → COH(g)	0.015
O <sub>2</sub> <sup>+</sup> (g) + BARC(s) → COH(g)	0.015
<i>Redeposition</i>	
PR(g) + M(s) → PR(s) + M(s)	0.01, e
BARC(g) + M(s) → BARC(s) + M(s)	0.01, e

- a. Unless specified, all ions neutralize on surfaces, returning as their neutral counterparts.
- b. Gas phase species have units of flux (cm<sup>-2</sup> s<sup>-1</sup>). Surface species have units of fractional coverage.
- c. In reactions with no chemical change, the gas species are reflected off the surface. These reactions are not shown.
- d. See Eq. (1).  $E_r=100$  eV,  $E_t=10$  eV.
- e. PR(g) and BARC(g) can redeposit on all surfaces. The redeposited material has the same characteristics as the original

## 7.8 Figures

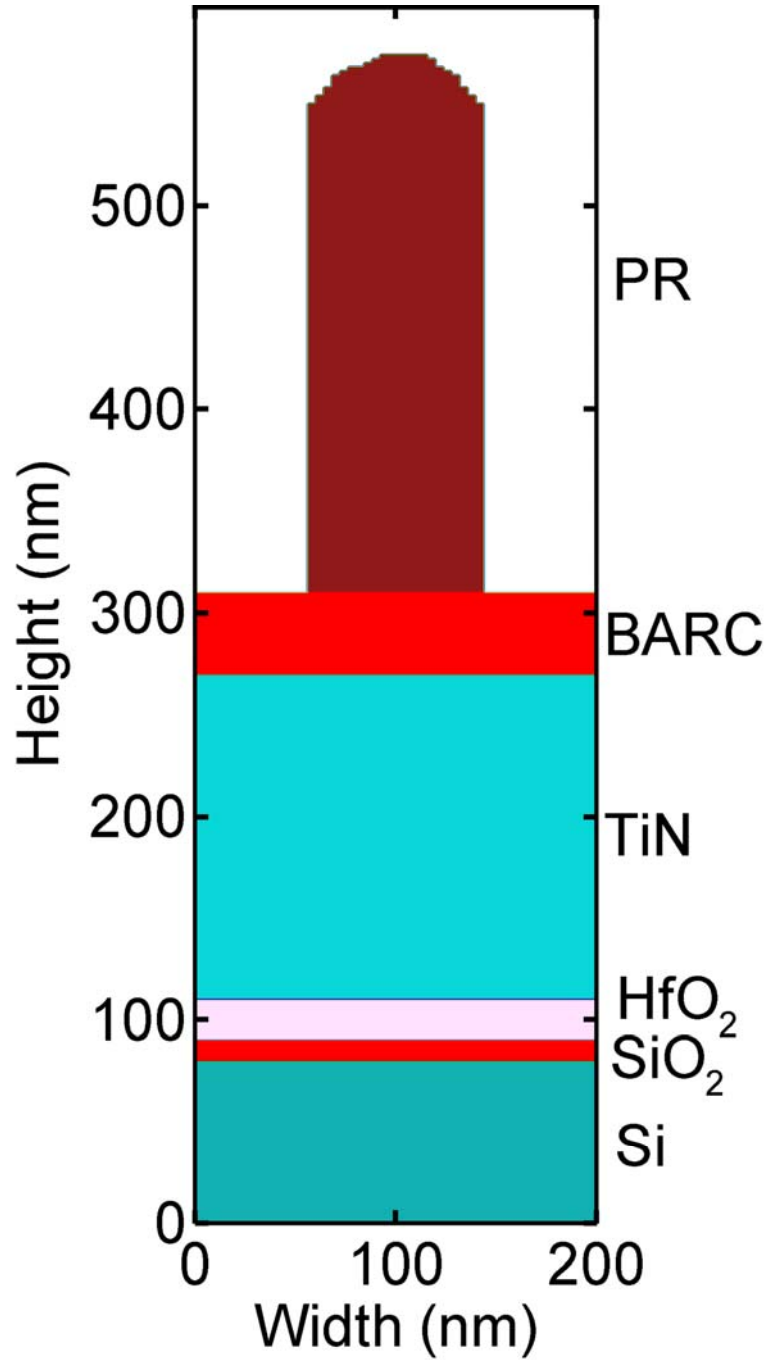


Fig. 7.1 Initial gate-stack. The PR width is 58 nm and height is 290 nm. The thickness of the layers are BARC 40 nm, TiN 160 nm, HfO<sub>2</sub> 20 nm and SiO<sub>2</sub> 10 nm.

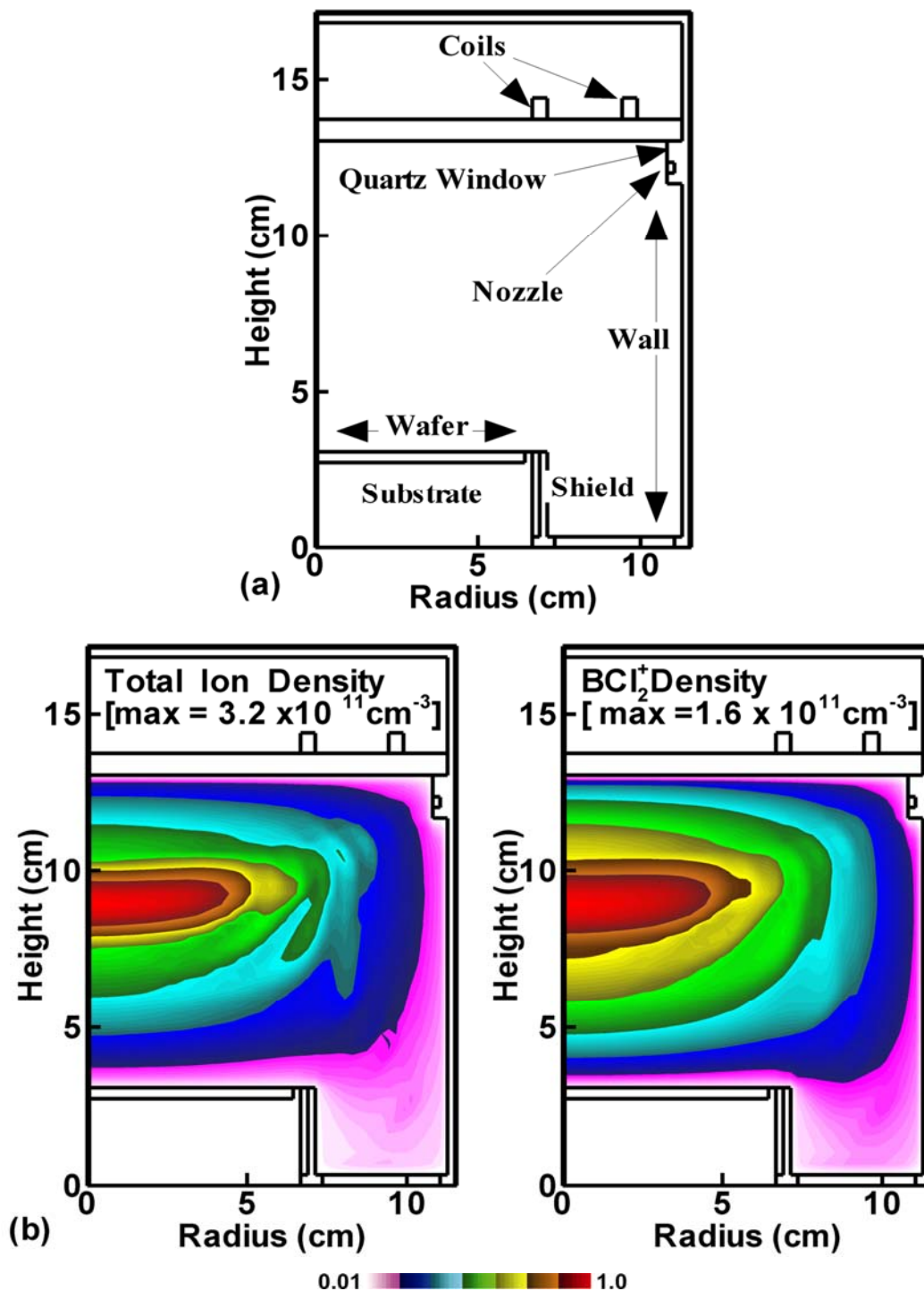


Fig. 7.2 ICP reactor and typical plasma properties for Ar/ $\text{BCl}_3$ / $\text{Cl}_2$ =5/40/55, 300 W ICP, 5 mTorr and 100 sccm. (a) Schematic of the reactor. (b) Total ion density and (c)  $\text{BCl}_2^+$  density.

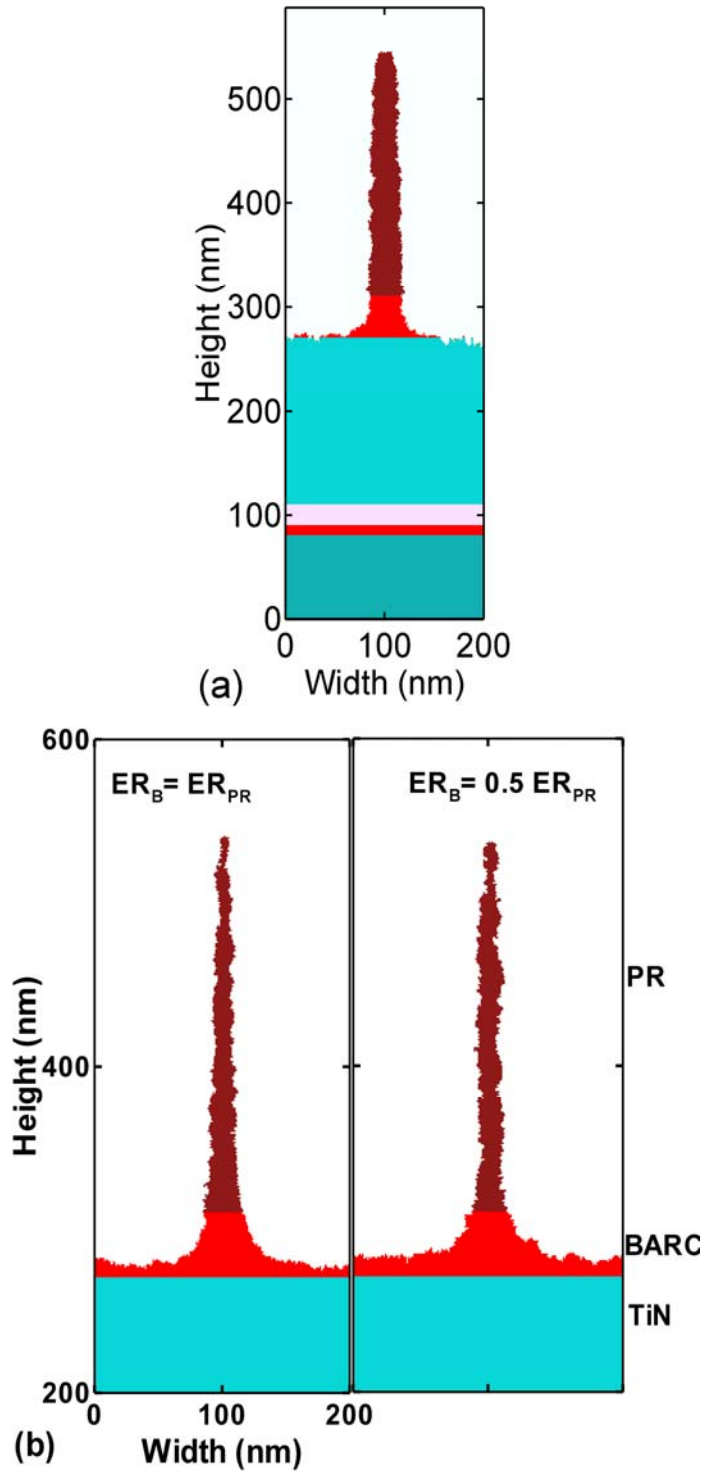


Fig. 7.3 Gate-stack after PR-trimming and BARC etching in Ar/O<sub>2</sub> plasmas. (a) Optimized post PR-trim profile with BARC to PR etching ratio of 1.5. (b) Post PR-trim profiles while varying PR and BARC etching probabilities. The ratios of etching of BARC to PR are 1.5, 1 and 0.5 respectively.

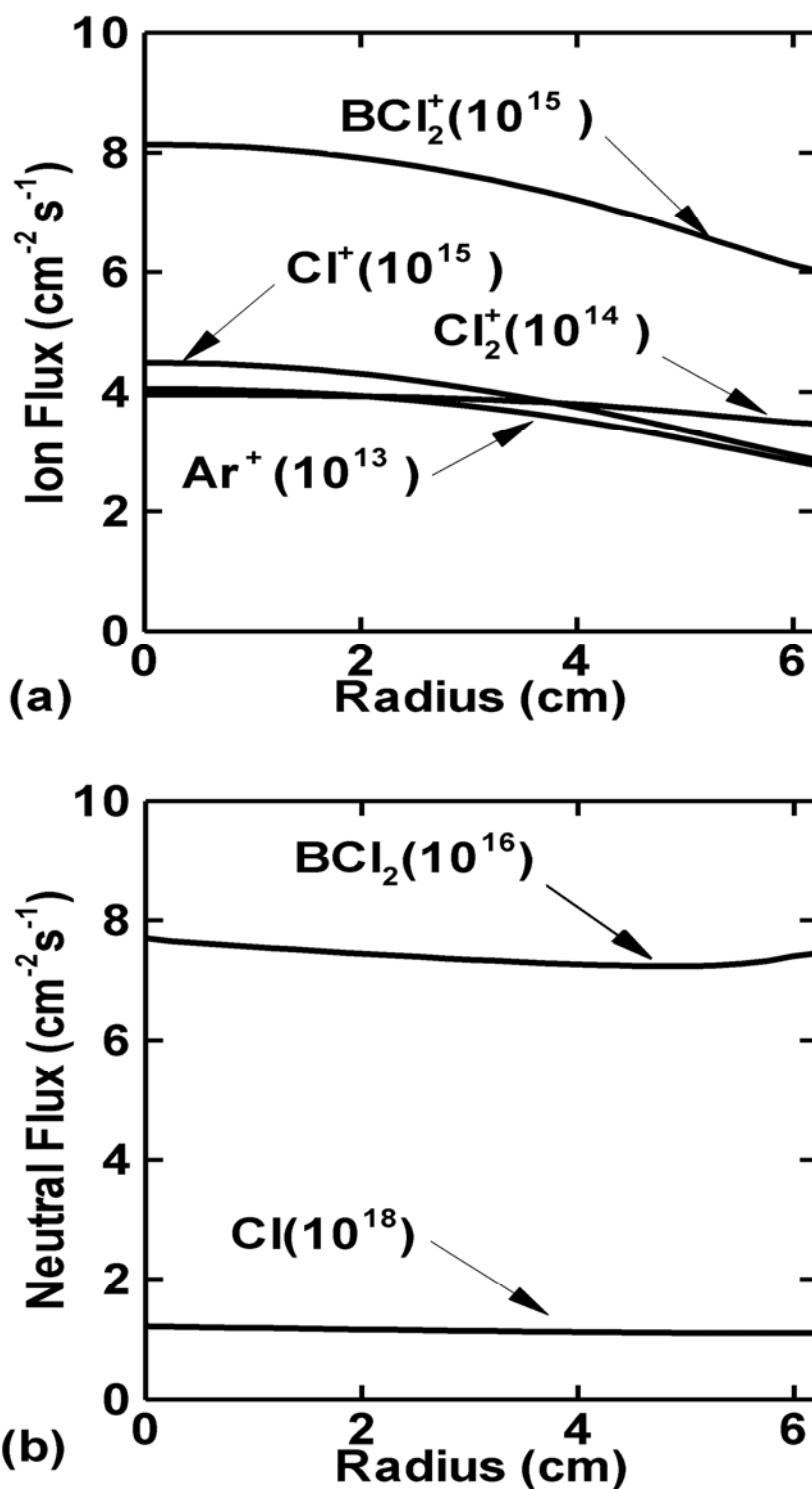


Fig. 7.4 Fluxes to the wafer as a function of radius ( $\text{Ar}/\text{BCl}_3/\text{Cl}_2=5/40/55$ , 300 W ICP, 5 mTorr, 100 sccm). (a) Ion fluxes and (b) neutral fluxes. The scaling for fluxes are indicated in the figure. Cl is the major neutral radical flux and  $\text{BCl}_2^+$  is the dominant ion.

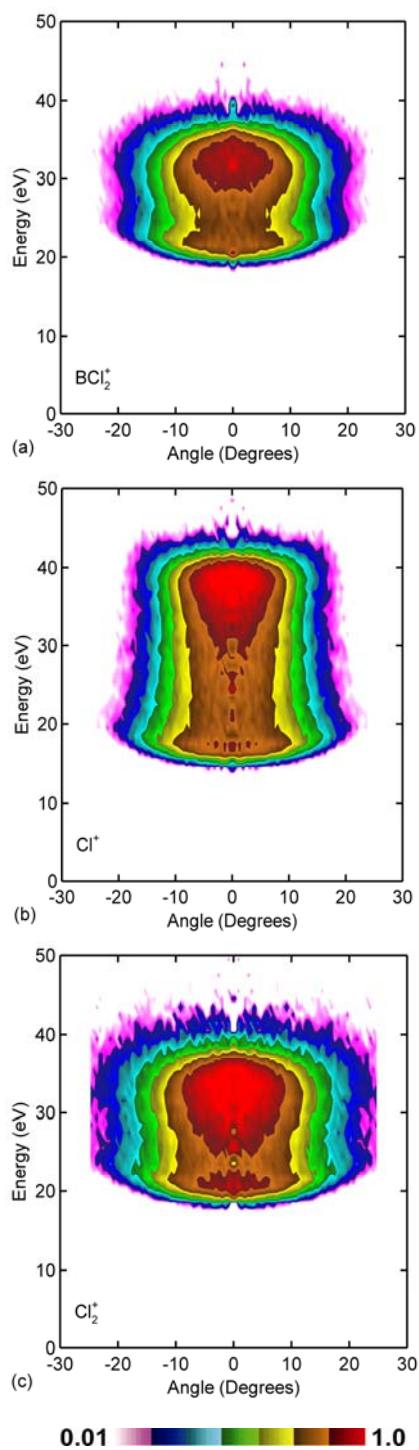


Fig. 7.5 IEADs to the wafer. (a)  $\text{BCl}_2^+$ , (b)  $\text{Cl}^+$ , and (c)  $\text{Cl}_2^+$ . Plasma conditions are Ar/ $\text{BCl}_3$ / $\text{Cl}_2$ =5/40/55, 300 W ICP, 5 mTorr, 100 sccm and a bias of 18 V.

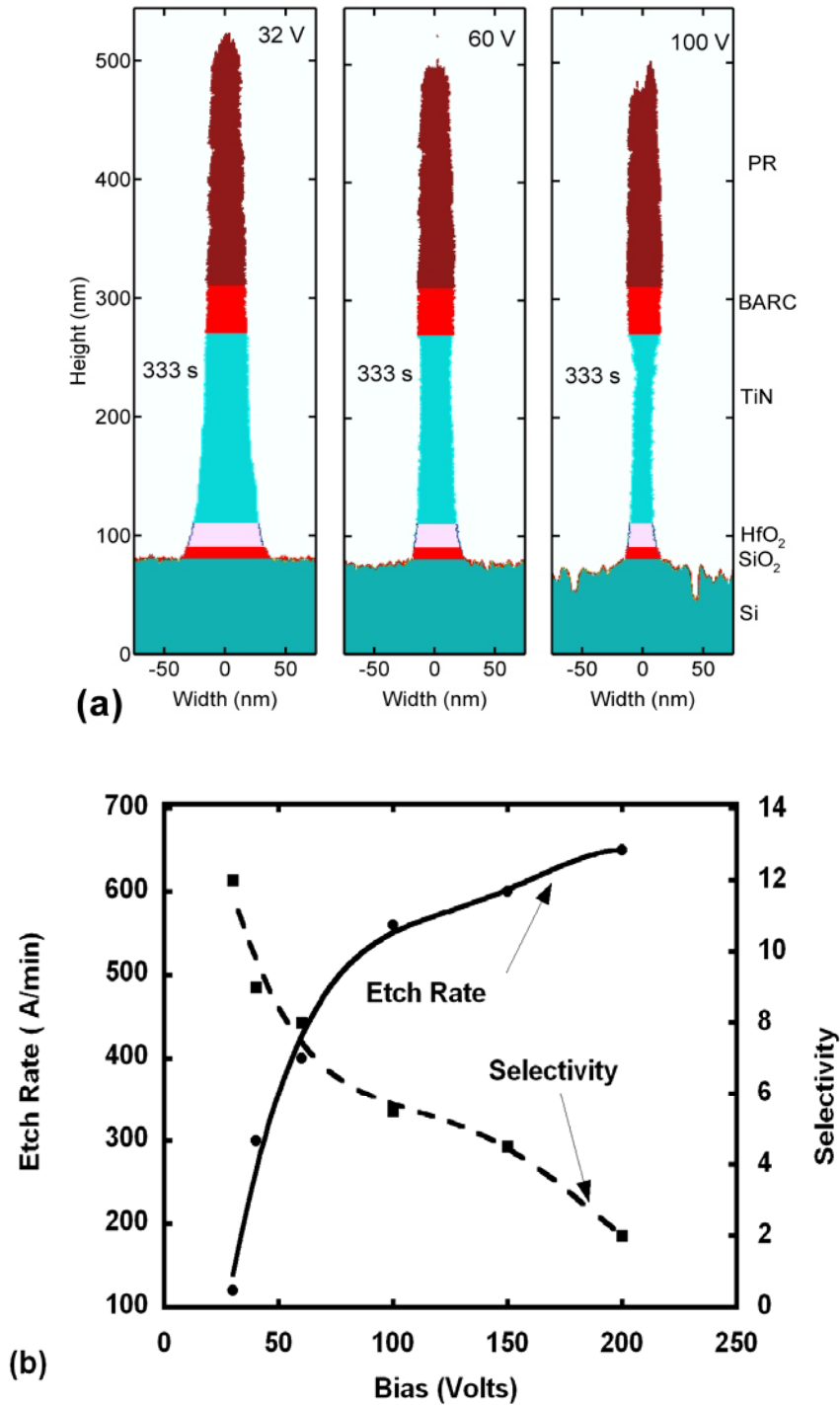


Fig. 7.6 Profiles and rates for gate-stack etching ( $\text{Ar}/\text{BCl}_3/\text{Cl}_2=5/40/55$ , 300 W ICP, 5 mTorr, and 100 sccm). a)  $\text{HfO}_2$  gate-stack profiles for biases of 32, 60 and 100 V for equal etch times corresponding to when the  $\text{SiO}_2$  layer is cleared with a 32 V bias. (b)  $\text{HfO}_2$  etch rate and selectivity as a function of bias voltage. Damage to the Si occurs for biases significantly above 30 V.

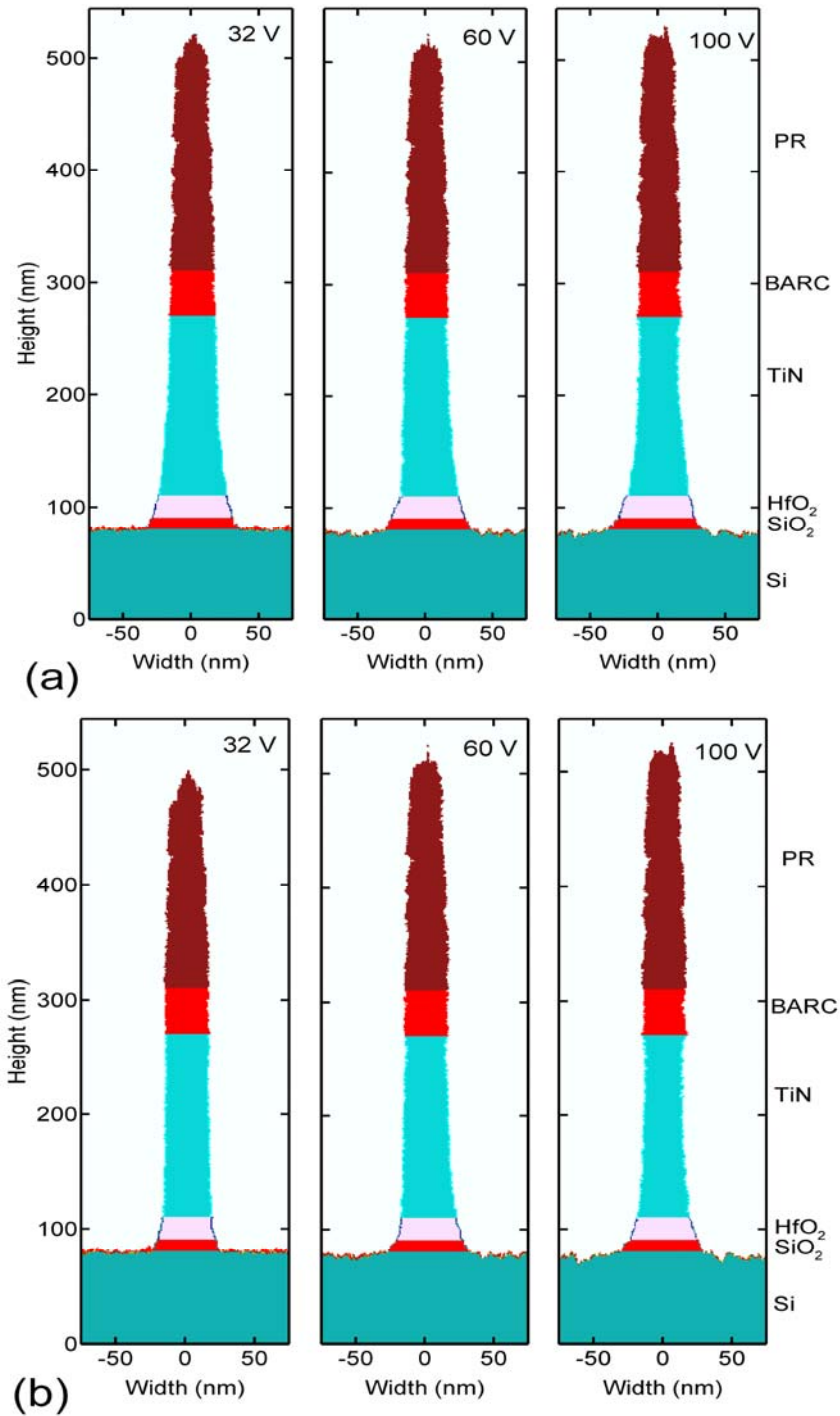


Fig. 7.7 Post-etch gate-stack profiles for 32, 60 and 100 V. (a) For times when the SiO<sub>2</sub> is cleared and (b) optimized profiles with respect to over-etch time.

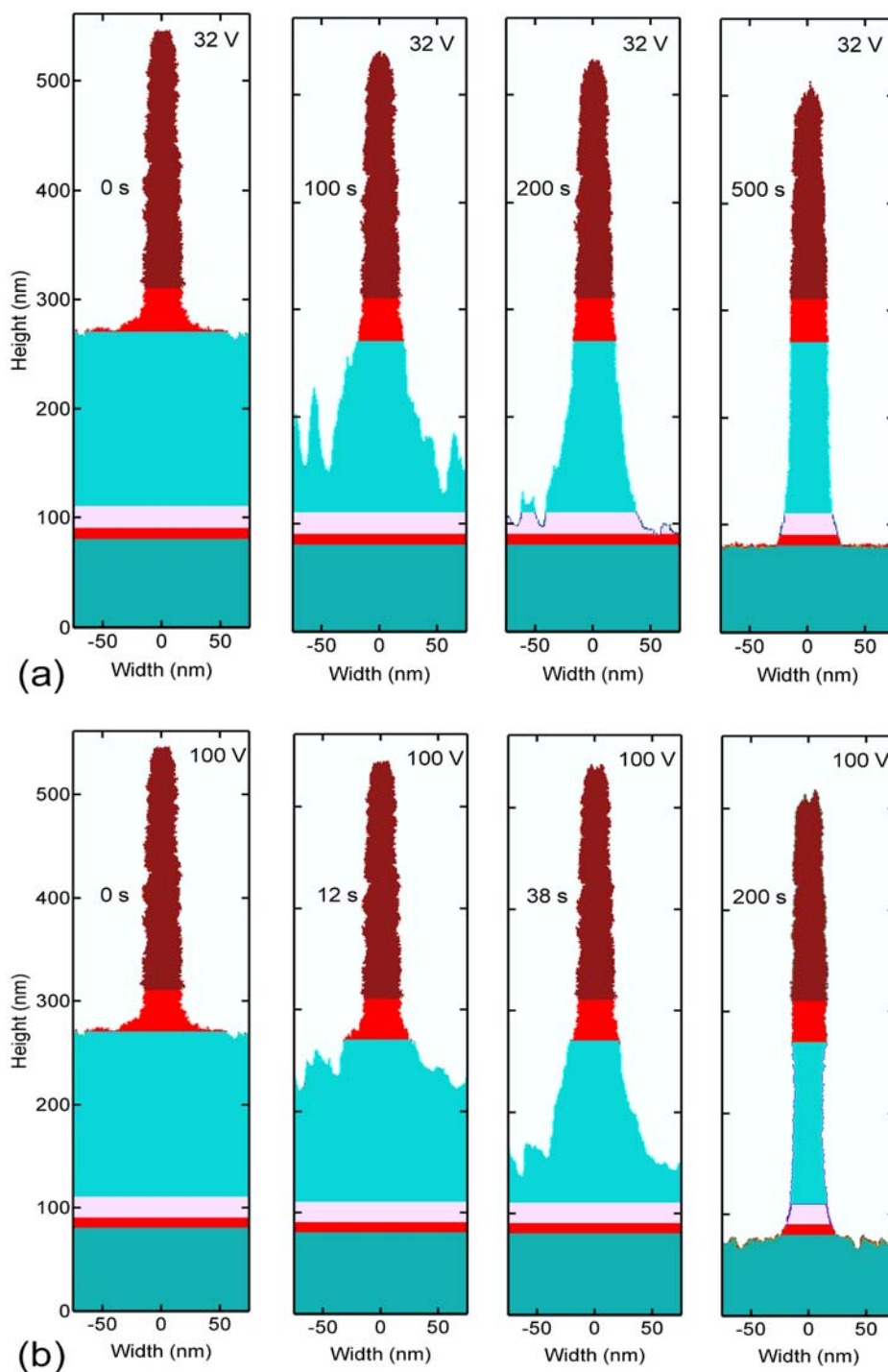


Fig. 7.8 Time sequences for gate-stack profile evolution showing the effect of BARC micro-masking on damage to the Si substrate with low and high bias voltages. (a) With a 32 V bias micro-masking does not cause significant damage to the Si during the over-etch due to the high selectivity. (b) With a 100 V bias the more rapid exposure of Si sites not micro-masked produces damage.

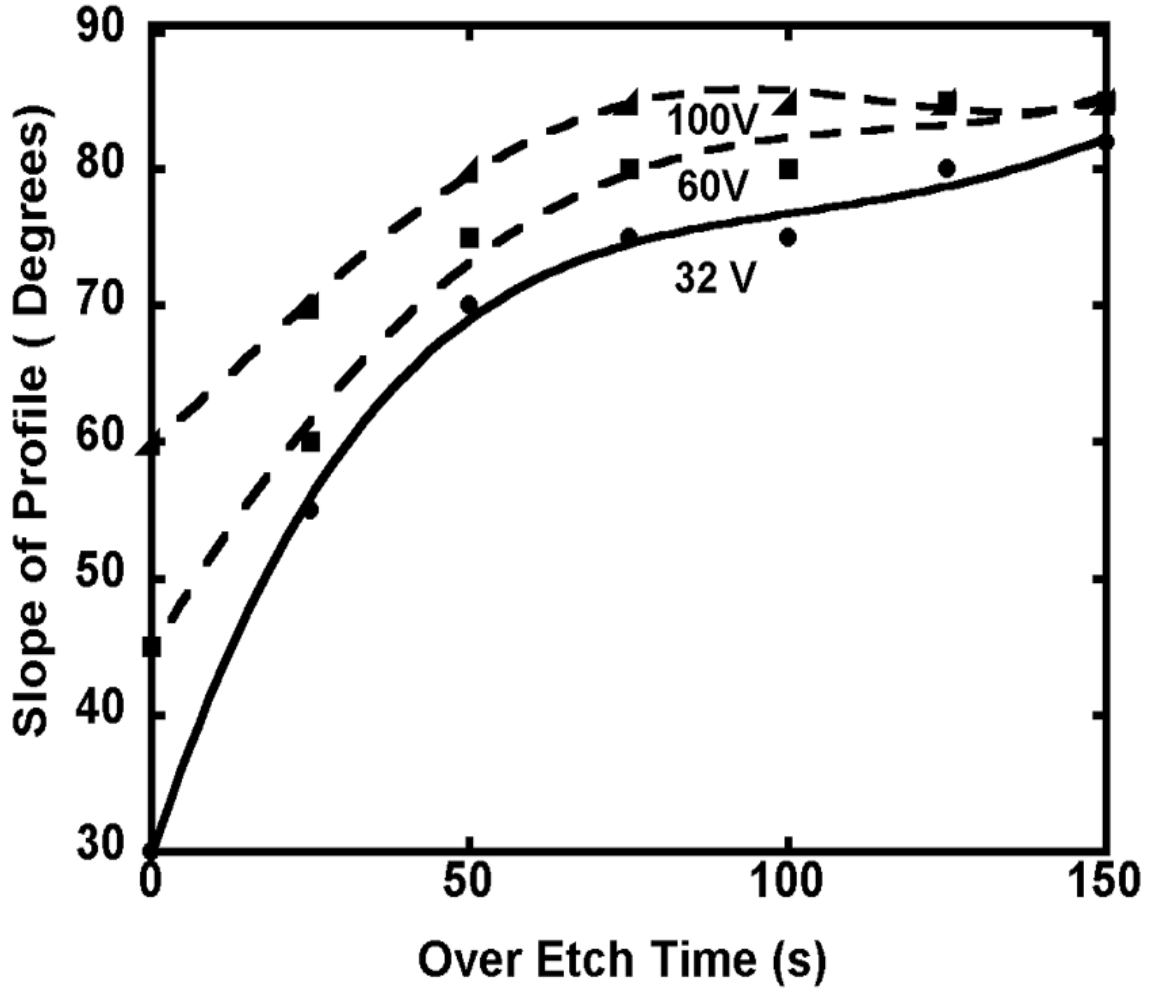


Fig. 7.9 Slopes of the gate-stack profile for different bias voltages as a function of over-etch time. A vertical profile corresponds to  $90^{\circ}$ . Higher bias voltages achieve more vertical profiles with less over-etch but at the cost of selectivity.

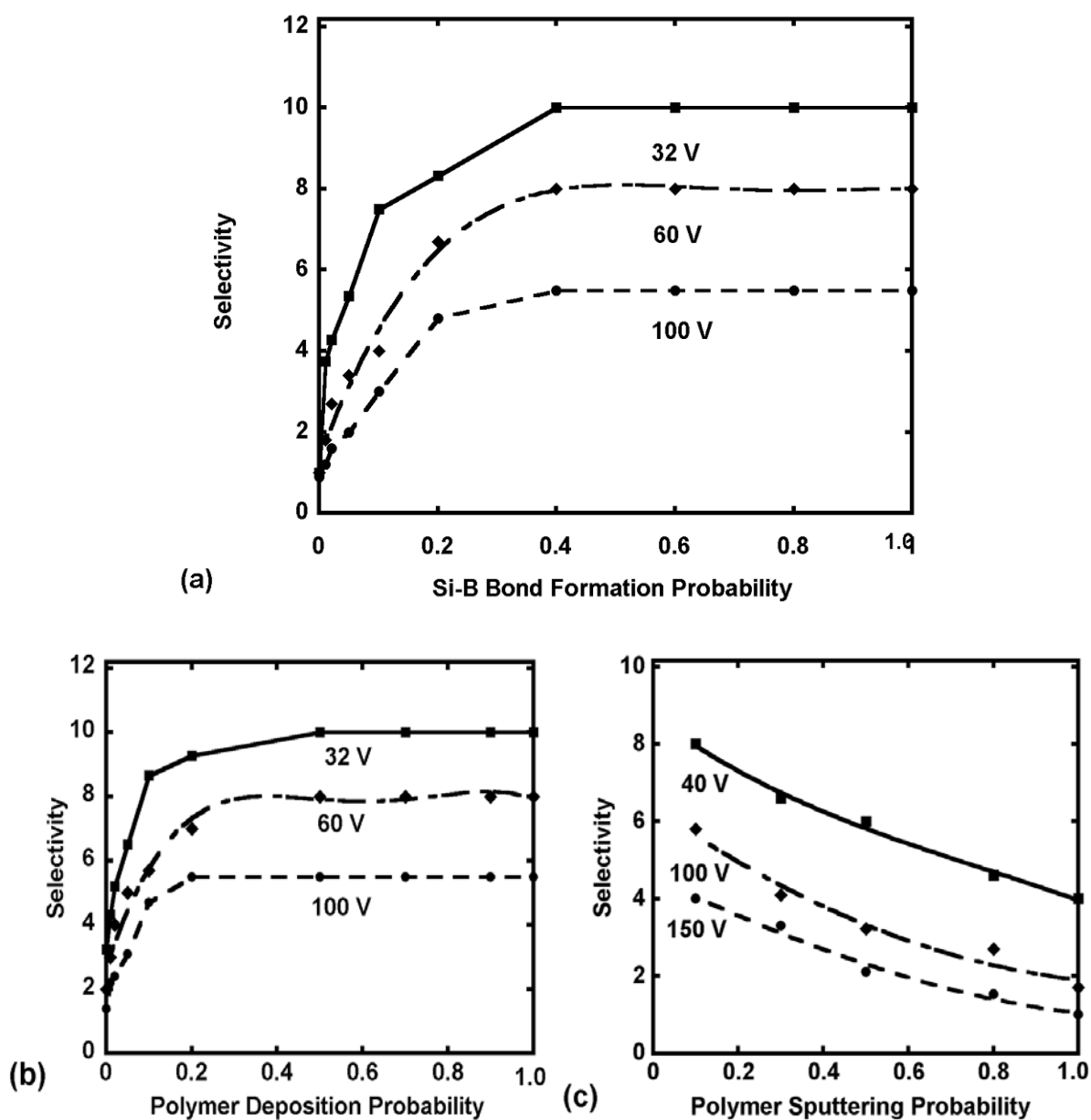


Fig. 7.10 HfO<sub>2</sub>/Si selectivity for different bias voltages as a function of the probabilities for (a) Si-B bond formation, (b) polymer deposition, and (c) polymer sputtering. (Ar/BCl<sub>3</sub>/Cl<sub>2</sub>=5/40/55, 300 W ICP, 5 mTorr, and 100 sccm).

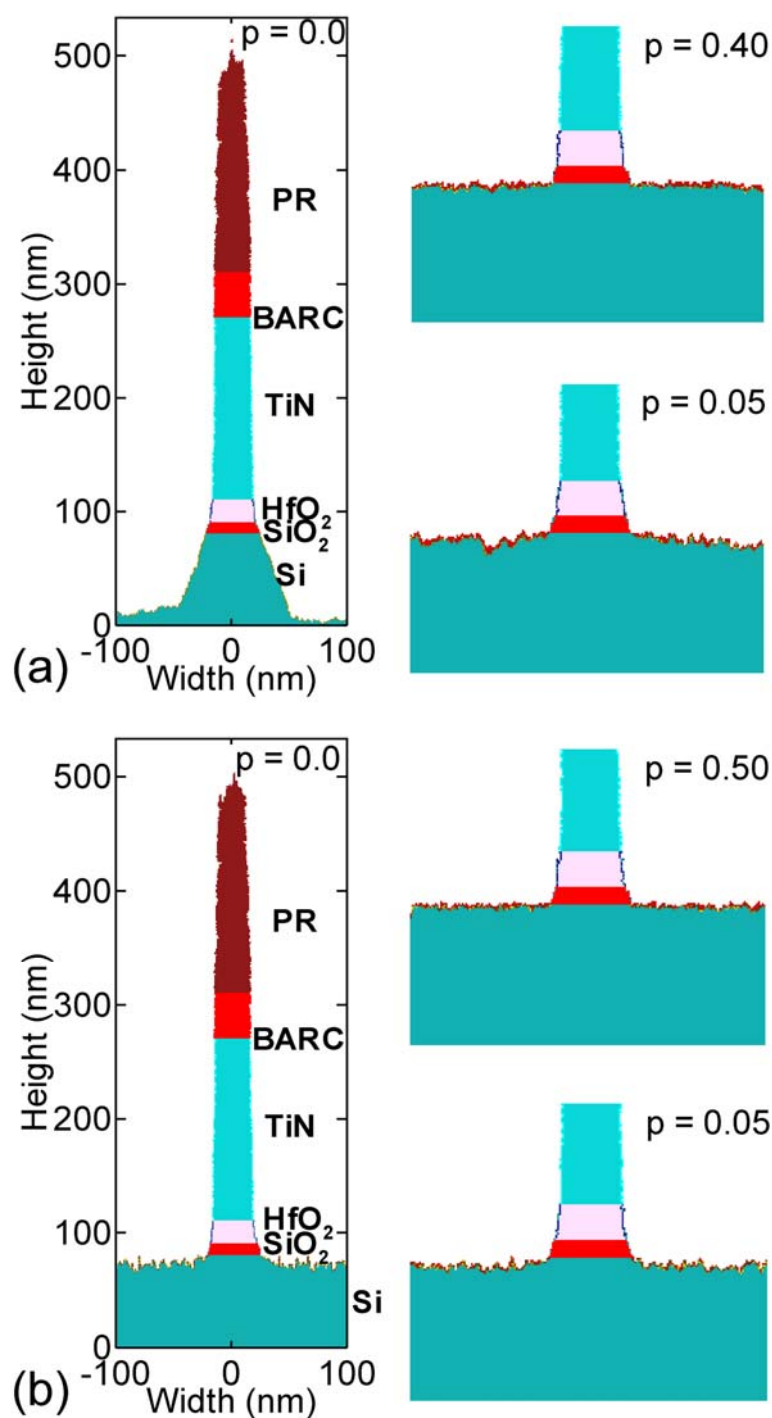


Fig. 7.11 Post-etch gate-stack profiles while varying Si-B formation and polymer formation probabilities. (a) Profiles for Si-B bond formation probabilities of 0.0, 0.05 and 0.4. (b) Profiles for polymer formation probabilities of 0.0, 0.05 and 0.4. For both cases selectivity improves with probability until the Si sites are nearly uniformly passivated. (Ar/BCl<sub>3</sub>/Cl<sub>2</sub>=5/40/55, 300 W ICP, 5 mTorr, and 100 sccm).

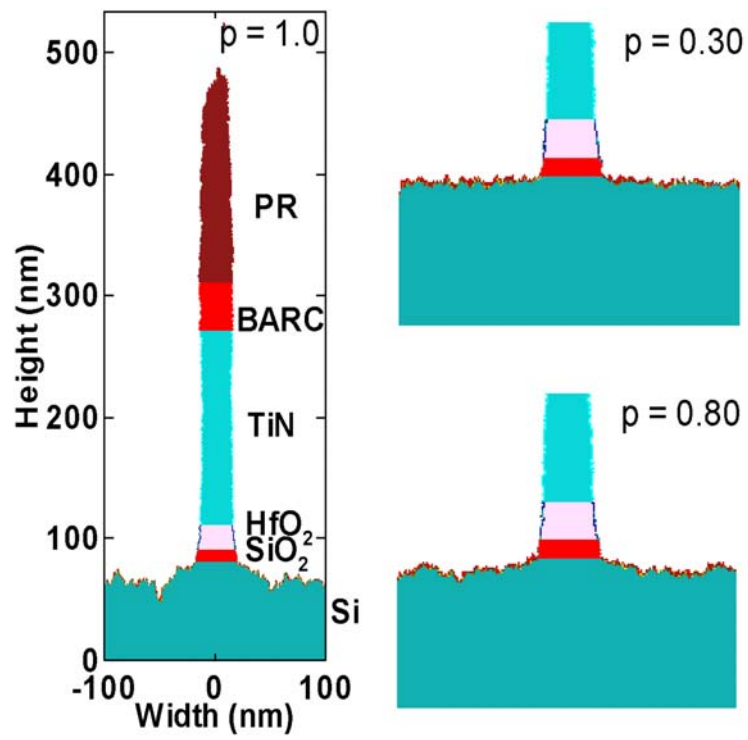


Fig. 7.12 Post-etch gate-stack profiles for polymer sputtering probabilities of 0.3, 0.8 and 1.0 (Ar/ $\text{BCl}_3$ / $\text{Cl}_2$ =5/40/55, 300 W ICP, 5 mTorr, and 100 sccm).

## 7.9 References

1. R. Chau, J. Brask, S. Datta, G. Dewey, M. Doczy, B. Doyle, J. Kavalieros, B. Jin, M. Metz, A. Majumdar, and M. Radosavljevic, *Microelectron. Engr.* **80**, 1 (2005).
2. B. H. Lee, L. Kang, R. Nieh, W.-J. Qi, and J. C. Lee, *Appl. Phys. Lett.* **76**, 1926 (2000).
3. R. Chau, S. Datta, M. Doczy, B. Doyle, J. Kavalieros, and M. Metz, *Elect. Dev. Lett.* **25**, 408 (2004).
4. O. Joubert, E. Sungauer, E. Pargon, X. Mellhaoui, R. Ramos, G. Cunge and L. Valier, *J. Vac. Sci. Technol. B* **25**, 1640 (2007).
5. M. J. Kushner, *J. Appl. Phys.* **94**, 1436 (2003).
6. C. F. Abrams and D. B. Graves, *J. Appl. Phys.* **86**, 2263 (1999).
7. A. Agarwal and M. J. Kushner, *J. Vac. Sci. Technol. A* **27**, 37 (2009).
8. L. Sha, and J. P. Chang, *J. Vac. Sci. Technol. A* **21**, 1915 (2003).
9. L. Sha, and J. P. Chang, *J. Vac. Sci. Technol. A* **22**, 88 (2003).
10. M. H. Sin, M. S. Park, and N.-E. Lee, *J. Vac. Sci. Technol. A* **24**, 1373 (2006).
11. C. Wang and V. M. Donnelly, *J. Vac. Sci. Technol. A* **26**, 597 (2008).
12. K. Nakamura, D. Hamada, Y. Ueda, K. Eriguchi, and K. Ono, *Appl. Phys. Exp.* **2**, 016503 (2009).
13. L. Sha, R. Puthenkovilakam, Y.-S. Lin, and J. P. Chang, *J. Vac. Sci. Technol. B* **21**, 2420 (2003).
14. M. Hayashi, Technical Report No. IPPJ-AM-19, Nagoya Institute of Technology, 1981.
15. K. Tachibana, *Phys. Rev. A* **34**, 1007 (1986).
16. D. Rapp and P. Englander-Golden *J. Chem. Phys.* **43**, 1464 (1965).
17. R. H. McFarland and J. Kinney, *Phys. Rev. A* **137**, 1058 (1965).

18. I. P. Zapesochnyi and L. L. Shimon, *Opt. Spectrosc.* **11** 155 (1966).
19. G. L. Rogoff, J. M. Kramer, and R. B. Piejak, *Trans. Plasma Sci.* **14**, 103 (1986).
20. R. Nagpal and A. Garscadden, *Appl. Phys. Lett.* **64**, 1626 (1994).
21. J. Marriott and J. D. Craggs, *J. Electron. Cont.* **3**, 194 (1957).
22. J. B. A. Mitchell, *Phys. Reports* **186**, 215 (1990).
23. S. G. Lias, J. E. Bartmess, J. F. Liebman, J. L. Holmes, R. D. Levin and W. G. Mallard, *J. Phys. Chem. Ref. Data* **17**, Supplement 1 (1998).
24. Y. Ikezoe, S. Matsuoka, M. Takabe, and A. Viggiano, *Gas Phase Ion-Molecule Reaction Rate Constants Through 1986* (Mass Spectroscopy Society of Japan, Tokyo, 1987).
25. NIST Chemical Kinetics Database 17, Version 2Q98, <http://kinetics.nist.gov/index.php>.
26. W. S. Hwang, J. Chen, and W. J. Yoo, *J. Vac. Sci. Technol. A* **23**, 964 (2005).
27. C. -Y. Sin, B. H. Chen, W. L. Loh, J. Yu, P. Yelehanka, A. See, and L.Chan, *J. Vac. Sci. Technol. B* **20**, 1974 (2002).
28. C. -Y. Sin, B. H. Chen, W. L. Loh, J. Yu, P. Yelehanka, A. See, and L.Chan, *AIChE J.* **50**, 1578 (2004).
29. T. -F. Yen, C. M. Chiu, and K. F. Chiu *Microelectron. Engr.* **75**, 201 (2004).
30. S. Mathew, R. Nagarajan, L. K. Bera, F. H. Hua, D. A. Yan, and N. Balasubramanian, *Thin Solid Films* **63**, 462 (2004).

## 8. CONCLUSIONS AND FUTURE WORK

### 8.1 Conclusions

The primary motivation of this thesis is the improved understanding of poorly-known surface-plasma interaction mechanisms for nano-scale processing. The thesis addresses reaction mechanisms for processes involving low- $k$  dielectrics and high- $k$  gate-stacks, both of which have been extensively investigated over the last few years. Understanding such mechanisms is important for better control and optimization of plasma processes in semiconductor fabrication. The mechanisms discussed in this thesis have been developed through extensive parameterization using fragmented data available in literature while reproducing experimental results. The mechanisms can be further refined as more (consistent) experimental results are made available.

For the processing of low- $k$  porous SiCOH, selection of a plasma mixture for a process should depend on its capability to preserve  $-\text{CH}_3$  groups. This is because  $-\text{CH}_3$  groups block water incorporation into the low- $k$  and thus prevent the rise of the  $k$  value of the porous film. For example, in the thesis, we found He/H<sub>2</sub> plasmas to be a better option compared to Ar/O<sub>2</sub> for cleaning and PR stripping. For an interconnected porous network, radicals play the dominant role in the demethylation process through diffusion into the network, which is responsible for the loss of  $-\text{CH}_3$  groups and subsequent water uptake and low- $k$  degradation. However, ions can also increase such damage to some extent near the surface.

We also found that VUV or UV photons with wavelengths  $<140$  nm have the energy to break Si-C bonds of SiO<sub>2</sub>-CH<sub>3</sub> groups which can then act as an accelerating factor for the demethylation process. Such bond scission produces the opportunity for radicals and even for molecules to speed demethylation. The capability of gaining control on the preservation

of the low- $k$  can be enhanced by implementing a technique that blocks or seals surface pore-openings. We have investigated the use of surface-pore sealing with sequential He and  $\text{NH}_3$  plasmas and predicted closing of surface pores which prevented pathways required by humid air to diffuse into the network.

For high- $k$  gate-stack etching, the important priority is a high high- $k$ /Si selectivity. Such selectivity protects the regions of the Si substrate where source and drain of the transistor are located. The prerequisite for such selectivity is to select plasmas that can form a passivation layer on the Si substrate and to control the substrate bias such that the ion energy is high enough to etch the high- $k$  material but still below the etching threshold of the passivation layer formed on the Si substrate. Such a passivation layer can be a compound with Si-M bonds where M is an element of the plasma, or a polymer deposited on the Si substrate, or both. It is important to understand the nature and characteristic of such Si-M bonding and polymers because such compounds will decide if the passivation is able to provide the expected selectivity under certain bias conditions.

We investigated selective  $\text{HfO}_2$ /Si etching in  $\text{Ar}/\text{Cl}_2/\text{BCl}_3$  plasmas. We found the formation of Si-B bonding on Si substrate and  $\text{BCl}_x$  polymers on the top of Si-B bonding is the mechanism responsible for the high  $\text{HfO}_2$ /Si selectivity. If the ion energy is controlled such that the ion energy is above the threshold of  $\text{HfO}_2$  etching but lower than the sputtering threshold of  $\text{BCl}_x$  polymers and Si-B bonding, then a high selectivity can be obtained.

## 8.2 Future Work

In our computational investigation, we simulated the etching of porous SiCOH in fluorocarbon plasmas and cleaned deposited  $\text{CF}_x$  polymers after such etching. To realize porous

low- $k$  in our model, we substituted pore bordering SiO<sub>2</sub> cells with hydrophobic –CH<sub>3</sub> groups. Future modeling can involve realization of more complex organic porous materials where such –CH<sub>3</sub> groups are included beyond the pore border. To investigate pore sealing mechanisms with successive He and NH<sub>3</sub> plasma treatment, we considered only chemical interactions between He plasma species and porous low- $k$  surface. These interactions are responsible for surface activation which prepares the surface for a better sealing in the subsequent NH<sub>3</sub> plasma treatment. However, some experimental results have suggested even more complex mechanisms during the He pretreatment which involve the shrinking of the pore-neck (surface densification). Along with the chemical modifications such shrinkage facilitates the pore sealing. Future work can include such pore-neck shrinking mechanisms during He pretreatment.

To clean deposited CF<sub>x</sub> polymer etching formed during fluorocarbon plasma etching of porous SiCOH and strip masking PR, we investigated both Ar/O<sub>2</sub> and He/H<sub>2</sub> plasmas. While He/H<sub>2</sub> plasmas produced little damage compared to Ar/O<sub>2</sub> plasmas, the PR stripping rate is much slower. Recently, industry has implemented cleaning methods based on CO or CO<sub>2</sub> plasmas. It has been reported that such cleaning is less harmful to –CH<sub>3</sub> groups compared to O<sub>2</sub> plasmas but can still strip PR with a faster rate compared to He/H<sub>2</sub> plasmas. The low damage in CO<sub>2</sub> cleaning may be attributed to the lower flux of O radicals in a CO<sub>2</sub> plasma, which is the dominant agent for cleaning. The O flux in CO/CO<sub>2</sub> plasmas is approximately one fifth that in comparable Ar/O<sub>2</sub> plasmas. Also, perhaps, VUV/UV photon fluxes with wavelengths <140 nm, which are agents for demethylation, are less dominant in CO<sub>2</sub> plasmas compared to Ar/O<sub>2</sub> plasmas.

Our reaction mechanism for gate-stack addressed TiN/HfO<sub>2</sub>/Si gate-stack etching. The reaction mechanism can be updated for a more complex high-*k* such as HfSiON etching and for etching a different metal gate than TiN. The gate-stack reaction mechanism can also be modified for a process that uses a different but still Cl<sub>2</sub> or BCl<sub>3</sub> based plasmas.

### **AUTHOR'S BIOGRAPHY**

Juline Shoeb received his BS in Electrical Engineering from Bangladesh University of Engineering and Technology in 2004. He completed his MS in Electrical Engineering in 2007 from North Dakota State University where his research involved modeling of maximum power extraction algorithms for solar panels. He joined Iowa State University in 2007 August as a PhD student in the group of Prof. Mark J. Kushner and has been working on plasma-surface interactions modeling for nano-scale processing. His PhD research includes modeling and development of reaction mechanisms and feature-scale profiling that addresses porous low- $k$  clean, sealing and degradation, and high- $k$  gate-stack etching with Si selectivity. Under the guidance of Prof. Kushner his work has resulted in 3 published refereed journal publications with 2 more submitted, 12 conference presentations and 3 conference publications. Upon graduation in February 2012 with his Ph. D in Electrical Engineering from Iowa State University, he will work with Lam Research Corp. in Fremont, CA as a process engineer.